2013

THERMOBAROMETRY OF METAMORPHOSED PSEUDOTACHYLYTE AND DETERMINATION OF SEISMIC RUPTURE DEPTH DURING DEVONIAN CALEDONIAN EXTENSION, NORTH NORWAY

Susan E. Leib
University of Kentucky, leib.susan@gmail.com

STUDENT AGREEMENT:

I represent that my thesis or dissertation and abstract are my original work. Proper attribution has been given to all outside sources. I understand that I am solely responsible for obtaining any needed copyright permissions. I have obtained and attached hereto needed written permission statements(s) from the owner(s) of each third-party copyrighted matter to be included in my work, allowing electronic distribution (if such use is not permitted by the fair use doctrine).

I hereby grant to The University of Kentucky and its agents the non-exclusive license to archive and make accessible my work in whole or in part in all forms of media, now or hereafter known. I agree that the document mentioned above may be made available immediately for worldwide access unless a preapproved embargo applies.

I retain all other ownership rights to the copyright of my work. I also retain the right to use in future works (such as articles or books) all or part of my work. I understand that I am free to register the copyright to my work.

REVIEW, APPROVAL AND ACCEPTANCE

The document mentioned above has been reviewed and accepted by the student's advisor, on behalf of the advisory committee, and by the Director of Graduate Studies (DGS), on behalf of the program; we verify that this is the final, approved version of the student's dissertation including all changes required by the advisory committee. The undersigned agree to abide by the statements above.

Susan E. Leib, Student

Dr. David P. Moecher, Major Professor

Dr. Alan E. Fryar, Director of Graduate Studies

THERMOBAROMETRY OF METAMORPHOSED PSEUDOTACHYLYTE AND DETERMINATION OF CO-SEISMIC SLIP DEPTH DURING DEVONIAN CALEDONIAN EXTENSION, NORTH NORWAY

THESIS

A thesis submitted in partial fulfillment of the
requirements for the degree of Master of Science in the
College of Arts and Sciences at the University of
Kentucky

By

Susan E. Leib

Lexington, Kentucky

Director: Dr. David Moecher, Professor of Geology

Lexington, Kentucky

2012

ABSTRACT OF THESIS

THERMOBAROMETRY OF METAMORPHOSED PSEUDOTACHYLYTE AND DETERMINATION OF SEISMIC RUPTURE DEPTH DURING DEVONIAN CALEDONIAN EXTENSION, NORTH NORWAY

Crustal faulting has long been known as the source of shallow seismicity, and the seismogenic zone is the depth (3-15 km) within the crust that is capable of co-seismic slip, largely under brittle conditions. However, some continental seismicity occurs at depths >> 15 km. I performed thermobarometry of mylonitic pseudotachylyte to determine the P-T of a seismogenic extensional fault in the Caledonian Norwegian margin. Two shear zones (Eidsfjord and Fiskfjord) located in northern Norway exhibit brittle extension propagating into the ductile regime of the lower crust as evidenced by the presence of pseudotachylyte. Averages from Eidsfjord (653 ± 38°C and 570 ± 115 MPa) and Fiskfjord (680 ± 70°C and 1121 ± 219 MPa) correspond to depths of co-seismic slip of 21 ±4 km and 41 ± 9 km, respectively. These depths are 5-25 km below the depth of the standard seismogenic zone in mature fault systems, and require another mechanism (e.g. dynamic downward rupture, unusually high shear stresses) to account for seismogenic rupture at such depths. Assuming Eidsfjord and Fiskfjord were uplifted at the same time, and considering they are currently at the same crustal level, Fiskfjord was uplifted a greater amount and at a faster rate as it was initially located at a greater crustal depth.

KEYWORDS: pseudotachylyte, seismogenic zone, crustal depth, thermobarometry, Norway

Susan E. Leib

11-19-2012

THERMOBAROMETRY OF METAMORPHOSED PSEUDOTACHYLYTE AND DETERMINATION OF SEISMIC RUPTURE DEPTH DURING DEVONIAN CALEDONIAN EXTENSION, NORTH NORWAY

By

Susan E. Leib

Dr. David P. Moecher
Director of Thesis

Dr. Alan E. Fryar
Director of Graduate Studies

11-19-2012

ACKNOWLEDGMENTS

I thank the Department of Earth and Environmental Sciences at the University of Kentucky for the opportunity to pursue a Master's Degree in geology, and especially my advisor, Dr. David P. Moecher who patiently provided a great deal of assistance and encouragement throughout the entire research and writing process. I would also like to thank committee members Dr. Kent Ratajeski and Dr. Sean Bemis for their helpful editing. Additional thanks are extended to Dr. Chris Berg at the University of Western Georgia for teaching a THERMOCALC short course and Jason Backus at the Kentucky Geological Survey for assistance in sample preparation.

Success would not have been possible without the moral support and shared suffering of my fellow graduate students in the Department of Earth and Environmental Sciences, most notably my officemates Gabriel RiCharde and Ryan Quinn and comrades Forrest Webb and Sara Federschmidt. Thanks also to friends and family for their support and encouragement along the way.

TABLE OF CONTENTS

Acknowledgements ……iii

Table of Contents ……...iv

List of Tables ……..v

List of Figures ……vi

Chapter 1: Introduction ……1
1.1 Pseudotachylyte ……5

Chapter 2: Geologic Setting ……...10
2.1 Eidsfjord ……11
2.2 Fiskfjord ……12
2.3 Pseudotachylyte ……13

Chapter 3: Petrology ……24
3.1 Sample Descriptions ……24
3.1.1 Eidsfjord Sample Descriptions ……..24
3.1.2 Detailed Eidsfjord Sample Descriptions ……26
3.1.3 Fiskfjord Sample Descriptions ……...27
3.1.4 Detailed Fiskfjord Sample Descriptions ……28

Chapter 4: Thermobarometry ……58
4.1 Methods ……61
4.2 Results ……61
4.2.1 Mineral Chemistry ……61
4.2.2 Results of Thermobarometry ……..62
4.2.3 Depth Estimates ……63

Chapter 5: Discussion ……..87
5.1 Study Comparison ……..88
5.2 Summary ……90

Chapter 6: Conclusion ……93

Appendices ……95
Appendix A ……95
Appendix B ……107
Appendix C ……119

References ……142

Vita ……..148

LIST OF TABLES

Table 4.1, Eidsfjord End-member averages ……65
Table 4.2, Fiskfjord End-member averages ……66
Table 4.3, Eidsfjord Domain P-T values……..67
Table 4.4, Fiskfjord Domain P-T values ……..68

LIST OF FIGURES

Figure 1.1, Simplified Crustal Strength Model ……8
Figure 1.2, Conceptual Fault Zone Model ……..9

Figure 2.1, Lofoten-Vesterålen Map and Cross section ……..14
Figure 2.2, Study Area Geologic Map (Eidsfjord and Fiskfjord) ……..15
Figure 2.3, Study Area Cross Section ……...16
Figure 2.4, Study Area Geologic Map Detail: Eidsfjord ……17
Figure 2.5, Eidsfjord Shear Zone Photo and Sketch ……18
Figure 2.6, Eidsfjord Lithology Progression ……19
Figure 2.7, Study Area Geologic Map Detail: Fiskfjord ……..20
Figure 2.8, Fiskfjord Shear Zone Photo and Sketch ……21
Figure 2.9, Fiskfjord Lithology Changes ……22
Figure 2.10, Pseudotachylyte photomicrograph ……..23

Figure 3.1, Hand Sample Photos ……29
Figure 3.2, Thin Section Photos ……30
Figure 3.3, Eidsfjord detachment cross section model ……31
Figure 3.4, Eidsfjord: Representative thin sections ……32
Figure 3.5, Photomicrographs of EID08-4-3 and EID08-3c2 ……33
Figure 3.6, Photomicrographs of EID08-5-1 ……34
Figure 3.7, Photomicrographs of EID08-7-1 ……35
Figure 3.8, Photomicrographs of EID08-5-1 ……36
Figure 3.9, Photomicrographs of EID08-2b ……..37
Figure 3.10, Photomicrographs of EID08-8-1 ……38
Figure 3.11, Photomicrographs of EID08-7-5 ……39
Figure 3.12, Thin section and Photomicrographs of EID08-8-2 ……..40
Figure 3.13, Photomicrographs of EID08-3a ……41
Figure 3.14, Garnet BSE image and X-ray maps ……..42
Figure 3.15, Photomicrographs of EID08-4-6a-2 ……..43
Figure 3.16, Photomicrographs of EID08-7-2b ……44
Figure 3.17, Fiskfjord: Representative thin sections ……45
Figure 3.18, Photomicrographs of 86-09-3-1 and FIS09-2a-1b ……46
Figure 3.19, Photomicrographs of FIS09-2b and FIS09-3a-1b ……47
Figure 3.20, Photomicrographs of 86-09-1b-2 and 86-09-3a ……..48
Figure 3.21, Photomicrographs of 86-09-1b-1 and FIS09-2d ……49
Figure 3.22, Photomicrographs of 86-09-3a ……50
Figure 3.23, Photomicrographs of 86-09-4-1 and 129-09-2-2a ……51
Figure 3.24, Photomicrographs of FIS09-2a-1b and FIS09-3a-1b ……52
Figure 3.25, Photomicrographs of FIS09-2b ……..53
Figure 3.26, Photomicrographs of FIS09-2b ……..54
Figure 3.27, Photomicrographs of FIS09-2d ……..55
Figure 3.28, Photomicrographs of FIS09-2d ……56
Figure 3.29, Photomicrographs of FIS09-3a-1b ……..57

Figure 4.1, Traverse, BSE, and Elemental X-ray images of EID08-3a Garnet 12 ……69
Figure 4.2, Traverse, BSE, and Elemental X-ray images of EID08-4-6a-2 Garnet 3 ……70
Figure 4.3, Traverse, BSE, and Elemental X-ray images of EID08-7-2b Garnet 4 ……..71
Figure 4.4, Traverse, BSE, and Elemental X-ray images of FIS09-2b Garnet 1 ……72
Figure 4.5, Traverse, BSE, and Elemental X-ray images of FIS09-2d Garnet 4 ……73

Figure 4.6, Traverse, BSE, and Elemental X-ray images of FIS09-3a-1b Garnet 2 ……..74
Figure 4.7, Eidsfjord Garnet Compositional plot ……..75
Figure 4.8, Eidsfjord Hornblende Compositonal plot ……..76
Figure 4.9, Eidsfjord Plagioclase Compositional plot ……..77
Figure 4.10, Fiskfjord Garnet Compositional plot ……78
Figure 4.11, Fiskfjord Hornblende Compositional plot ……79
Figure 4.12, Fiskfjord Plagioclase Compositional plot ……80
Figure 4.13, Eidsfjord P-T plot (all samples) ……..81
Figure 4.14, Fiskfjord P-T plot (all samples) ……..82
Figure 4.15, Eidsfjord and Fiskfjord P-T plot (Mg calculations) ……83
Figure 4.16, Eidsfjord and Fiskfjord P-T plot (Fe calculations) ……84
Figure 4.17, Fiskfjord High Mg Barometers ……85
Figure 4.18, All Eidsfjord and Fiskfjord P-T ……...86

Figure 5.1, Tectonic Model ……92

CHAPTER 1: Introduction

Earthquakes and the production of seismic waves are a few of the primary tools that allow study of the earth's inner structure. Because earthquakes are directly linked to crustal faulting, any seismic event provides additional information regarding the nucleation and propagation of fault rupture in the seismogenic zone (Rice and Cocco, 2007). The seismogenic zone is defined as the section of crust where earthquakes nucleate, or rather, the volume of rock surrounding a fault that is capable of seismicity (Ruff, 2004). Though the seismogenic zone may constrain the crustal location for earthquake nucleation, it does not necessarily determine the limit of fault propagation (Scholz, 2002). A study of seismicity in Japan (Iio and Kobayashi, 2002) finds that some intraplate earthquakes exhibit lower crustal extension, and that strain accumulation in an aseismic zone can lead to faulting in the upper crust.

The location of the seismogenic zone in the crust is directly related to variations in the frictional behavior of the surrounding rock (Scholz, 1988). Ruina (1983) identified the frictional rate parameter (A-B), where any stability in the crust is defined by a positive (A-B) value and friction is velocity strengthening. Any instability in the crust is then defined by a negative (A-B) value, where friction is considered velocity weakening. Scholz (1988) has identified an 'upper stability boundary' at 2 km depth in the crust to account for the unconsolidated material found in shallow fault gouge material as well as the critical stiffness dependence on normal stress (Scholz, 2002). This is supported by the idea that earthquakes are not generated in the uppermost (2 km) section of crust, and would correlate to a positive frictional rate. The lower stability boundary is defined by the transition of wear in fault rock mechanisms from an abrasive frictional regime to an adhesive ductile regime (Scholz, 1988; 2002). This ductile regime correlates to a 'velocity weakening' zone due to the loss of friction (negative frictional rate). Velocity weakening due to the decreasing friction rate defines the seismogenic zone, which exists between the transitions of the upper and lower stability boundaries in the crust (Scholz, 1988, 2002). A simplified model of

the lithosphere rheology (Figure 1.1) shows the transition between the brittle and ductile regimes in the crust.

Temperature constraints pertaining to fault rupture depth in the lithosphere are commonly set by the onset of crystal plasticity for both quartz and feldspar, assuming a granitic mineralogic composition (Tullis and Yund, 1980). The first parameter concerns quartz plasticity, defined as the brittle-semibrittle boundary (Scholz, 2002) which occurs around 300°C. This temperature marks complete plastic flow in quartz-rich rocks, which is associated with lattice strain recovery and recrystallization (Scholz, 1988). This is also the zone in the crust identified by Sibson (1977) to be a relative elastic-frictional/quasi-plastic boundary, where shear within a fault reaches a peak value, at a depth of 10-15 km. The second parameter concerns feldspar plasticity, defined as the semibrittle-plastic boundary (Scholz, 2002). This occurs around 450°C and marks plastic flow for feldspar (Scholz, 1988). In relation to metamorphism, quartz becomes ductile towards the beginning of the greenschist facies, and feldspar becomes ductile at lower amphibolite facies (Scholz, 1988). Figure 1.2 refers to the Scholz (1988, 2002) shear zone model, with a temperature gradient based on a San Andreas heat flow model (Lachenbruch and Sass, 1980).

In previous studies, the only way to determine the various depth ranges of the seismogenic zone was via seismological methods (earthquake focal depth solutions), or modeling geodetic data (Sibson, 2003). Current understanding of the thickness of the seismogenic zone derives from either earthquake focal depth distributions, or from qualitative data obtained from rocks in exhumed fault zones. Sibson (2003) states that while the thickness of the seismic slip zone does not have any direct seismological constraints, many modern techniques have the ability to incorporate seismology to record earthquake locations to within a few meters and define the thickness of the crustal brittle section of a major fault. However, recent research completed in the central Andes (Devlin et al., 2012) observes that many reported earthquakes from routine seismic wave analyses in standard global reports are not useful due to location inaccuracies, especially with respect to depth. Their study was completed to determine more accurate continental

earthquake depths using surface reflected seismic wave phases and ground deformation measurements. When coupled together, these two processes constrain a more accurate seismogenic zone depth for any regional scale. On a local scale, seismological studies are required for the depth resolution of earthquake focal mechanisms to constrain the thickness of the seismogenic crust.

In addition to using seismology to constrain the lower depth limit of the seismogenic zone, ancient exhumed fault zones have been reported to contain unique rock types indicative of coseismic slip, i.e., veins of pseudotachylyte (Sibson and Toy, 2006), which can be used to quantify the earthquake focal depths. With the application of thermobarometry, pseudotachylyte with an appropriate mineral assemblage can be used to determine a generalized location and depth of the seismogenic zone in a specific area. To properly apply thermobarometry, the mineral assemblage of the rock sample is assumed to represent a preserved equilibrium section of the P-T path through which the rock sample moved (Powell and Holland, 2008). Calculated pressures can be used to calculate depth, assuming a crustal density distribution, at which the pseudotachylyte formed during coseismic slip in the seismogenic zone. The depth can then be used to estimate other crustal parameters during seismic faulting and extensional rifting, e.g., temperature and geothermal gradient, which have a direct bearing on rock strength.

Low-angle normal faults throughout northern Norway display shear zones that imply large scale post-Caledonian continental extension (Steltenpohl, 2004). The western margin of Norway is interpreted as the subducted margin of the Baltic plate during early Devonian collision with Laurentia which resulted in the Scandian phase of the Caledonian Orogeny. The shallowly dipping normal faults and subsequent shear zones are a manifestation of the continental rifting and crustal extension that was initiated in the Late Devonian (Osmundsen and Ebbing, 2008). Various fault rock types have been identified from two main shear zones, Eidsfjord and Fiskfjord. A variety of high-temperature mylonite is abundant in the shear zones, along with a range of fault

rocks from cataclasite to ultracataclasite, and pseudotachylyte (Plattner et al., 2003; Moecher and Steltenpohl, 2009, 2011; Steltenpohl et al., 2011).

The presence of pseudotachylyte in these shear zones is rather unique, due to its relationship to the seismogenic zone at the time of formation (Swanson, 1992). The occurrence of pseudotachylyte in the study areas of northern Norway is generally restricted to shear zones in direct contact with continental basement rock at granulite- or upper-amphibolite-facies (Steltenpohl et al., 2006, 2011). Obtaining P-T data for the occurrences of coseismic slip in northern Norway has implications for deep crustal seismicity at extensional margins, and the occurrence of ancient earthquakes. Evidence for multiple generations of pseudotachylyte likely represents multiple ancient large-magnitude earthquakes that occurred on the fault zone, indicating multiple phases of coseismic slip. This idea coincides with the shear zone location on an actively extending plate margin, and is unique due to the melt preservation alone, regardless of the fact that several melt phases have been preserved throughout the evolution of this crustal margin.

The existence of high strains in the brittle regime of the crust to produce a large-magnitude earthquake, when transferred to the ductile regime, would merely translate into increased plastic deformation and dynamic recrystallization of feldspar and quartz (Lin et al., 2005). Within the brittle regime of the crust, strain is accumulated because a fault is locked in the seismogenic zone, the base of which is identified as the brittle-ductile transition. Below the transition in the ductile regime, the crust is freely deforming so strain is not accumulated. To produce a brittle rupture in the ductile zone, an earthquake must nucleate in the brittle regime of the crust (within the seismogenic zone), and due to the extremely high strain rate that results, the rupture can then propagate into the ductile zone, where pseudotachylyte formation occurs.

1.1 Pseudotachylyte

The formation of pseudotachylyte within the ductile regime of the crust presents a question of the depth where brittle features may terminate within the crust, and where ductile features begin and dictate deformation in the lower crust. This phenomenon can be explained by brittle fault segments propagating from the brittle crustal regime down into the ductile region. However, if the fault continues through a crustal discontinuity (similar to that of the western Norwegian margin) then coseismic slip may occur on the fault through much of the middle and lower crust (Osmundsen et al., 2002; Moecher and Steltenpohl, 2011).

The formation of pseudotachylyte within the crust requires that at one point, the host rock contained a melt phase (Magloughlin and Spray, 1992) and therefore, since being observed at the surface, pseudotachylyte should have been exhumed without further deformation overprinting the initial melt phase (Kirkpatrick et al., 2009). The research presented by Kirkpatrick et al. (2009) confirms that pseudotachylyte is generated more commonly than previously thought, however, continuous deformational processes (such that might occur along an extensional tectonic boundary) will certainly affect the pseudotachylyte preservation, and has high probability to destroy any primary indication of melt generation. This would uniquely apply to pseudotachylytes within fault systems that continue to experience deformation through exhumation. This may explain the rarity of pseudotachylyte reported in the literature (Di Toro et al., 2006).

Pseudotachylyte is the only known fault rock to record evidence of coseismic slip in the form of a frictional melt (Magloughlin and Spray, 1992; Steltenpohl et al., 2006). Because it requires high-velocity slip (0.1 to 1.0 m sec^{-1}) to generate sufficient frictional heating (Sibson, 1975; Kirkpatrick et al., 2009), pseudotachylyte is often used to determine the past behavior of fault zones, particularly earthquake activity along faults (Spray, 1995), where stress in the crust has the ability to be rapidly released through brittle failure (Austrheim and Boundy, 1994). Di Toro et al. (2006) describe this as a large drop in fault strength and dynamic stress, where heating

and melt formation cause melt lubrication and potential thermal runaway on the fault. The presence of pseudotachylyte melt provides support for earthquake nucleation and propagation models that predict melting at the fault interface.

Almost every pseudotachylyte occurrence within exhumed fault zones worldwide is associated with either cataclasite or mylonite (Swanson, 1992; Magloughlin, 1992). It has been suggested that the process of comminution (crushing and grinding of solid materials) is a necessary precursor step in the formation of pseudotachylyte (Spray, 1995). This idea is supported by an analysis of clasts within pseudotachylyte veins (Ray, 1999), where a fraction of the pseudotachylyte was found to contain microfine material (ultracataclastic) while the remaining portion of the vein was glass material (the product of fusion). Lin (1999) suggests that rounded clasts involve a higher degree of frictional melting, whereas less-round clasts involve more of a fracturing process. The composition of pseudotachylyte is strongly dependent on the matrix in which they form (Magloughlin, 1992), and in many cases pseudotachylyte formation is preceded by cataclasite formation.

When generated on fault surfaces, pseudotachylyte requires rapid, non-equilibrium melting. The melting process partially decreases shear stress and strain energy on a fault during a slip event (Spray, 1987). It has been suggested that melting can occur selectively in a fault zone during pseudotachylyte formation (Maddock et al., 1987). In a study of mullite-bearing pseudotachylyte, Moecher and Brearley (2004) suggest that pseudotachylyte is a completely molten phase when it intrudes its host rock. A study of textures commonly found in pseudotachylyte exposures have led most workers to accept that pseudotachylyte is formed by frictional fusion at a shallow depth, as opposed to being related to brittle processes and formation of an ultracataclasite (Maddock, 1983).

The unique characteristic of both the Eidsfjord and Fiskfjord shear zones is the presence of garnet within the pseudotachylyte and surrounding mylonites. Compared to other localities of mylonitized pseudotachylyte, the garnet-bearing pseudotachylyte is the key phase for calculating

the ambient thermal and pressure conditions at the time of fault rupture (Lin et al., 2005; Moecher and Steltenpohl, 2011).

Extensional tectonic environments contain geologic evidence showing that the crustal brittle-ductile boundary is where strain is primarily localized (Regenauer-Lieb et al., 2008). With preliminary P-T evidence from co-seismic fault zones in northern Norway pointing to a deeper seismogenic zone, more evidence is necessary to further constrain the precise location of brittle faulting. Evidence of pseudotachylyte within lower-crustal rocks is not described for many localities (Lin et al., 2005; Sibson and Toy, 2006; Altenberger et al., 2011; White, 2012). The purpose of this thesis research is to calculate P-T values for pseudotachylyte veins found in the Eidsfjord and Fiskfjord shear zones of Lofoten-Vesterålen, northern Norway, and relate those values to a crustal depth estimate and tectonic model that account for any difference in depth of the two fault zones.

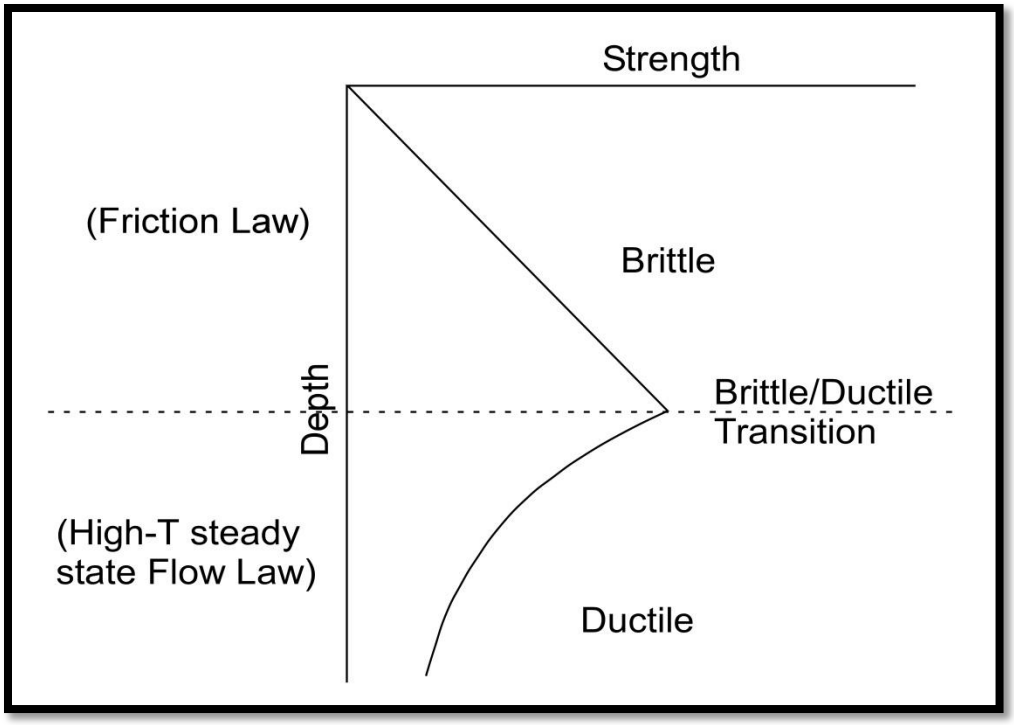

Figure 1.1. Simplified model relating strength to depth, which in turn is related to temperature dependence of mineral ductility on temperature (after Scholz, 1988). The strength first increases linearly based on $P=\rho gz$ then decreases exponentially based on the temperature dependence of creep behavior.

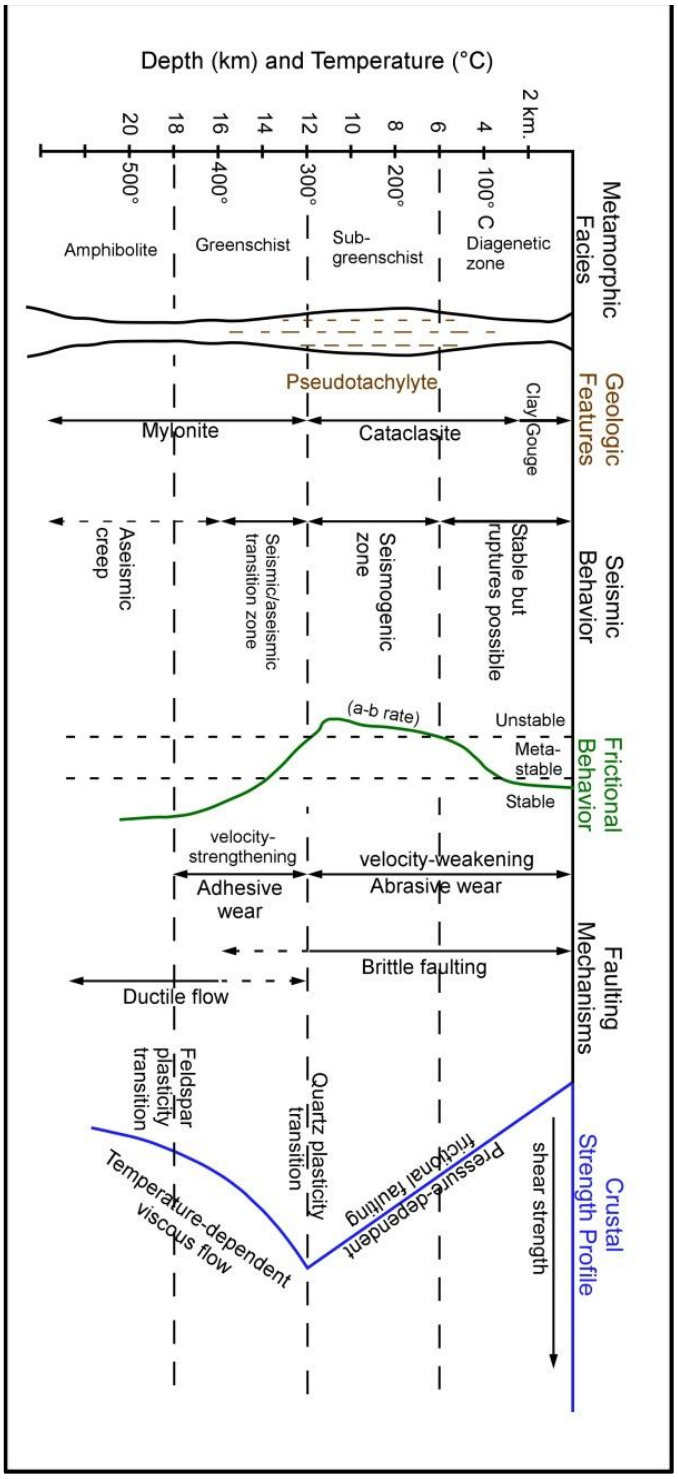

F**igure 1.2**. Conceptual model of a fault zone, showing location/depth of pseudotachylyte and other fault-generated rocks as they relate to seismic, frictional, and faulting behavior and crustal strength. Modified from Sibson (1983), Scholz (1988, 2002), and Fagereng and Toy (2011).

CHAPTER 2: Geologic Setting

The Lofoten-Vesterålen area (Fig. 2.1) represents the only exposed Precambrian basement bedrock on the Norwegian continental margin, making it an excellent locality to observe post-Caledonian extensional features (Løseth and Tveten, 1996; Hendriks et al., 2010). These Proterozoic basement rocks (mostly mangerite, monzonite, felsic migmatite, and anorthosite) were initially metamorphosed to granulite-facies at ca. 1.8 Ga (Griffin et al., 1978). The entire archipelago region comprising Lofoten and Vesterålen is part of the exposed basement where seismic surveys have revealed large-scale (5-10 km) displacement related to low-angle normal faults (Osmundsen et al., 2002; Osmundsen and Ebbing, 2008). Additional extensional faults and basins occur offshore, which were initiated as early as Carboniferous but continued into the Cretaceous rifting event (Osmundsen et al., 2010; Løseth and Tveten, 1996). A recent apatite fission track (AFT) dating study along a major normal fault in Lofoten identifies brittle fault movement occurring in the Mesozoic or younger (Hendriks et al., 2010; Osmundsen et al., 2010). Reflection seismic surveys across the continental-oceanic margin indicate normal basin flank detachment faults cutting Late Paleozoic-Early Mesozoic half-graben structures (Osmundsen and Ebbing, 2008).

During initial post-orogenic extensional collapse of the Caledonian orogen, a series of low-angle normal faults and shear zones accommodated regional continental extension, which provided the environment for the formation of pseudotachylyte. There have been several phases of pseudotachylyte found in mylonitic shear zones in the Lofoten-Vesterålen area, which are considered evidence for coseismic faulting in exhumed rocks (Plattner et al., 2003; Steltenpohl et al., 2006; Moecher and Steltenpohl, 2011). Løseth and Tveten (1996) observed that pseudotachylyte post-dated a mylonitic fault zone on Langøya (Vesterålen), based on the pseudotachylyte cutting across the ultramylonitic foliation observed in the fault zone. Occurrences of pseudotachylyte in northern Norway are generally restricted to shear zones in

granulite- or upper-amphibolite-facies continental basement (Heier and Thoresen, 1971; Løseth and Tveten,1996; Steltenpohl et al. (2006); Steltenpohl et al., 2011).

Two major ductile faults identified in northern Norway warrant more detailed study. The Eidsfjord and Fiskfjord shear zones located within the Vesterålen region (Fig. 2.2) have both been found to contain unique geological and mineralogical features (e.g. garnet-bearing pseudotachylytes, mylonites), as evidence for deep shear below the base of the seismogenic zone (Heier and Thoresen, 1971; Moecher and Steltenpohl, 2011). A simplified cross section extending from the Fiskfjord Shear zone on Hinnøya across the Sortlandsundet into the Eidsfjord Shear zone on Langøya through the Eidsfjord exhibits multiple normal faults in both regions as further evidence for extensional tectonic displacement (Fig. 2.3).

2.1 Eidsfjord

The primary detachment of the Eidsfjord Shear Zone (ESZ) is located on Langøya, along the southeast coast of Eidsfjord (Fig. 2.4). The best exposure of the ESZ is situated along a small inlet between Grønning and Slåttnes (Moecher and Steltenpohl, 2011) and exhibits a mylonite zone approximately 100 m thick (Fig. 2.5). The ESZ has a N50°E strike along foliation with a measured dip ranging between 7° and 35° NW, while the entire detachment has a surface dip of only 25°-30°NW (Moecher and Steltenpohl, 2011). Lithologies deformed within the ESZ are Paleoproterozoic mangerite, monzonite, anorthosite, amphibolite, and paragneiss (Steltenpohl et al., 2006). The shear zone also contains cataclasite and pseudotachylyte. The strongest foliated rocks of Grønning near the top of the detachment contain abundant, thick, well-preserved pseudotachylyte (Moecher and Steltenpohl, 2011). Several phases of pseudotachylyte found in mylonitic shear zones are evidence for repeated coseismic displacement in the exhumed rocks, and in the Eidsfjord shear zone, most pseudotachylyte phases occur in the hanging wall (Steltenpohl et al., 2006; Steltenpohl et al., 2011). The hanging wall is primarily granulite-facies anorthosite, which grades toward the shear zone into mylonitic meta-anorthosite (Fig. 2.6), some of which has been recyrstallized and bleached white (Moecher and Steltenpohl, 2011; Steltenpohl

et al., 2011). The footwall consists of mylonitic monzonite exhibiting several simple shear sense indicators, including delta and sigma porphyroclasts, all displaying top-to-the-west normal movement (Steltenpohl et al., 2001). The shear zone follows the lithologic contact, as many larger shear zones have been observed, perhaps taking advantage of a difference in shear strength between rocks in the hanging wall (anorthosite: plagioclase and pyroxene-rich) and footwall (mangerite and monzonite; more quartz-rich) (Passchier, 1984). $^{40}Ar/^{39}Ar$ analysis of muscovite from tectonites in the shear zone yielded an age of 403.6 ± 1.1 Ma, which is inferred to represent the time of ductile displacement along the ESZ (Steltenpohl et al., 2011). As pseudotachylyte is locally crosscut by mylonites with a foliation parallel to the dated tectonites, it is assumed that pseudotachylyte generation is ca. 400 Ma in age.

2.2 Fiskfjord

The Fiskfjord Shear Zone (FSZ) is located on Hinnøya, on the southeast coast of Sortlandsundet (Fig. 2.7). Løseth and Tveten (1996) first described Fiskfjord as a horizontal ductile shear zone with mangerites in the footwall, and anorthosite and augen gneiss in the hanging wall (Fig. 2.8). This shear zone is much thinner (~20 m thickness) and is comprised of mylonites and tectonites (Fig. 2.9; Moecher and Steltenpohl, 2011). Upon further investigation, the hanging wall was found to contain mylonitic gneiss with pseudotachylyte, and the footwall is primarily an L-S tectonite that grades downward to a granitic orthogneiss at the base (Moecher and Steltenpohl, 2011).

Recent work in the Fiskfjord shear zone involves $^{40}Ar/^{39}Ar$ step heating analysis for muscovite from the mylonite lithologies, yielding that the upper plate was reactivated and had already cooled through the ~350°C isotherm around 457 Ma (Steltenpohl et al., 2006, 2011). They also dated potassium feldspar using $^{40}Ar/^{39}Ar$ geochronology. The ages (235 to 185 Ma) indicate uplift and cooling through the closure temperature for argon diffusion in potassium feldspar (~150°C), which is consistent with the Triassic-Jurassic rift basins forming in

northwestern Norway (Steltenpohl et al., 2006). The near horizontal nature of the fault has been offset extensively by subsequent vertical faulting (Løseth and Tveten, 1996).

2.3 Pseudotachylyte

Pseudotachylyte found in the ESZ and FSZ is generally very dark brown to black, and aphanitic, and tends to contain lithic and mineral clasts of the surrounding rock (Fig. 2.10). In some cases, multiple generations of melt can be distinguished in thin section due to variations in color, grain size, and flow banding. As most pseudotachylyte is found in close proximity to the shear zone, the multiple generations of the melt may have contributed to the state of the shear zone over time (Price et al., 2012). It has been suggested that throughout the life of a shear zone, its core is progressively weakened with repeated episodes of coseismic slip until enough pseudotachylyte melt has accumulated to stabilize the core of the shear zone (Price et al., 2012).

Pseudotachylyte located in the FSZ is generally less than 1 cm thick, though some occurrences have been measured at over 14 cm thick (Steltenpohl et al., 2011). They have been classified as typically planar and tabular, with smaller offshoots from the main vein. Sibson (1975) describes two common types of pseudotachylyte veins as fault veins and injection veins. Fault veins exist along planar fractures usually parallel with shear direction, and injection veins are considered offshoots from fault veins, and exist mostly in areas with no clear lateral offset (Sibson, 1975). The granulite-facies mangerite has mylonitic and ultramylonitic pseudotachylyte veins produced from normal shear bands striking N20°E dipping 60°NW with an observed lineation at N42°E to N20°W determined from feldspar streaks (Steltenpohl et al., 2011). Feldspars, amphibole, and pyroxene all display recrystallization along grain margins both in pseudotachylyte features as well as wall rocks (Moecher and Steltenpohl, 2011). Neo- and recrystallized garnet has been identified both within pseudotachylyte melt veins, in mylonitic shear bands cutting veins, around opaque mineral grain boundaries (Moecher and Steltenpohl, 2009).

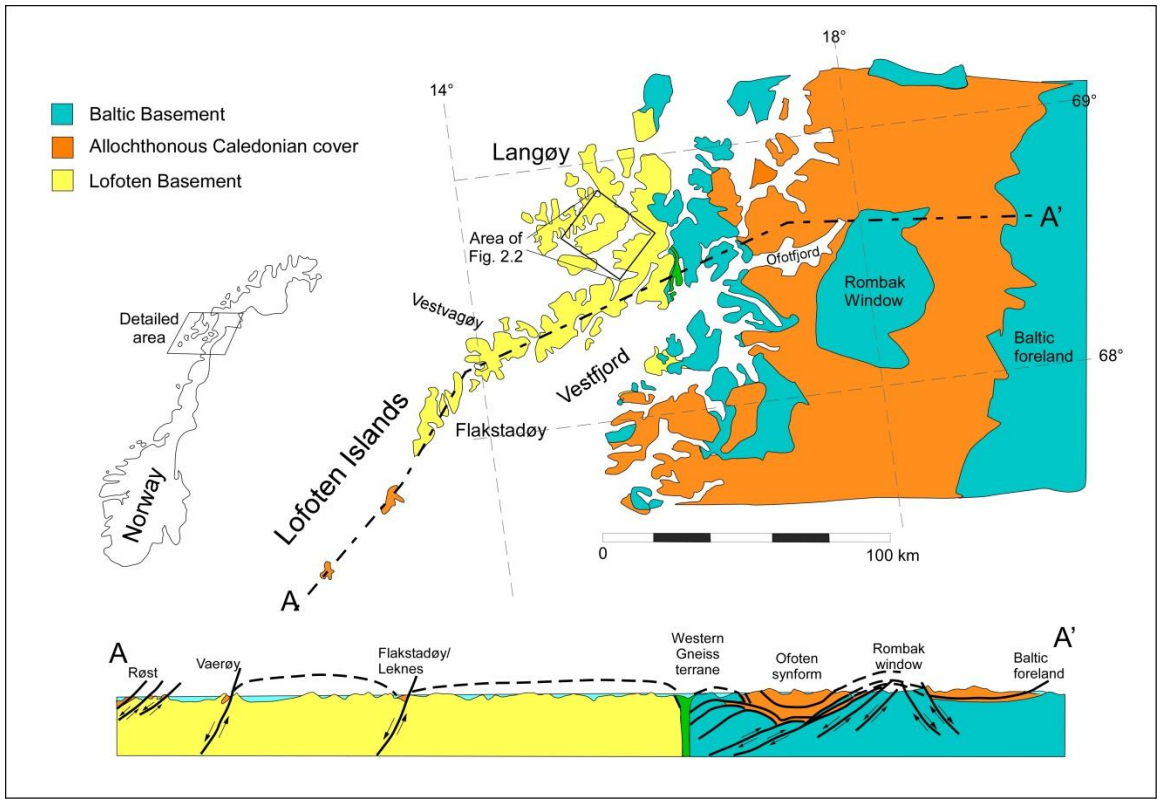

Figure 2.1. Map of the Lofoten-Vesterålen area of northern Norway (Steltenpohl et al., 2006; Steltenpohl et al., 2011), with a generalized depiction of the local geology. The cross section A-A' shows variations from offshore Lofoten basement through inland Baltic basement.

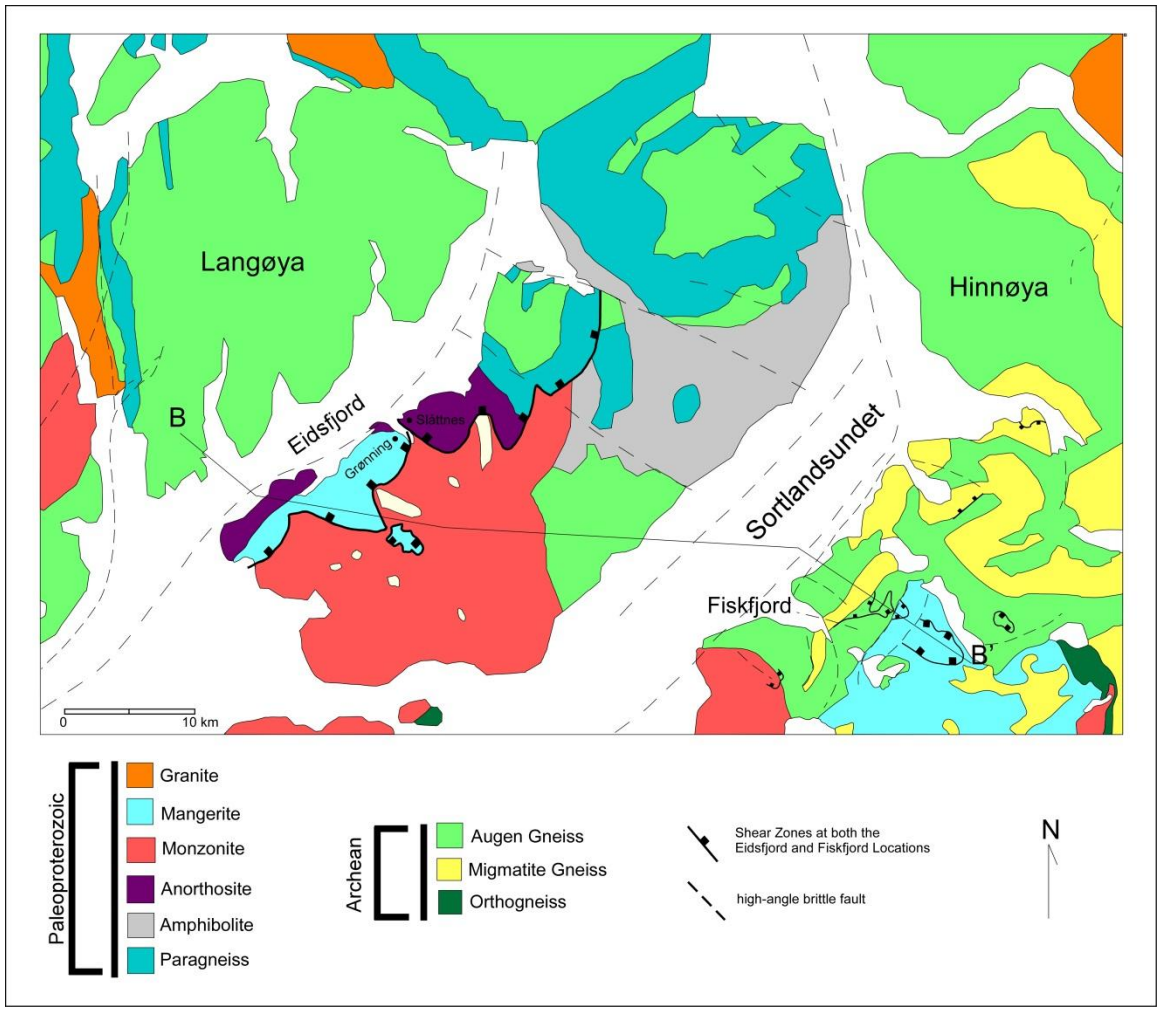

Figure 2.2. Detailed geologic map from Figure 2.1, focusing on the Eidsfjord and Fiskfjord localities (after Steltenpohl et al., 2006; Steltenpohl et al., 2011).

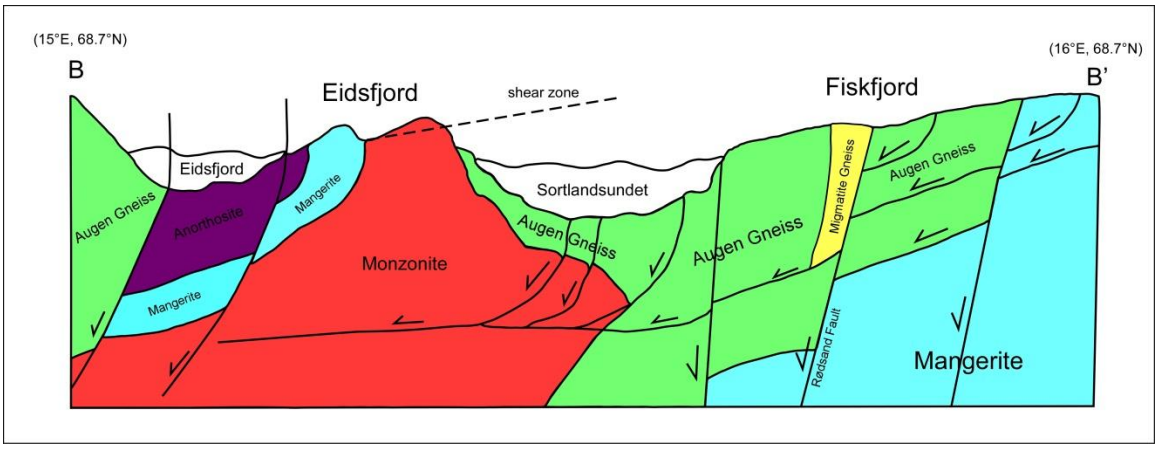

Figure 2.3. Cross section B-B' (vertically exaggerated) from Figure 4 showing structural and geologic differences between the Eidsfjord and Fiskfjord shear zones (after Bergh et al., 2007; Steltenpohl et al., 2011).

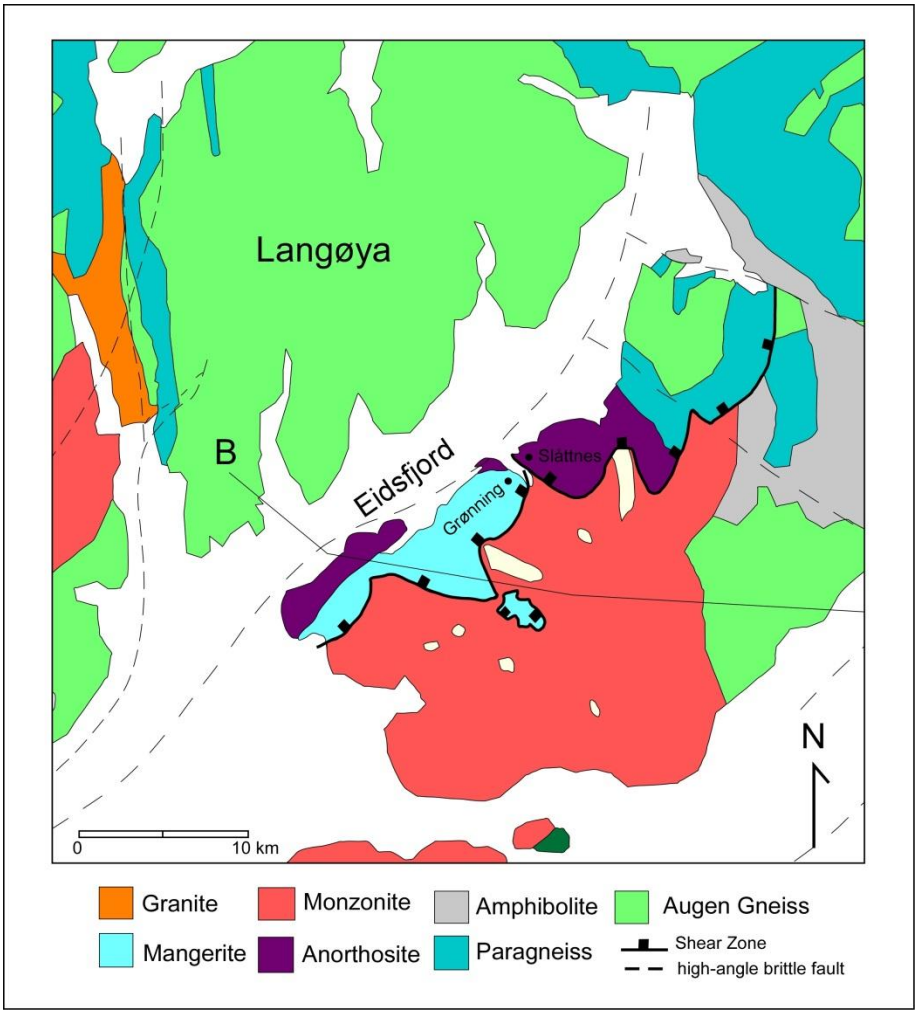

Figure 2.4. Eidsfjord location detail from the geologic map (Fig. 2.2). (after Steltenpohl et al., 2006, 2011).

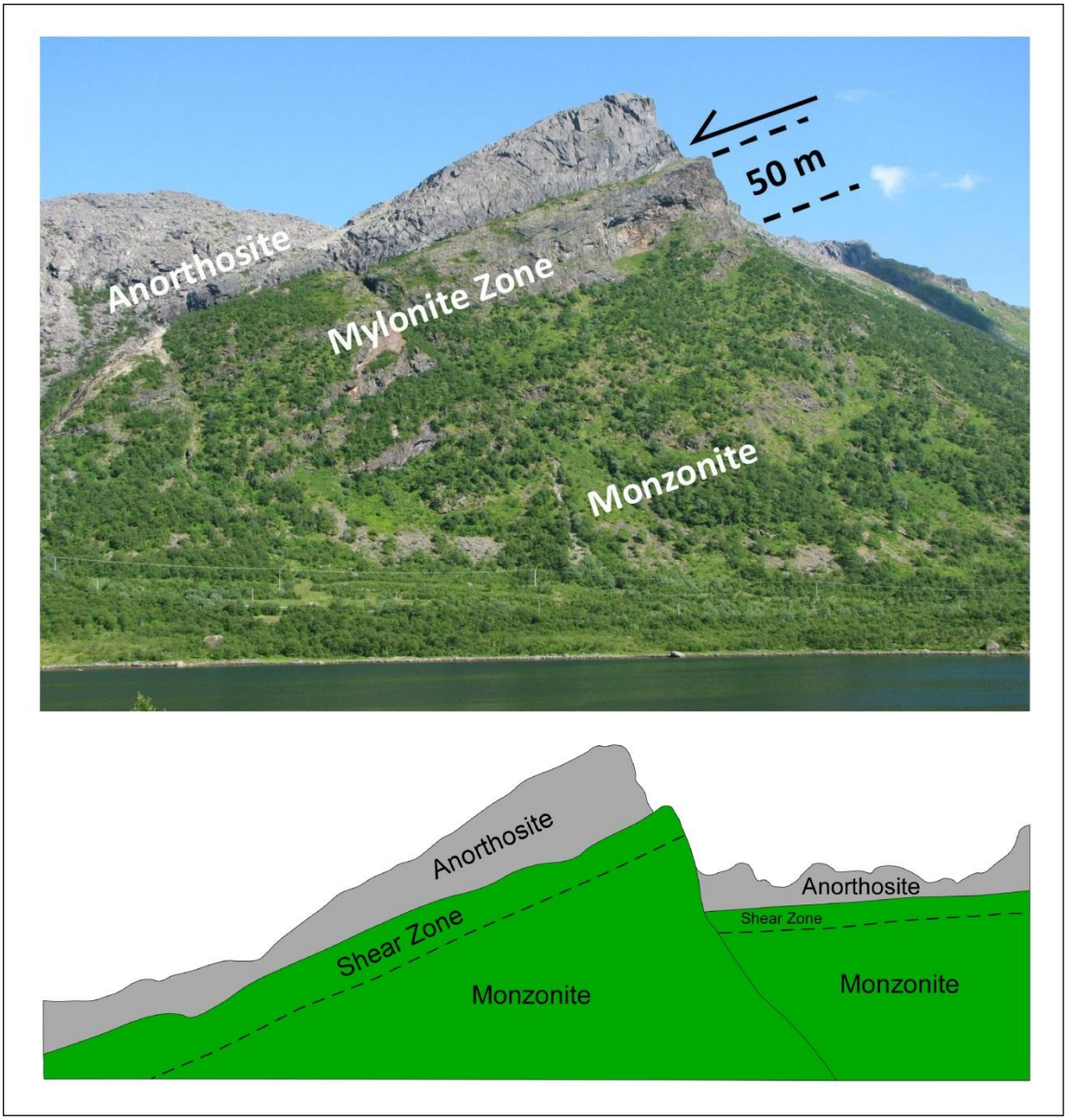

Figure. 2.5. Eidsfjord Shear Zone photo, facing northeast across Slåttnesbugen. Field photo (top) (Moecher and Steltenpohl, 2011) and general sketch (bottom) (Plattner et al., 2003) of the ESZ and location of the ductile fault zone bounding the two lithologies.

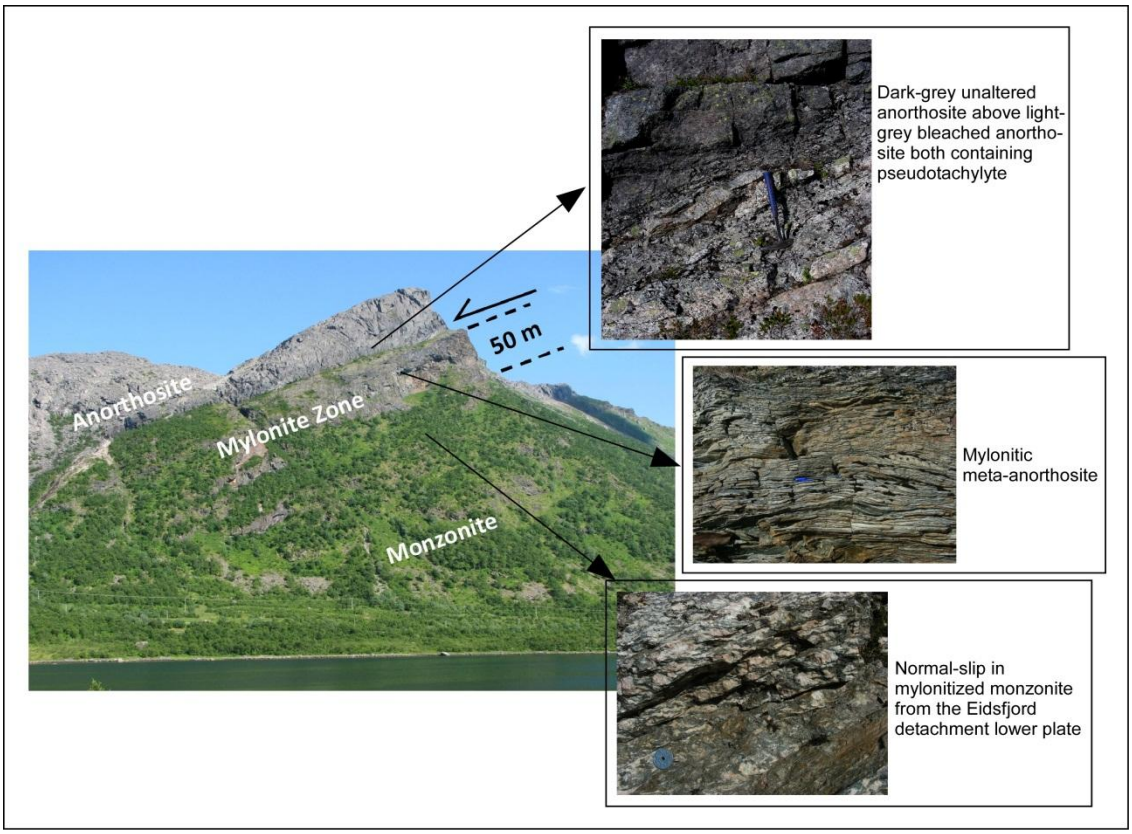

Figure 2.6. Changes in Eidfjord lithologies through the shear zone (after Moecher and Steltenpohl, 2011).

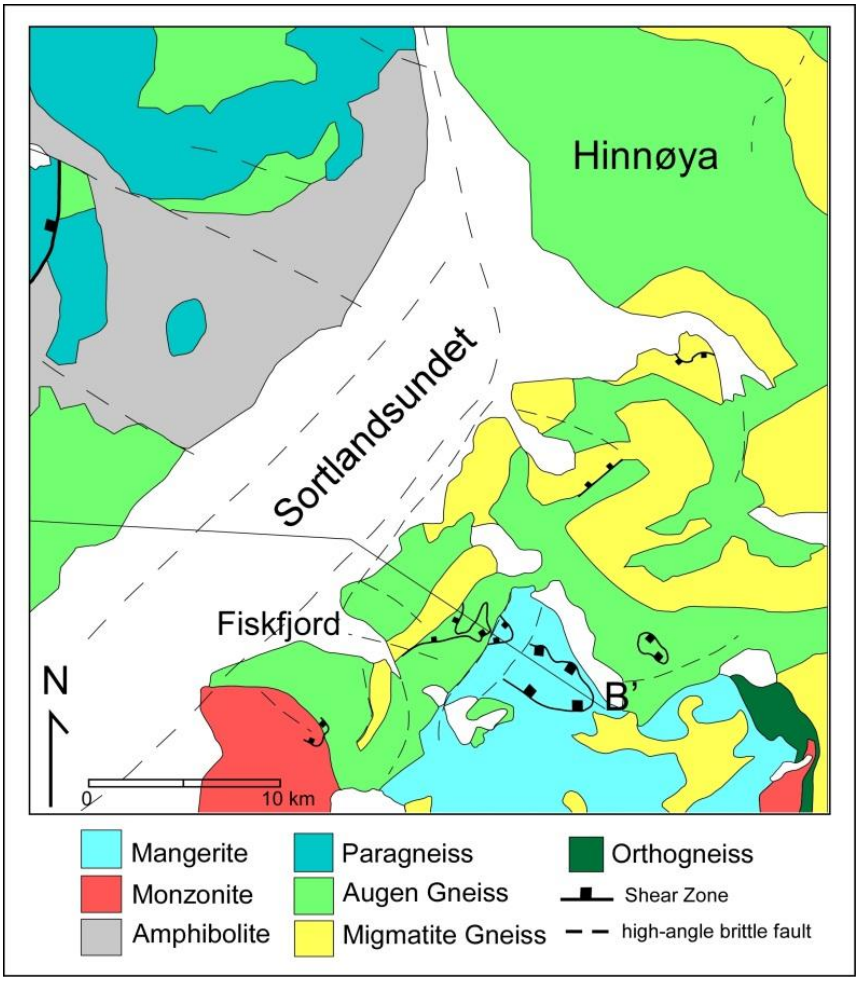

Figure 2.7. Fiskfjord location detail from the geologic map (Fig. 2.2) (after Steltenpohl et al., 2006, 2011).

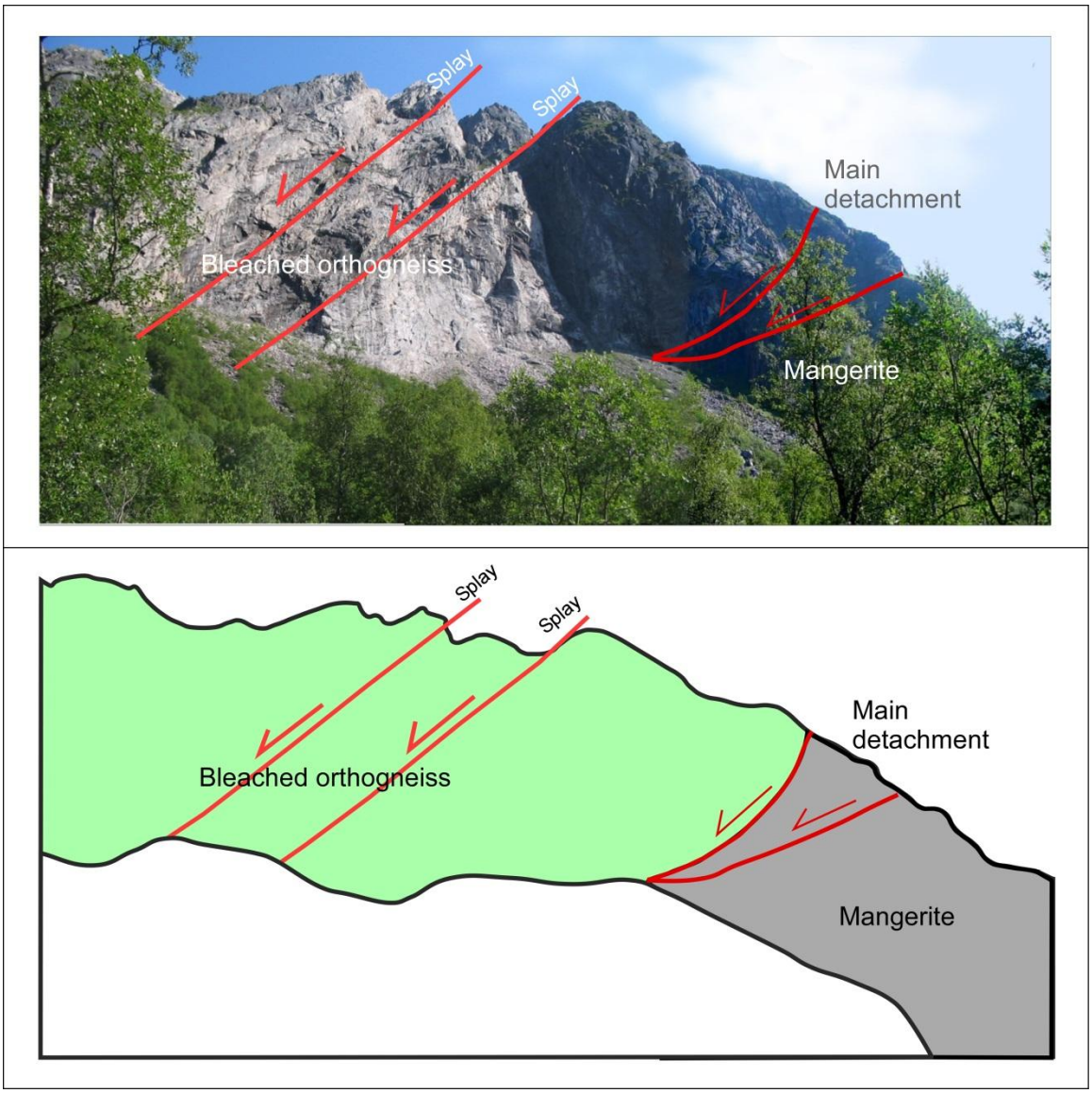

Figure. 2.8 Fiskfjord Shear Zone field photo (looking northeast) and sketch (Steltenpohl et al., 2011) showing the main detachment at the FSZ and several corresponding splays within the bleached orthogneiss.

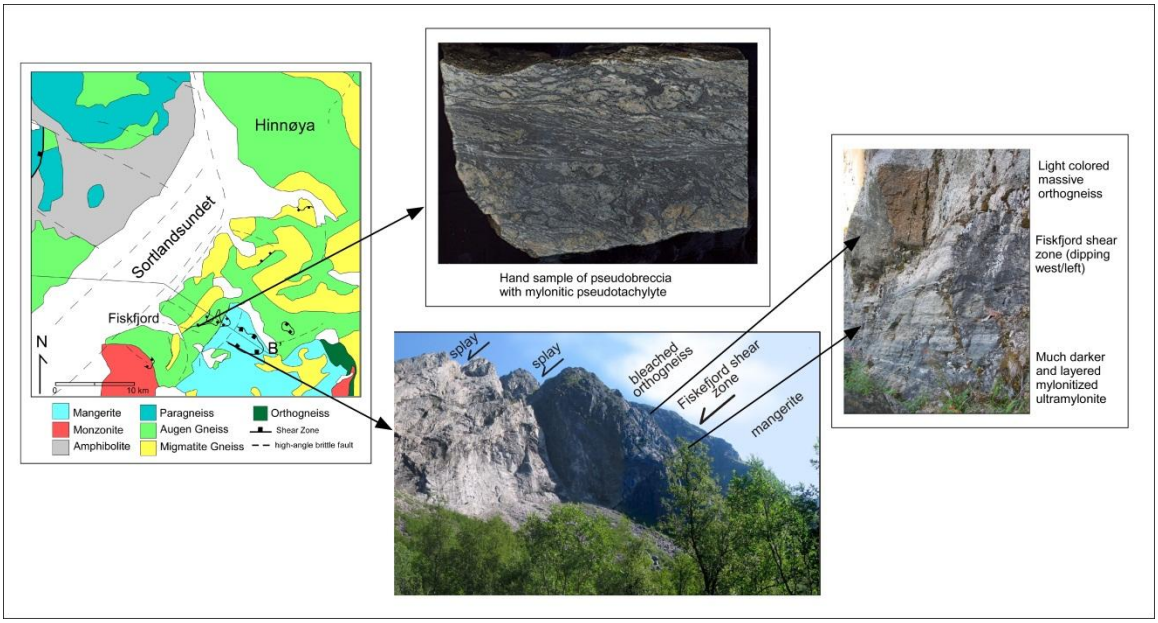

Figure 2.9. Changes in Fiskfjord lithologies through the shear zone area (after Moecher and Steltenpohl, 2011).

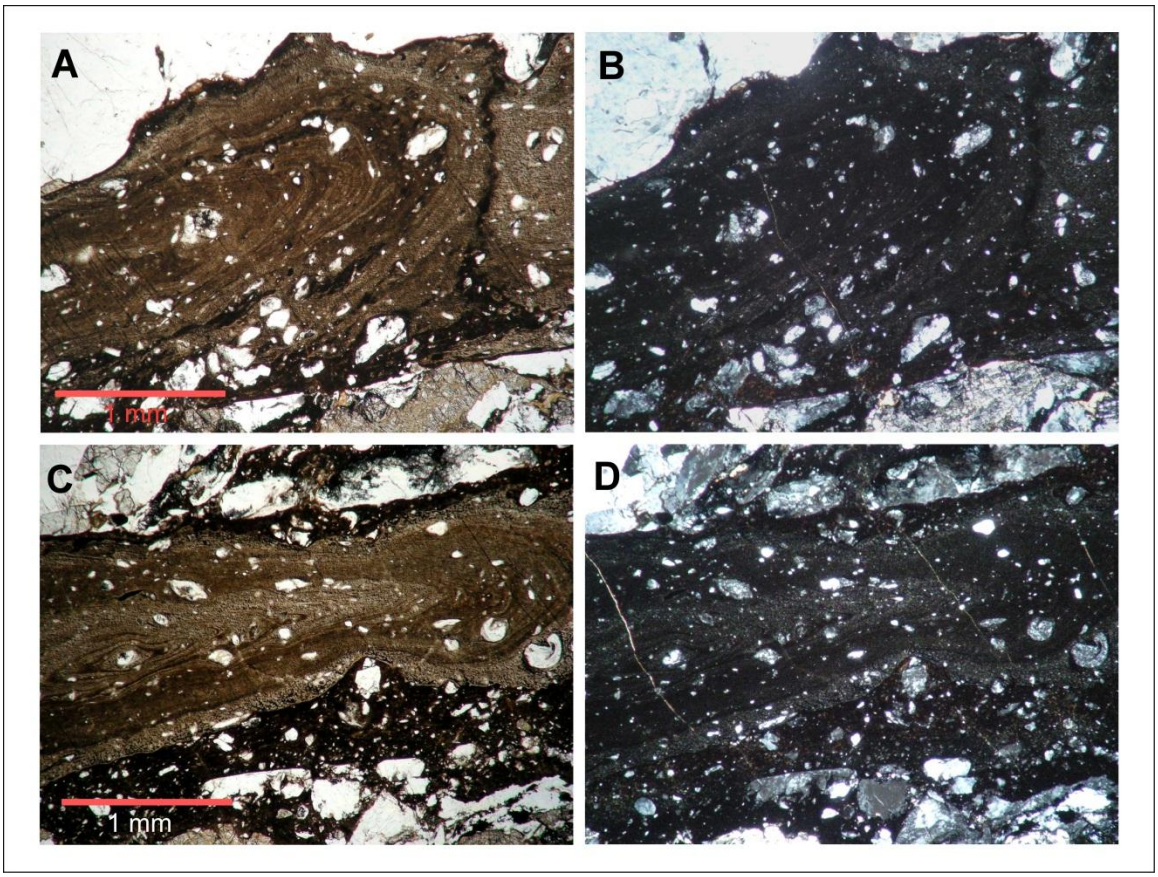

Figure 2.10. Photomicrographs of pseudotachylyte in anorthosite (sample EID08-2a) showing flow banding and plagioclase clasts from the surrounding rock. A and C: plane polarized light; B and D: crossed polars. C shows two generations of pseudotachylyte (light brown flow banded melt intruding dark pseudotachylyte).

CHAPTER 3: Petrology

Faults produce a wide range of rock types and features including cataclasite, mylonite, and pseudotachylyte, all of which are present in the Eidsfjord and Fiskfjord shear zones (Fig. 3.1). Anorthosite constitutes the hanging wall and monzonite is the footwall lithology at Eidsfjord. Both lithologies are present around the Fiskfjord locality, however there they do not clearly define the fault, and several additional lithologies are present. The shear zone at Fiskfjord is much more complex, with several normal fault splays through bleached orthogneiss (which is generally depicted as the hanging block) above a footwall block of mangerite. Seventy-nine thin sections were examined from samples along these two shear zones; 65 thin sections correspond with sample locations within or near the ESZ, and 14 thin sections correspond with sample locations within or near the FSZ. Six thin sections were analyzed in detail, three from Eidsfjord and three from Fiskfjord (Fig. 3.2), to gather additional data for thermobarometric calculations.

Most samples of interest are from either bleached anorthosite or monzonite near the shear zone boundary (Fig. 3.3). Of particular interest are samples of pseudotachylyte, mylonite, or mylonitic pseudotachylyte containing the mineral assemblage garnet + hornblende + plagioclase, which permit application of at least one geothermometer and one geobarometer. Most thin sections include evidence of faulting, in the form of re-crystallized grains, cataclasite, fractured grains, and/or pseudotachylyte veins.

3.1 Sample Descriptions

3.1.1 Eidsfjord Sample Descriptions

Many of the Eidsfjord samples were taken across the shear zone in succession from the anorthosite downward into the monzonite (Fig. 3.4). The anorthosite samples are very distinct, easily identified by coarse-grained plagioclase, with anorthosite becoming more bleached approaching the shear zone. In nearing the ESZ, the plagioclase porphyroclasts become bounded by crushed, recrystallized plagioclase grains, becoming steadily more cataclastic in appearance.

Different phases of melt are also observed in sharp contact with the surrounding rock. Several phases of melt can be identified in a single sample, due to changes in color and grain size (Fig. 3.5). Often multiple melt phases are identified from flow bands or features juxtaposing two strikingly different looking melts, usually indicative of multiple melt phases, clast proportions or compositions. Pseudotachylyte often contains plagioclase or lithic clasts from the surrounding host rock (Fig. 3.6). In some of the bleached anorthosites, melt flow bands deflect around larger plagioclase grains (Fig. 3.7, Fig. 3.8). In several cases, quench crystals of plagioclase or quartz were located within the melt, and devitrified zones of the same composition were located around the melt boundary (Fig. 3.9). In the Eidsfjord Shear Zone, quench features were usually identified in plagioclase grains.

In several thin sections fractures were evident, displaying significant offset through mylonitic or gneissic layering. Sample EID08-4-8 displayed several generations of both cataclasite and pseudotachylyte, which have offset veins due to fracture (Fig. 3.10).

Some melts seem to follow "lineation features" in the surrounding rock, while other melt injections have no clear pattern. Some occurrences of melt features in the Eidsfjord samples are much lighter in color with slightly larger, more visible grains, which may imply a more cataclastic feature rather than pseudotachylyte. Some samples exhibit a distinct dynamic recrystallization of hornblende which includes poly-crystalline aggregates in a recrystallized matrix.

In several samples of relatively pristine anorthosite, (EID08-7-5 and EID08-7-6), several large ilmenite grains were identified, on which small garnet rims had nucleated (Fig. 3.11). This is unusual because no garnet has been reported in the granulite facies Proterozoic gneisses of the Lofoten-Vesterålen area. Plagioclase and other grains became more deformed near the shear zone. As the rock graded from mylonite into ultramylonite, the feldspar grain boundaries became more rounded, while some displayed perthitic textures and/or rims of dynamically recrystallized plagioclase (Fig. 3.12). The addition of a larger percentage of K-feldspar marked the transition

into monzonite. Thermobarometry on the Eidsfjord samples was described by Moecher and Steltenpohl (2009, 2011).

3.1.2 Detailed Eidsfjord Sample Descriptions

EID08-3a: The section is of a monzonite sample with relict pseudotachylyte. Evidence of the former melt includes dark aphanitic veins, the presence of feldspar quench crystals, devitrified quartz crystals, and several fractures propagating through the rock sample (Fig. 3.2-A). Other minerals present include epidote, garnet, and hornblende (Fig. 3.13). Because of the dark, aphanitic, nearly opaque nature of the pseudotachylyte, the average thin section thickness of 30 microns made locating and identifying garnets difficult using the petrographic microscope. Garnets and other minerals were much more easily identified using backscattered electron (BSE) imaging on the CAMECA SX50 electron probe microanalyzer (Fig. 3.14).

EID08-4-6a-2: This sample is a bleached meta-anorthosite (Fig. 3.2-B). Minerals present in this thin section include garnet, plagioclase, hornblende, scapolite, pyroxene, and quartz. The overall matrix is composed of plagioclase, and several areas within the pseudotachylyte contain blebs of poly-crystalline aggregates of plagioclase and hornblende (Fig 3.15).

EID08-7-2b: This sample of meta-anorthosite is characterized by coarse plagioclase feldspar grains which are separated by quartz and scapolite veins (Fig. 3.2-C). With the exception of these veins, the sample is composed almost entirely of plagioclase and quartz. The plagioclase lamellae all seem to be oriented in the same direction. Several smaller garnet grains have been identified in close proximity to hornblende. Other minerals present include pyroxene, biotite, and muscovite. Garnets found in this thin section are extremely small (100 nm to a few microns: Fig. 3.16) and are often found in strings or clusters oriented parallel with the mylonitic foliation.

3.1.3 Fiskfjord Sample Descriptions

Samples from the Fiskfjord area display many of the same features and lithologies as seen in the Eidsfjord thin sections. However, the range of samples from the FSZ seems to span a wide range of lithologies (Fig. 3.17). A variety of samples contain pseudotachylyte, and several samples have been altered to mylonite, yet they do not contain evidence of melt. The samples containing pseudotachylyte were investigated and included for the sake of comparison to the Eidsfjord samples also containing pseudotachylyte, however only the mylonitic samples were utilized for thermobarometry for this study.

Garnet occurs as fine grains (on the order of 100 nm to a few μm) nucleating on clinopyroxene and opaque minerals as well as dispersed throughout the matrix (Fig. 3.18). A few samples had garnet grains nucleating on the rims of almost every opaque grain in thin section. In thin sections displaying a greater amount of shear, opaque grains were often stretched out, which allowed for additional garnet growth. Generally, Fiskfjord samples contained more euhedral garnet grains in greater abundance than Eidsfjord (Fig. 3.19). Several of the coarser garnets (on the order of 50-100 microns) contain inclusions of ilmenite, hematite, rutile, pyrite, hornblende, biotite, quartz, and plagioclase.

Feldspar-rich lithologies at Fiskfjord displayed many examples of perthitic texture (Fig. 3.20), and often had dynamic recrystallization occurring along transgranular fractures in plagioclase (Fig. 3.21). At the beginning of the shear zone area, brittle processes are dominant, as evidences by unaltered pseudotachylyte melt injections (Fig. 3.22). Moving down through the shear zone, melt features become mylonitic moving from brittle into ductile processes, where biotite and hornblende were also observed along melt margins in mylonitic samples, usually with grains oriented with the foliation (Fig. 3.23). In the footwall, moving through the shear zone, monzonite lithologies are bleached and minerals indicate sense of shear and/or direction of foliation (Fig. 3.24).

3.1.4 Detailed Fiskfjord Sample Descriptions

FIS09-2b: This thin section is characterized by relatively coarse plagioclase and garnet grains in the sample with a distinct gneissic foliation. Other minerals present are scapolite, biotite, and hornblende (Fig. 3.25). Garnet contains inclusions of ilmenite, hematite, quartz, rutile, hornblende, pyrite, biotite, and albite (Fig. 3.26).

FIS09-2d: Minerals identified in this thin section include biotite, garnet, several opaque minerals (mostly ilmenite and some pyrite), quartz, hornblende, altered clinopyroxene, and plagioclase (Fig. 3.27). There were several areas in this thin section comprised of a large garnet grain surrounded by biotite, hornblende, clinopyroxene, and plagioclase. Garnet contains inclusions of pyrite, quartz, biotite, hornblende, ilmenite, and rutile (Fig. 3.28).

FIS09-3a-1b: This thin section is well foliated with a mineral assemblage of biotite, hornblende, scapolite, quartz, garnet, plagioclase, and opaque grains (Fig. 3.29). Garnet contains inclusions of ilmenite, hematite, and pyrite.

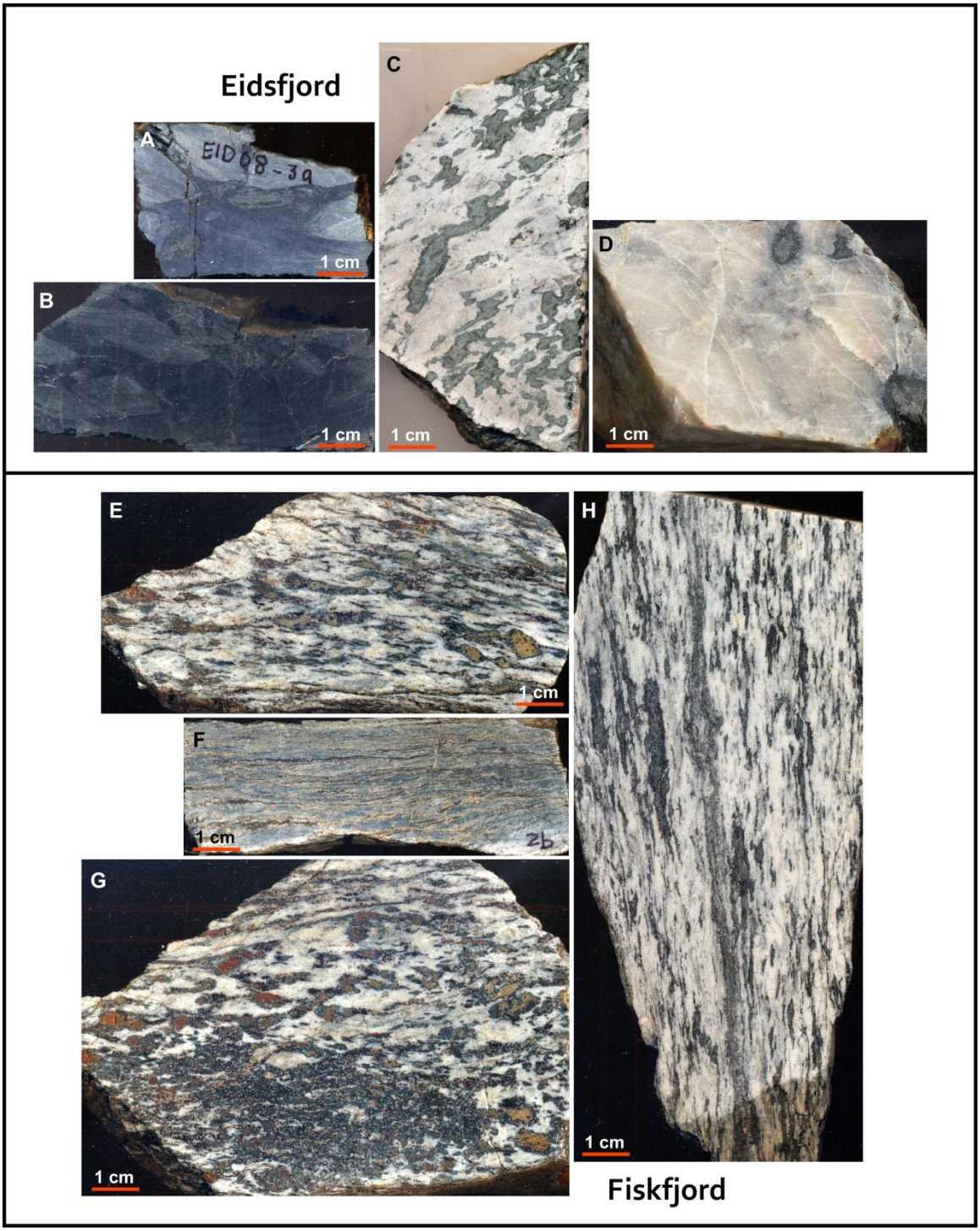

Figure 3.1. Hand sample photos of all samples used in geothermobarometric calculations. Eidsfjord samples (A and B) EID08-3a, (C) EID08-4-6a-2, and (D) EID08-7-2b and Fiskfjord samples (E and F) FIS09-2b, (G) FIS09-2d, (H) FIS09-3a-1b.

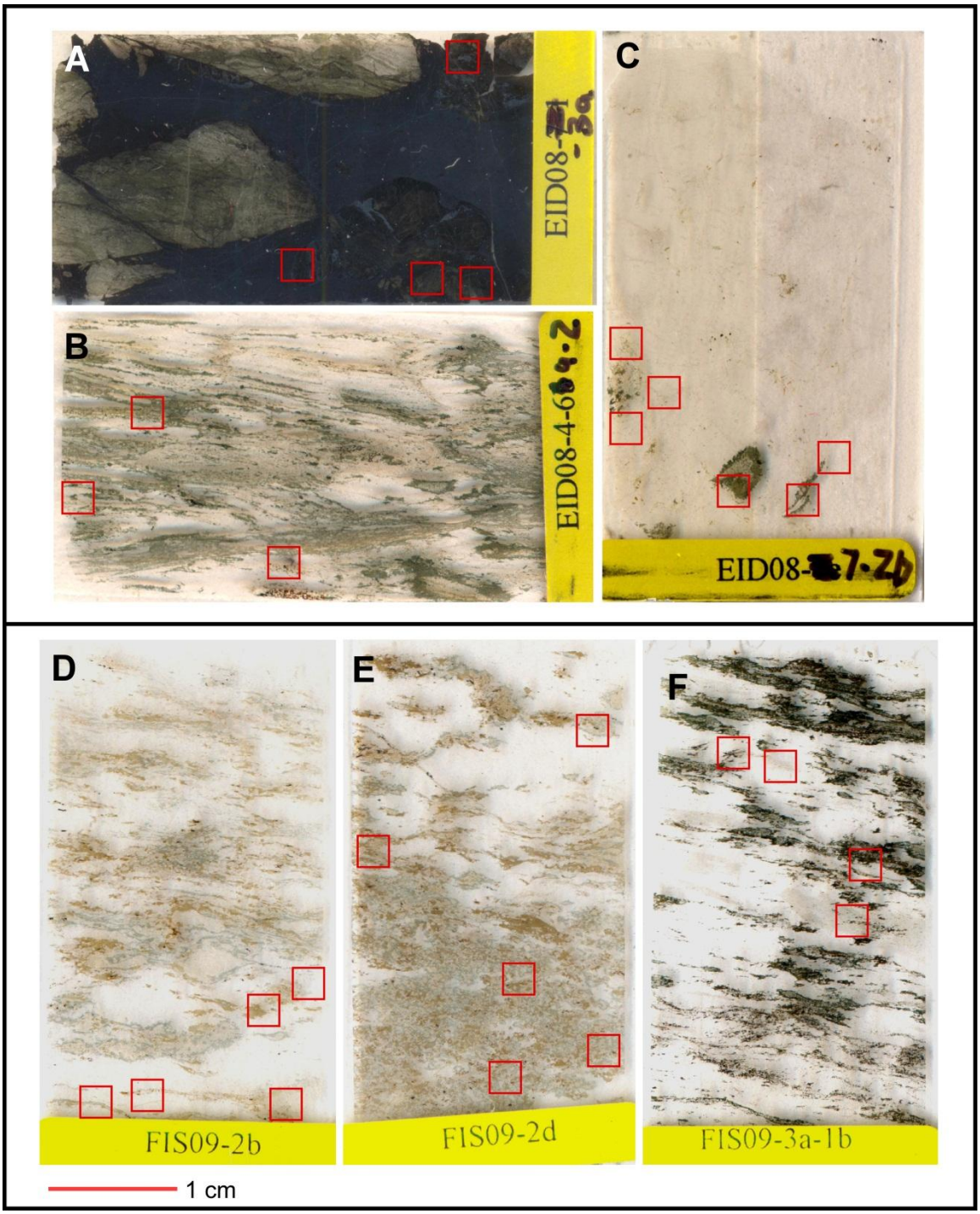

Figure 3.2. Thin section photos of all samples used in geothermobarometric calculations. Eidsfjord samples (A) EID08-3a, (B) EID08-4-6a-2, and (C) EID08-7-2b and Fiskfjord samples (D) FIS09-2b, (E) FIS09-2d, and (F) FIS09-3a-1b. Red boxes represent analyzed domains containing the assemblage garnet + hornblende + plagioclase ± quartz.

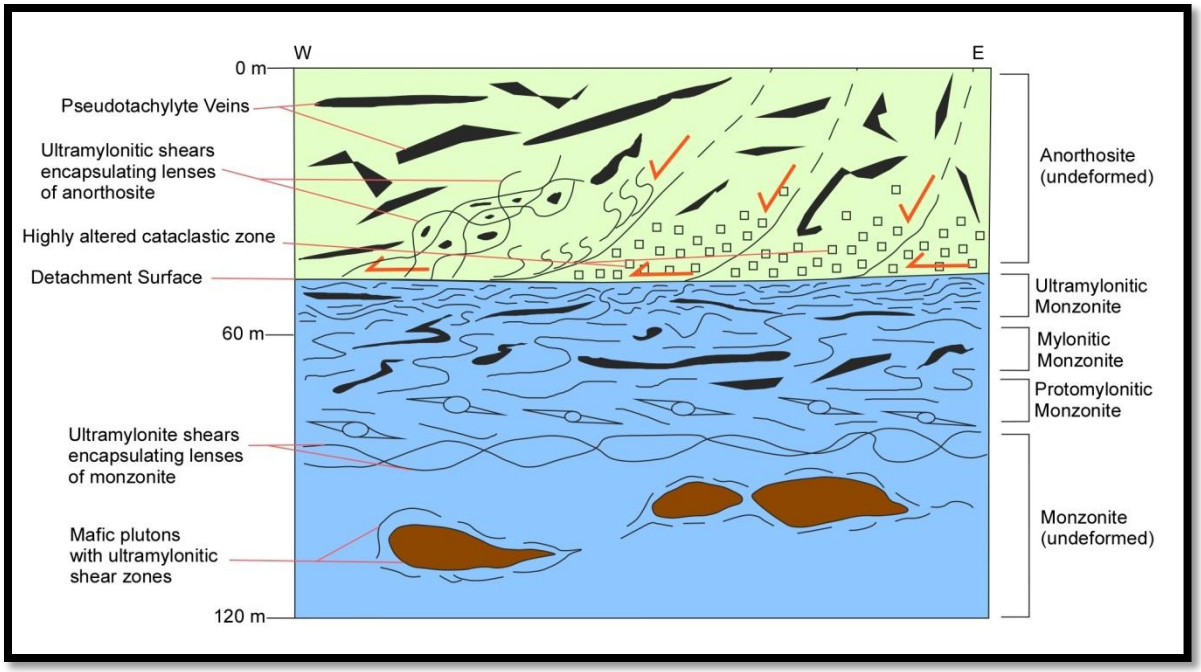

Figure 3.3. Schematic depiction of the lithologic and structural relations within the Eidsfjord shear zone (Steltenpohl et al., 2011) showing anorthosite in the hanging wall and monzonite in the footwall along with distribution of structural features.

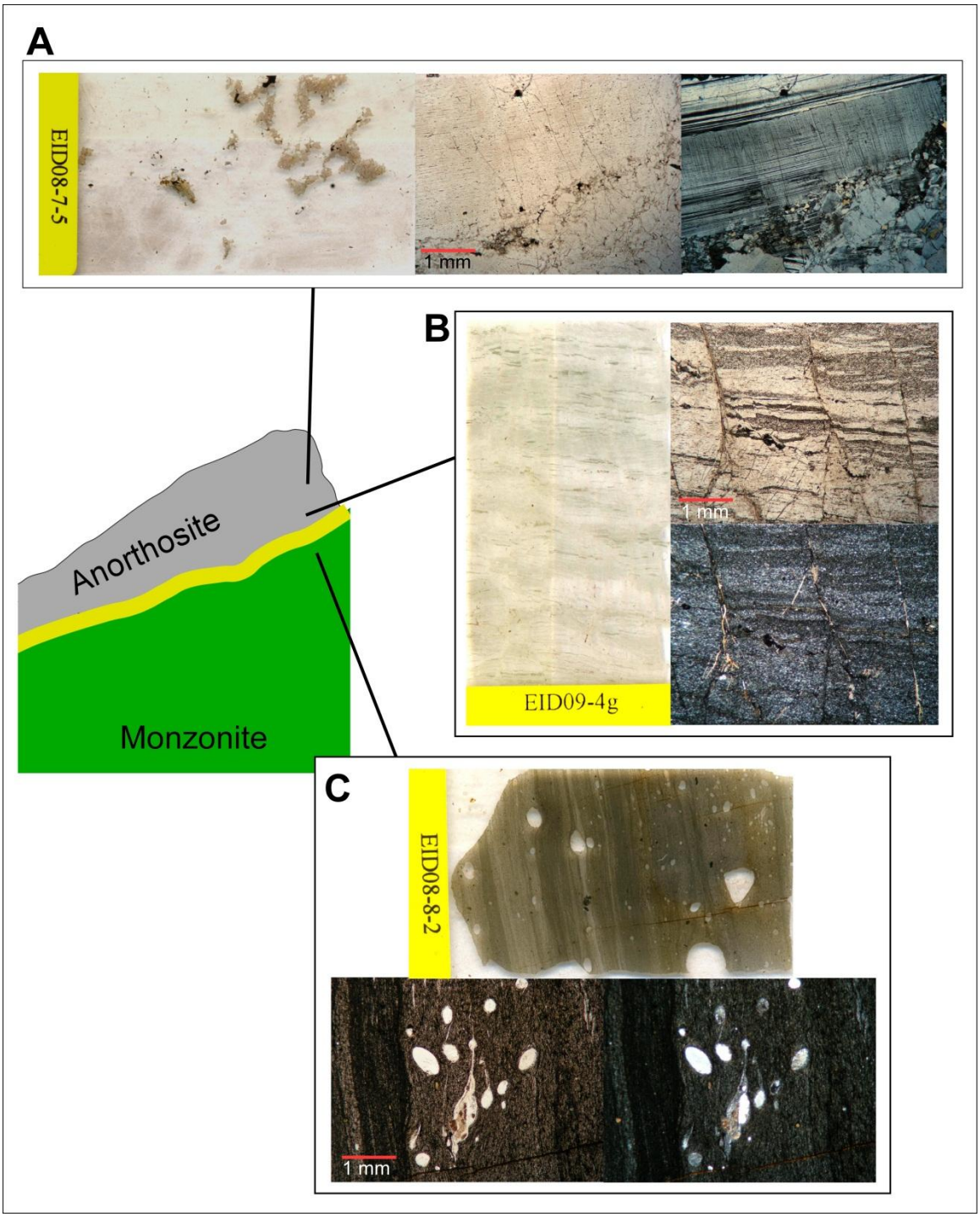

Figure 3.4. Eidsfjord sample progression from brittle to ductile processes into the shear zone. Area (A) shows sample EID09-4g, a fractured bleached anorthosite. (B) Sample EID08-8-2, a bleached anorthosite with large intact plagioclase grains and some dynamic recrystallization around grain edges. (C) Ultramylonitic monzonite with rounded plagioclase porphyroclasts.

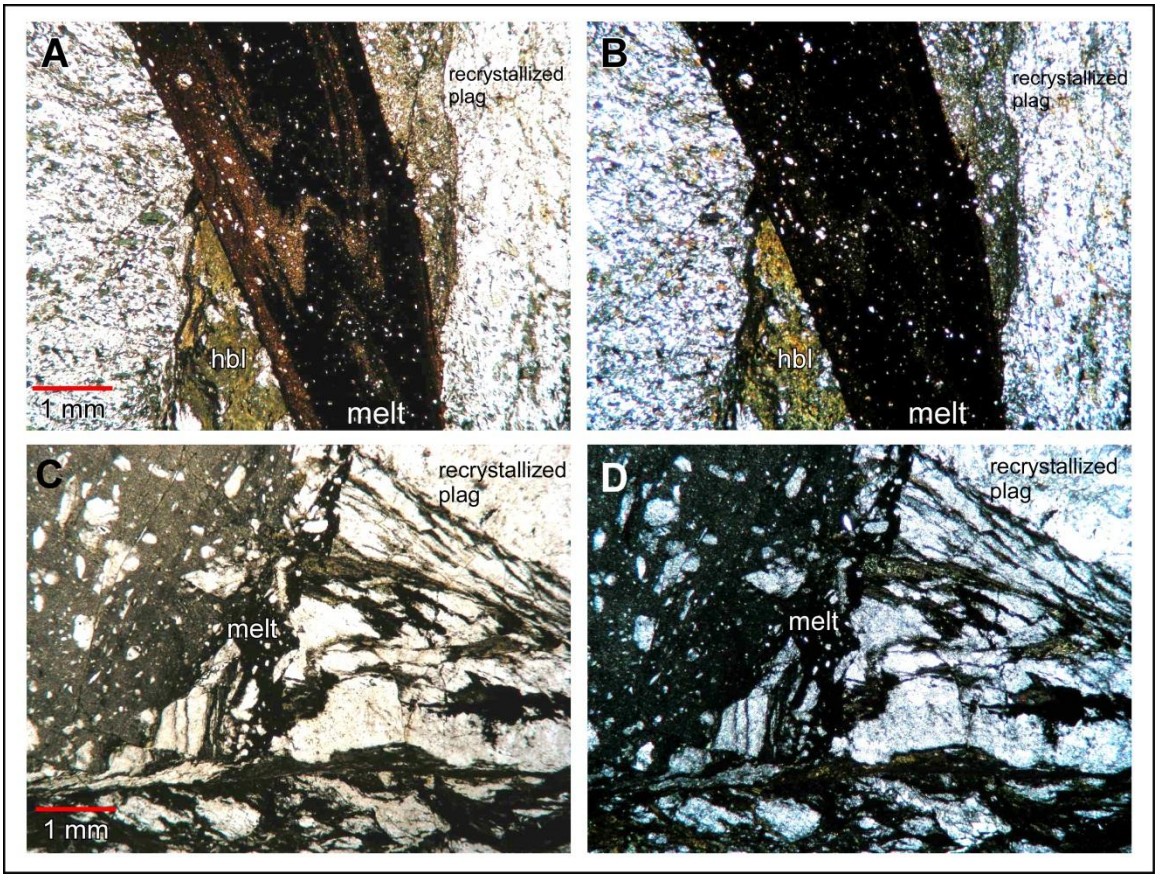

Figure 3.5. Photomicrographs from the ESZ showing changes in melt resulting from multiple melt phases, or changes in composition. Sample EID08-4-3 in (A) ppl and (B) xpl and sample EID08-3c2 in (C) ppl and (D) xpl.

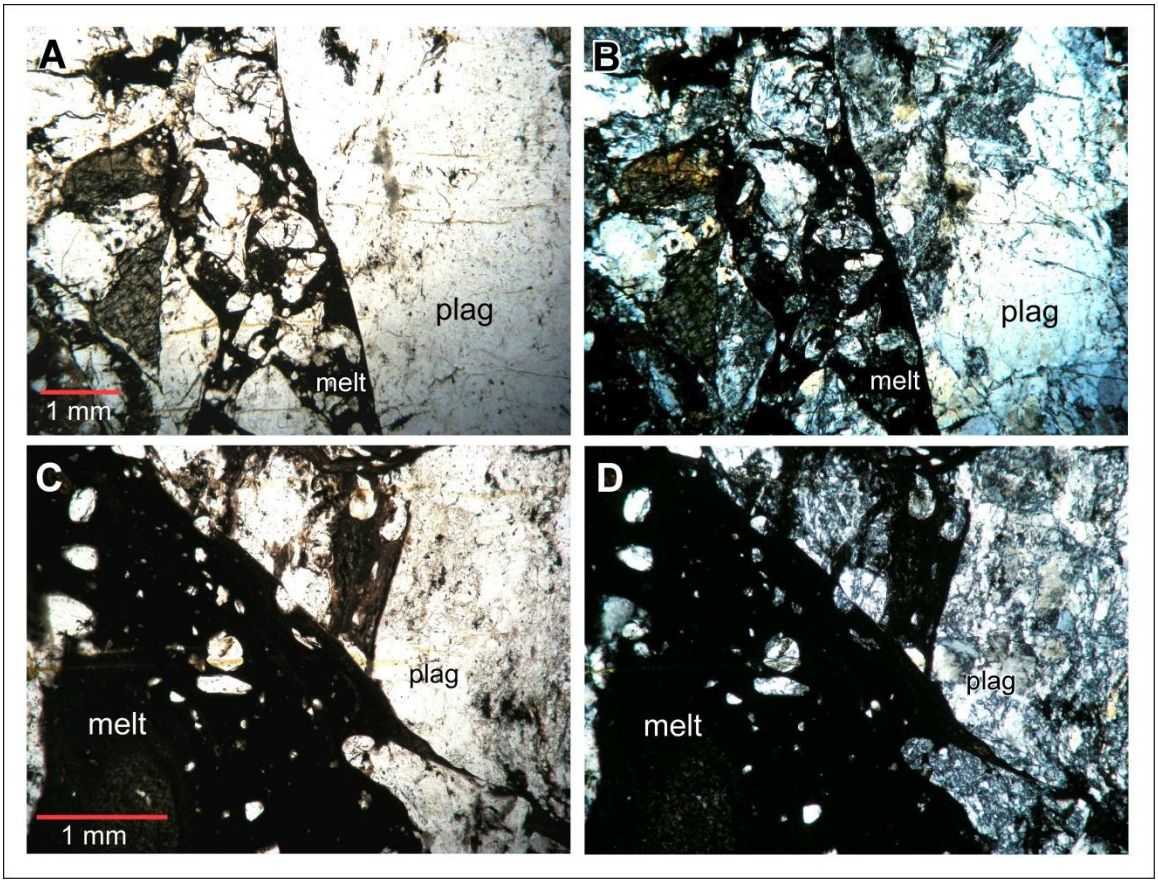

Figure 3.6. Photomicrographs from the ESZ showing melt intruding the country rock and collecting plagioclase clasts. Two cross-cutting generations of pseudotachylyte are evidence in C and D. Sample EID08-5-1 in (A) ppl and (B) xpl and sample EID08-5-1 (different area) in (C) ppl and (D) xpl.

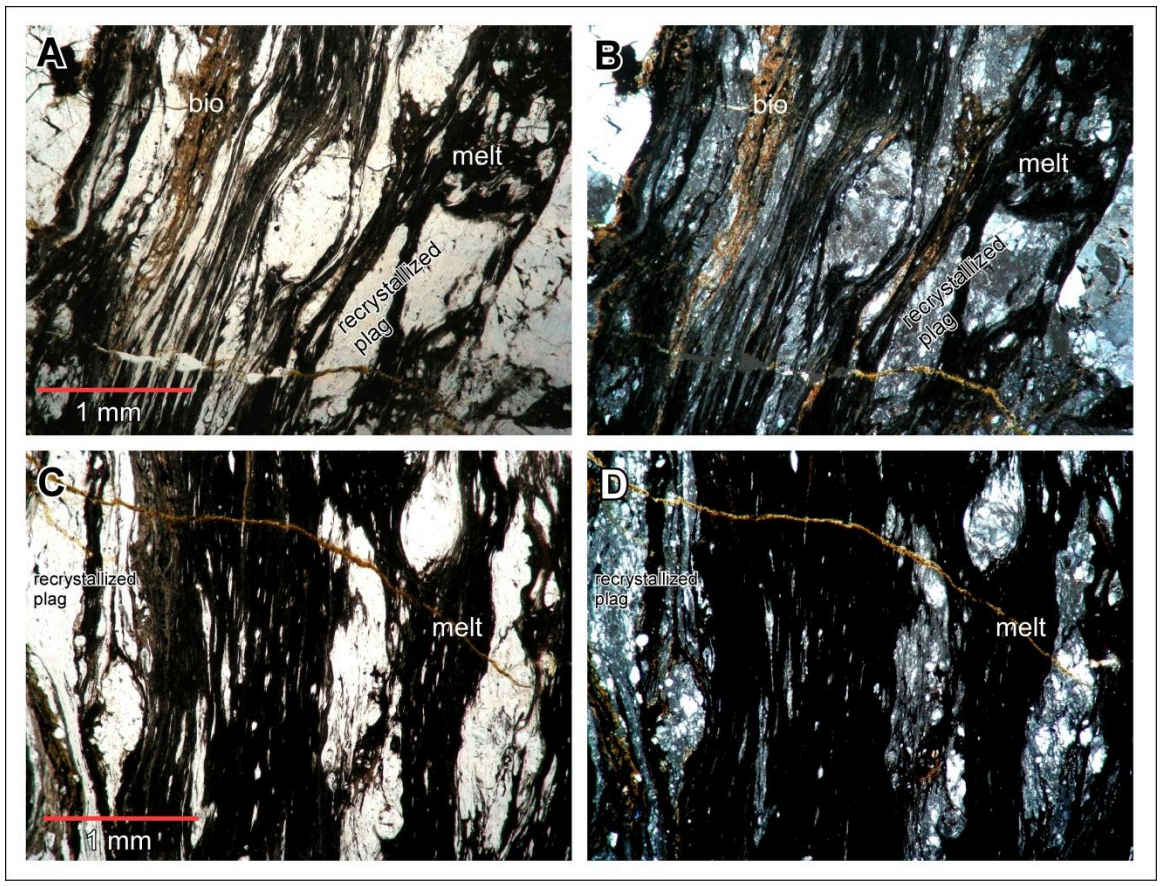

Figure 3.7. Photomicrographs from the ESZ showing melt becoming more mylonitic and flowing around larger plagioclase grains. Sample EID08-7-1 in (A) ppl and (B) xpl and sample EID08-7-1 (different area) in (C) ppl and (D) xpl.

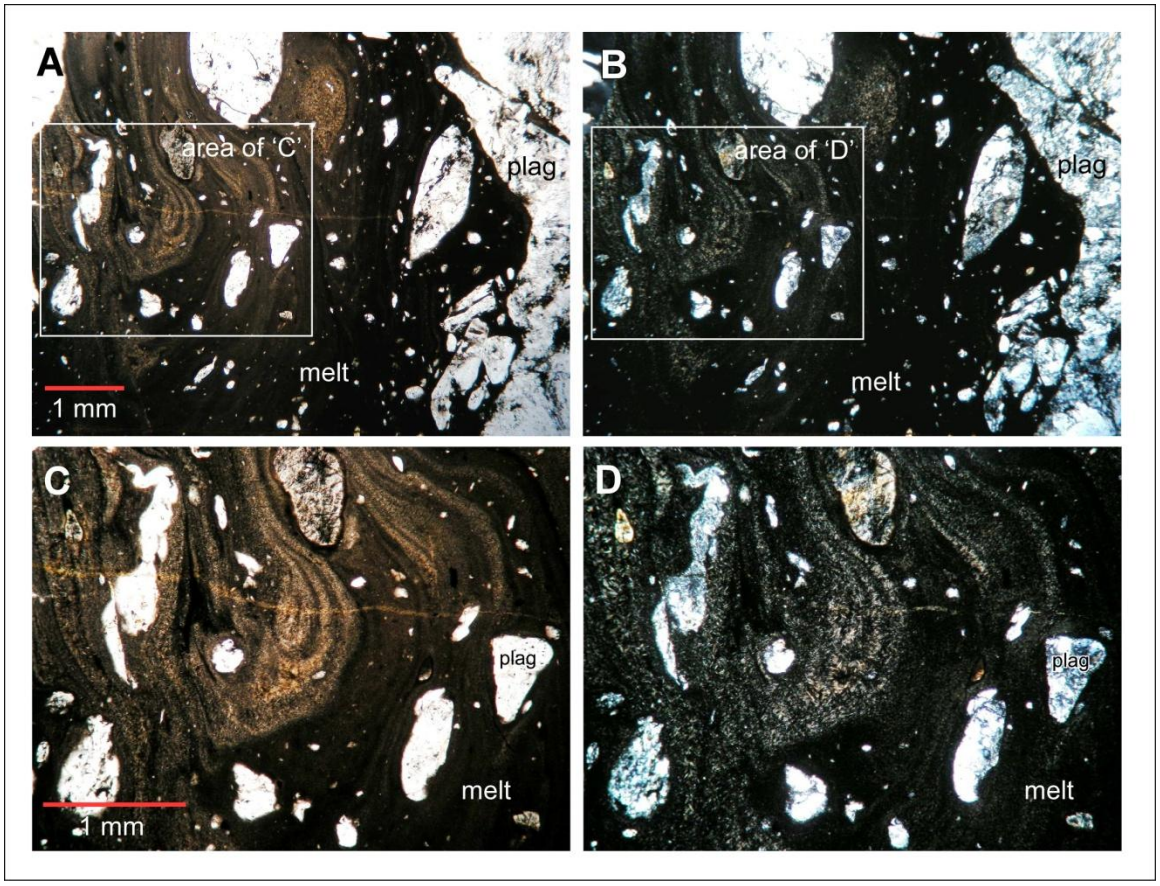

Figure. 3.8. Photomicrographs from the ESZ showing evidence of melt mixing and flow bands. Sample EID08-5-1 in (A) ppl and (B) xpl and the same area in more detail in (C) ppl and (D) xpl.

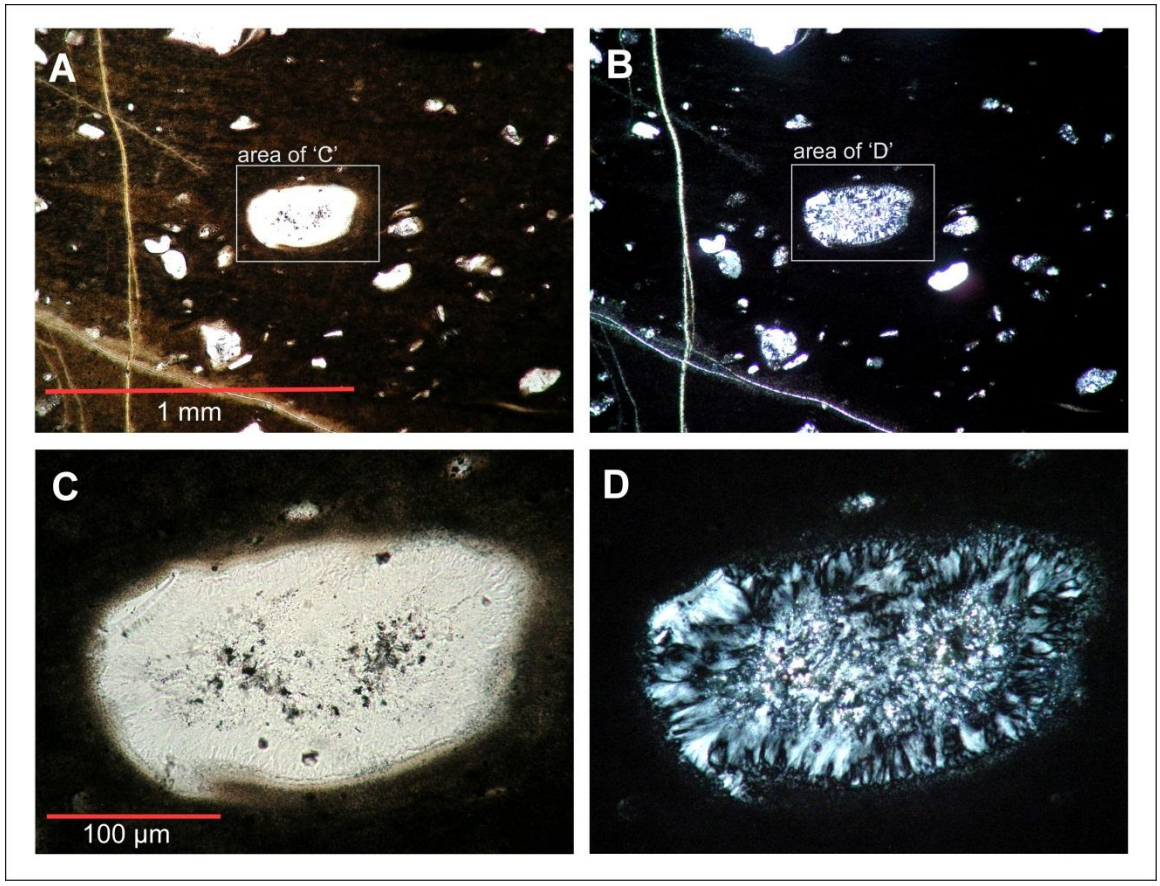

Figure. 3.9. Photomicrographs from the ESZ showing a quenched plagioclase grain within the pseudotachylyte melt. Sample EID08-2b in (A) ppl and (B) xpl and the same grain in more detail in (C) ppl and (D) xpl.

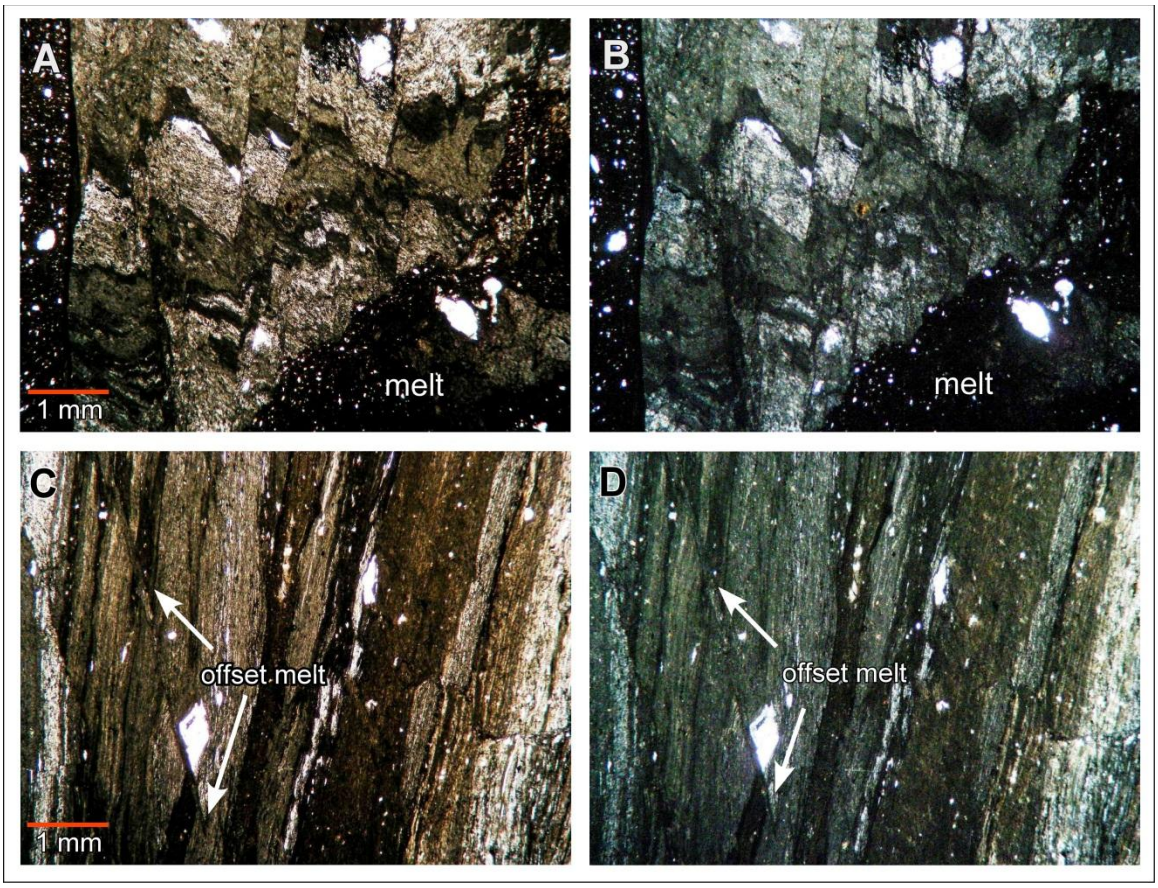

Figure. 3.10 Photomicrographs from the ESZ showing a fractured ultramylonite with crosscutting melt veins. Sample EID08-8-1 in (A) ppl and (B) xpl the same sample in a different area in (C) ppl and (D) xpl.

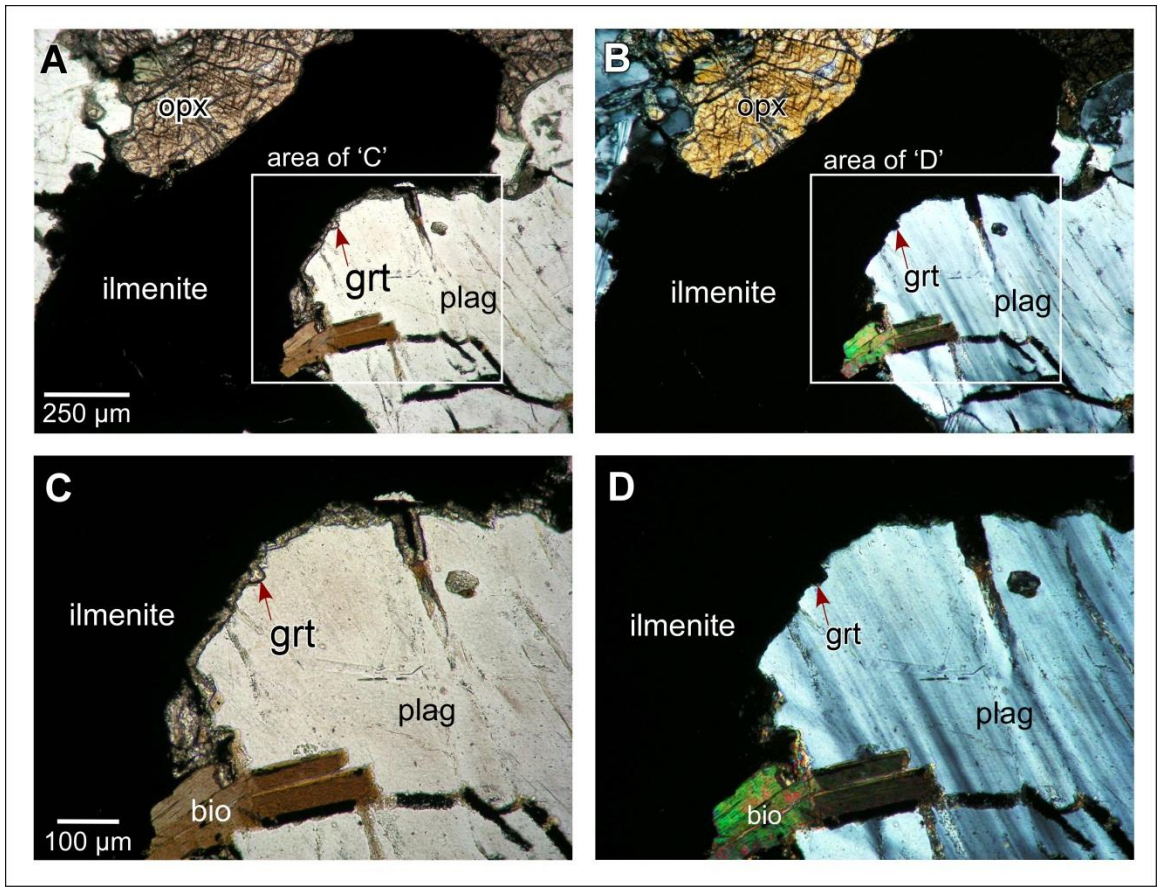

Figure 3.11. Photomicrographs from the ESZ showing an ilmenite grain with garnet nucleating on the rim. Mostly undeformed anorthosite, with some evidence of early metamorphic strain on the plagioclase grain. Anorthosite sample EID08-7-5 in (A) ppl and (B) xpl and the same sample in more detail in (C) ppl and (D) xpl.

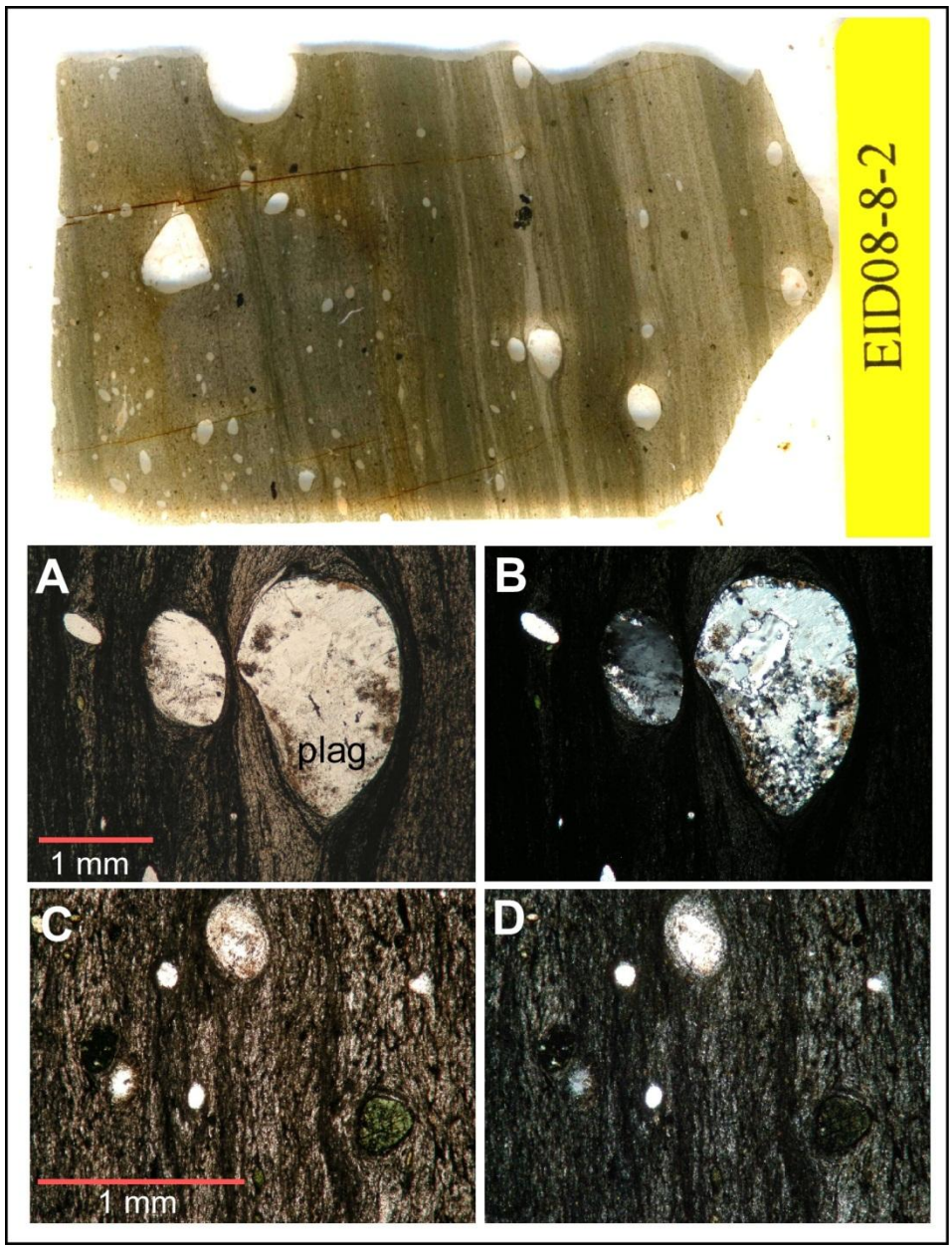

Figure 3.12. Thin section photo and subsequent photomicrographs showing ultramylonitic features (in monzonite) containing rounded feldspar, hornblende, and quartz clasts. Photos (a) and (b) correspond to plain polarized light (ppl) images and (c) and (d) correspond to cross polarized light (xpl) images.

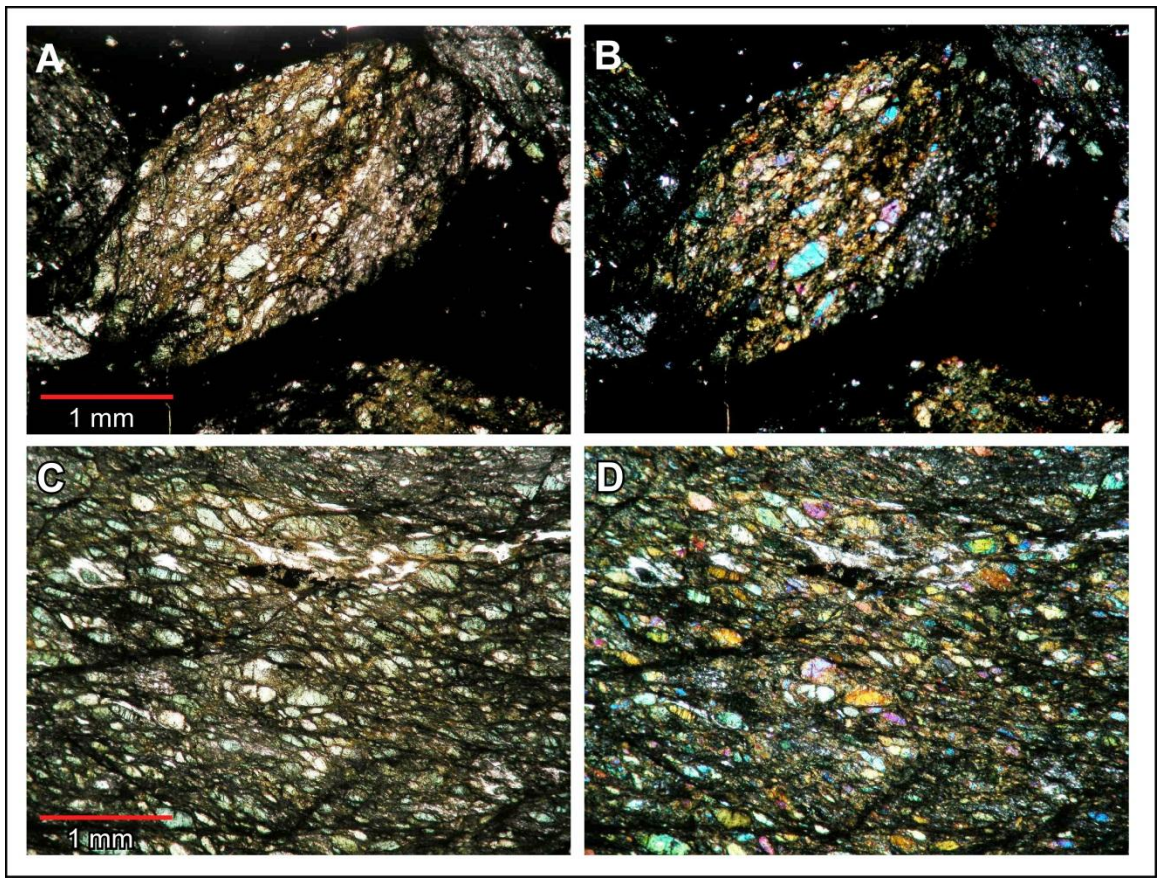

Figure 3.13. Photomicrographs from EID08-3a showing relict pseudotachylyte melt containing clasts of the surrounding mylonitic meta-anorthosite containing shear bands. Sample EID08-3a in (A) ppl and (B) xpl and a different area of the same sample in (C) ppl and (D) xpl.

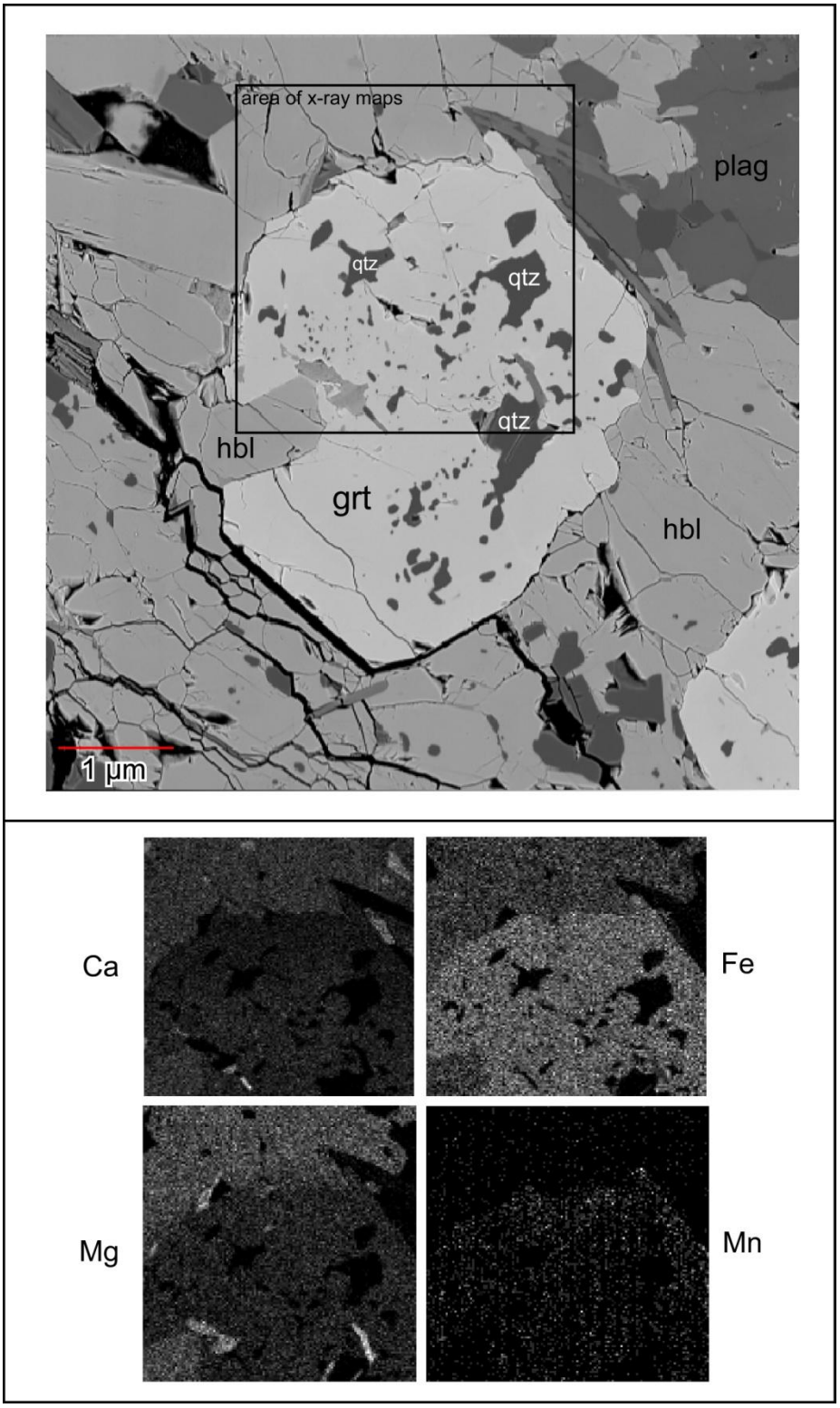

Figure 3.14. Representative BSE image (above) and elemental X-ray maps (below) from sample EID08-7-2b, domain 4. BSE images identifying mineral assemblage, and X-ray maps showing concentrations of calcium, iron, magnesium, and manganese.

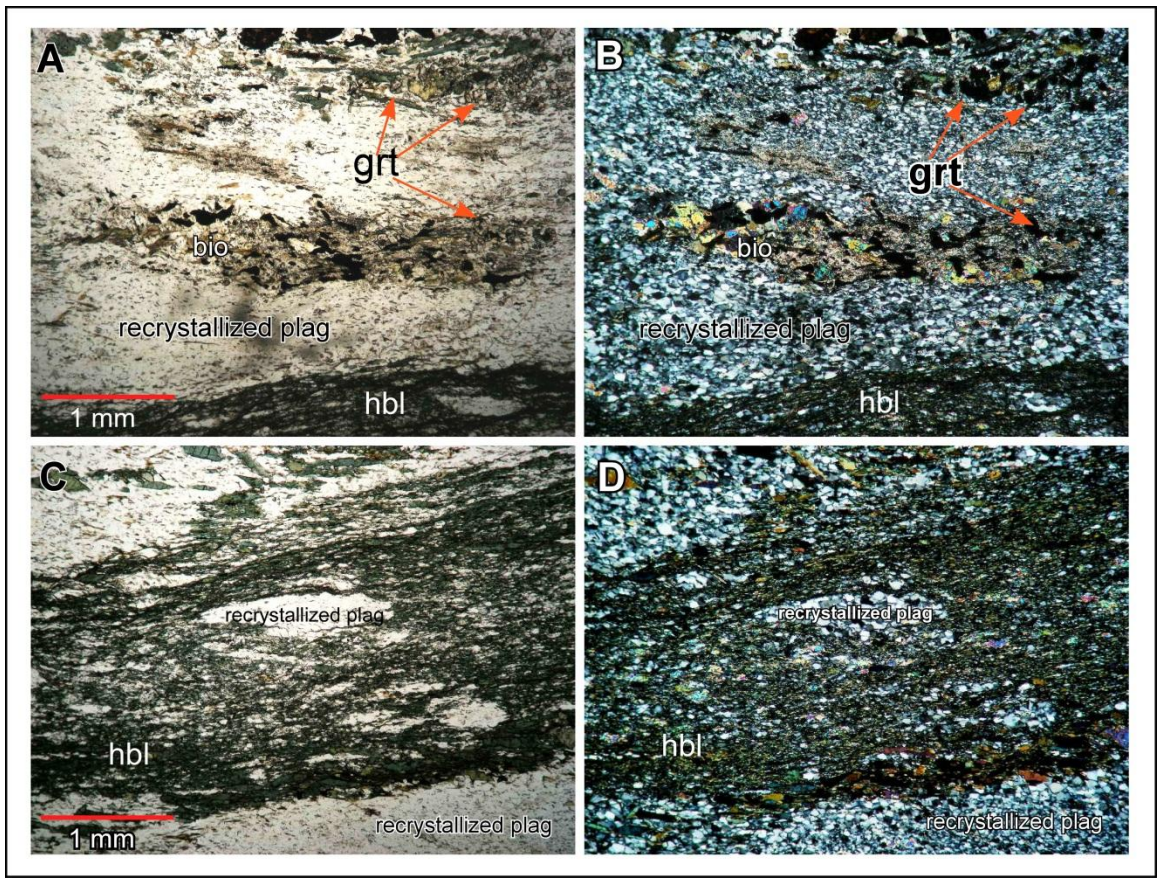

Figure 3.15. Photomicrographs from EID08-4-6a-2 showing the mineral assemblage and textures. Sample EID08-4-6a-2 in (A) ppl and (B) xpl and a different area of the same sample in (C) ppl and (D) xpl.

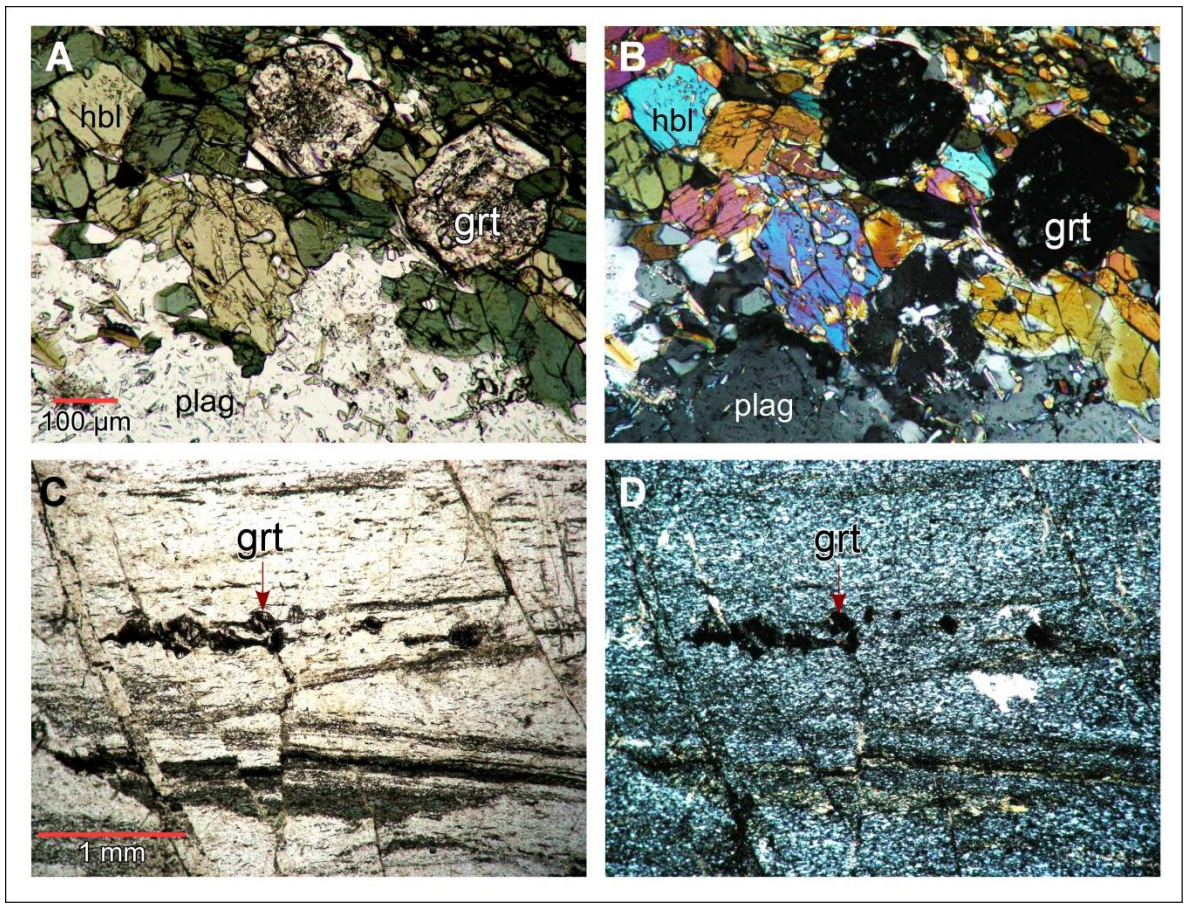

Figure 3.16. Photomicrographs from the ESZ showing examples of garnet grains. Sample EID08-7-2b in (A) ppl and (B) xpl and sample EID09-4g in (C) ppl and (D) xpl.

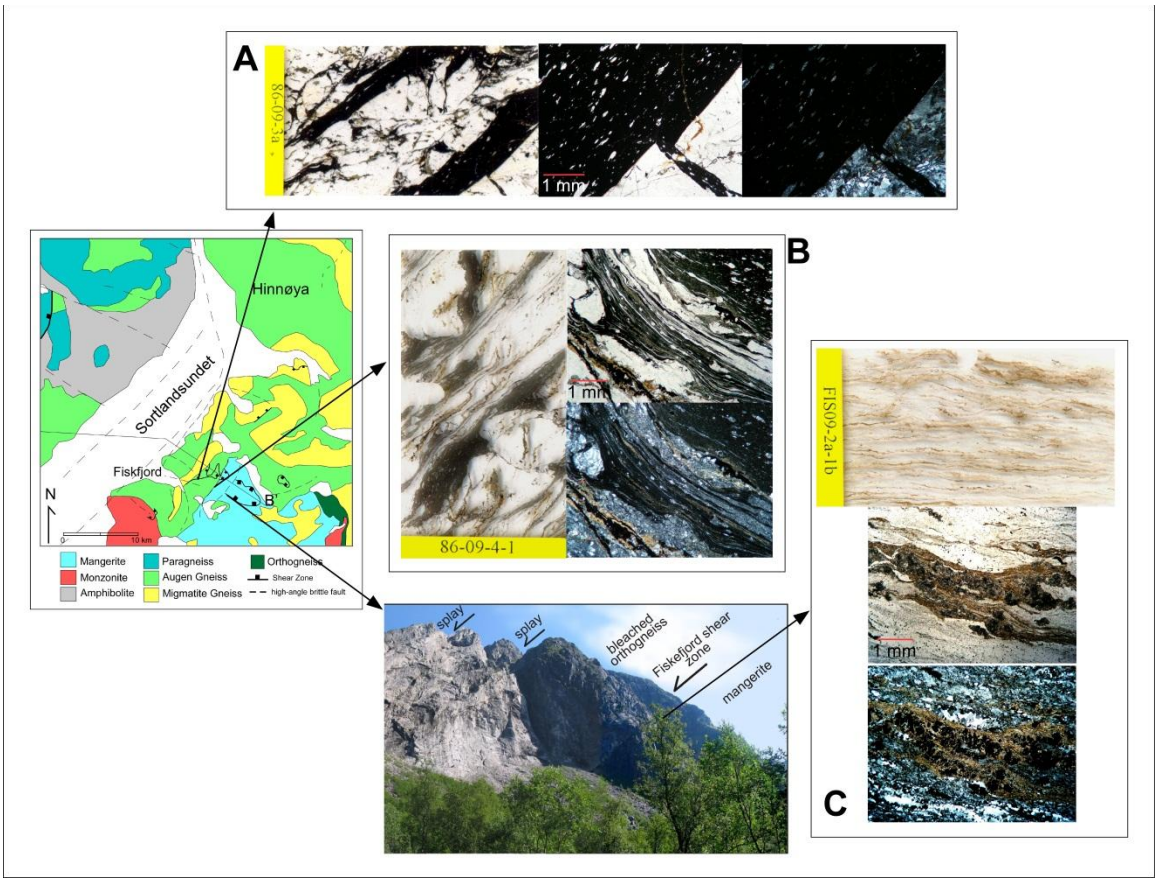

Figure 3.17. Fiskfjord sample progression from brittle to ductile processes moving across the shear zone. Photomicrographs (A) shows sample 86-09-3a, a fractured bleached orthogneiss with unaltered injection of pseudotachylyte melt. (B) shows sample 86-09-4-14, a bleached orthogneiss with evidence of melt becoming more mylonitic, and flowing around dynamically recrystallized plagioclase. (C) depicts an mylonitic bleached mangerite with hornblende and garnet nucleating along the foliation.

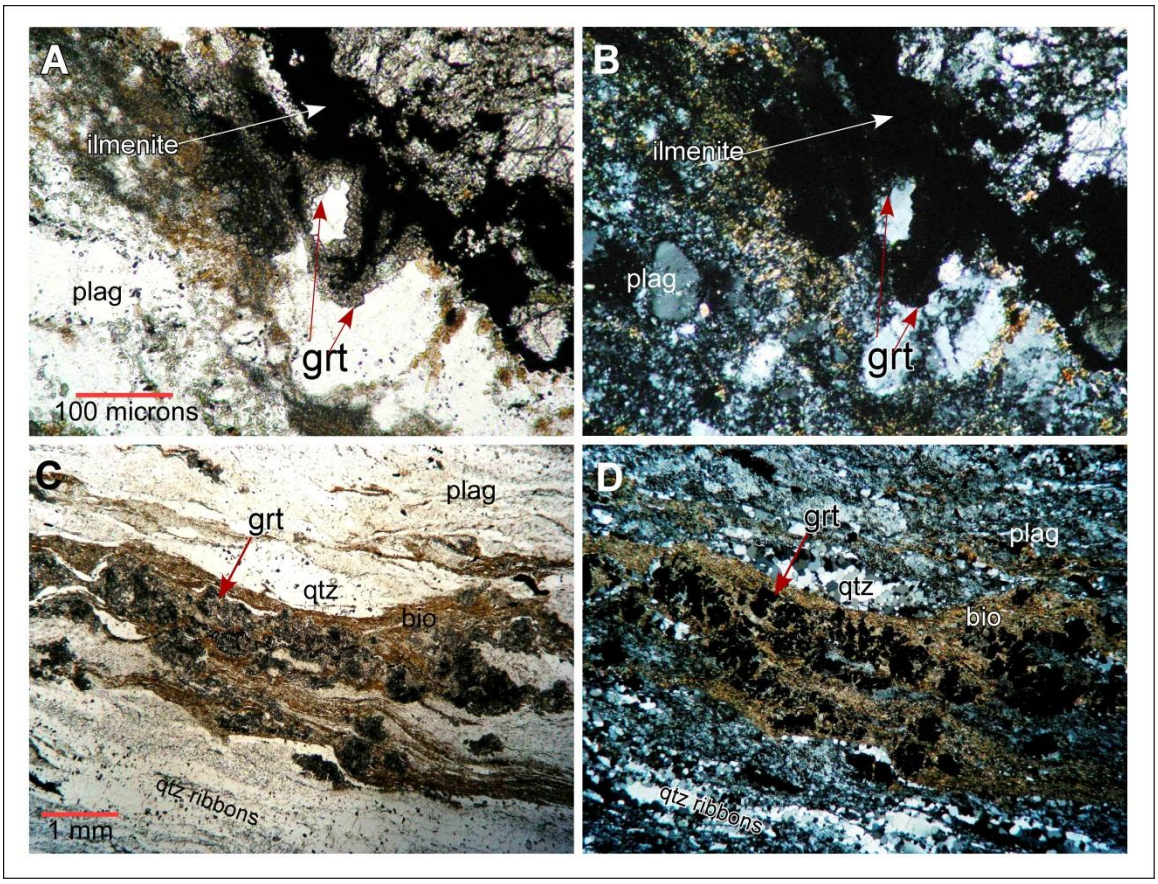

Figure 3.18. Photomicrographs from the FSZ showing garnets nucleating on ilmenite rims in sample 86-09-3-1 in (A) ppl and (B) xpl, and garnets forming in clusters with biotite in sample FIS09-2a-1b in (C) ppl and (D) xpl.

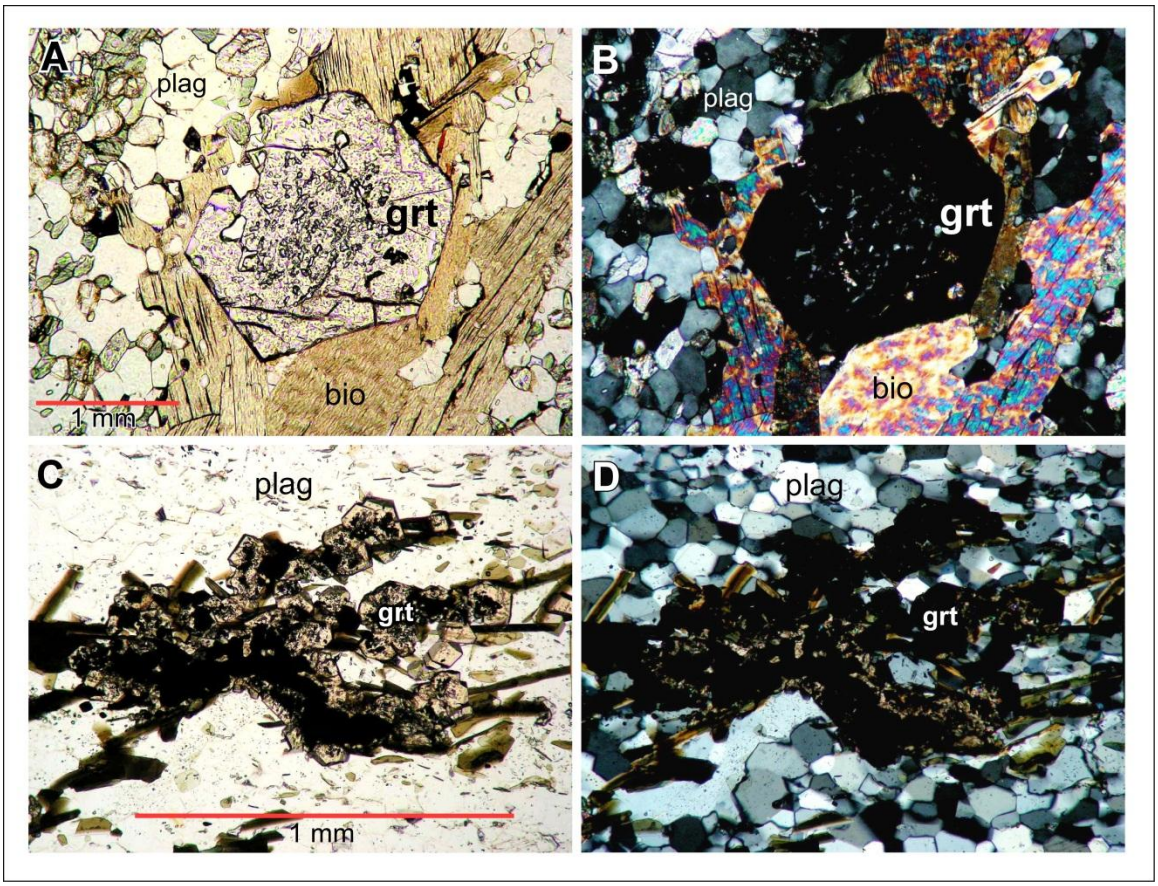

Figure 3.19 Photomicrographs from the FSZ showing euhedral garnets forming with biotite in sample FIS09-2b in (A) ppl and (B) xpl, with clusters of euhedral garnets forming with biotite in sample FIS09-3a-1b in (C) ppl and (D) xpl.

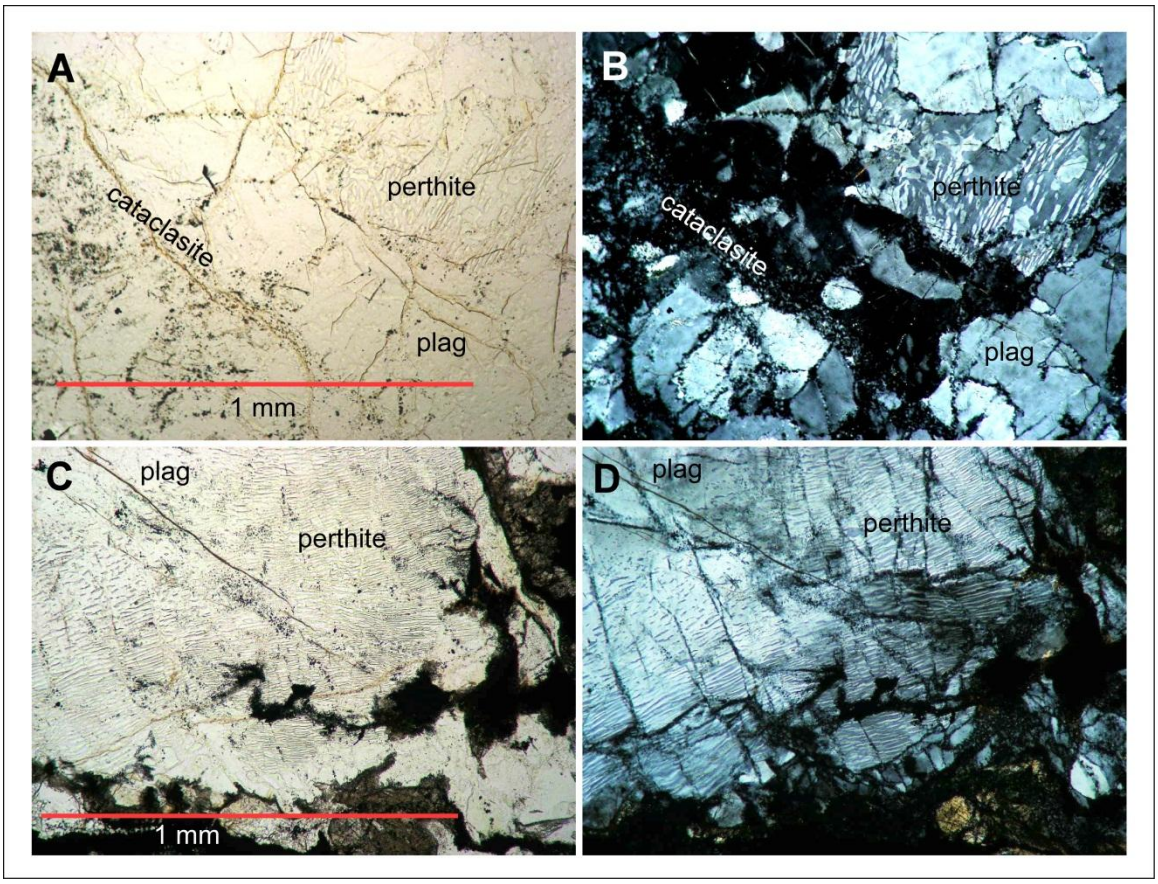

Figure. 3.20 Photomicrographs from the FSZ showing perthitic textures in feldspar forming with dynamically recrystallized plagioclase and cataclasite. Sample 86-09-1b-2 (A) ppl and (B) xpl and sample 86-09-3a (C) ppl and (D) xpl.

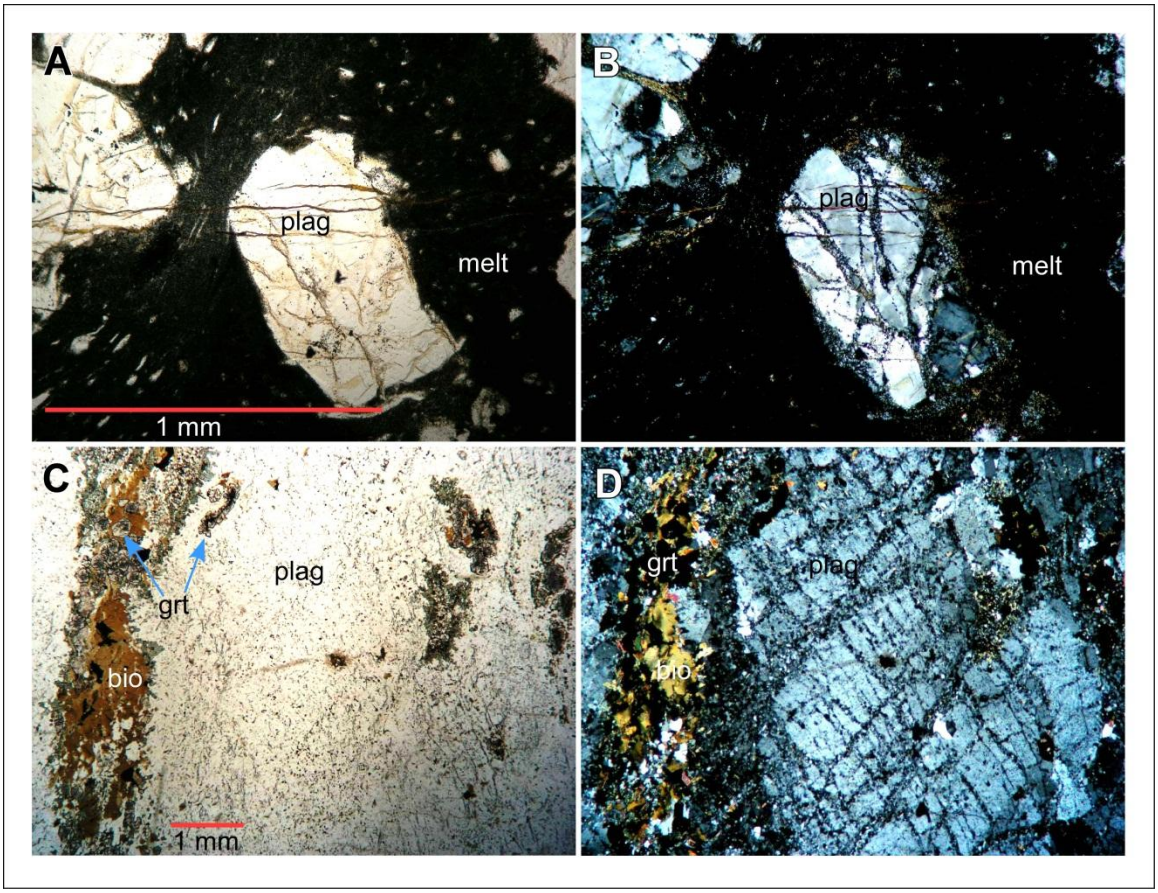

Figure 3.21 Photomicrographs from the FSZ showing plagioclase grains being fractured and dynamically recrystallized in samples 86-09-1b-1 (A) ppl and (B) xpl and sample FIS09-2d (C) ppl and (D) xpl.

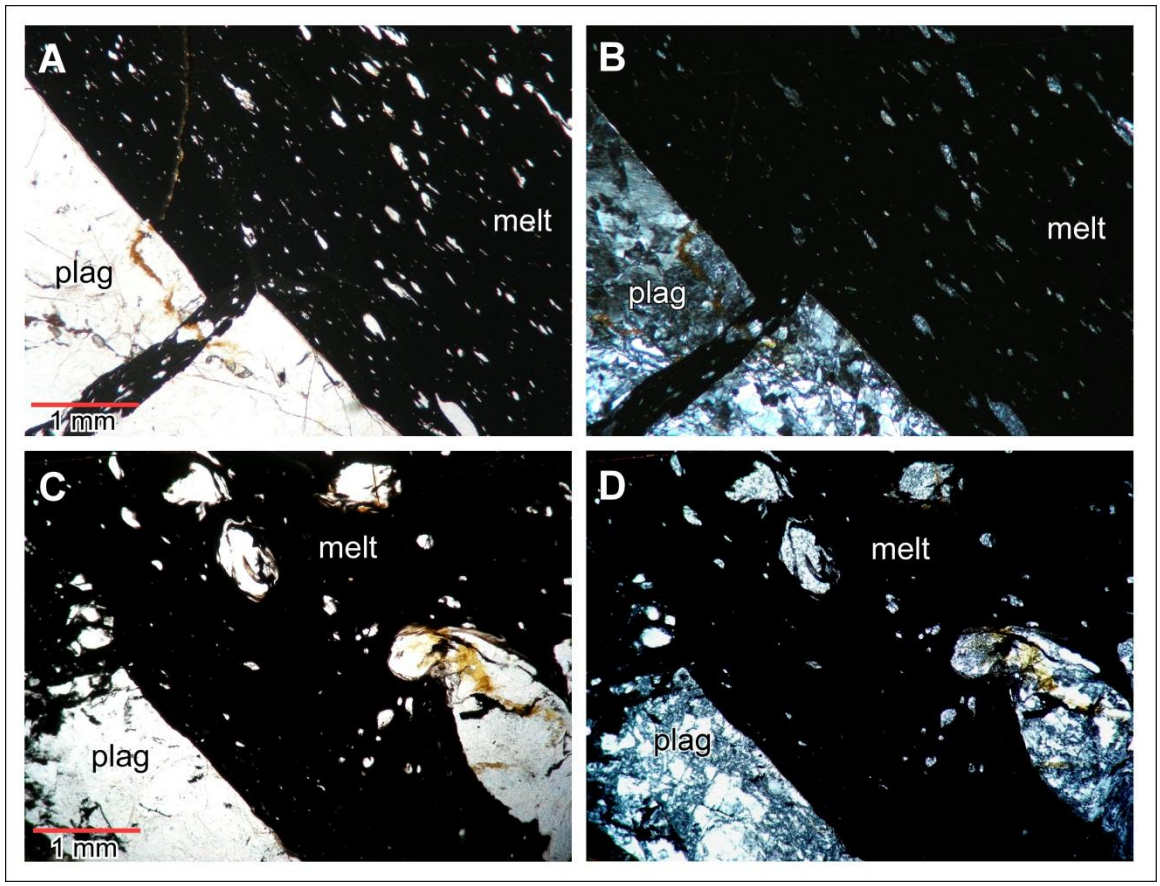

Figure 3.22. Photomicrographs from the FSZ showing pseudotachylyte in sample 86-09-3a (C) ppl and (D) xpl, and elongated plagioclase clasts (A) ppl and (B) xpl.

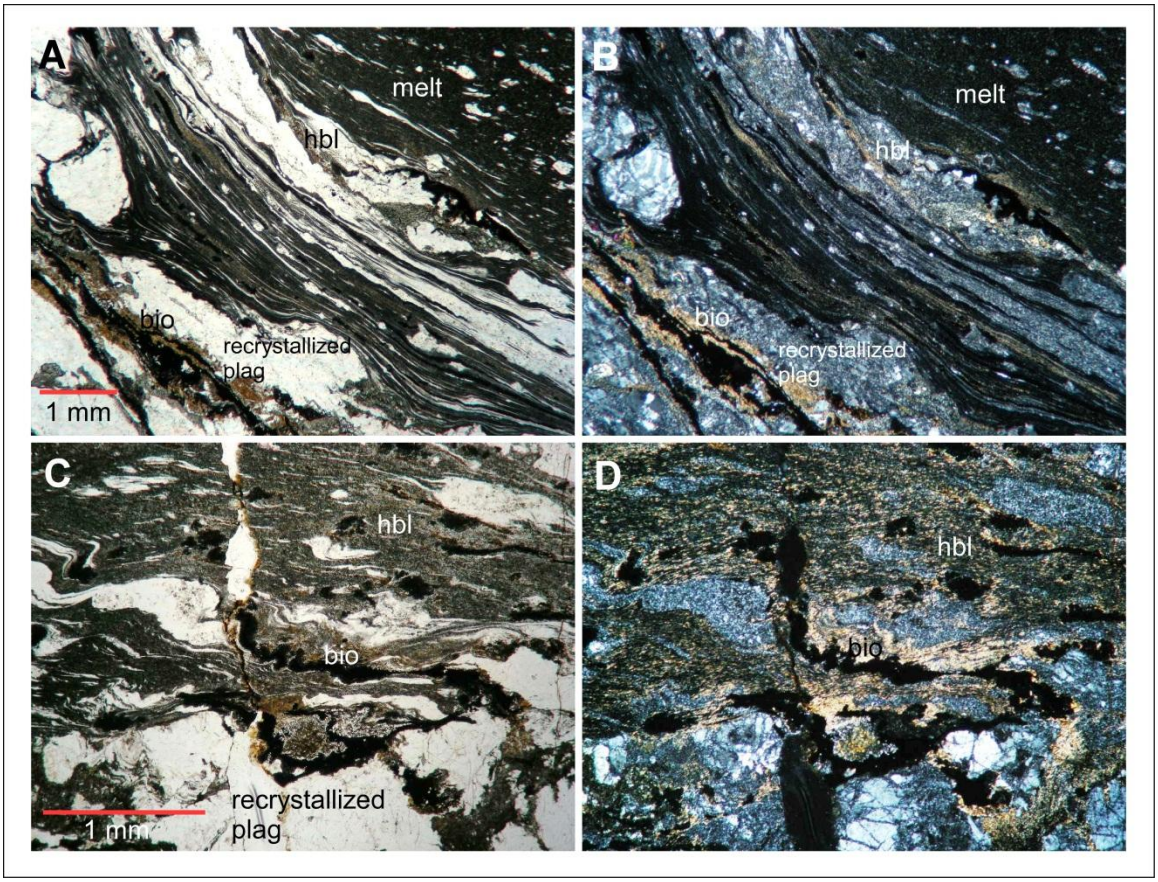

Figure 3.23. Photomicrographs from the FSZ showing mylonitized melt flowing around recrystallized plagioclase in sample 86-09-4-1 (A) ppl and (B) xpl and melt with dynamically recrystallized hornblende and plagioclase in sample 129-09-2-2a (C) ppl and (D) xpl.

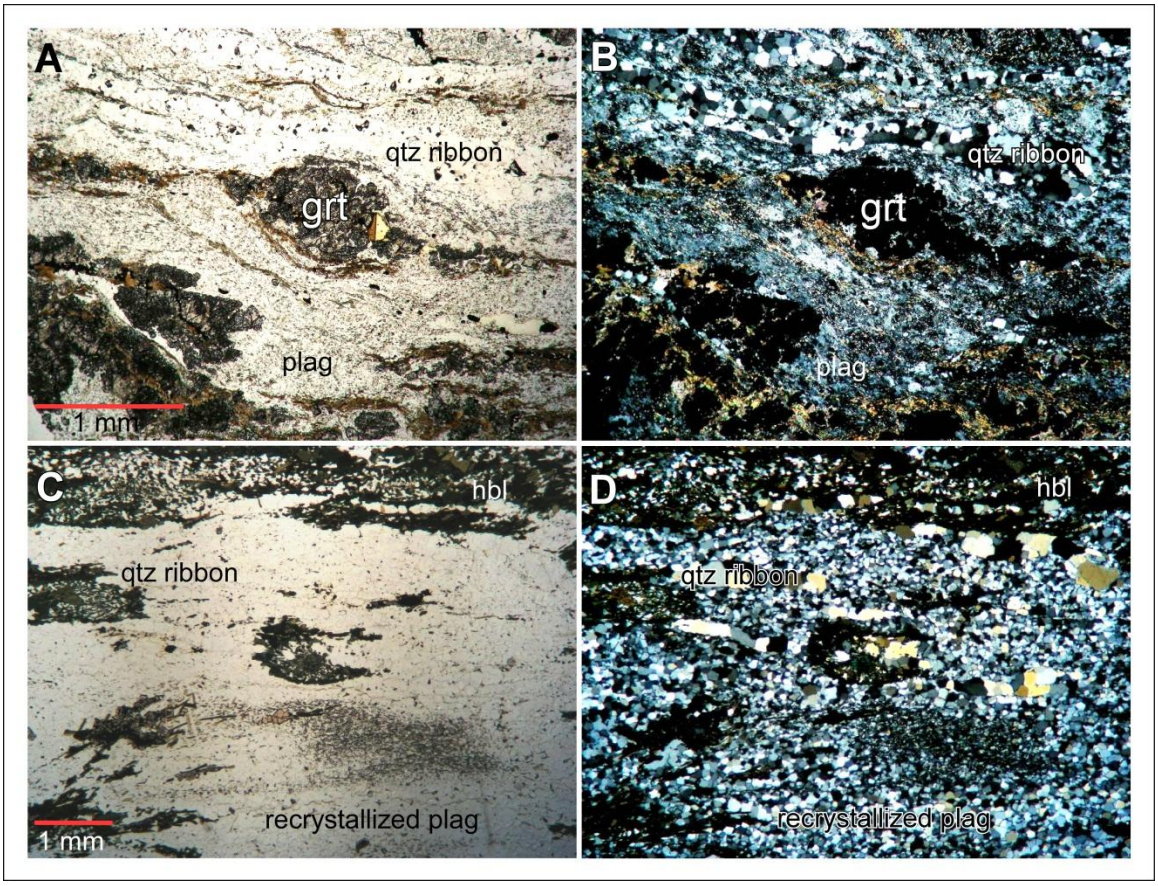

Figure. 3.24. Photomicrographs from the FSZ showing quartz ribbons stretched out along the foliation with garnet in sample FIS09-2a-1b (A) ppl and (B) xpl and with recrystallized plagioclase in sample FIS09-3a-1b (C) ppl and (D) xpl.

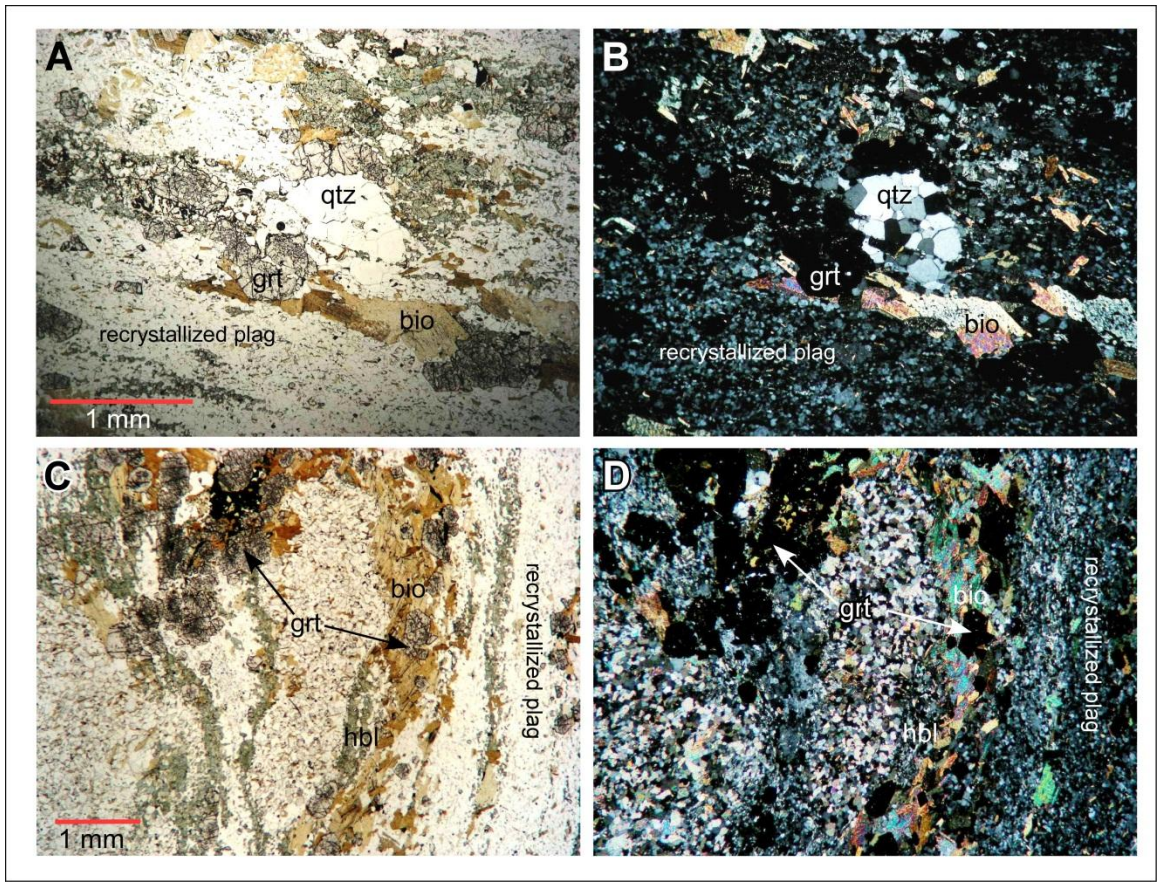

Figure 3.25. Photomicrographs from FIS09-2b showing the mineral assemblage and textures present in the sample, including recrystallized plagioclase in contrast to recrystallized quartz, biotite, garnet, and hornblende. Sample FIS09-2b in (A) ppl and (B) xpl and a different area of the same sample in (C) ppl and (D) xpl.

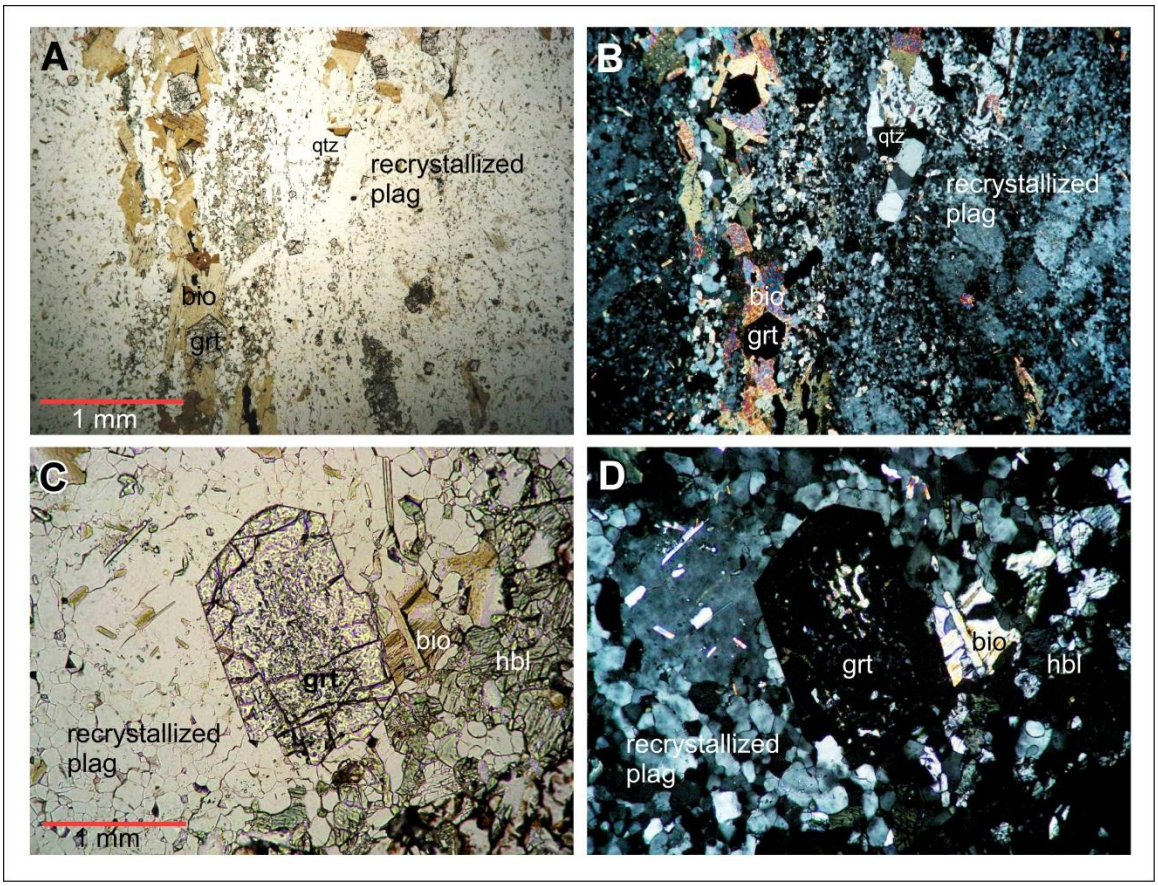

Figure 3.26. Photomicrographs from FIS09-2b showing the mineral assemblage in relation to garnet grains, and examples of garnet inclusions. Most inclusions are of ilmenite, hematite, quartz, rutile, hornblende, pyrite, biotite, and occasionally albite. Sample FIS09-2b in (A) ppl and (B) xpl and a different area of the same sample in (C) ppl and (D) xpl.

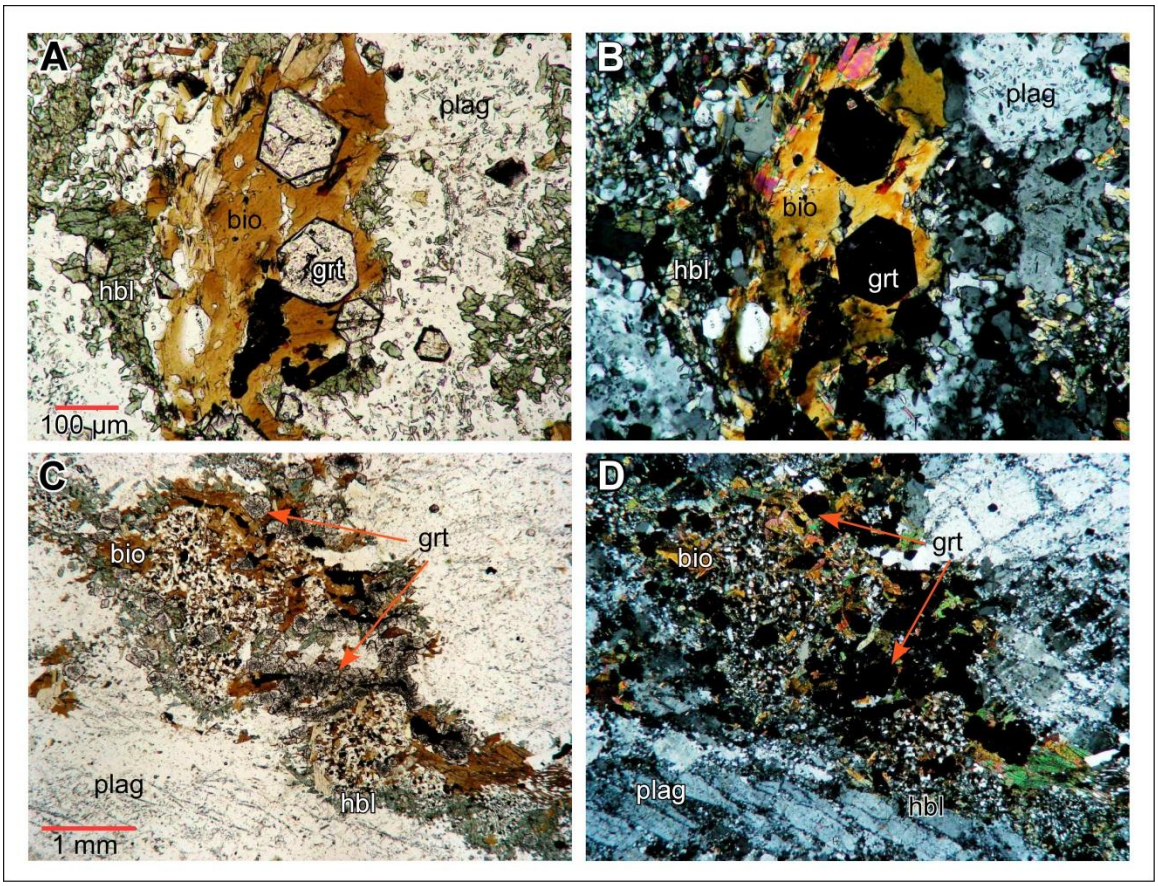

Figure 3.27. Photomicrographs from FIS09-2d showing the mineral assemblage and textures present in the sample, including plagioclase, garnet, hornblende, biotite, opaque (ilmenite and pyrite) as well as quartz. Sample FIS09-2d in (A) ppl and (B) xpl and a different area of the same sample in (C) ppl and (D) xpl.

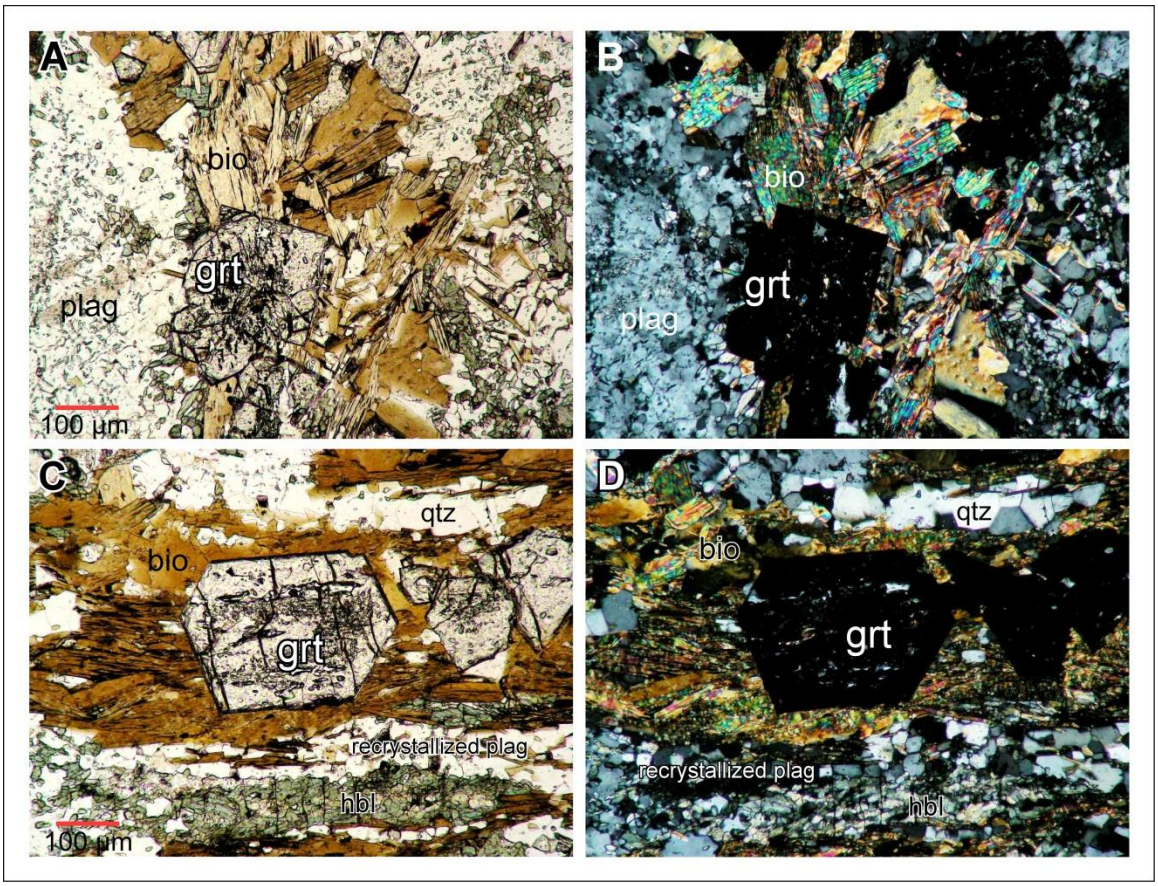

Figure 3.28. Photomicrographs from FIS09-2d showing the mineral assemblage surrounding garnets, and their inclusions which usually consist of pyrite, quartz, biotite, hornblende, and ilmenite. Sample FIS09-2d in (A) ppl and (B) xpl and a different area of the same sample in (C) ppl and (D) xpl.

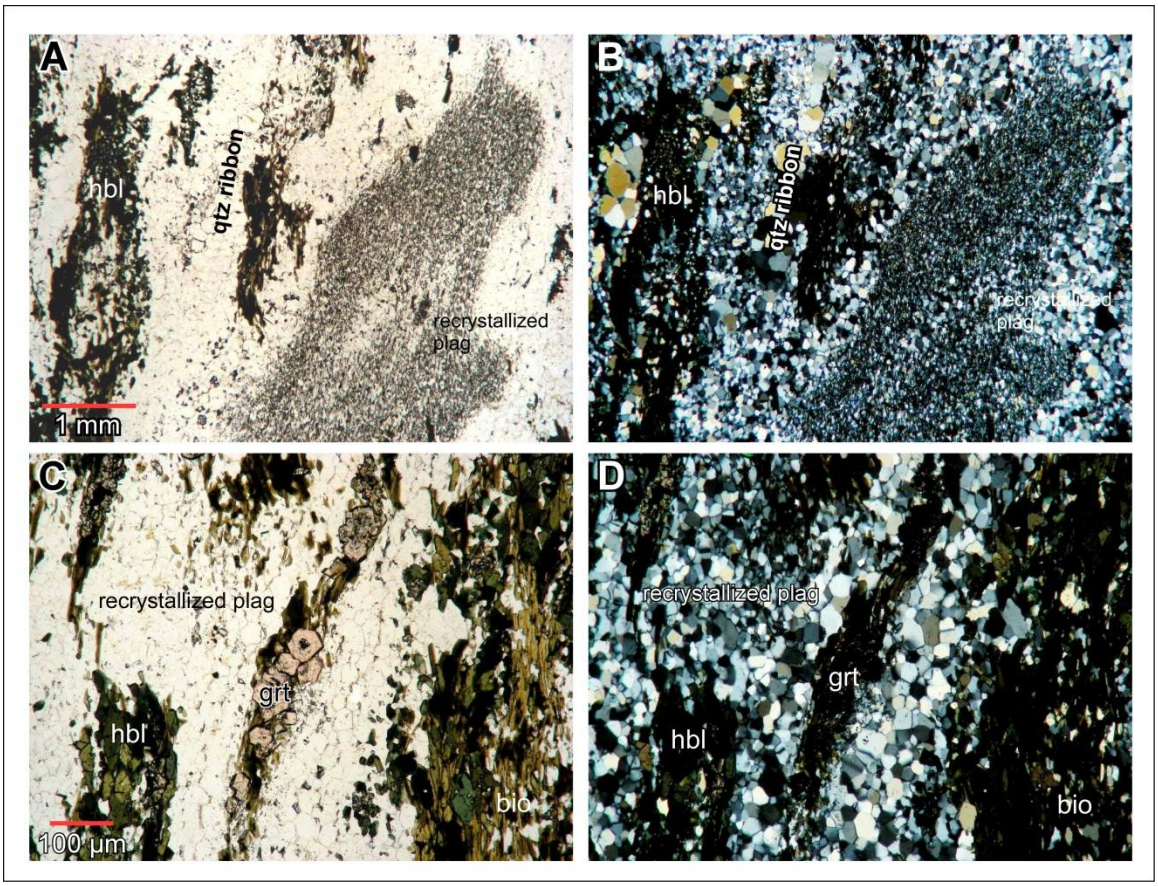

Figure 3.29. Photomicrographs from FIS09-3a-1b showing the mineral assemblage and textures present in the sample, including plagioclase, garnet, hornblende, biotite, opaque (ilmenite and pyrite) as well as quartz ribbons. Sample FIS09-3a-1b in (A) ppl and (B) xpl and a different area of the same sample in (C) ppl and (D) xpl.

CHAPTER 4: Thermobarometry

The petrotectonic history of adjoining terranes in an orogen can be compared by elucidation of the mineral reaction history and calculation of the P-T history via thermobarometry. The Eidsfjord and Fiskfjord shear zones occur within chemically similar lithologies, including monzonite, mangerite, and anorthosite. Two common mineral assemblages appearing in both the ESZ and FSZ are clinopyroxene + hornblende + plagioclase + biotite + quartz and hornblende + biotite + plagioclase + quartz, which result from amphibolite facies retrogression overprinting granulite facies mineral assemblages in monzonite, mangerite, and anorthosite protoliths (Steltenpohl et al., 2011). It is the presence of garnet + hornblende + plagioclase that permits application of thermometers and barometers in all samples to determine the depth of coseismic slip and whether there is a difference in the tectonic evolution of the two crustal blocks in which the shear zones occur.

The significance of calculating P-T values for the two shear zones is that pressure reflects the depth of the seismogenic zone, and temperature reflects the geothermal gradient in the crust at the time of deformation. The presence of pseudotachylyte at both the ESZ and the FSZ implies that coseismic displacement was occurring at the calculated depth, which may or may not coincide with depths commonly inferred for the seismogenic zone (3-20 km) in mature plate boundary faults such as the San Andreas.

Thermobarometry in this study is based on the garnet—hornblende Fe—Mg exchange thermometer of Ravna (2000) and the geobarometers of Kohn and Spear (1990) based on the following equilibria:

Anorthite + Tremolite = Grossular + Pyrope + Tschermakite + Quartz

Anorthite + Fe-Actinolite = 2 Grossular + Almandine + Fe-Tschermakite + Quartz

The two barometers differ only in that one is for the Mg endmember for the mafic phases, and the other corresponds to the Fe end-member reaction. Mineral compositions acquired from microprobe analysis revealed that hornblendes from the ESZ tended to be intermediate in Mg#

(0.5). Hornblendes from the FSZ tended to be slightly more Fe-rich, with average values of Mg# around 0.4. Although other thermobarometers and methods for thermobarometry exist (TWEEQU, THERMOCALC), and the accuracy of calculated P-T values is difficult to quantify, it is the *difference* in calculated P-T values (and, subsequently, the corresponding depths) between the Eidsfjord and Fiskfjord samples that is significant for this study. Assuming all microprobe analytical errors and errors in calibrations of thermobarometers are the same for all samples, then those errors cancel and the differences in pressure and temperature are more significant than absolute values. Another advantage of applying the Kohn and Spear calibrations is that they are based on natural Grt-Hbl-Plag-Qtz assemblages in rocks of similar bulk composition to the samples studied here. This further minimizes error in thermobarometric calibrations and activity models.

To account for differential site preferences of Mg^{2+} and Fe^{2+} in amphiboles, Graham and Powell (1984) calibrated the garnet—hornblende Fe—Mg exchange thermometer against a pre-existing garnet—clinopyroxene Fe—Mg thermometer. They were able to establish a linear relationship between the two thermometers by assuming that all Fe in the system is Fe^{2+}, after stating that any thermometer calculations correcting for the ferric—ferrous iron content using microprobe analysis were not completely accurate when compared to previous wet chemical analyses (Graham and Powell 1984; Ravna 2000). Regarding the hornblende parameters, Ravna (2000) uses the method suggested by Graham and Powell (1984) in assuming all Fe in the hornblende and garnet is Fe^{2+}, along with the structural formula calculation from Schuhmacher (1991) estimating $Fe^{2+}/(Fe^{2+} + Fe^{3+})$ in calcium-rich amphiboles. In addressing the barometer, Kohn and Spear (1989) assume Mg and Fe are partitioned equally in each site (M1 through M4) and all iron is Fe^{2+}.

For the purposes of this study, the calculations to correct for the presence of Fe^{3+} have been dismissed due to natural samples being used for thermobarometric calibrations, which contain mostly Fe^{2+} and an extremely small percentage of Fe^{3+}. Likewise, the Ravna (2000)

thermometer does not contain a pressure correction for hornblende. Graham and Powell (1984) state that in assuming all iron is Fe^{2+} in hornblendes, any accidental errors present in the calculation will be self-correcting.

The activity models used in barometer calculations were those recommended for hornblende, garnet, and plagioclase from Kohn and Spear (1989). The two thermobarometers have been applied to mineral compositional data determined via microprobe analysis from three Fiskfjord samples and three Eidsfjord samples of appropriate assemblages in order to determine the differences between P-T values in each area.

Garnet is extremely useful in relation to pseudotachylyte because of its ability to record and control the rate of many metamorphic processes and reactions (Austrheim et al., 1996). Therefore, the samples chosen for geothermobarometric calculations were selected based on the presence of garnet along with the other necessary phases (plagioclase and hornblende) for the Ravna (2000) thermometer and Kohn and Spear (1989) barometer. The garnets found in the ESZ and FSZ samples represent equilibration of the mineral composition after the termination of deformation from tectonic extension, as indicated by to the presence of euhedral, neoformed garnet porphyroblasts within each sample. The euhedral garnets (on the order of 50-100 μm, and 200 μm in FIS09-3a-1b) found in the FSZ samples are evidence for equilibration as they have not been deformed by subsequent tectonism. Pseudotachylyte is present in other samples from the FSZ (Moecher and Steltenpohl, 2009, 2011), but it was not observed in direct relation to any garnet in the samples of mylonite studied here. The mylonitic samples analyzed were located near the main detachment of the Fiskfjord Shear Zone. Some samples of pseudotachylyte from the area of the Fiskfjord Shear Zone contain garnet, but as the occurrences of pseudotachylyte at the Fiskfjord location were farther west from the main shear zone detachment, these were not analyzed for this thesis (see Moecher and Steltenpohl, 2009).

Microprobe traverses and elemental X-ray maps were made for all garnets used in thermobarometry. If compositional zoning was present, compositions for thermobarometry were

chosen from the garnet rim, which were in equilibrium with the surrounding minerals. BSE images were also collected to keep a record of the location of the garnet within the corresponding thin section. Figures 4.1 through 4.3 show representative garnets from each of the Eidsfjord samples, and Figures 4.4 through 4.6 show representative garnets from each of the Fiskfjord samples.

4.1 Methods

Mineral compositions were collected from selected samples from both the ESZ and the FSZ via electron probe microanalysis on the CAMECA SX50 at the University of Kentucky. For all data collected, accelerating potential was set at 15 kV, peak count time was 10 seconds, and background count time was 5 seconds. Before each analytical session, the microprobe was calibrated using the U.S. National Museum Standards, which were also run as unknowns to ensure accuracy. Sample current varied based on the mineral being analyzed. For plagioclase, sample current was 10 nA, and for garnet and hornblende, the sample current was 20 nA. All data collected and used for this study are presented in Appendices A and B. Representative microprobe data from the Eidsfjord samples are presented in Appendix A, (Tables A.4, A.8, and A.12), and representative data from the Fiskfjord samples are presented in Appendix B, (Tables B.4, B.8, and B.12). Several textural domains in each section consisting of garnet, hornblende, and plagioclase were selected for analysis. After first collecting Fe, Ca, Mg, and Mn elemental X-ray compositional maps for garnet in each domain, BSE images were acquired and quantitative microprobe traverses on garnet and point analyses were collected for each phase in the domain.

4.2 Results

4.2.1 Mineral Chemistry

In sample EID08-3a, some slight zoning was identified in the grossular and almandine traverses, so points for thermobarometry were taken from the garnet rim. In sample EID08-4-6a-2, no significant zoning was observed, however, due to the presence of cracks and a large number of inclusions along the traverse, points were chosen based on mole fraction almandine values

close to 0.6. Garnets in sample EID08-7-2b were not zoned. Samples FIS09-2b and FIS09-2d were found to be slightly zoned, and analysis points were chosen at the garnet rim after filtering out inclusion data. FIS09-3a-1b did contain compositionally zoned garnets, and points for thermobarometry were chosen from the garnet rim.

Figures 4.7 through 4.12 demonstrate compositional variations of the data collected from garnet traverses, as well as plagioclase and hornblende point analyses for both the Eidsfjord and Fiskfjord shear zones. Eidsfjord garnet compositional data (Fig. 4.7) illustrate the heterogeneity among garnet grains. Sample EID08-3a domains plotted at the low end of both grossular and Fe/(Fe+Mg) content, however garnet in the sample as a whole is relatively homogeneous. Sample EID08-4-6a-2 exhibits the greatest heterogeneity in grossular. The EID08-7-2b sample domains seem to have high precision plotting in a cluster. A similar plot of Fiskfjord garnets (Fig. 4.10) shows a slight rise in grossular content, suggesting an approach to equilibrium. Variation in hornblende compositional data are shown in Figures 4.8 and 4.11, and plagioclase compositions are shown in Figures 4.9 and 4.12. All average mineral end-member compositions used for thermobarometry calculations are located in Tables 4.1 and 4.2.

4.2.2 Results of Thermobarometry

The results of thermobarometry for this study are shown in graphical format in Figures 4.13 through 4.16. Each figure shows the barometers as relatively flat to gently sloping horizontal lines and the geothermometers as vertical lines. Each intersection corresponds to the average composition of plagioclase and hornblende in that domain matched with several points from homogeneous regions in the garnet compositional traverse. Each thin section includes several domains with the requisite assemblage, with each domain represented by a specific color. The geobarometer and geothermometer for each domain intersect at a point, and the intersection points for the various domains tend to cluster in an area of P-T space that represents the inferred equilibration T and P for that sample. Tables 4.3 and 4.4 summarize the intersection points for each domain in the three Eidsfjord and three Fiskfjord samples.

One particular thin section, FIS09-3a-1b, exhibits high spessartine contents (X_{sp} ~0.21%) which affects the activity calculations of pyrope and grossular, making them erroneously high (Fig. 4.17). For this reason, the Fe barometers from this thin section were not included in depth calculations for the Fiskfjord area. The activity and high spessartine content for FIS09-3a-1b did not affect the Mg barometers because X_{sp} does appear in a-X relations for the Mg end-member equilibrium, which are included in the P-T plots and also used for calculation of depth.

4.2.3 Depth Estimates

Depth was calculated from the relation

$$P = \rho g z$$

where P = pressure in MPa, ρ = density in kg m^{-3}, g = 9.8 m s^{-2}, and z = depth in m. The average crustal density is assumed at 2.8 x 10^3 kg m^{-3}. Depth was calculated for an average range of temperatures and both the [Mg] and [Fe] pressure calculations.

At the Eidsfjord locality (Table 4.3), two samples yield a P-T intersection at approximately 635 MPa between 640 and 700 °C. The third sample yields a distinctly lower pressure (330 MPa) at the lower end of the temperature range for the other two samples. The pressures correspond to depths of 23 km for the higher pressure samples and 12 km for the lower pressure sample.

At the Fiskfjord locality (Table 4.4), pressures have a much wider range, especially considering the erroneously high Mg of FIS09-3a-1b which yielded a pressure of 1670 MPa. Including this pressure, two samples yield a P-T intersection at approximately 1400 MPa with a temperature range of 630 to 700 °C. Excluding this high Mg barometer, pressures for all three Fiskfjord samples would be approximately 1000 MPa. These pressures correspond to depths between 30 and 40 km with the exclusion of the FIS09-3a-1b high Mg pressure, which alone corresponds to a depth estimate of 60 km.

A variety of methods were utilized to minimize error and assess precision of the results. To insure instrument precision during data collection, the microprobe was standardized using National Museum Standards, Appendix C, Table.C.1, before each analytical session, and those standards were subsequently analyzed as unknowns (Appendix C, Table C.2) before any analyses were collected to insure reproducibility of any given data. Instrument precision in this study is extremely high, as demonstrated by Appendix C, Table C.2, which is the Gore Mt. Garnet standard being analyzed as an unknown.

While uncertainties associated with calculated temperatures and pressures remain relatively unresolved (Worley and Powell, 2000), the necessity for error propagation is minimal in the case of differential thermobarometry studies. Propagation of reliable error analyses are often much more involved than the thermobarometric calculations being analyzed. Worley and Powell (2000) state that any systematic uncertainties will be minimized in calculating differences in P-T values for multiple rock samples. Even if the absolute P-T calculations contain error, if the same process is used to calculate values for multiple samples, the difference in P-T is ultimately significant (Fig. 4.18), especially when evaluating metamorphic processes (Worley and Powell, 2000).

The average and standard deviation was calculated for each sample at Eidsfjord and Fiskfjord. An additional evaluation of error involves garnet, plagioclase, and hornblende compositions plotted with various end-members to demonstrate heterogeneity among grains. These plots show variation within each shear zone, and also within each sample analyzed from the two shear zones. Figures 4.7 through 4.9 correspond to Eidsfjord compositional data, and Figures 4.10 through 4.12 corresponds to Fiskfjord compositional data. Eidsfjord data are compiled in Table 4.3, and Fiskfjord data are compiled in Table 4.4.

	Samples	EID08-3a	EID08-4-6a-2	EID08-7-2b
Garnet	Grossular	7.3 ± 0.9	19.4 ± 0.7	16.1 ± 1.0
	Almandine	66.6 ± 0.9	59.4 ± 0.7	59.4 ± 1.0
	Spessartine	4.7 ± 0.1	10.9 ± 0.2	9.8 ± 0.4
	Pyrope	21.3 ± 0.1	10.3 ± 1.2	14.7 ± 1.0
Hornblende	Tschermakite	32.7 ± 1.7	30.8 ± 3.9	29.6 ± 2.9
	Tremolite	1.9 ± 0.2	1.6 ± 0.4	1.6 ± 0.3
	Fe-Tschermakite	35.7 ± 1.7	35.4 ± 2.5	34.7 ± 2.3
	Fe-Actinolite	2.3 ± 0.2	2.2 ± 0.3	2.2 ± 0.3
	X_{Mg}	47.8 ± 1.4	45.7 ± 4.1	46.1 ± 0.8
	X_{Fe}	52.2 ± 1.4	54.3 ± 4.1	53.9 ± 0.8
Plagioclase	Albite	62.5 ± 4.7	55.1 ± 6.5	56.4 ± 3.5
	Anorthite	37.1 ± 4.9	44.6 ± 6.6	43.3 ± 3.6

Table 4.1. Average garnet, hornblende, and plagioclase compositions for Eidsfjord samples with 2σ standard deviation of the average. These compositions were used for thermobarometric calculations.

	Samples	FIS09-2b	FIS09-2d	FIS09-3a-1b
Garnet	Grossular	13.9 ± 0.9	11.4 ± 0.7	28.2 ± 1.8
	Almandine	60.9 ± 0.8	62.0 ± 1.9	42.7 ± 2.7
	Spessartine	2.9 ± 0.4	1.9 ± 0.4	24.6 ± 2.2
	Pyrope	22.4 ± 0.8	24.7 ± 2.3	4.5 ± 1.0
Hornblende	Tschermakite	37.6 ± 6.5	39.2 ± 3.2	22.8 ± 4.6
	Tremolite	2.6 ± 1.0	2.8 ± 0.5	9.5 ± 0.4
	Fe-Tschermakite	31.1 ± 2.8	30.8 ± 0.9	45.9 ± 3.0
	Fe-Actinolite	1.8 ± 0.4	1.7 ± 0.1	3.8 ± 0.5
	X_{Mg}	54.7 ± 2.8	55.9 ± 1.7	33.1 ± 3.5
	X_{Fe}	45.3 ± 2.8	44.0 ± 1.7	66.9 ± 3.5
Plagioclase	Albite	79.9 ± 5.6	77.4 ± 3.7	75.1 ± 7.0
	Anorthite	19.5 ± 5.9	22.4 ± 3.5	24.2 ± 7.1

Table 4.2. Average mineral compositions within each domain of Fiskfjord samples with 2σ standard deviations of the average. These compositions were used for thermobarometry calculations.

EID08-3a				
	Mg	Fe		
Domain	P (MPa)	P (MPa)	T (°C)	Depth (km)
1	307	300	722	11.1
5	322	324	698	11.8
11	330	401	529	13.3
12	316	340	648	11.9
Average	319	341	649	12.0
Std. Dev.	9.7	43.1	86.0	0.9

EID08-4-6a-2				
	Mg	Fe		
Domain	P (MPa)	P (MPa)	T (°C)	Depth (km)
1	617	629	657	22.7
3	625	683	615	23.8
4	590	628	640	22.2
Average	611	647	637	22.9
Std. Dev.	18.1	31.4	21.2	0.8

EID08-7-2b				
	Mg	Fe		
Domain	P (MPa)	P (MPa)	T (°C)	Depth (km)
1	567	567	696	20.6
2	624	622	730	22.7
3	665	652	744	24.0
4	698	678	709	25.1
5	674	668	708	24.4
7	659	660	705	24.0
Average	648	641	715	23.5
Std. Dev.	46.4	41	17.8	1.6

Table 4.3 Domain P-T intersections of Eidsfjord samples, listing intersections for both the [Mg] and [Fe] barometers as the 'Y' values, where the 'X' values are representative of the thermometer.

FIS09-2b				
	Mg	Fe		
Domain	P (MPa)	P (MPa)	T (°C)	Depth (km)
1	1217	1143	735	43.0
2	1216	1162	696	43.3
3	1065	1025	671	38.1
4	1143	1091	672	40.7
5	1092	1064	658	39.3
Average	1147	1097	686	40.9
Std. Dev.	69.5	56.5	30.6	2.3

FIS09-2d				
	Mg	Fe		
Domain	P (MPa)	P (MPa)	T (°C)	Depth (km)
1	897	873	634	32.3
2	940	912	641	33.7
3	910	889	628	32.8
4	861	851	606	31.2
5	840	824	619	30.3
Average	890	870	626	32.1
Std. Dev.	39.6	33.8	13.5	1.3

FIS09-3a-1b				
	Mg	Fe		
Domain	P (MPa)	P (MPa)	T (°C)	Depth (km)
1	1728	1067	710	50.9
2	1568	1008	713	46.9
3	1733	1118	729	51.9
4	1649	1039	668	49.0
Average	1669	1058	705	49.7
Std. Dev.	77.8	46.4	26.0	2.2

Table 4.4 Domain P-T intersections of Fiskfjord samples, listing intersections for both the [Mg] and [Fe] barometers as the 'Y' values, where the 'X' values are representative of the thermometer.

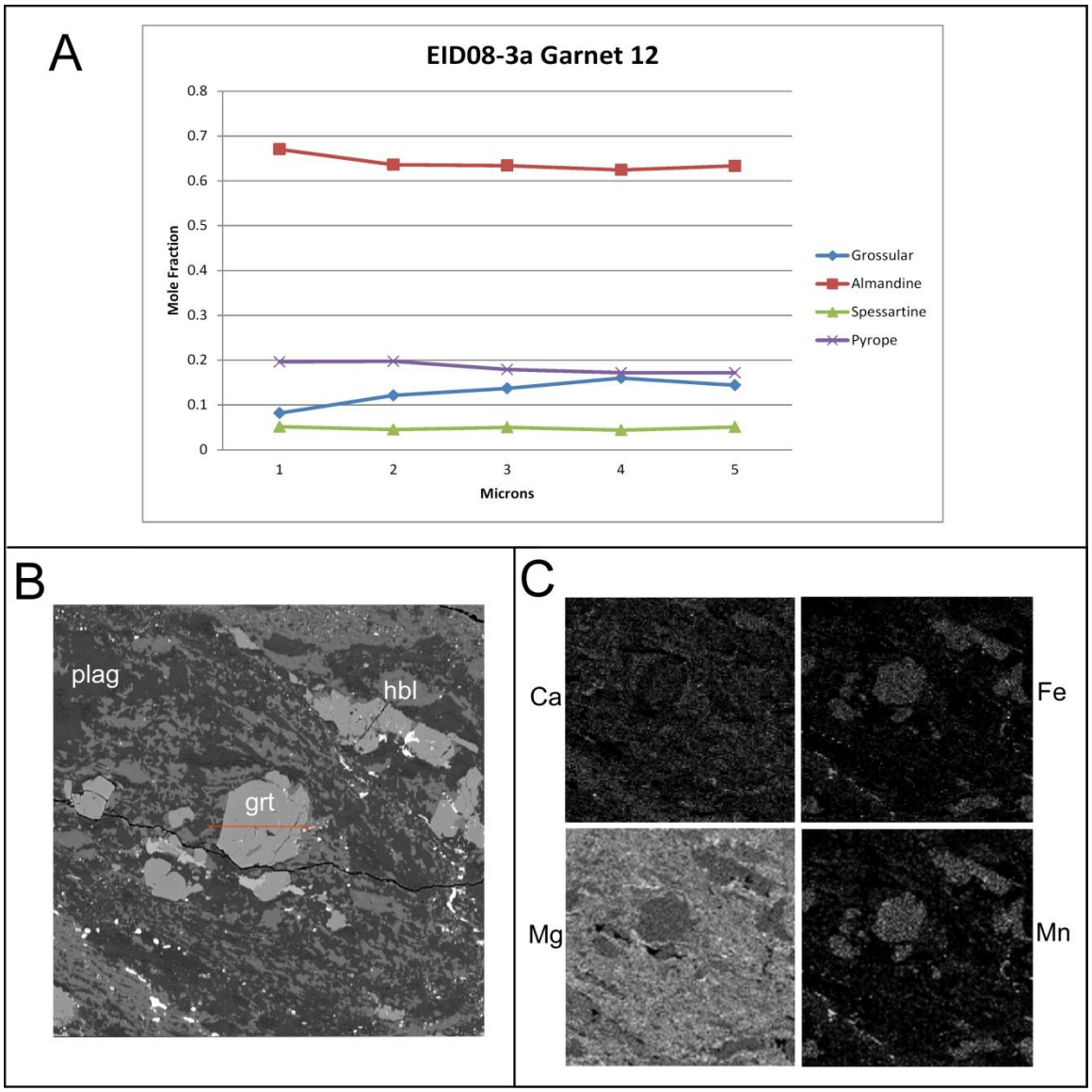

Figure 4.1. Eidsfjord sample EID08-3a, data for garnet 12. A) Garnet traverse data corresponding to the line illustrated in figure B. B) BSE image for EID08-3a garnet 12, showing mineral assemblages present and traverse location. C) Elemental X-ray maps for the area of figure B.

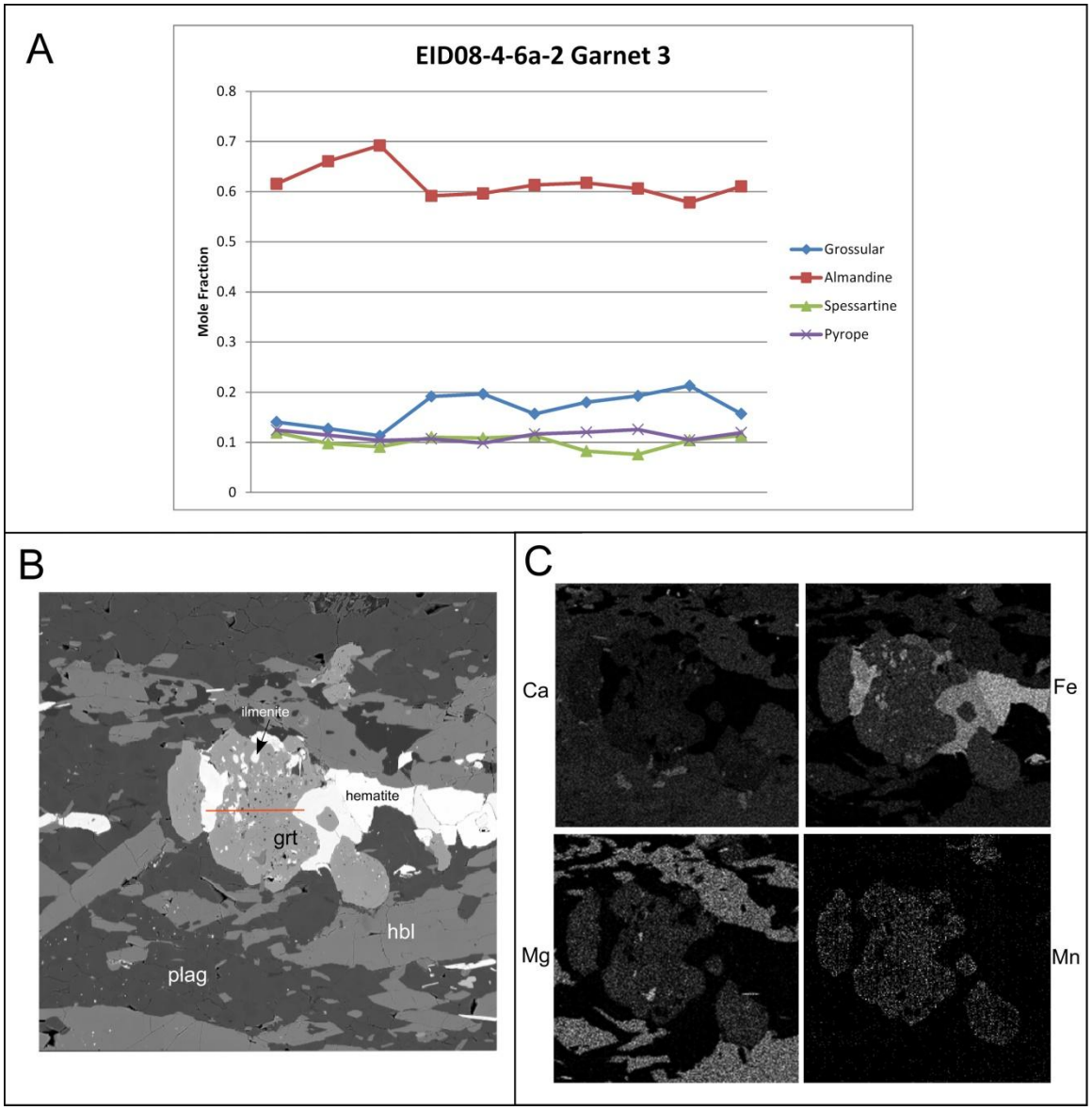

Figure 4.2 Eidsfjord sample EID08-4-6a-2, data for garnet 3. A) Garnet traverse data corresponding to the line illustrated in figure B. B) BSE image for EID08-4-6a-2 garnet 3, showing mineral assemblages present and traverse location. C) Elemental X-ray maps for the area of figure B.

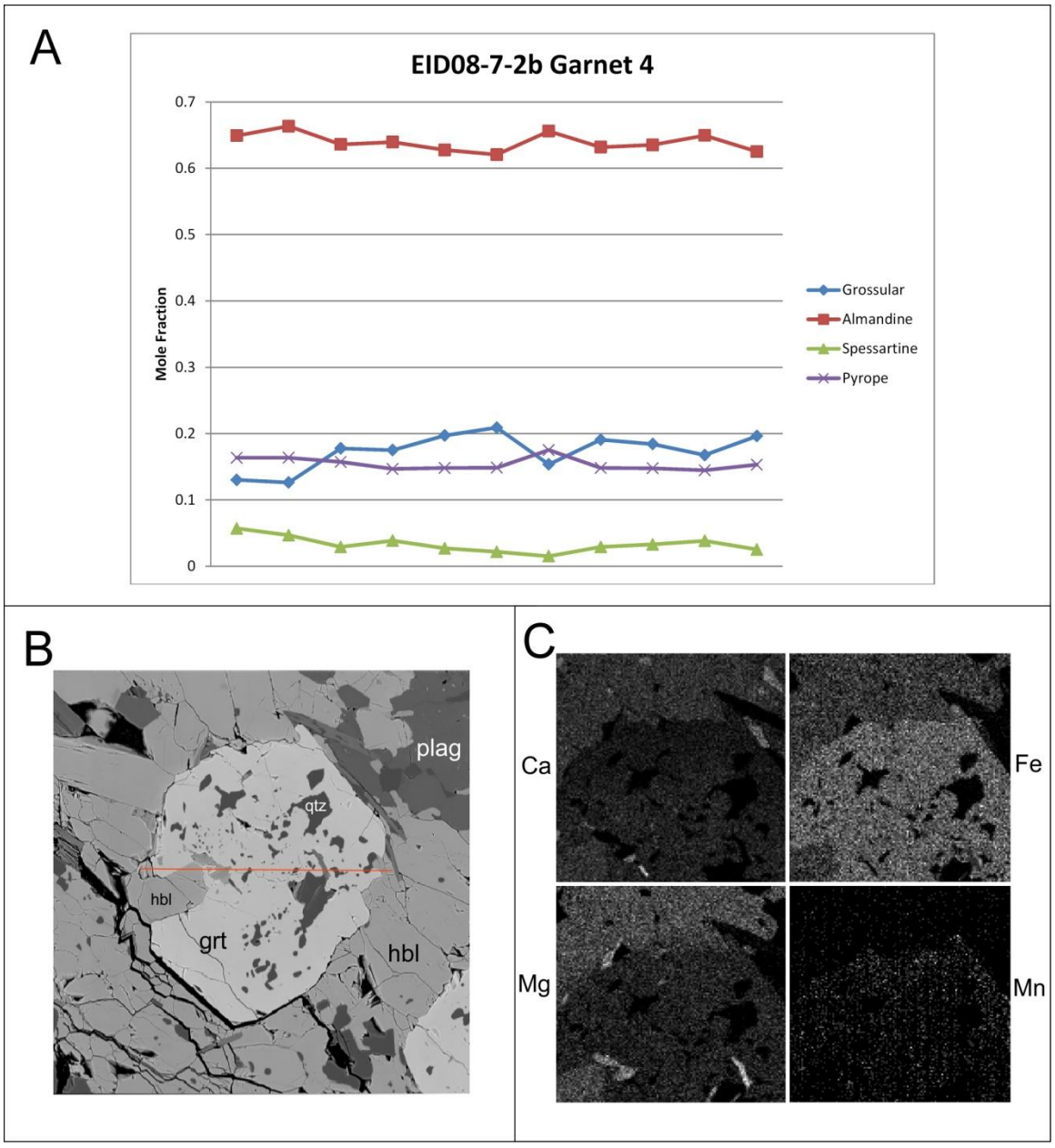

Figure 4.3 Eidsfjord sample EID08-7-2b, data for garnet 4. A) Garnet traverse data corresponding to the line illustrated in figure B. B) BSE image for EID08-7-2b garnet 4, showing mineral assemblages present and traverse location. C) Elemental X-ray maps for the area of figure B.

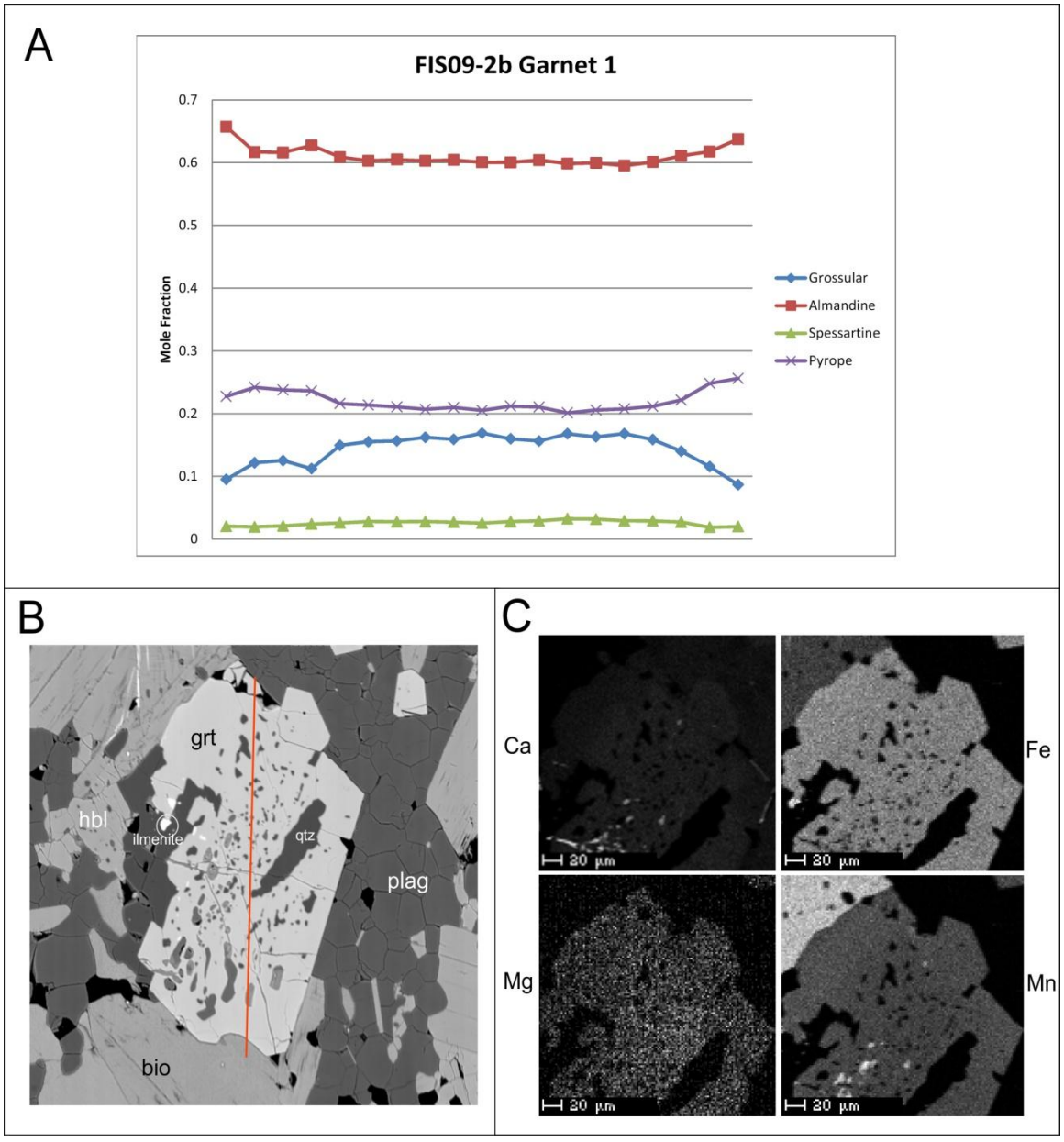

Figure. 4.4 Fiskfjord sample FIS09-2b, data for garnet 1. A) Garnet traverse data corresponding to the line illustrated in figure B. B) BSE image for FIS09-2b garnet 1, showing mineral assemblages present and traverse location. C) Elemental X-ray maps for the area of figure B.

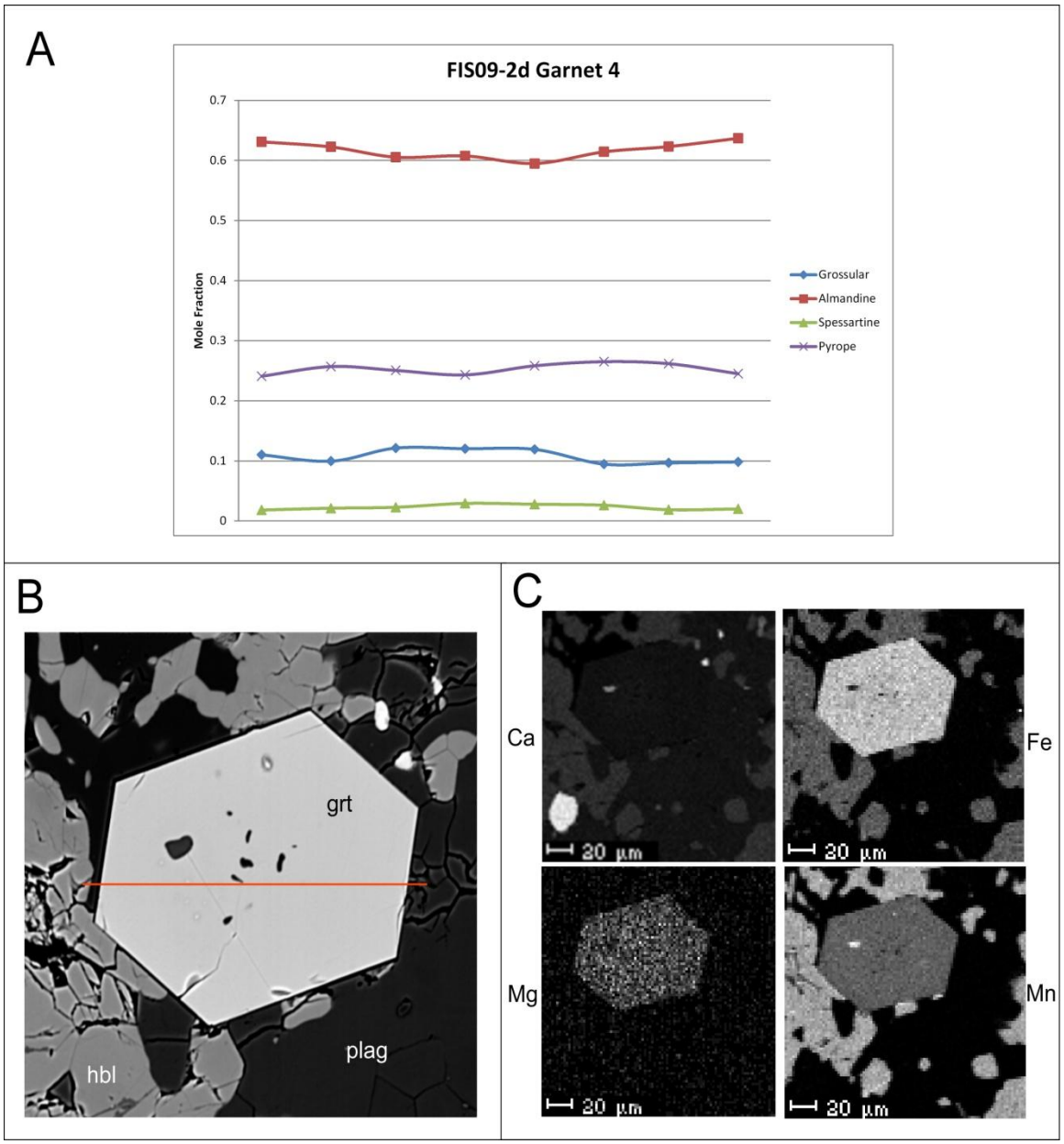

Figure 4.5 Fiskfjord sample FIS09-2d, data for garnet 4. A) Garnet traverse data corresponding to the line illustrated in figure B. B) BSE image for FIS09-2d garnet 4, showing mineral assemblages present and traverse location. C) Elemental X-ray maps for the area of figure B.

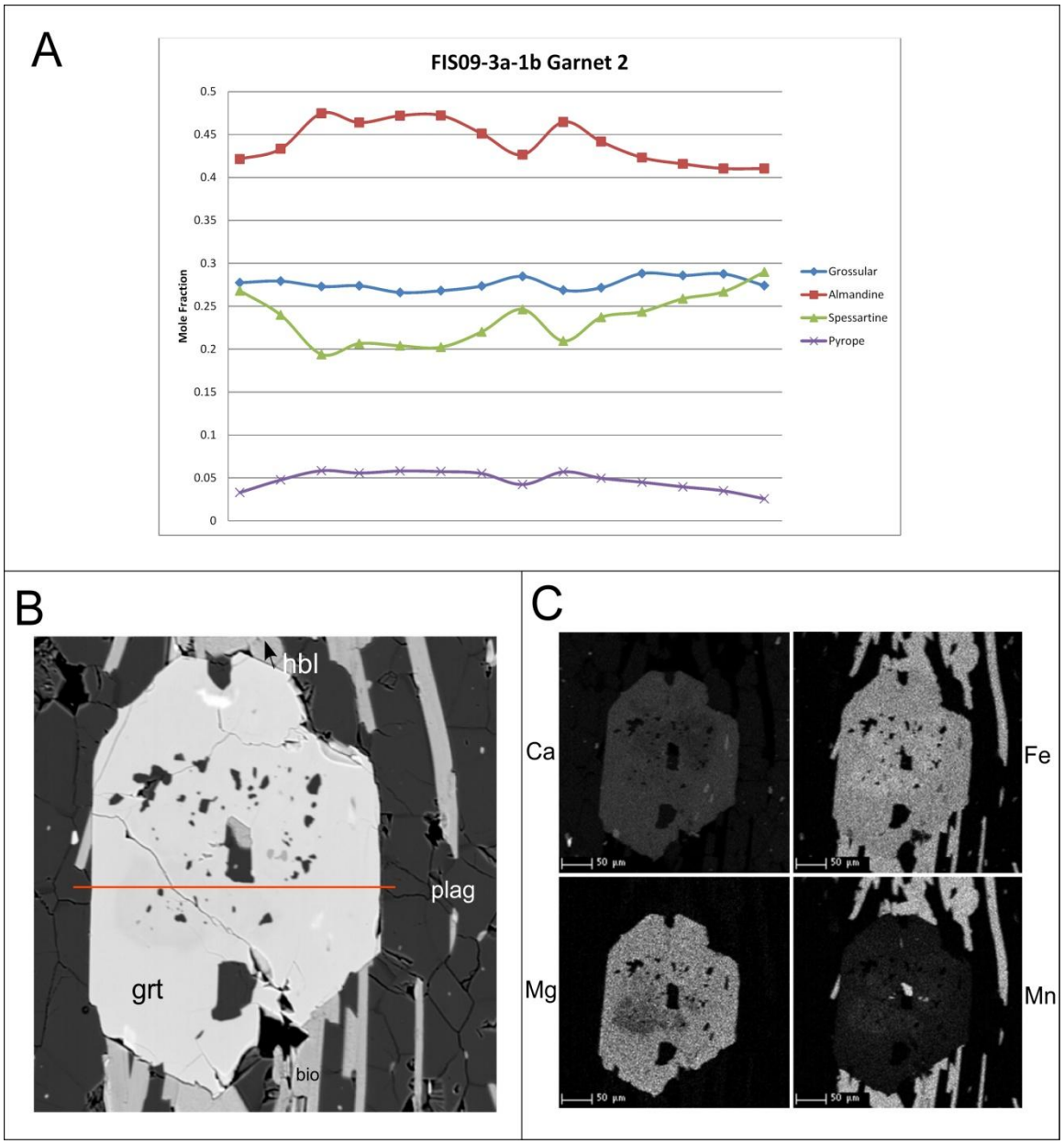

Figure. 4.6 Fiskfjord sample FIS09-3a-1b, data for garnet 2. A) Garnet traverse data corresponding to the line illustrated in figure B. B) BSE image for FIS09-3a-1b garnet 2, showing mineral assemblages present and traverse location. C) Elemental X-ray maps for the area of figure B.

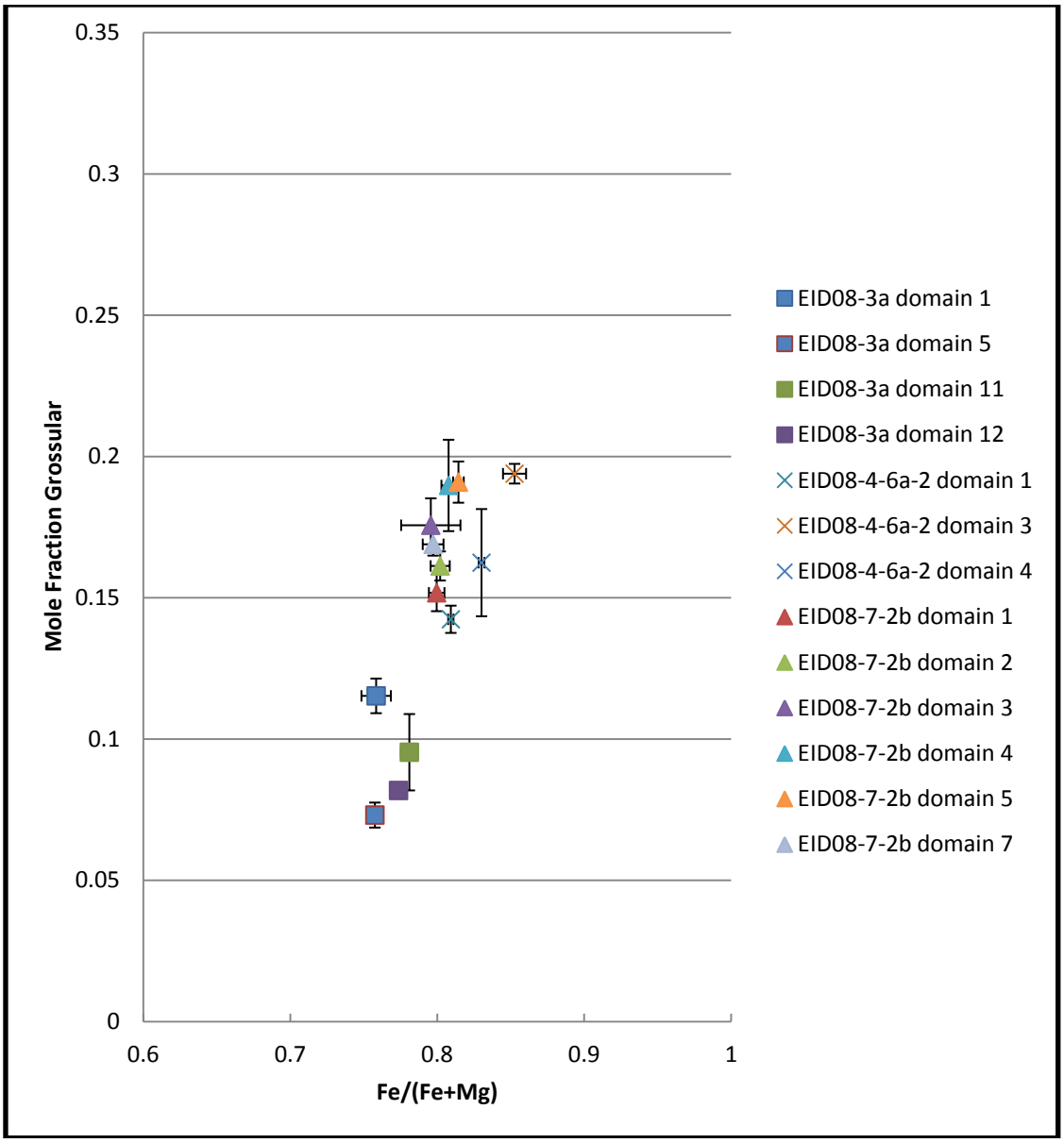

Figure 4.7. Compositional range of Eidsfjord garnets used in thermobarometry. Horizontal and vertical bars show the standard deviation for values averaged in a domain for Fe/(Fe+Mg) and Mole fraction of grossular, respectively.

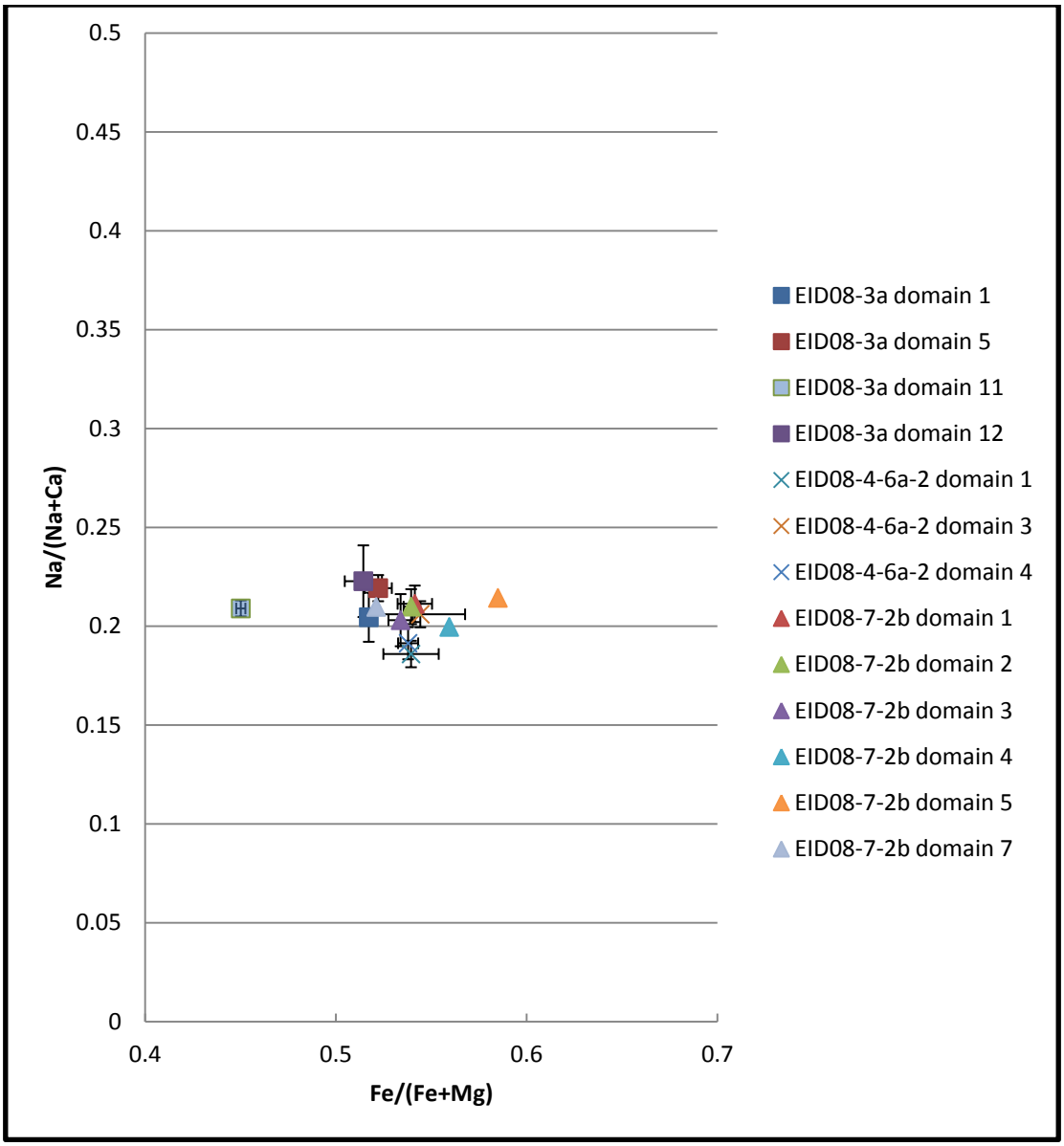

Figure 4.8. Compositional range of Eidsfjord hornblendes used in thermobarometry. Hornblende is relatively homogeneous in each sample with regard to Na/(Na+Ca), with variation less than 0.1. Horizontal and vertical bars show the standard deviation for values averaged in a domain for Fe/(Fe+Mg) and Na/(Na+Ca), respectively.

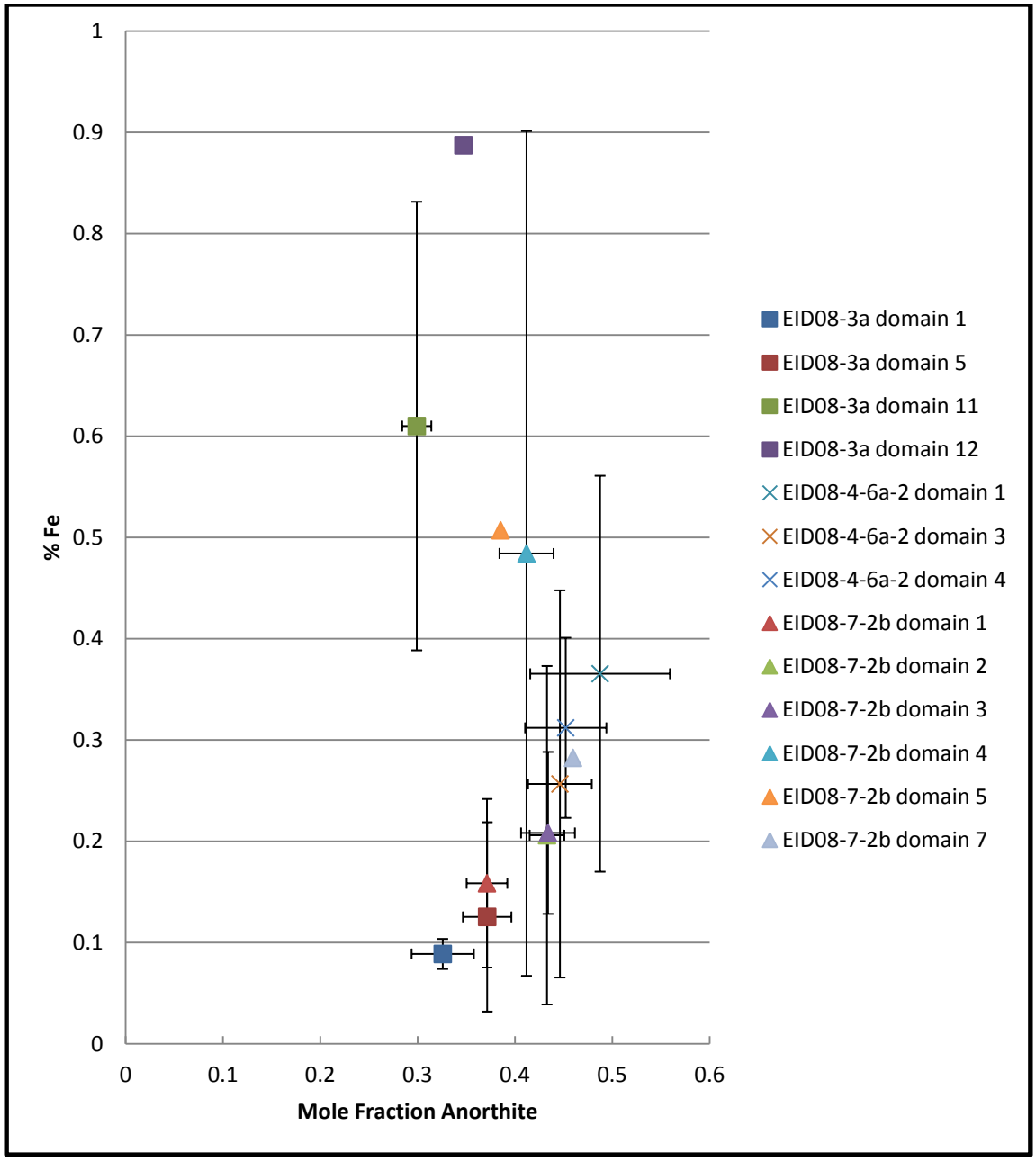

Figure 4.9. Compositional range of Eidsfjord plagioclases used in thermobarometry. Individual samples show a 0.2 mole fraction variation in anorthite content and a steep array with a wide range in iron compositions. Horizontal and vertical bars show the standard deviation for values averaged in a domain for mole fraction anorthite and iron content, respectively.

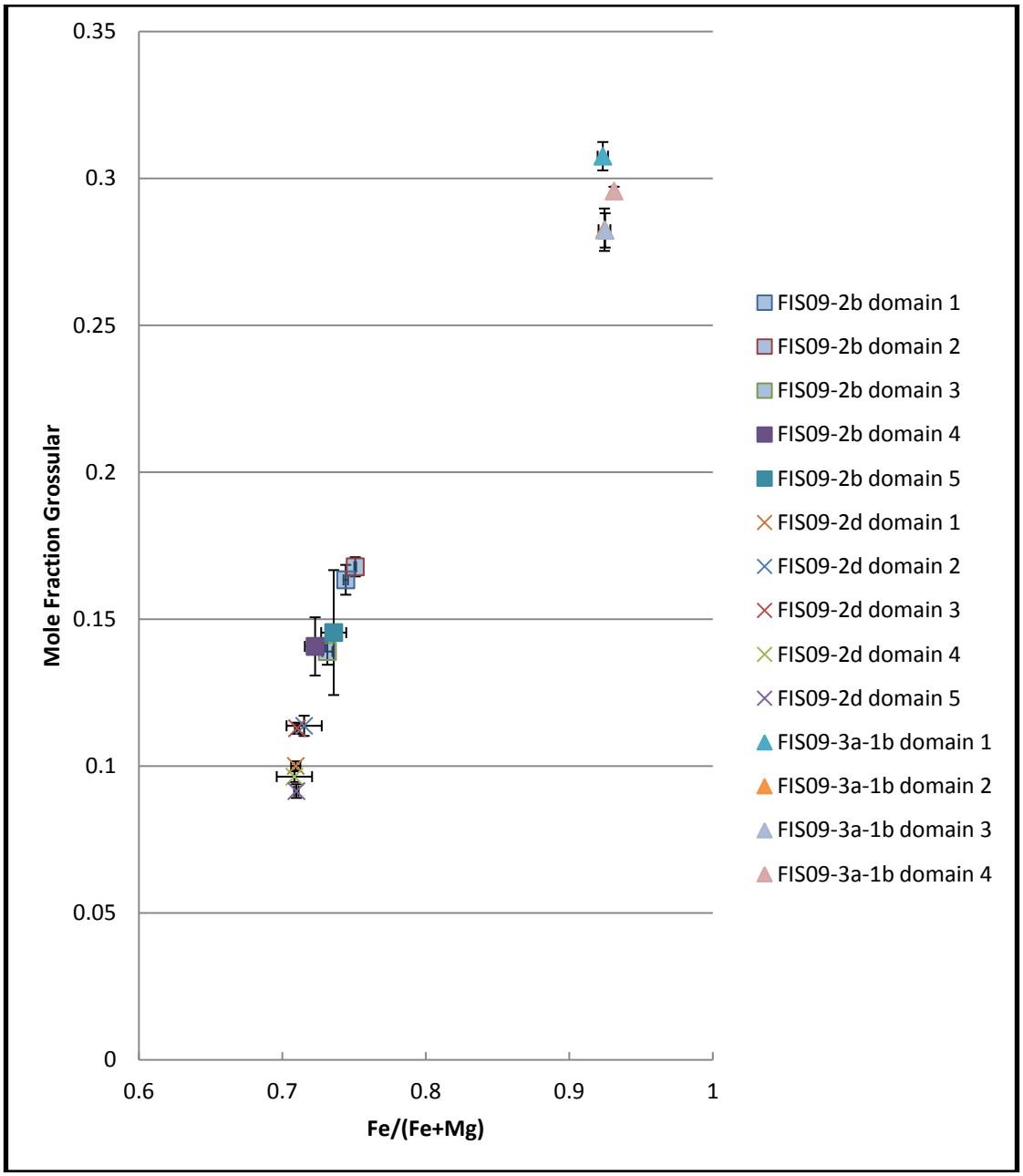

Figure 4.10. Compositional range of Fiskfjord garnets used in thermobarometry. Garnet compositions show only a slight increase in grossular content within each domain, which suggests an approach to equilibrium within samples. Horizontal and vertical bars show the standard deviation for values averaged in a domain for Fe/(Fe+Mg) and Mole fraction of grossular, respectively.

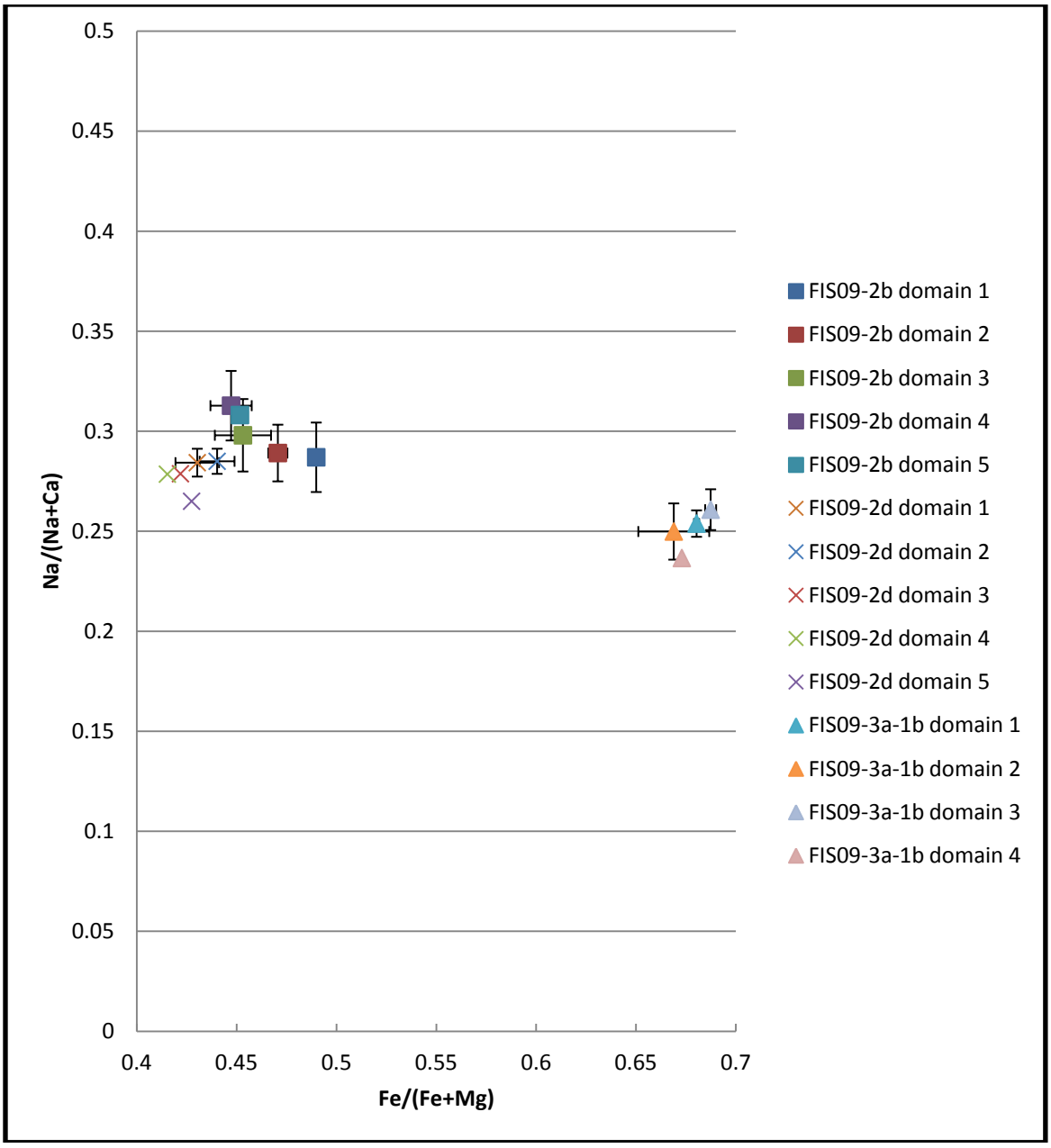

Figure 4.11. Compositional range of Fiskfjord hornblendes used in thermobarometry. Hornblende is relatively homogeneous in each sample domain with regard to Fe/(Fe+Mg), and all samples vary in Na/(Na+Ca) only by 0.1. Horizontal and vertical bars show the standard deviation for values averaged in a domain for Fe/(Fe+Mg) and Na/(Na+Ca), respectively.

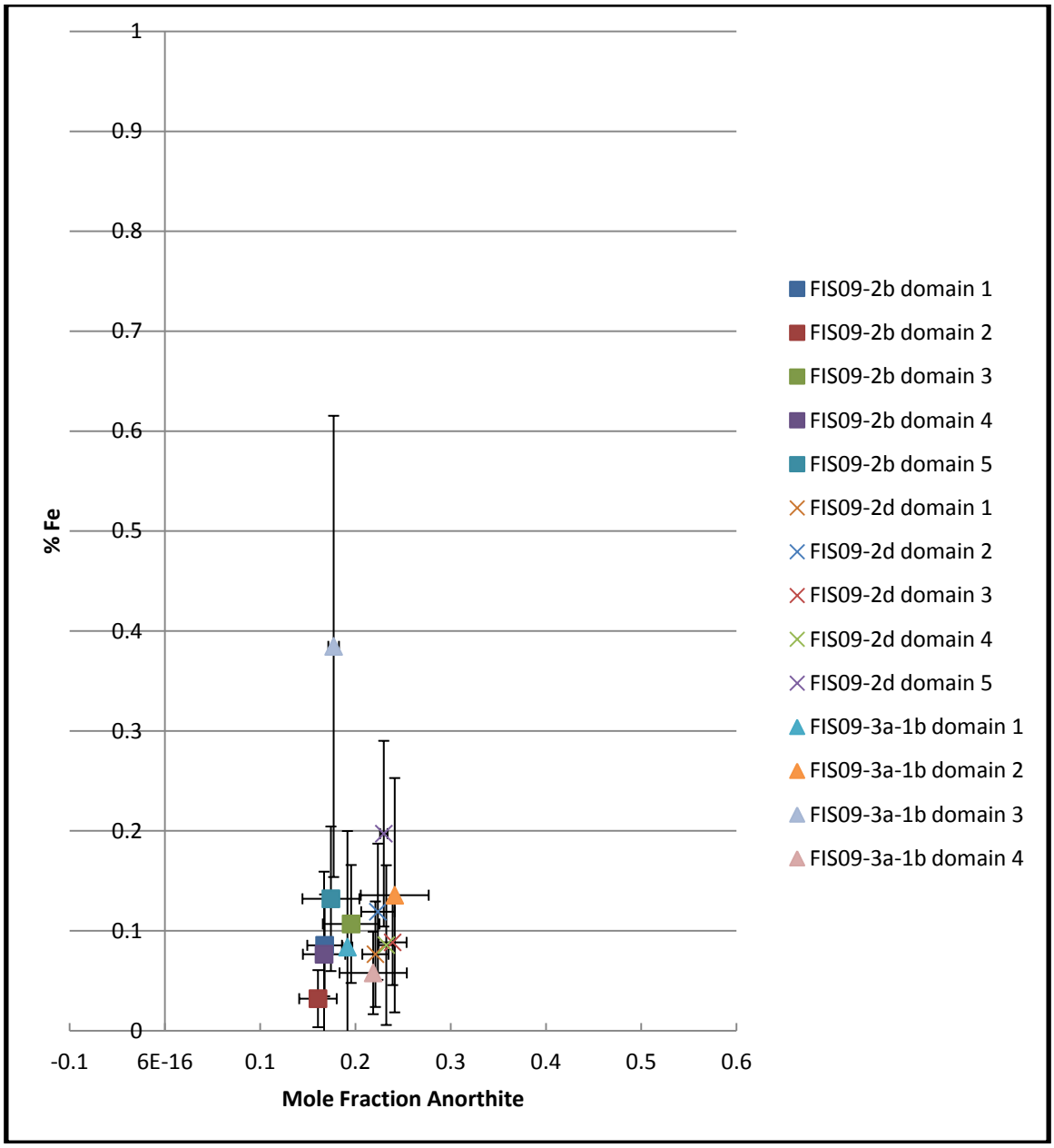

Figure 4.12. Compositional range of Fiskfjord plagioclases used in thermobarometry. Horizontal and vertical bars plot the standard deviation for values averaged in a domain for mole fraction anorthite and iron content, respectively.

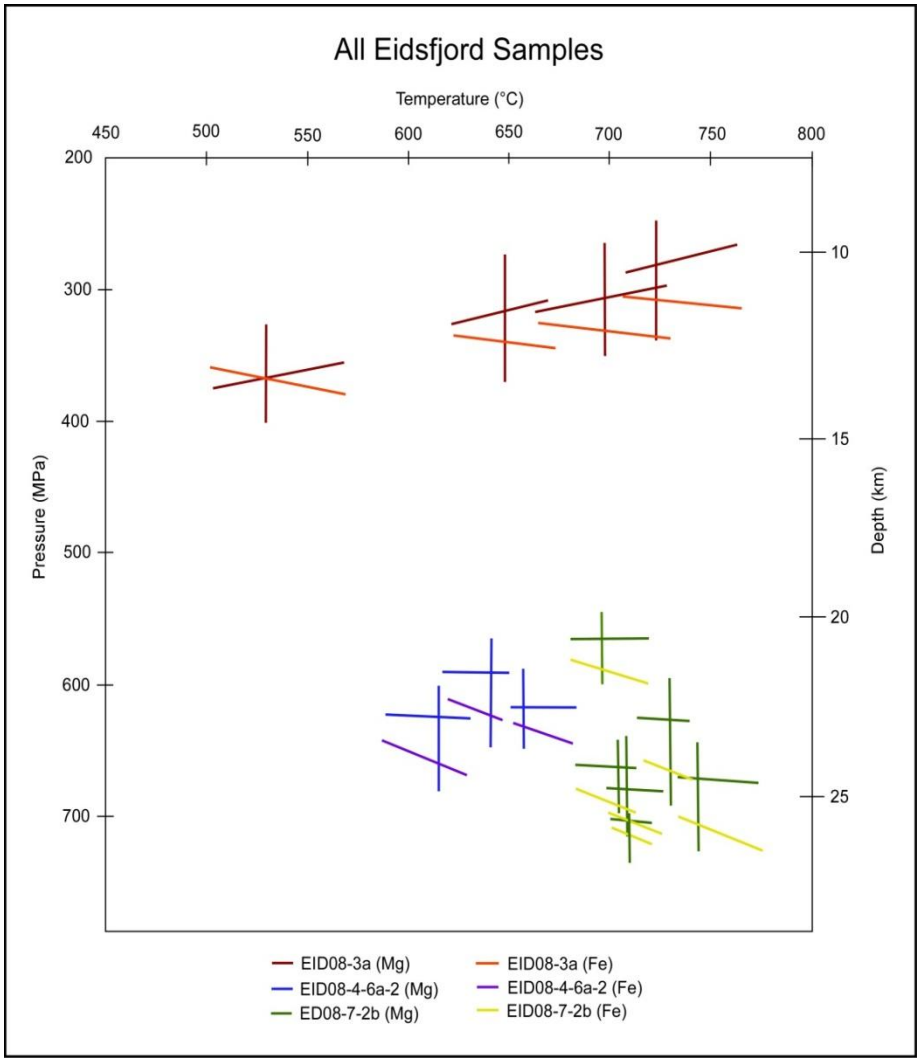

Figure 4.13 P-T intersections for each sample from the ESZ. Vertical lines are the thermometers, and the sub-horizontal lines are the barometers. Colors correspond to [Mg] or [Fe] equilibria for the geobarometers.

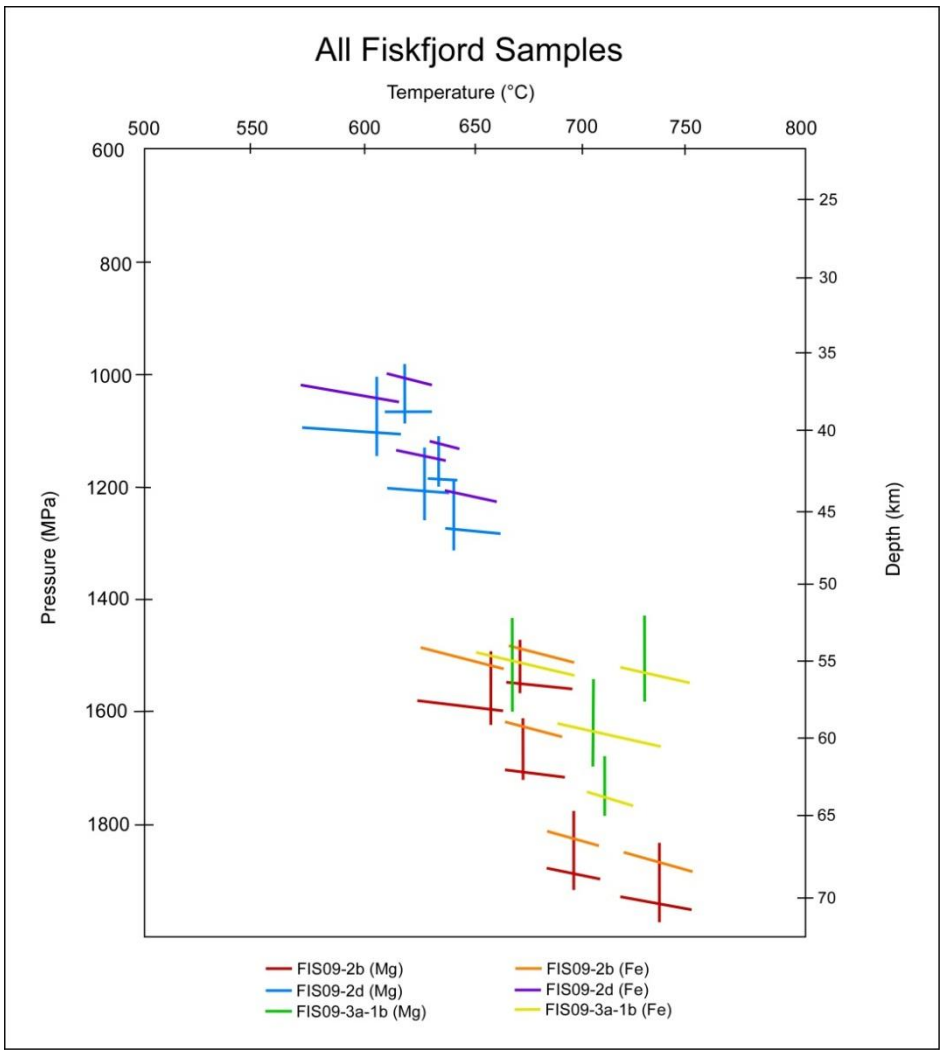

Figure 4.14. P-T intersections for each sample from the FSZ. Vertical lines are the thermometers, and the sub-horizontal lines are the barometers. Colors correspond to [Mg] or [Fe] end-member equilibria for the geobarometers.

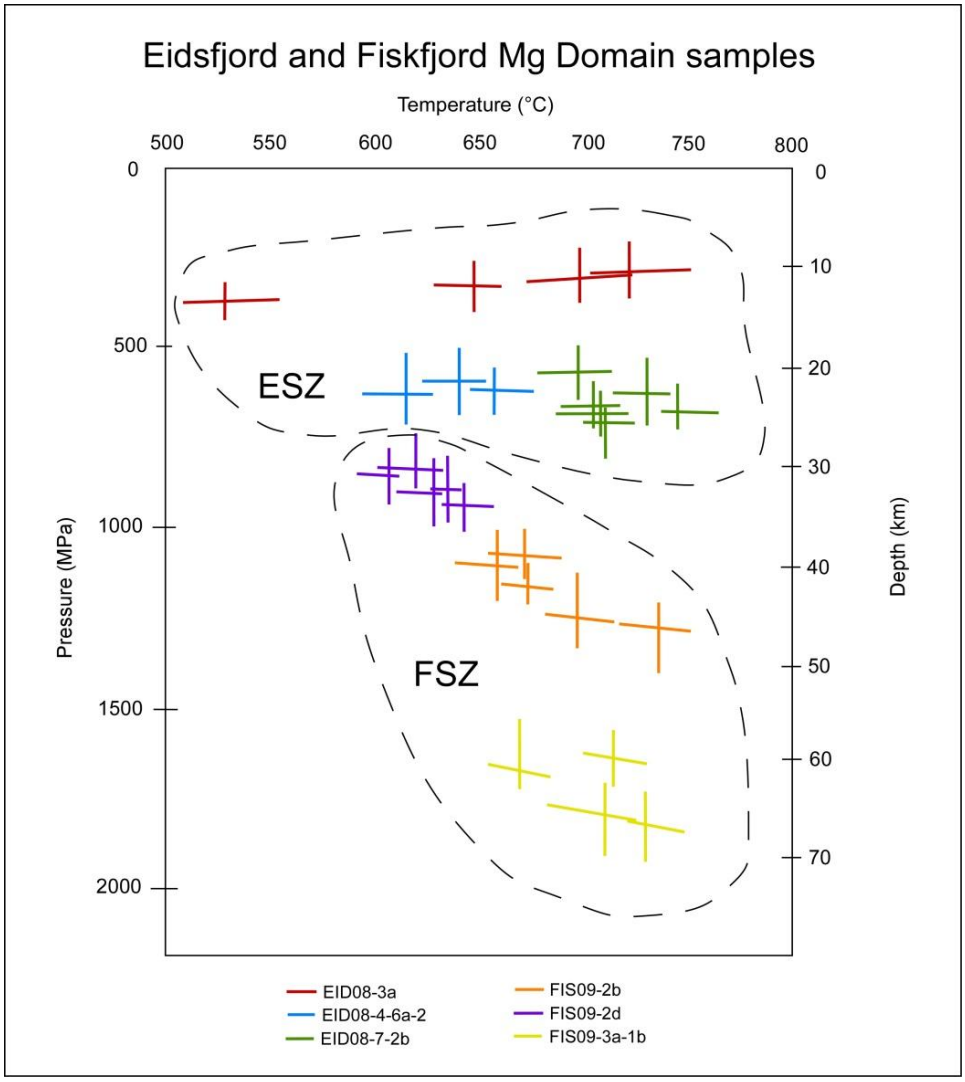

Figure 4.15. P-T intersection plot of each sample from both the ESZ and the FSZ calculated with the [Mg] barometer only.

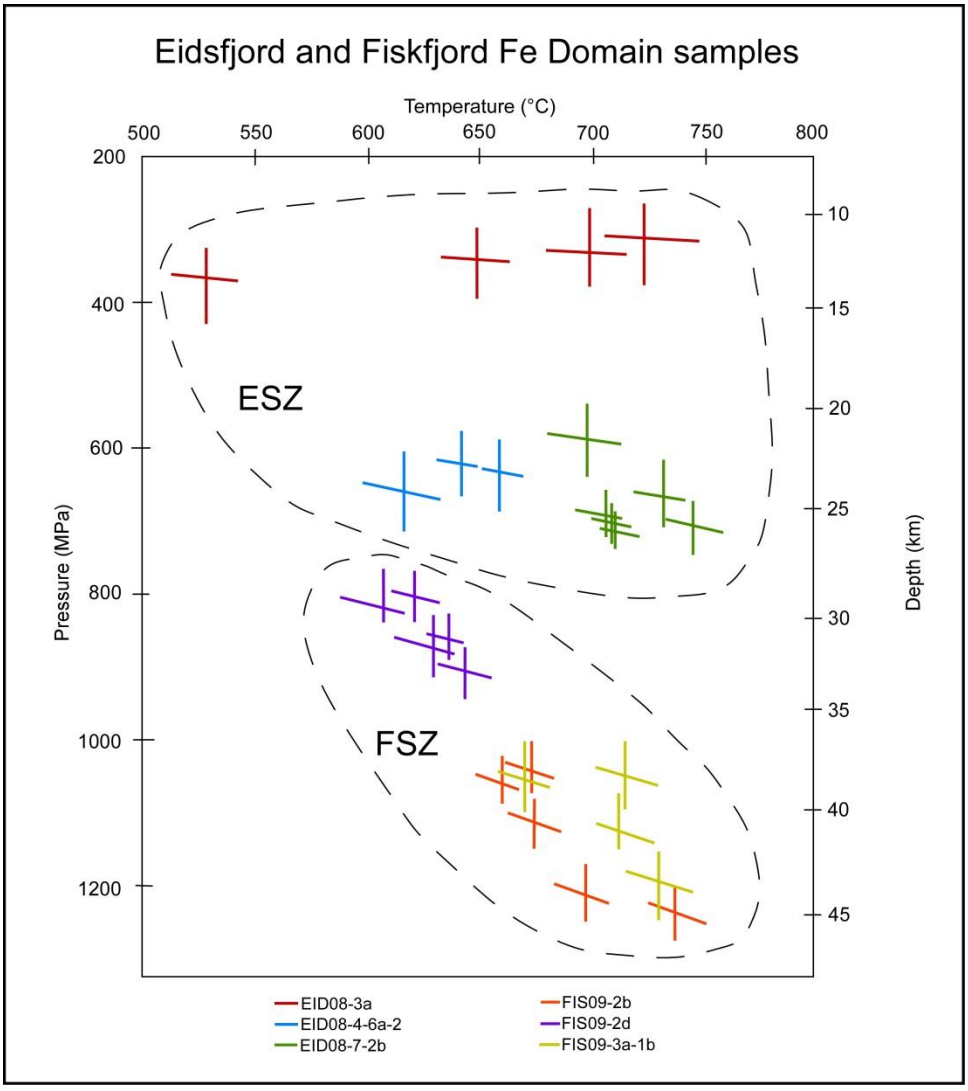

Figure 4.16. P-T intersection plot of each sample from both the ESZ and the FSZ calculated with the [Fe] barometer only.

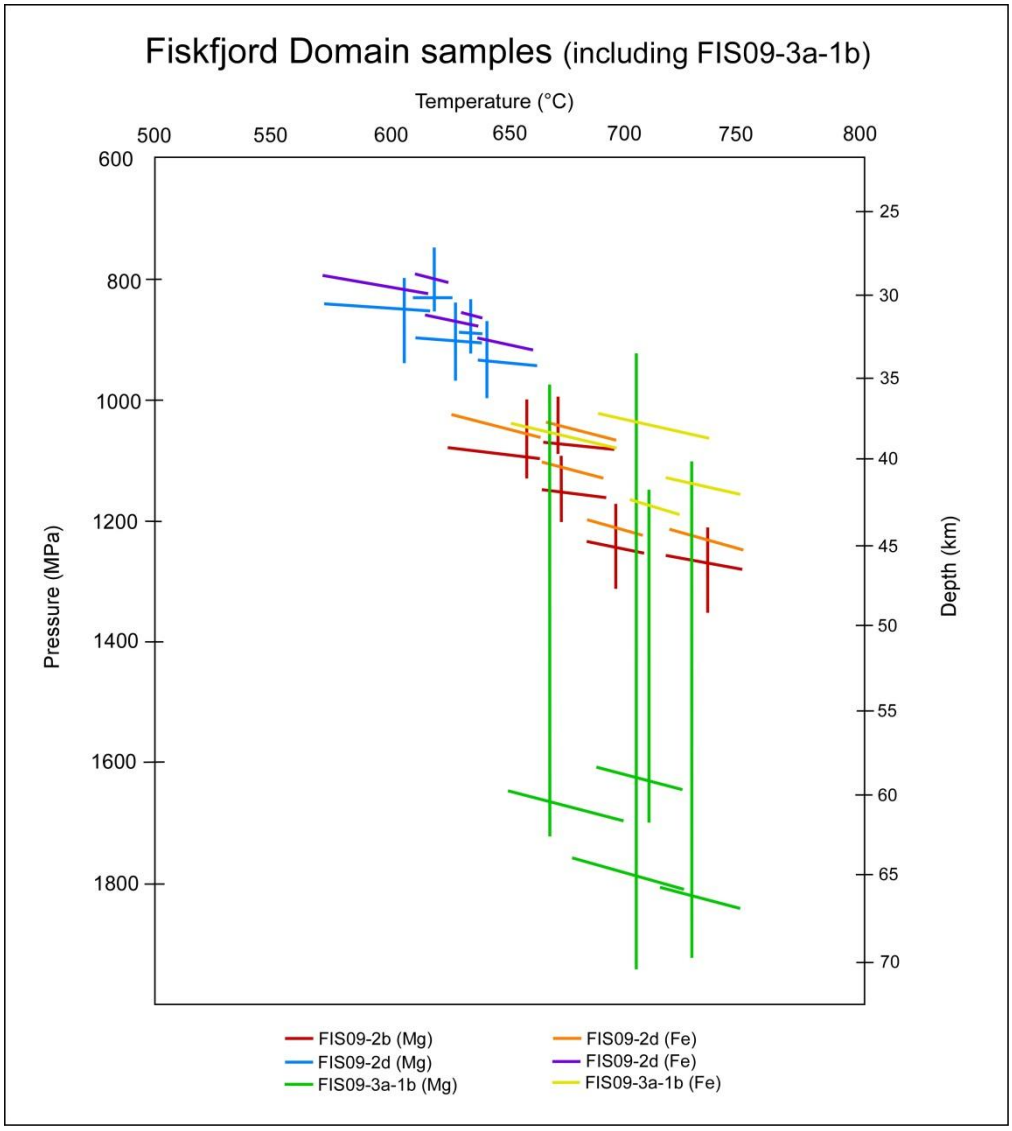

Figure 4.17. P-T intersection plot of each sample from the FSZ, showing the erroneous [Mg] barometer for samples FIS09-3a-1b.

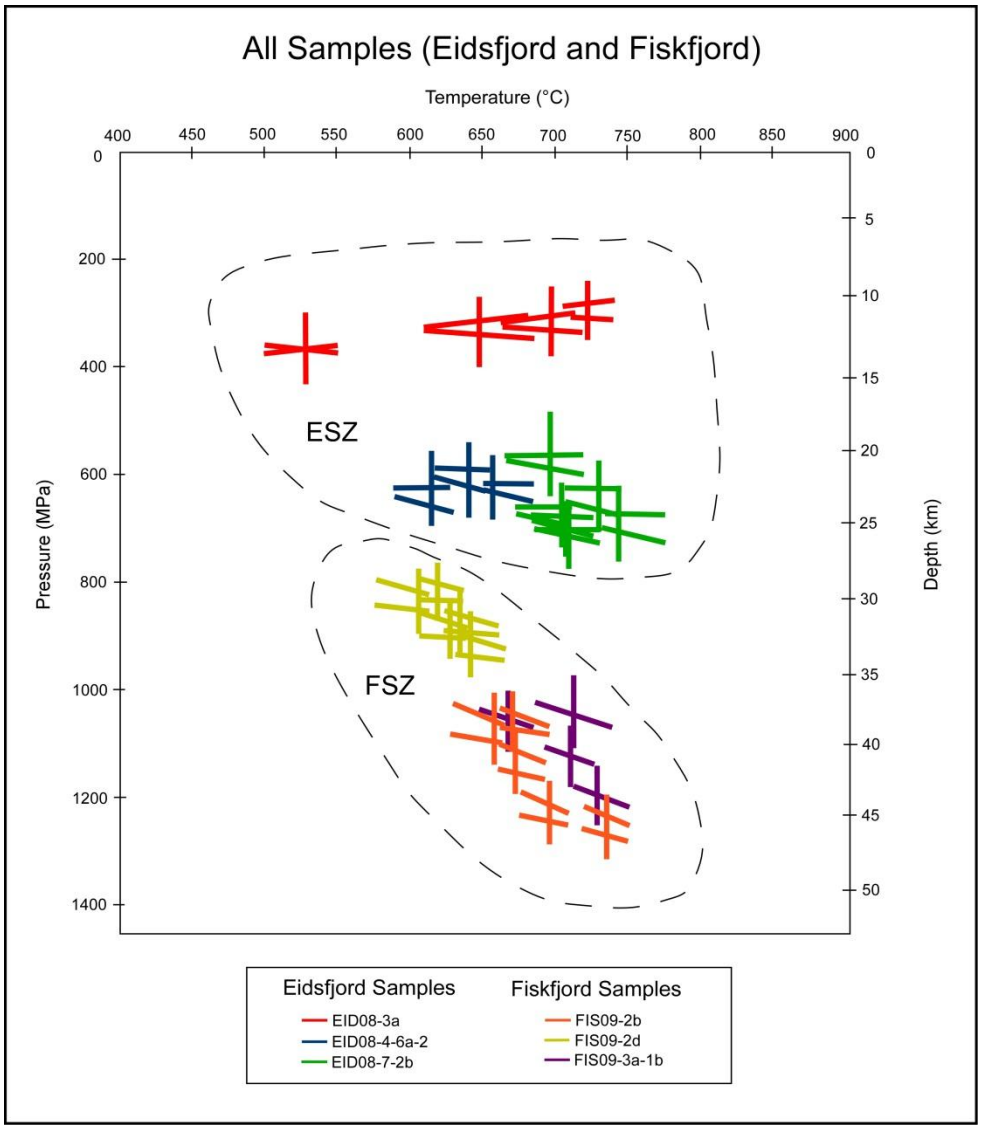

Figure 4.18. P-T intersection plot of each sample from both the ESZ and FSZ (excluding [Mg] barometers from FIS09-3a-1b), showing the overall difference between the two shear zone areas.

CHAPTER 5: Discussion

Extensional tectonics overprinted contractional tectonics throughout the Caledonide orogen in the Devonian (Fossen 1992). The presence of pseudotachylyte that crosscuts mylonites and is also crosscut by mylonites formed during ductile extension indicates that extensional motion was associated with seismogenic slip that occurred below the standard seismogenic zone. The implication of multiple occurrences of pseudotachylyte and mylonite within the Eidsfjord-Fiskfjord shear zone system is that repeated co-seismic slip events occurred at varying depths within the crust. Abundant plagioclase, garnet, and hornblende within the pseudotachylyte and mylonite allow for P-T constraints to be calculated with mineralogic geobarometers and geothermometers, indicating that coseismic slip occurred at much deeper levels than the standard seismogenic zone. Thermobarometric calculations for this study indicate that fault rupture propagated much deeper than the seismogenic zone and deeper than typical ruptures on other modern, well-studied plate boundary faults.

The data presented in this thesis determined the range of P and T conditions of ductile deformation and seismicity for three samples from the ESZ and three from the FSZ. The domains from three ESZ samples yielded a temperature range of 637 to 715 °C, and a pressure range of 319 to 648 MPa for the Mg equilibria, and a range of 341 to 647 MPa for the Fe equilibria. The crustal depth range at Eidsfjord is from 12 to 24 km, and the geothermal gradient ranges from 31 to 55 °C/km. The domains from the three FSZ samples yielded an average temperature range of 626 to 705 °C, and a pressure range of 890 to 1147 MPa for the Mg equilibria, and a range of 870 to 1097 MPa for the Fe equilibria. The crustal depth range at Fiskfjord is from 32 to 42 km, and the geothermal gradient ranges from 17 to 20 °C/km.

The ductile deformation at Eidsfjord was found to have occurred at ca. 400 Ma (Steltenpohl et al., 2011). No geochronology has been performed on the Fiskfjord samples. It will be assumed for these purposes that ductile deformation at Fiskfjord was contemporaneous with that at Eidsfjord.

Temperatures between the two terranes are not drastically different (Tables 4.3 and 4.4) Pressures for the Fiskfjord samples average 1120 MPa, significantly higher than the pressure of the Eidsfjord samples at 570 MPa. The depth calculated from the FSZ samples indicates that the FSZ was approximately 20 km deeper in the crust than the ESZ at the time of deformation and pseudotachylyte generation.

The significant difference in pressure between the ESZ and the FSZ implies a similar difference in depth for the two shear zones. When displacement began in the Devonian, Eidsfjord and Fiskfjord were initially at different crustal depths (see Figs. 4.15 and 4.16). Subsequently through the Jurassic, a normal fault must have developed between the two shear zone localities. Based on the depth differences, movement along the normal fault must have resulted in Fiskfjord being uplifted a greater amount. Barometric calculations indicate a greater degree of uplift of the Fiskfjord terrane. The Eidsfjord area also was uplifted, but by a lesser amount due to its location on the hanging wall block of the inferred normal fault. At the termination of fault activity, erosional processes brought the crustal surface to its current location, and the Eidsfjord and Fiskfjord samples are now located at equal depth in the crust (Fig. 5.1).

5.1 Study Comparison

Most other studies calculating a depth component from thermobarometry data in pseudotachylyte occurrences involve either pyroxene- or biotite-bearing equilibria, which differs from the garnet-hornblende-plagioclase thermobarometers in this study. For instance, Lund and Austrheim (2003) calculate P-T of 2000 MPa and 650-700°C for eclogite facies pseudotachylytes, yielding a crustal depth of 70 km. Lund and Austrheim compared the results of three different geothermometers against one CaO-FeO-MgO-Al_2O_3-SiO_2 geobarometer and several assumed pressures. The Ellis and Green (1979) thermometer was heavily dependent on Fe^{3+} calculated from stoichiometry, making it sensitive to the calculation of Fe^{3+} based on microprobe analyses. This approach yields minimum temperatures using Fe^{3+} and Fe^{2+} and maximum temperatures using total iron. The Krogh Ravna (2000) garnet-clinopyroxene

thermometer is also heavily dependent on Fe^{3+}, yielding a larger range of temperatures, some much too low for the eclogite assemblage being analyzed, so it was disregarded. The Harley (1984) garnet—orthopyroxene geothermometer assumes all iron is Fe^{2+} which allowed for minimum temperatures. While this thermometer has produced reasonable temperatures from natural samples, it is known that both the precision and accuracy are affected by large relative errors in the data as well as variation in the distribution coefficient with temperature (Harley, 1984).

A thermobarometric study of mylonitic PST-bearing amphibolites near the brittle-ductile transition in the Italian Western Alps yielded temperatures of 510-580 °C and pressures of 250-450 MPa which correlate to depths of 9-17 km (Pennacchioni and Cesare, 1997). This study used the garnet-biotite Fe-Mg exchange thermometer of Ferry and Spear (1978) and a garnet-Al_2SiO_5-quartz-plagioclase (GASP) barometer on an assemblage of quartz, biotite, muscovite, plagioclase, garnet, sillimanite, ilmenite, and graphite. The presence of stable sillimanite within the mylonites presented a difficulty in determining an appropriate pressure constraint, as pressures were too high for stable sillimanite at the given temperatures (Pennacchioni and Cesare, 1997). These findings, assuming the thermobarometry is accurate, suggest a pre-Alpine metamorphic path related to an extensional tectonic boundary, with deformed pseudotachylyte suggesting the samples originated near the brittle-ductile boundary in the crust. Most pseudotachylytes were found to be folded and/or foliated by ductile overprinting within samples containing the original mylonitic assemblage, and are therefore inferred to have been formed under the same metamorphic conditions as the mylonites.

Another thermobarometric study of a faulted peridotite exhibiting ultramylonitic pseudotachylyte yielded temperatures of approximately 800°C and pressures of 700 to 1100 MPa (Ueda et al., 2008). These conditions reflect crustal depths of approximately 26-41 km (White, 2012). Deformation temperature was determined using a Ca-Mg pyroxene thermometer, and pressure was determined using carbonate equilibria. The thermometer calculates pre-seismic

temperatures, based on microprobe data collected from pyroxene neoblasts within the mylonitic texture, which was considered to be representative of the conditions during seismicity (Ueda et al., 2008). Because the post-seismic mylonite is extremely fine-grained, microprobe analysis was insufficient to obtain accurate data and the dolomite-enstatite equilibrium was utilized to estimate post-seismic conditions. The presence of amphibole and dolomite suggests different amounts of water present throughout metamorphism. Ueda et al., (2008) interpret this as alteration from H_2O-rich to CO_2-rich fluid, which may represent the transition from ductile to brittle conditions in the crust.

White (2012) focused on the Minas fault zone in Canada, which is a ductile fault located between the Meguma and Avalon terranes (White, 2012). The exhumed fault zone contained granulites with well-preserved mylonitic pseudotachylyte, where some mylonitic microstructures were thought to exhibit ductile disaggregation of the rock. Even though high-velocity slip is widely accepted as evidence for melt formation during ductile deformation, it cannot account for the nucleation of earthquakes at a depth below the seismogenic zone. This study determined that localized plastic shear in crystals may lead to shear heating with ductile melting, and not melting by frictional slip. Samples were taken from the least deformed granulite areas where mylonitic features still occurred. Mylonitic wall rock hosting pseudotachylyte yielded a temperature range of 700-860°C, a pressure of 750-950 MPa, and a depth estimate of 28-35 km (White, 2012) as outlined by Gibbons et al. (1996) using core compositions of porphyroclastic garnet, clinopyroxene, orthopyroxene, magnetite, ilmenite, and plagioclase equilibria in mylonitic granulite facies assemblages in wall rocks.

5.2 Summary

Similar geothermobarometers applied to samples from the same localities of ESZ and FSZ constrain the depth of ductile deformation of mylonitic pseudotachylyte at the Fiskfjord locality to be between 30-40 km at 625-675 °C (Moecher and Steltenpohl, 2009, 2011). Thermobarometry for mylonitic pseudotachylyte at Eidsfjord yielded 650 ± 30 to 730 ± 30 MPa

at 650°C, which corresponds to a depth of 25-28 km (Moecher and Steltenpohl, 2011). These findings are well below the standard seismogenic zone limit, and are consistent with the temperature, pressure, and depth values calculated for this study.

These depth calculations imply a deeper seismogenic zone in the Fiskfjord area than at Eidsfjord. The lower limit of seismicity in the Eidsfjord and Fiskfjord extensional fault zones is 10-25 km deeper than the approximate standard seismogenic zone depth within a continent at 15 to 20 km (Sibson, 1980, 1982). The depth of seismicity in the Eidsfjord and Fiskfjord shear zones requires that they be located partially within the ductile region of the crust. However, the presence of pseudotachylyte within these shear zones suggests that these depths correspond to the seismogenic zone, extending well below what is identified as the brittle crust. Additional evidence toward brittle faulting in these regions is the presence of micro-fractures through and around melt phases in thin section.

It is generally well-accepted that pseudotachylytes are common features within a seismogenic zone as a result of friction melting (Sibson and Toy, 2006). However, the means of pseudotachylyte formation within the ductile regime of the crust is still debated (White, 2012). Iio and Kobayashi (2002) suggest that intraplate earthquakes have downward extensions into the ductile regime, which allows stress to become focused on the main fault. This is partially due to localized stress in the lower crust, partitioned into smaller ductile shear zones that will, in turn, experience higher strain rates (Iio and Kobayashi, 2002; Regenauer-Lieb and Yuen, 2003; Hobbs et al. 2002; Regenauer-Lieb et al., 2008). This can result in propagation of dynamic rupture down along the ductile fault, which can lead to slip, plastic failure, and pseudotachylyte formation in nominally ductile crust (Moecher and Steltenpohl, 2011).

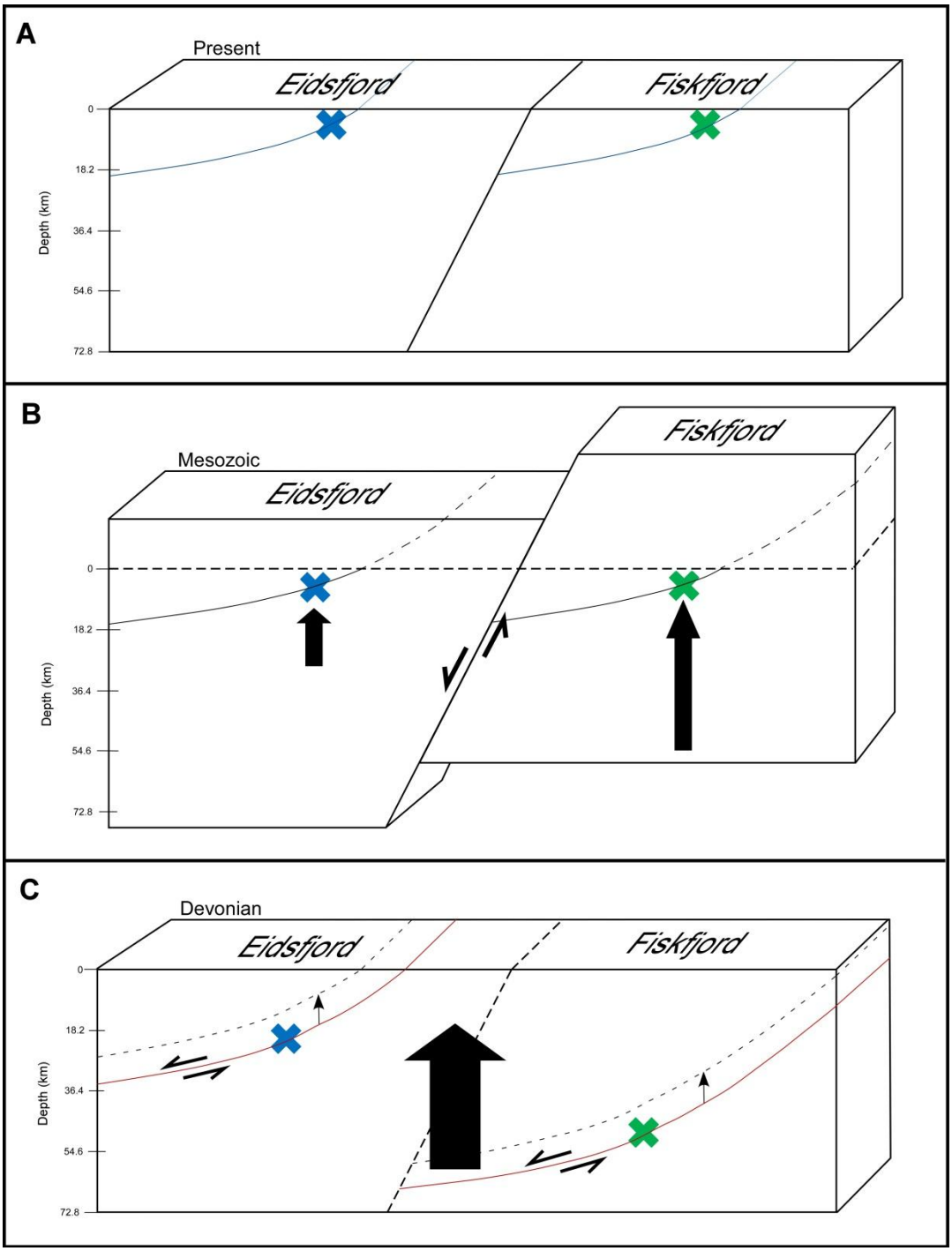

Figure 5.1. Basic tectonic model for the Eidsfjord and Fiskfjord shear zones, showing movement of the sample areas in the crust. (A) Shows the present location at the surface, where the blue solid lines imply a cold/inactive shear zone. (B) Displays the location as it appeared in the Mesozoic, where the dotted lines imply the surface location after erosion. (C) Shows the shear zones in the Devonian, where red solid lines imply a hot/active shear zone and dotted lines imply the future location of the shear zones after crustal uplift. Vertical black arrows show crustal uplift, where arrow length relates to magnitude of overall movement.

CHAPTER 6: Conclusion

Mylonitic pseudotachylyte in northern Norway forms in the ductile regime of the crust with a mineral assemblage useful for geothermobarometry calculations. The shear zones of both Eidsfjord and Fiskfjord utilize a lithologic contact between anorthosite and monzonite for the development of a normal fault resulting from post-Caledonian extension. Samples of bleached anorthosite and monzonite taken from near the shear zones were found to contain cataclasite, dynamic recrystallization of plagioclase, and pseudotachylyte features along with a mineral assemblage containing garnet, hornblende, plagioclase, and quartz that was necessary for geothermobarometric calculations.

The main conclusions of this study are:

1. Thermometer calculations based on Ravna (2000) and barometer calculations from Kohn and Spear (1989, 1990) yielded a temperature range of 615°C to 691°C and a pressure range of 455 MPa to 685 MPa for the ESZ, and a temperature range of 610°C to 750°C and a pressure range of 902 MPa to 1340 MPa for the FSZ.
2. Results from the geothermobarometry yielded a crustal depth range of 17 to 25 km for Eidsfjord and 32 to 50 km for Fiskfjord , putting the FSZ much deeper in the crust than the ESZ, implying the Fiskfjord area (on the footwall block of the normal fault) experienced a greater amount of exhumation during extension.

The objective of this study was to obtain thermobarometric values from the Eidsfjord and Fiskfjord shear zones to further establish a significant difference in seismogenic depth between the two. Additional research opportunities exist for both the ESZ and FSZ in the form of dating studies to determine the specific timing of extension, pseudotachylyte formation, and crustal uplift. Additional P-T studies of brittle rupture in the predominately ductile lower crust would also be beneficial as similar data are relatively rare and evidence of brittle fault extension into a

ductile regime is infrequent and has the potential to expand current knowledge of earthquake nucleation and seismic rupture propagation (White, 2012).

APPENDICES

Appendix A. Eidsfjord Thermobarometry Microprobe Data

Table A.1 EID08-3a Garnet Microprobe Data

Sample	EID08-3a						
Mineral	Garnet						
Domain	1		5		11		12
Point	2	3	2	3	2	6	2
SiO_2	36.44	37.02	37.52	37.47	36.46	39.55	37.36
TiO_2	0.08	0.01	0.04	0.08	0.01	0.14	0.05
Al_2O_3	20.48	21.05	21.35	21.17	20.48	21.95	21.08
FeO	30.31	31.69	30.61	31.10	31.82	29.09	30.55
MnO	2.14	1.67	2.14	2.17	2.21	1.95	2.32
MgO	6.07	5.89	5.53	5.55	4.89	4.69	5.02
CaO	2.90	2.60	2.75	2.54	3.13	3.61	2.91
Total	**98.41**	**99.93**	**99.94**	**100.07**	**98.99**	**100.97**	**99.29**
Si	2.94	2.95	2.97	2.97	2.95	3.06	2.99
Ti	0.00	0.00	0.00	0.00	0.00	0.01	0.00
Al	1.95	1.97	1.99	1.98	1.95	2.00	1.99
Fe	2.05	2.11	2.03	2.06	2.15	1.88	2.04
Mn	0.15	0.11	0.14	0.15	0.15	0.13	0.16
Mg	0.73	0.70	0.65	0.66	0.59	0.54	0.60
Ca	0.25	0.22	0.23	0.22	0.27	0.30	0.25
Grossular	0.08	0.07	0.08	0.07	0.09	0.10	0.08
Pyrope	0.23	0.22	0.21	0.21	0.19	0.19	0.20
Almandine	0.64	0.67	0.66	0.67	0.68	0.66	0.67
Spessartine	0.05	0.04	0.05	0.05	0.05	0.04	0.05
Mg#	0.26	0.25	0.24	0.24	0.21	0.22	0.23
Fe#	0.74	0.75	0.76	0.76	0.79	0.78	0.77

Table A.2 EID08-3a Hornblende Microprobe Data

Sample	EID08-3a									
Mineral	Hornblende									
Domain	1		5			11		12		
Point	1	3	6	8	11	8	9	23	25	26
SiO_2	41.62	41.55	41.72	41.40	41.41	42.19	42.20	41.35	41.93	42.48
TiO_2	0.15	0.18	0.18	0.17	0.11	0.30	0.19	0.26	0.18	0.19
Al_2O_3	17.24	17.24	17.80	17.62	17.80	18.36	18.63	17.38	17.33	17.84
FeO	16.91	16.94	17.08	17.62	16.67	14.66	14.82	17.70	16.89	16.44
MnO	0.19	0.32	0.18	0.19	0.20	0.09	0.11	0.26	0.20	0.27
MgO	8.83	8.90	8.61	8.91	8.84	10.12	10.09	8.98	9.23	8.82
CaO	10.66	10.02	10.54	10.56	10.46	10.82	10.99	10.16	10.55	10.26
Na_2O	1.44	1.50	1.57	1.66	1.67	1.61	1.58	1.81	1.55	1.55
K_2O	0.60	0.60	0.53	0.50	0.53	0.40	0.42	0.66	0.52	0.52
Cl	0.31	0.35	0.32	0.36	0.31	0.32	0.30	0.32	0.35	0.27
Total	**97.95**	**97.59**	**98.52**	**98.99**	**98.01**	**98.85**	**99.32**	**98.87**	**98.71**	**98.63**
Si	6.20	6.21	6.18	6.13	6.16	6.15	6.12	6.14	6.20	6.24
Ti	0.02	0.02	0.02	0.02	0.01	0.03	0.02	0.03	0.02	0.02
Al	3.03	3.04	3.11	3.08	3.12	3.15	3.19	3.04	3.02	3.09
Fe	2.11	2.12	2.11	2.18	2.07	1.79	1.80	2.20	2.09	2.02
Mn	0.02	0.04	0.02	0.02	0.03	0.01	0.01	0.03	0.02	0.03
Mg	1.96	1.98	1.90	1.97	1.96	2.20	2.18	1.98	2.03	1.93
Ca	1.70	1.60	1.67	1.68	1.67	1.69	1.71	1.62	1.67	1.62
Na	0.41	0.44	0.45	0.48	0.48	0.45	0.44	0.52	0.44	0.44
K	0.11	0.11	0.10	0.09	0.10	0.07	0.08	0.12	0.10	0.10
Cl	0.08	0.09	0.08	0.09	0.08	0.08	0.07	0.08	0.09	0.07
XMg	0.48	0.48	0.47	0.47	0.49	0.55	0.55	0.47	0.49	0.49
XFe	0.52	0.52	0.53	0.53	0.51	0.45	0.45	0.53	0.51	0.51

Table A.3 EID08-3a Plagioclase Microprobe Data

Sample	EID08-3a							
Mineral	Plagioclase							
Domain	1					5		
Point	310	312	313	314	315	324	325	326
SiO_2	58.48	58.78	59.31	59.72	60.10	57.88	57.82	57.44
Al_2O_3	26.66	26.22	26.06	28.41	26.70	26.87	27.00	27.07
Fe_2O_3	0.10	0.06	0.09	0.09	0.10	0.07	0.18	0.27
CaO	7.32	7.20	6.38	5.11	5.94	7.81	7.74	7.80
Na_2O	7.04	7.23	7.62	6.96	7.29	6.80	6.46	6.94
K_2O	0.03	0.08	0.06	0.04	0.10	0.02	0.08	0.01
Total	**99.63**	**99.58**	**99.52**	**100.32**	**100.24**	**99.46**	**99.28**	**99.53**
Si	2.62	2.63	2.65	2.63	2.66	2.60	2.60	2.58
Al	1.41	1.38	1.37	1.47	1.39	1.42	1.43	1.43
Fe	0.00	0.00	0.00	0.00	0.00	0.00	0.01	0.01
Ca	0.35	0.35	0.31	0.24	0.28	0.38	0.37	0.38
Na	0.61	0.63	0.66	0.59	0.62	0.59	0.56	0.60
K	0.00	0.00	0.00	0.00	0.01	0.00	0.00	0.00
Albite	0.63	0.64	0.68	0.71	0.69	0.61	0.60	0.62
Anorthite	0.36	0.35	0.32	0.29	0.31	0.39	0.40	0.38

Sample	EID08-3a						
Mineral	Plagioclase						
Domain	5			11			12
Point	327	328	329	338	339	340	347
SiO_2	57.95	57.92	57.49	59.56	60.45	61.53	59.14
Al_2O_3	26.34	28.57	28.84	25.73	25.18	24.22	25.77
Fe_2O_3	0.13	0.00	0.10	0.42	0.56	0.85	0.89
CaO	7.69	6.13	6.37	6.40	5.67	5.51	6.69
Na_2O	6.94	6.80	6.39	7.60	7.75	7.31	6.94
K_2O	0.05	0.10	0.10	0.09	0.02	0.02	0.02
Total	**99.09**	**99.52**	**99.28**	**99.79**	**99.64**	**99.44**	**99.44**
Si	2.61	2.58	2.57	2.66	2.69	2.74	2.65
Al	1.40	1.50	1.52	1.35	1.32	1.27	1.36
Fe	0.00	0.00	0.00	0.01	0.02	0.03	0.03
Ca	0.37	0.29	0.30	0.31	0.27	0.26	0.32
Na	0.61	0.59	0.55	0.66	0.67	0.63	0.60
K	0.00	0.01	0.01	0.00	0.00	0.00	0.00
Albite	0.62	0.66	0.64	0.68	0.71	0.71	0.65
Anorthite	0.38	0.33	0.35	0.32	0.29	0.29	0.35

Table A.4 EID08-3a Representative Average Microprobe Data

Sample	EID08-3a													
Mineral	Hornblende				Mineral	Plagioclase				Mineral	Garnet			
Domain	1	5	11	12	Domain	1	5	11	12	Domain	1	5	11	12
SiO_2	41.59	41.51	42.20	41.92	SiO_2	59.28	57.75	60.51	59.14	SiO_2	41.15	36.74	38.06	37.33
TiO_2	0.17	0.15	0.25	0.21	Al_2O_3	26.81	27.45	25.04	25.77	TiO_2	0.06	0.09	0.12	0.02
Al_2O_3	17.24	17.74	18.32	17.52	Fe_2O_3	0.09	0.13	0.61	0.89	Al_2O_3	19.48	20.90	21.25	21.04
FeO	16.93	17.12	15.00	17.01	CaO	6.39	7.26	5.86	6.69	FeO	28.68	31.43	29.53	29.33
MnO	0.25	0.19	0.09	0.24	Na_2O	7.23	6.72	7.56	6.94	MnO	1.53	2.18	2.02	2.19
MgO	8.86	8.79	9.92	9.01	K_2O	0.06	0.06	0.04	0.02	MgO	5.91	5.75	4.76	4.72
CaO	10.34	10.52	10.93	10.32	***Total***	**99.86**	**99.36**	**99.62**	**99.44**	CaO	3.04	2.57	4.39	4.61
Na_2O	1.47	1.63	1.53	1.63	Si	2.64	2.59	2.70	2.65	***Total***	**99.84**	**99.65**	**100.11**	**99.24**
K_2O	0.60	0.52	0.42	0.56	Al	1.40	1.45	1.31	1.36	Si	3.19	2.94	3.00	2.98
Cl	0.33	0.33	0.33	0.31	Fe	0.00	0.00	0.02	0.03	Ti	0.00	0.01	0.01	0.00
Total	**97.77**	**98.51**	**98.99**	**98.74**	Ca	0.30	0.35	0.28	0.32	Al	1.80	1.97	1.98	1.98
Si	6.21	6.16	6.15	6.19	Na	0.62	0.58	0.65	0.60	Fe	1.88	2.10	1.95	1.96
Ti	0.02	0.02	0.03	0.02	K	0.00	0.00	0.00	0.00	Mn	0.10	0.15	0.13	0.15
Al	3.03	3.10	3.15	3.05	Albite	0.67	0.62	0.70	0.65	Mg	0.68	0.69	0.56	0.56
Fe	2.11	2.12	1.83	2.10	Anorthite	0.33	0.37	0.30	0.35	Ca	0.26	0.22	0.37	0.39
Mn	0.03	0.02	0.01	0.03						Grossular	0.09	0.07	0.12	0.13
Mg	1.97	1.94	2.16	1.98						Pyrope	0.24	0.22	0.19	0.18
Ca	1.65	1.67	1.71	1.63						Almandine	0.64	0.67	0.65	0.64
Na	0.43	0.47	0.43	0.47						Spessartine	0.03	0.05	0.04	0.05
K	0.11	0.10	0.08	0.11										
Cl	0.08	0.08	0.08	0.08										

Table A.5 EID08-4-6a-2 Garnet Microprobe Data

Sample	EID08-4-6a-2					
Mineral	Garnet					
Domain	1		3		4	
Point	5	6	7	8	7	9
SiO_2	37.56	37.53	37.18	37.02	37.36	37.61
TiO_2	0.11	0.07	0.10	0.09	0.44	0.15
Al_2O_3	20.92	20.68	20.88	20.08	20.36	20.67
FeO	28.80	29.56	26.63	27.62	27.96	28.40
MnO	3.04	2.43	4.90	4.96	4.20	4.67
MgO	3.78	3.94	2.70	2.56	3.18	3.29
CaO	5.14	4.92	6.73	7.10	6.31	5.33
Total	**99.35**	**99.12**	**99.12**	**99.42**	**99.80**	**100.12**
Si	3.00	3.01	2.99	2.99	2.99	3.00
Ti	0.01	0.00	0.01	0.01	0.03	0.01
Al	1.97	1.95	1.98	1.91	1.92	1.94
Fe	1.93	1.98	1.79	1.87	1.87	1.90
Mn	0.21	0.16	0.33	0.34	0.28	0.32
Mg	0.45	0.47	0.32	0.31	0.38	0.39
Ca	0.44	0.42	0.58	0.61	0.54	0.46
Grossular	0.15	0.14	0.19	0.20	0.18	0.15
Pyrope	0.15	0.15	0.11	0.10	0.12	0.13
Almandine	0.64	0.65	0.59	0.60	0.61	0.62
Spessartine	0.07	0.05	0.11	0.11	0.09	0.10
Mg#	0.19	0.19	0.15	0.14	0.17	0.17
Fe#	0.81	0.81	0.85	0.86	0.83	0.83

Table A.6 EID08-4-6a-2 Hornblende Microprobe Data

Sample	EID08-4-6a-2												
Mineral	Hornblende												
Domain	1				3					4			
Point	1	2	3	5	11	12	13	14	15	16	17	18	20
SiO_2	41.79	40.45	40.89	41.31	40.83	41.22	41.23	40.62	41.46	41.58	41.55	40.94	41.67
TiO_2	0.43	0.45	0.44	0.33	0.54	0.55	0.42	0.51	0.57	0.46	0.60	0.71	0.53
Al_2O_3	17.72	17.54	17.19	17.45	17.20	17.46	17.66	17.21	16.96	16.74	16.73	16.88	17.13
FeO	16.87	18.10	18.19	17.12	17.36	16.97	16.82	19.60	17.54	17.12	17.31	17.97	17.45
MnO	0.19	0.27	0.33	0.18	0.29	0.18	0.26	0.32	0.21	0.29	0.25	0.23	0.43
MgO	8.66	8.46	8.16	8.40	8.41	8.19	8.70	8.09	8.32	8.38	8.49	8.42	8.39
CaO	11.45	10.73	11.55	11.86	11.37	11.56	11.61	10.87	11.63	11.39	11.89	11.51	11.49
Na_2O	1.35	1.38	1.49	1.53	1.55	1.48	1.63	1.42	1.67	1.47	1.50	1.62	1.46
K_2O	0.58	0.52	0.58	0.64	0.56	0.66	0.62	0.60	0.61	0.64	0.59	0.61	0.59
Cl	0.22	0.22	0.28	0.19	0.24	0.23	0.19	0.23	0.23	0.24	0.22	0.23	0.23
Total	**99.26**	**98.13**	**99.10**	**99.01**	**98.34**	**98.50**	**99.14**	**99.47**	**99.21**	**98.31**	**99.13**	**99.11**	**99.38**
Si	6.14	6.06	6.09	6.11	6.10	6.13	6.09	6.05	6.14	6.20	6.15	6.09	6.15
Ti	0.05	0.05	0.05	0.04	0.06	0.06	0.05	0.06	0.06	0.05	0.07	0.08	0.06
Al	3.07	3.10	3.02	3.04	3.03	3.06	3.07	3.02	2.96	2.94	2.92	2.96	2.98
Fe	2.07	2.27	2.27	2.12	2.17	2.11	2.08	2.44	2.17	2.13	2.14	2.23	2.15
Mn	0.02	0.03	0.04	0.02	0.04	0.02	0.03	0.04	0.03	0.04	0.03	0.03	0.05
Mg	1.90	1.89	1.81	1.85	1.87	1.81	1.91	1.80	1.84	1.86	1.87	1.87	1.85
Ca	1.80	1.72	1.84	1.88	1.82	1.84	1.84	1.74	1.85	1.82	1.89	1.83	1.82
Na	0.38	0.40	0.43	0.44	0.45	0.43	0.47	0.41	0.48	0.42	0.43	0.47	0.42
K	0.11	0.10	0.11	0.12	0.11	0.13	0.12	0.11	0.12	0.12	0.11	0.12	0.11
Cl	0.06	0.06	0.07	0.05	0.06	0.06	0.05	0.06	0.06	0.06	0.06	0.06	0.06
XMg	0.48	0.45	0.44	0.47	0.46	0.46	0.48	0.42	0.46	0.47	0.47	0.45	0.46
XFe	0.52	0.55	0.56	0.53	0.54	0.54	0.52	0.58	0.54	0.53	0.53	0.55	0.54

Table A.7 EID08-4-6a-2 Plagioclase Microprobe Data

Sample	EID08-4-6a-2										
Mineral	Plagioclase										
Domain	1							3			
Point	268	269	270	274	275	276	277	288	289	290	291
SiO_2	57.33	56.28	56.35	54.13	52.74	53.36	53.00	55.70	56.53	56.86	57.49
Al_2O_3	27.51	27.90	27.96	29.70	30.22	29.76	29.34	28.34	27.58	27.10	26.93
Fe_2O_3	0.23	0.31	0.29	0.19	0.39	0.38	0.78	0.00	0.22	0.20	0.56
CaO	7.94	8.93	8.56	10.63	11.17	10.63	10.88	10.15	9.15	8.39	7.81
Na_2O	7.06	6.56	6.20	5.16	4.67	5.23	5.07	5.61	6.10	6.52	6.76
K_2O	0.10	0.01	0.04	0.01	0.04	0.04	0.01	0.04	0.07	0.04	0.06
Total	**100.17**	**99.99**	**99.39**	**99.82**	**99.22**	**99.40**	**99.09**	**99.84**	**99.64**	**99.10**	**99.61**
Si	2.56	2.53	2.54	2.44	2.40	2.42	2.42	2.51	2.54	2.57	2.58
Al	1.45	1.48	1.48	1.58	1.62	1.59	1.58	1.50	1.46	1.44	1.43
Fe	0.01	0.01	0.01	0.01	0.01	0.01	0.03	0.00	0.01	0.01	0.02
Ca	0.38	0.43	0.41	0.51	0.54	0.52	0.53	0.49	0.44	0.41	0.38
Na	0.61	0.57	0.54	0.45	0.41	0.46	0.45	0.49	0.53	0.57	0.59
K	0.01	0.00	0.00	0.00	0.00	0.00	0.00	0.00	0.00	0.00	0.00
Albite	0.61	0.57	0.57	0.47	0.43	0.47	0.46	0.50	0.54	0.58	0.61
Anorthite	0.38	0.43	0.43	0.53	0.57	0.53	0.54	0.50	0.45	0.41	0.39

Sample	EID08-4-6a-2									
Mineral	Plagioclase									
Domain	3				4					
Point	292	293	294	295	296	297	298	299	300	301
SiO_2	55.97	55.21	56.05	55.70	55.49	56.25	58.32	55.61	55.56	57.97
Al_2O_3	28.55	28.67	27.83	28.10	28.50	26.45	26.50	28.49	28.54	27.64
Fe_2O_3	0.43	0.07	0.40	0.17	0.28	0.29	0.49	0.31	0.25	0.25
CaO	9.44	9.06	9.30	9.16	9.92	10.31	7.64	9.75	9.26	8.78
Na_2O	6.01	6.06	6.29	6.03	5.75	6.68	7.13	5.93	6.13	5.50
K_2O	0.07	0.01	0.09	0.05	0.04	0.05	0.07	0.03	0.06	0.02
Total	**100.48**	**99.09**	**99.96**	**99.21**	**99.98**	**100.03**	**100.15**	**100.12**	**99.81**	**100.17**
Si	2.50	2.50	2.52	2.52	2.50	2.54	2.60	2.50	2.50	2.58
Al	1.50	1.53	1.48	1.50	1.51	1.41	1.39	1.51	1.51	1.45
Fe	0.01	0.00	0.01	0.01	0.01	0.01	0.02	0.01	0.01	0.01
Ca	0.45	0.44	0.45	0.44	0.48	0.50	0.37	0.47	0.45	0.42
Na	0.52	0.53	0.55	0.53	0.50	0.59	0.62	0.52	0.53	0.47
K	0.00	0.00	0.01	0.00	0.00	0.00	0.00	0.00	0.00	0.00
Albite	0.53	0.55	0.55	0.54	0.51	0.54	0.63	0.52	0.54	0.53
Anorthite	0.46	0.45	0.45	0.46	0.49	0.46	0.37	0.47	0.45	0.47

Table A.8 EID08-4-6a-2 Representative Average Microprobe Data

Sample	EID08-4-6a-2										
Mineral	Hornblende			Mineral	Plagioclase			Mineral	Garnet		
Domain	1	3	4	Domain	1	3	4	Domain	1	3	4
SiO2	41.11	41.07	41.43	SiO2	54.74	56.19	56.53	SiO2	37.55	37.10	37.48
TiO2	0.41	0.52	0.57	Al2O3	28.91	27.89	27.69	TiO2	0.09	0.09	0.30
Al2O3	17.47	17.30	16.87	Fe2O3	0.37	0.26	0.31	Al2O3	20.80	20.48	20.51
FeO	17.57	17.66	17.46	CaO	9.82	9.06	9.28	FeO	29.18	27.12	28.18
MnO	0.24	0.25	0.30	Na2O	5.71	6.17	6.19	MnO	2.73	4.93	4.44
MgO	8.42	8.34	8.42	K2O	0.04	0.05	0.04	MgO	3.86	2.63	3.24
CaO	11.40	11.41	11.57	***Total***	**99.58**	**99.62**	**100.04**	CaO	5.03	6.91	5.82
Na2O	1.44	1.55	1.51	Si	2.47	2.53	2.54	***Total***	**99.24**	**99.27**	**99.96**
K2O	0.58	0.61	0.61	Al	1.54	1.48	1.46	Si	3.01	2.99	3.00
Cl	0.23	0.22	0.23	Fe	0.01	0.01	0.01	Ti	0.01	0.01	0.02
Total	**98.88**	**98.93**	**98.98**	Ca	0.48	0.44	0.45	Al	1.96	1.95	1.93
Si	6.10	6.10	6.15	Na	0.50	0.54	0.54	Fe	1.95	1.83	1.88
Ti	0.05	0.06	0.06	K	0.00	0.00	0.00	Mn	0.19	0.34	0.30
Al	3.06	3.03	2.95	Albite	0.51	0.55	0.55	Mg	0.46	0.32	0.39
Fe	2.18	2.19	2.17	Anorthite	0.49	0.45	0.45	Ca	0.43	0.60	0.50
Mn	0.03	0.03	0.04					Grossular	0.14	0.19	0.16
Mg	1.86	1.85	1.86					Pyrope	0.15	0.10	0.13
Ca	1.81	1.82	1.84					Almandine	0.64	0.59	0.61
Na	0.41	0.45	0.44					Spessartine	0.06	0.11	0.10
K	0.11	0.12	0.12								
Cl	0.06	0.06	0.06								

Table A.9 EID08-7-2b Garnet Microprobe Data

Sample	EID08-7-2b										
Mineral	Garnet										
Domain	1		2				3			4	
Point	5	6	8	9	10	11	3	4	5	6	7
SiO_2	37.23	37.19	37.00	37.41	37.14	37.36	37.04	37.07	37.34	37.15	36.85
TiO_2	0.04	0.06	0.03	0.02	0.03	0.00	0.00	0.01	0.04	0.00	0.00
Al_2O_3	21.06	20.84	21.13	21.08	21.21	21.07	21.11	20.85	20.81	21.03	20.96
FeO	29.27	28.66	26.98	27.64	27.96	27.29	26.67	27.47	26.37	29.50	29.46
MnO	2.65	2.64	4.35	4.46	4.66	4.48	4.05	4.29	3.78	1.33	1.76
MgO	4.21	3.93	3.83	3.88	3.64	3.86	3.40	3.91	4.30	4.09	3.79
CaO	5.31	5.55	6.03	5.64	5.90	5.72	6.47	5.99	6.40	6.44	6.30
Total	**99.78**	**98.85**	**99.36**	**100.13**	**100.55**	**99.78**	**98.74**	**99.59**	**99.04**	**99.54**	**99.12**
Si	2.97	2.99	2.96	2.98	2.95	2.98	2.98	2.97	2.99	2.97	2.96
Ti	0.00	0.00	0.00	0.00	0.00	0.00	0.00	0.00	0.00	0.00	0.00
Al	1.98	1.97	2.00	1.98	1.99	1.98	2.00	1.97	1.96	1.98	1.99
Fe	1.95	1.93	1.81	1.84	1.86	1.82	1.79	1.84	1.76	1.97	1.98
Mn	0.18	0.18	0.30	0.30	0.31	0.30	0.28	0.29	0.26	0.09	0.12
Mg	0.50	0.47	0.46	0.46	0.43	0.46	0.41	0.47	0.51	0.49	0.45
Ca	0.45	0.48	0.52	0.48	0.50	0.49	0.56	0.51	0.55	0.55	0.54
Grossular	0.15	0.16	0.17	0.16	0.16	0.16	0.18	0.17	0.18	0.18	0.18
Pyrope	0.16	0.15	0.15	0.15	0.14	0.15	0.13	0.15	0.17	0.16	0.15
Almandine	0.63	0.63	0.59	0.60	0.60	0.59	0.59	0.59	0.57	0.64	0.64
Spessartine	0.06	0.06	0.10	0.10	0.10	0.10	0.09	0.09	0.08	0.03	0.04
Mg#	0.20	0.20	0.20	0.20	0.19	0.20	0.18	0.20	0.23	0.20	0.19
Fe#	0.80	0.80	0.80	0.80	0.81	0.80	0.82	0.80	0.77	0.80	0.81

Sample	EID08-7-2b										
Mineral	Garnet										
Domain	4		5			7					
Point	8	9	12	13	14	7	8	9	10	11	12
SiO_2	37.35	37.13	37.49	37.26	37.76	37.14	37.12	37.42	37.14	37.36	37.46
TiO_2	0.02	0.03	0.03	0.02	0.00	0.07	0.00	0.00	0.00	0.00	0.00
Al_2O_3	21.10	21.21	20.95	21.21	21.21	20.92	20.79	20.88	21.23	21.23	20.88
FeO	28.84	29.06	29.78	29.47	29.57	27.23	27.20	27.24	27.51	27.16	26.96
MnO	1.23	1.01	0.52	1.10	1.00	3.44	4.25	4.15	4.03	3.73	3.87
MgO	3.82	3.91	3.74	3.74	3.88	4.17	3.72	3.79	3.87	4.01	3.75
CaO	7.07	7.64	6.48	6.89	7.22	6.33	6.02	5.86	6.05	5.92	6.08
Total	**99.43**	**99.99**	**98.99**	**99.68**	**100.65**	**99.29**	**99.10**	**99.34**	**99.83**	**99.41**	**98.99**
Si	2.98	2.95	3.00	2.97	2.98	2.97	2.98	2.99	2.96	2.98	3.00
Ti	0.00	0.00	0.00	0.00	0.00	0.00	0.00	0.00	0.00	0.00	0.00
Al	1.98	1.99	1.98	1.99	1.97	1.97	1.97	1.97	2.00	2.00	1.97
Fe	1.92	1.93	1.99	1.96	1.95	1.82	1.83	1.82	1.83	1.81	1.81
Mn	0.08	0.07	0.03	0.07	0.07	0.23	0.29	0.28	0.27	0.25	0.26
Mg	0.45	0.46	0.45	0.44	0.46	0.50	0.45	0.45	0.46	0.48	0.45
Ca	0.60	0.65	0.56	0.59	0.61	0.54	0.52	0.50	0.52	0.51	0.52
Grossular	0.20	0.21	0.18	0.19	0.20	0.18	0.17	0.16	0.17	0.17	0.17
Pyrope	0.15	0.15	0.15	0.14	0.15	0.16	0.14	0.15	0.15	0.16	0.15
Almandine	0.63	0.62	0.66	0.64	0.63	0.59	0.59	0.60	0.59	0.59	0.59
Spessartine	0.03	0.02	0.01	0.02	0.02	0.08	0.09	0.09	0.09	0.08	0.09
Mg#	0.19	0.19	0.18	0.18	0.19	0.21	0.20	0.20	0.20	0.21	0.20
Fe#	0.81	0.81	0.82	0.82	0.81	0.79	0.80	0.80	0.80	0.79	0.80

Table A.10 EID08-7-2b Hornblende Microprobe Data

Sample	EID08-7-2b							
Mineral	Hornblende							
Domain	1					2		
Point	1	2	3	4	5	6	7	9
SiO_2	40.92	41.22	41.02	41.69	40.67	40.67	41.25	40.83
TiO_2	0.18	0.18	0.23	0.03	0.19	0.25	0.14	0.23
Al_2O_3	17.49	17.77	18.17	16.93	17.41	18.28	17.85	18.09
FeO	17.76	17.42	17.37	16.97	17.54	17.31	17.43	17.42
MnO	0.20	0.13	0.28	0.20	0.31	0.32	0.29	0.19
MgO	8.18	8.53	7.99	8.45	8.24	8.17	8.45	8.24
CaO	11.49	11.12	11.15	11.28	11.30	11.38	11.31	11.52
Na_2O	1.54	1.71	1.70	1.70	1.69	1.76	1.72	1.60
K_2O	0.59	0.67	0.56	0.56	0.64	0.54	0.51	0.56
Cl	0.29	0.35	0.34	0.29	0.32	0.35	0.37	0.36
Total	**98.65**	**99.11**	**98.81**	**98.10**	**98.29**	**99.03**	**99.34**	**99.02**
Si	6.10	6.11	6.09	6.22	6.09	6.04	6.10	6.06
Ti	0.02	0.02	0.03	0.00	0.02	0.03	0.02	0.03
Al	3.07	3.10	3.18	2.98	3.07	3.20	3.11	3.17
Fe	2.22	2.16	2.16	2.12	2.20	2.15	2.16	2.16
Mn	0.03	0.02	0.04	0.02	0.04	0.04	0.04	0.02
Mg	1.82	1.88	1.77	1.88	1.84	1.81	1.86	1.82
Ca	1.84	1.77	1.77	1.80	1.81	1.81	1.79	1.83
Na	0.45	0.49	0.49	0.49	0.49	0.51	0.49	0.46
K	0.11	0.13	0.11	0.11	0.12	0.10	0.10	0.11
Cl	0.07	0.09	0.08	0.07	0.08	0.09	0.09	0.09
XMg	0.45	0.47	0.45	0.47	0.46	0.46	0.46	0.46
XFe	0.55	0.53	0.55	0.53	0.54	0.54	0.54	0.54

Sample								
Mineral								
Domain	2	3			4		5	7
Point	10	11	13	15	16	17	16	17
SiO_2	41.08	41.29	41.03	41.05	40.79	40.71	39.55	41.45
TiO_2	0.14	0.17	0.16	0.16	0.37	0.40	0.31	0.12
Al_2O_3	17.78	17.84	17.92	17.60	18.30	17.81	18.91	18.37
FeO	16.67	17.35	17.35	17.06	17.13	17.89	17.72	16.34
MnO	0.28	0.20	0.14	0.27	0.26	0.25	0.27	0.27
MgO	8.11	8.31	8.45	8.59	7.78	7.91	7.06	8.43
CaO	11.43	11.46	11.43	11.40	11.39	11.30	11.56	11.39
Na_2O	1.61	1.60	1.48	1.74	1.59	1.56	1.74	1.67
K_2O	0.47	0.56	0.50	0.50	0.53	0.61	0.77	0.51
Cl	0.32	0.33	0.27	0.34	0.37	0.36	0.50	0.30
Total	**97.90**	**99.13**	**98.73**	**98.73**	**98.50**	**98.80**	**98.39**	**98.84**
Si	6.14	6.11	6.09	6.10	6.08	6.07	5.96	6.12
Ti	0.02	0.02	0.02	0.02	0.04	0.05	0.04	0.01
Al	3.13	3.11	3.13	3.08	3.21	3.13	3.36	3.19
Fe	2.08	2.15	2.15	2.12	2.13	2.23	2.23	2.02
Mn	0.04	0.03	0.02	0.03	0.03	0.03	0.03	0.03
Mg	1.81	1.83	1.87	1.90	1.73	1.76	1.58	1.85
Ca	1.83	1.82	1.82	1.82	1.82	1.81	1.87	1.80
Na	0.47	0.46	0.43	0.50	0.46	0.45	0.51	0.48
K	0.09	0.11	0.10	0.10	0.10	0.12	0.15	0.10
Cl	0.08	0.08	0.07	0.09	0.09	0.09	0.13	0.08
XMg	0.46	0.46	0.46	0.47	0.45	0.44	0.42	0.48
XFe	0.54	0.54	0.54	0.53	0.55	0.56	0.58	0.52

Table A.11 EID08-7-2b Plagioclase Microprobe Data

Sample	EID08-7-2b											
Mineral	Plagioclase											
Domain	1		2				3					
Point	352	353	354	355	356	357	358	360	361	363	364	365
SiO_2	58.49	58.61	57.83	56.63	56.72	55.47	55.25	57.16	55.95	57.83	56.23	55.89
Al_2O_3	27.09	26.86	27.58	27.66	27.70	28.40	28.10	27.45	28.25	27.07	28.77	28.17
Fe_2O_3	0.10	0.22	0.14	0.45	0.08	0.14	0.20	0.08	0.19	0.28	0.19	0.31
CaO	7.30	7.84	8.35	9.12	8.64	9.09	9.58	8.42	9.41	7.92	9.23	9.16
Na_2O	7.27	6.83	6.44	6.23	6.55	6.09	6.22	6.64	6.19	6.84	6.17	6.40
K_2O	0.03	0.09	0.06	0.09	0.06	0.02	0.05	0.05	0.04	0.02	0.12	0.08
Total	**100.28**	**100.45**	**100.42**	**100.18**	**99.76**	**99.21**	**99.40**	**99.80**	**100.03**	**99.96**	**100.69**	**100.00**
Si	2.60	2.60	2.57	2.54	2.55	2.51	2.50	2.56	2.51	2.59	2.51	2.51
Al	1.42	1.41	1.45	1.46	1.47	1.51	1.50	1.45	1.49	1.43	1.51	1.49
Fe	0.00	0.01	0.00	0.02	0.00	0.00	0.01	0.00	0.01	0.01	0.01	0.01
Ca	0.35	0.37	0.40	0.44	0.42	0.44	0.46	0.40	0.45	0.38	0.44	0.44
Na	0.63	0.59	0.56	0.54	0.57	0.53	0.55	0.58	0.54	0.59	0.53	0.56
K	0.00	0.01	0.00	0.01	0.00	0.00	0.00	0.00	0.00	0.00	0.01	0.00
Albite	0.64	0.61	0.58	0.55	0.58	0.55	0.54	0.59	0.54	0.61	0.54	0.56
Anorthite	0.36	0.39	0.42	0.44	0.42	0.45	0.46	0.41	0.46	0.39	0.45	0.44

Sample	EID08-7-2b									
Mineral	Plagioclase									
Domain	4				5	7				
Point	367	368	369	370	371	373	374	376	377	379
SiO_2	57.53	56.11	56.59	57.47	58.12	55.17	55.78	56.18	55.26	55.74
Al_2O_3	27.03	26.52	27.81	27.46	27.09	28.20	27.87	28.09	28.50	28.23
Fe_2O_3	0.47	1.06	0.07	0.34	0.51	0.14	0.18	0.36	0.36	0.37
CaO	7.50	8.47	8.52	8.40	7.74	9.55	9.25	9.19	9.43	9.34
Na_2O	7.03	6.12	6.39	6.37	6.80	5.90	6.05	6.07	6.11	6.09
K_2O	0.00	0.05	0.01	0.03	0.05	0.06	0.04	0.05	0.05	0.06
Total	**99.57**	**98.34**	**99.39**	**100.07**	**100.30**	**99.02**	**99.17**	**99.93**	**99.72**	**99.82**
Si	2.58	2.56	2.55	2.57	2.59	2.50	2.52	2.52	2.49	2.51
Al	1.43	1.43	1.48	1.45	1.42	1.51	1.49	1.49	1.52	1.50
Fe	0.02	0.04	0.00	0.01	0.02	0.00	0.01	0.01	0.01	0.01
Ca	0.36	0.41	0.41	0.40	0.37	0.46	0.45	0.44	0.46	0.45
Na	0.61	0.54	0.56	0.55	0.59	0.52	0.53	0.53	0.53	0.53
K	0.00	0.00	0.00	0.00	0.00	0.00	0.00	0.00	0.00	0.00
Albite	0.63	0.57	0.58	0.58	0.61	0.53	0.54	0.54	0.54	0.54
Anorthite	0.37	0.43	0.42	0.42	0.39	0.47	0.46	0.45	0.46	0.46

Table A.12 EID08-7-2b Representative Average Microprobe Data

Sample	EID08-7-2b												
Mineral	Hornblende						Mineral	Plagioclase					
Domain	1	2	3	4	5	7	Domain	1	2	3	4	5	7
SiO_2	41.10	40.96	41.12	40.75	39.55	41.45	SiO_2	58.55	56.66	56.39	56.92	58.12	55.63
TiO_2	0.16	0.19	0.16	0.39	0.31	0.12	Al_2O_3	26.98	27.84	27.97	27.21	27.09	28.18
Al_2O_3	17.55	18.00	17.79	18.05	18.91	18.37	Fe_2O_3	0.16	0.21	0.21	0.48	0.51	0.28
FeO	17.41	17.21	17.26	17.51	17.72	16.34	CaO	7.57	8.80	8.95	8.22	7.74	9.35
MnO	0.22	0.27	0.20	0.26	0.27	0.27	Na_2O	7.05	6.33	6.41	6.48	6.80	6.04
MgO	8.28	8.24	8.45	7.84	7.06	8.43	K_2O	0.06	0.06	0.06	0.02	0.05	0.05
CaO	11.27	11.41	11.43	11.35	11.56	11.39	***Total***	**100.37**	**99.89**	**99.98**	**99.34**	**100.30**	**99.53**
Na_2O	1.67	1.68	1.61	1.57	1.74	1.67	Si	2.60	2.54	2.53	2.56	2.59	2.51
K_2O	0.60	0.52	0.52	0.57	0.77	0.51	Al	1.41	1.47	1.48	1.44	1.42	1.50
Cl	0.32	0.35	0.32	0.36	0.50	0.30	Fe	0.01	0.01	0.01	0.02	0.02	0.01
Total	**98.59**	**98.82**	**98.86**	**98.65**	**98.39**	**98.84**	Ca	0.36	0.42	0.43	0.40	0.37	0.45
Si	6.12	6.09	6.10	6.08	5.96	6.12	Na	0.61	0.55	0.56	0.57	0.59	0.53
Ti	0.02	0.02	0.02	0.04	0.04	0.01	K	0.00	0.00	0.00	0.00	0.00	0.00
Al	3.08	3.15	3.11	3.17	3.36	3.19	Albite	0.63	0.56	0.56	0.59	0.61	0.54
Fe	2.17	2.14	2.14	2.18	2.23	2.02	Anorthite	0.37	0.43	0.43	0.41	0.39	0.46
Mn	0.03	0.03	0.03	0.03	0.03	0.03							
Mg	1.84	1.83	1.87	1.74	1.58	1.85							
Ca	1.80	1.82	1.82	1.81	1.87	1.80							
Na	0.48	0.48	0.46	0.45	0.51	0.48							
K	0.11	0.10	0.10	0.11	0.15	0.10							
Cl	0.08	0.09	0.08	0.09	0.13	0.08							

Sample	EID08-7-2b					
Mineral	Garnet					
Domain	1	2	3	4	5	7
SiO_2	37.21	37.23	37.15	37.12	37.50	37.27
TiO_2	0.05	0.02	0.01	0.01	0.02	0.01
Al_2O_3	20.95	21.12	20.92	21.08	21.12	20.99
FeO	28.96	27.47	26.84	29.21	29.61	27.22
MnO	2.65	4.49	4.04	1.33	0.87	3.91
MgO	4.07	3.81	3.87	3.90	3.79	3.88
CaO	5.43	5.82	6.29	6.86	6.86	6.04
Total	**99.31**	**99.95**	**99.12**	**99.52**	**99.77**	**99.33**
Si	2.98	2.97	2.98	2.96	2.98	2.98
Ti	0.00	0.00	0.00	0.00	0.00	0.00
Al	1.98	1.98	1.98	1.98	1.98	1.98
Fe	1.94	1.83	1.80	1.95	1.97	1.82
Mn	0.18	0.30	0.27	0.09	0.06	0.27
Mg	0.49	0.45	0.46	0.46	0.45	0.46
Ca	0.47	0.50	0.54	0.59	0.58	0.52
Grossular	0.15	0.16	0.18	0.19	0.19	0.17
Pyrope	0.16	0.15	0.15	0.15	0.15	0.15
Almandine	0.63	0.59	0.58	0.63	0.64	0.59
Spessartine	0.06	0.10	0.09	0.03	0.02	0.09

Appendix B. Fiskfjord Thermobarometry Microprobe Data

Table B.1 FIS09-2b Garnet Microprobe Data

Sample	EID08-7-2b								
Mineral	Garnet								
Domain	1			2			3		
Point	229	230	231	250	251	252	268	269	270
SiO2	38.02	38.10	38.62	38.27	37.80	38.35	38.18	38.21	38.05
TiO2	0.08	0.09	0.10	0.02	0.02	0.05	0.01	0.00	0.01
Al2O3	20.41	20.35	20.49	20.62	20.71	20.52	20.78	20.77	33.47
FeO	28.08	27.65	27.44	27.81	27.75	28.14	28.01	28.04	20.26
MnO	1.28	1.22	1.15	1.29	1.31	1.29	1.17	1.25	0.93
MgO	5.41	5.38	5.26	5.19	5.15	5.25	5.91	5.85	4.13
CaO	5.90	5.68	6.03	5.91	6.17	6.09	5.03	4.98	3.38
Total	**99.18**	**98.48**	**99.09**	**99.11**	**98.91**	**99.69**	**99.09**	**99.10**	**100.23**
Si	3.02	3.04	3.05	3.03	3.01	3.03	3.02	3.02	2.80
Ti	0.00	0.01	0.01	0.00	0.00	0.00	0.00	0.00	0.00
Al	1.91	1.91	1.91	1.93	1.94	1.91	1.94	1.94	2.91
Fe	1.86	1.84	1.81	1.84	1.85	1.86	1.85	1.85	1.25
Mn	0.09	0.08	0.08	0.09	0.09	0.09	0.08	0.08	0.06
Mg	0.64	0.64	0.62	0.61	0.61	0.62	0.70	0.69	0.45
Ca	0.50	0.48	0.51	0.50	0.53	0.52	0.43	0.42	0.27
Grossular	0.16	0.16	0.17	0.16	0.17	0.17	0.14	0.14	0.13
Pyrope	0.21	0.21	0.21	0.20	0.20	0.20	0.23	0.23	0.22
Almandine	0.60	0.60	0.60	0.61	0.60	0.60	0.61	0.61	0.62
Spessartine	0.03	0.03	0.03	0.03	0.03	0.03	0.03	0.03	0.03
Mg#	0.26	0.26	0.25	0.25	0.25	0.25	0.27	0.27	0.27
Fe#	0.74	0.74	0.75	0.75	0.75	0.75	0.73	0.73	0.73

Sample	EID08-7-2b								
Mineral	Garnet								
Domain	3		4			5			
Point	271	272	300	301	303	318	324	325	326
SiO2	38.36	38.24	38.37	38.26	38.51	38.84	38.34	37.98	38.22
TiO2	0.01	0.01	0.01	0.01	0.03	0.00	0.01	0.03	0.01
Al2O3	20.72	20.64	20.48	20.64	20.69	20.45	20.84	20.69	20.51
FeO	28.06	28.01	28.72	28.16	27.82	28.90	27.98	28.64	28.66
MnO	1.33	1.44	0.83	0.77	0.74	0.87	1.02	0.98	0.93
MgO	5.71	5.68	6.03	5.97	6.23	6.33	5.54	5.76	5.88
CaO	5.14	5.14	4.72	5.46	5.11	3.90	5.77	5.17	4.86
Total	**99.33**	**99.16**	**99.16**	**99.28**	**99.14**	**99.29**	**99.50**	**99.25**	**99.07**
Si	3.03	3.03	3.03	3.02	3.03	3.06	3.02	3.01	3.03
Ti	0.00	0.00	0.00	0.00	0.00	0.00	0.00	0.00	0.00
Al	1.93	1.93	1.91	1.92	1.92	1.90	1.94	1.93	1.92
Fe	1.85	1.85	1.90	1.86	1.83	1.90	1.84	1.90	1.90
Mn	0.09	0.10	0.06	0.05	0.05	0.06	0.07	0.07	0.06
Mg	0.67	0.67	0.71	0.70	0.73	0.74	0.65	0.68	0.69
Ca	0.43	0.44	0.40	0.46	0.43	0.33	0.49	0.44	0.41
Grossular	0.14	0.14	0.13	0.15	0.14	0.11	0.16	0.14	0.13
Pyrope	0.22	0.22	0.23	0.23	0.24	0.24	0.21	0.22	0.23
Almandine	0.61	0.61	0.62	0.60	0.60	0.63	0.60	0.62	0.62
Spessartine	0.03	0.03	0.02	0.02	0.02	0.02	0.02	0.02	0.02
Mg#	0.27	0.27	0.27	0.27	0.29	0.28	0.26	0.26	0.27
Fe#	0.73	0.73	0.73	0.73	0.71	0.72	0.74	0.74	0.73

Table B.2 FIS09-2b Hornblende Microprobe Data

Sample	FIS09-2b											
Mineral	Hornblende											
Domain	1			2		3				4		5
Point	228	230	232	233	234	235	236	237	238	239	240	241
SiO2	40.20	39.15	40.34	40.95	40.41	41.06	41.34	42.32	40.62	42.07	41.79	41.88
TiO2	0.72	0.88	0.72	0.53	0.40	0.49	0.16	0.50	0.47	0.37	0.13	0.70
Al2O3	16.23	16.03	16.09	16.34	17.29	15.73	17.39	15.34	16.50	15.97	17.36	15.09
FeO	16.57	17.24	16.77	15.62	15.81	16.42	15.68	15.33	15.84	15.29	15.43	15.96
MnO	0.10	0.00	0.08	0.01	0.01	0.07	0.01	0.07	0.10	0.00	0.07	0.00
MgO	9.72	9.93	9.91	9.99	9.85	10.49	10.57	11.22	10.57	10.92	10.39	10.87
CaO	10.76	10.97	10.52	10.79	10.44	10.41	9.91	10.56	10.49	10.59	10.12	10.11
Na2O	2.45	2.22	2.51	2.31	2.46	2.55	2.56	2.26	2.33	2.51	2.70	2.49
K2O	0.81	0.80	0.75	0.73	0.73	0.67	0.72	0.62	0.73	0.58	0.58	0.61
Cl	1.00	1.01	1.06	0.97	1.04	0.89	0.92	0.86	0.96	0.75	0.80	0.80
Total	**98.54**	**98.22**	**98.75**	**98.24**	**98.46**	**98.78**	**99.25**	**99.08**	**98.60**	**99.06**	**99.36**	**98.49**
Si	6.08	5.97	6.09	6.16	6.07	6.16	6.12	6.27	6.09	6.22	6.16	6.26
Ti	0.08	0.10	0.08	0.06	0.05	0.06	0.02	0.06	0.05	0.04	0.01	0.08
Al	2.89	2.88	2.86	2.90	3.06	2.78	3.03	2.68	2.92	2.78	3.01	2.66
Fe	2.09	2.20	2.12	1.96	1.99	2.06	1.94	1.90	1.99	1.89	1.90	1.99
Mn	0.01	0.00	0.01	0.00	0.00	0.01	0.00	0.01	0.01	0.00	0.01	0.00
Mg	2.19	2.26	2.23	2.24	2.20	2.34	2.33	2.48	2.36	2.41	2.28	2.42
Ca	1.74	1.79	1.70	1.74	1.68	1.67	1.57	1.68	1.69	1.68	1.60	1.62
Na	0.72	0.66	0.73	0.67	0.72	0.74	0.74	0.65	0.68	0.72	0.77	0.72
K	0.16	0.16	0.14	0.14	0.14	0.13	0.14	0.12	0.14	0.11	0.11	0.12
Cl	0.26	0.26	0.27	0.25	0.27	0.23	0.23	0.21	0.24	0.19	0.20	0.20
XMg	0.51	0.51	0.51	0.53	0.53	0.53	0.55	0.57	0.54	0.56	0.55	0.55
XFe	0.49	0.49	0.49	0.47	0.47	0.47	0.45	0.43	0.46	0.44	0.45	0.45

Table B.3 FIS09-2b Plagioclase Microprobe Data

Sample	FIS09-2b												
Mineral	Plagioclase												
Domain	1					2					3		
Point	239	240	241	242	243	245	247	249	250	251	253	254	255
SiO2	63.20	63.44	64.67	62.45	62.86	64.24	64.17	62.46	61.98	62.64	64.40	63.41	61.22
Al2O3	22.98	22.33	22.99	23.37	23.12	22.15	23.19	23.18	23.76	23.31	22.46	22.95	24.88
Fe2O3	0.13	0.02	0.04	0.12	0.12	0.00	0.01	0.04	0.07	0.04	0.19	0.13	0.10
CaO	3.34	3.02	3.15	3.74	3.96	2.66	3.40	3.42	3.84	3.60	4.04	3.10	4.60
Na2O	9.60	9.59	9.33	9.25	9.19	9.89	9.81	9.57	9.46	9.89	8.20	9.67	8.58
K2O	0.05	0.05	0.06	0.08	0.08	0.06	0.06	0.07	0.01	0.09	0.08	0.12	0.04
Total	**99.31**	**98.45**	**100.25**	**99.00**	**99.34**	**99.00**	**100.65**	**98.73**	**99.12**	**99.58**	**99.37**	**99.37**	**99.41**
Si	2.81	2.84	2.84	2.79	2.79	2.85	2.81	2.79	2.76	2.78	2.85	2.81	2.72
Al	1.20	1.18	1.19	1.23	1.21	1.16	1.20	1.22	1.25	1.22	1.17	1.20	1.30
Fe	0.00	0.00	0.00	0.00	0.00	0.00	0.00	0.00	0.00	0.00	0.01	0.00	0.00
Ca	0.16	0.14	0.15	0.18	0.19	0.13	0.16	0.16	0.18	0.17	0.19	0.15	0.22
Na	0.83	0.83	0.79	0.80	0.79	0.85	0.83	0.83	0.82	0.85	0.70	0.83	0.74
K	0.00	0.00	0.00	0.00	0.00	0.00	0.00	0.00	0.00	0.01	0.00	0.01	0.00
Albite	0.84	0.85	0.84	0.81	0.80	0.87	0.84	0.83	0.82	0.83	0.78	0.84	0.77
Anorthite	0.16	0.15	0.16	0.18	0.19	0.13	0.16	0.16	0.18	0.17	0.21	0.15	0.23

Sample	FIS09-2b												
Mineral	Plagioclase												
Domain	3		4					5					
Point	257	258	259	260	262	263	265	269	270	271	273	274	275
SiO2	62.86	62.22	62.67	64.02	63.79	63.15	63.25	62.21	60.49	63.62	63.61	62.18	62.82
Al2O3	23.46	23.67	23.62	22.80	22.83	23.47	22.96	23.23	24.11	22.36	22.30	22.95	23.21
Fe2O3	0.09	0.03	0.21	0.06	0.00	0.03	0.08	0.19	0.20	0.00	0.12	0.15	0.12
CaO	4.00	3.90	4.13	3.05	3.22	3.36	3.36	3.66	4.58	3.02	2.78	3.61	3.87
Na2O	8.98	9.11	8.78	9.41	9.69	9.60	9.54	9.39	8.86	9.97	9.34	9.23	9.32
K2O	0.10	0.08	0.03	0.06	0.04	0.12	0.08	0.08	0.07	0.06	0.06	0.03	0.10
Total	**99.49**	**99.00**	**99.44**	**99.40**	**99.57**	**99.73**	**99.26**	**98.75**	**98.31**	**99.03**	**98.21**	**98.15**	**99.45**
Si	2.79	2.78	2.78	2.83	2.82	2.79	2.81	2.78	2.73	2.83	2.85	2.80	2.79
Al	1.23	1.24	1.24	1.19	1.19	1.22	1.20	1.23	1.28	1.17	1.18	1.22	1.22
Fe	0.00	0.00	0.01	0.00	0.00	0.00	0.00	0.01	0.01	0.00	0.00	0.01	0.00
Ca	0.19	0.19	0.20	0.14	0.15	0.16	0.16	0.18	0.22	0.14	0.13	0.17	0.18
Na	0.77	0.79	0.76	0.81	0.83	0.82	0.82	0.81	0.77	0.86	0.81	0.80	0.80
K	0.01	0.00	0.00	0.00	0.00	0.01	0.00	0.00	0.00	0.00	0.00	0.00	0.01
Albite	0.80	0.81	0.79	0.84	0.84	0.83	0.83	0.82	0.77	0.85	0.86	0.82	0.81
Anorthite	0.20	0.19	0.21	0.15	0.15	0.16	0.16	0.18	0.22	0.14	0.14	0.18	0.19

Table B.4 FIS09-2b Representative Average Microprobe Data

Sample	FIS09-2b																
Mineral	Hornblende					Mineral	Plagioclase					Mineral	Garnet				
Domain	1	2	3	4	5	Domain	1	2	3	4	5	Domain	1	2	3	4	5
SiO2	39.90	40.68	41.33	41.93	41.88	SiO2	63.32	63.10	62.82	63.38	62.49	SiO2	44.29	38.31	38.23	47.00	38.88
TiO2	0.77	0.47	0.41	0.25	0.70	Al2O3	22.96	23.12	23.48	23.14	23.03	TiO2	0.05	0.02	0.02	0.02	0.02
Al2O3	16.12	16.82	16.24	16.66	15.09	Fe2O3	0.09	0.03	0.11	0.08	0.13	Al2O3	18.65	20.67	22.22	17.64	20.46
FeO	16.86	15.72	15.82	15.36	15.96	CaO	3.44	3.39	3.93	3.42	3.59	FeO	25.56	28.34	27.13	24.14	28.53
MnO	0.06	0.01	0.06	0.03	0.00	Na2O	9.39	9.72	8.91	9.40	9.35	MnO	1.05	1.02	1.18	0.66	0.85
MgO	9.85	9.92	10.71	10.65	10.87	K2O	0.07	0.06	0.08	0.06	0.06	MgO	5.10	6.03	5.64	5.19	6.16
CaO	10.75	10.61	10.34	10.36	10.11	***Total***	**99.27**	**99.42**	**99.33**	**99.48**	**98.65**	CaO	4.67	4.99	4.94	4.61	4.48
Na2O	2.39	2.39	2.43	2.60	2.49	Si	2.81	2.80	2.79	2.81	2.80	***Total***	**99.36**	**99.38**	**99.36**	**99.27**	**99.37**
K2O	0.78	0.73	0.68	0.58	0.61	Al	1.20	1.21	1.23	1.21	1.21	Si	3.32	3.02	3.00	3.46	3.06
Cl	1.02	1.01	0.91	0.78	0.80	Fe	0.00	0.00	0.00	0.00	0.00	Ti	0.00	0.00	0.00	0.00	0.00
Total	**98.51**	**98.35**	**98.93**	**99.21**	**98.49**	Ca	0.16	0.16	0.19	0.16	0.17	Al	1.73	1.92	2.05	1.63	1.90
Si	6.05	6.11	6.16	6.19	6.26	Na	0.81	0.84	0.77	0.81	0.81	Fe	1.69	1.87	1.78	1.58	1.88
Ti	0.09	0.05	0.05	0.03	0.08	K	0.00	0.00	0.00	0.00	0.00	Mn	0.07	0.07	0.08	0.04	0.06
Al	2.88	2.98	2.85	2.90	2.66	Albite	0.83	0.84	0.80	0.83	0.82	Mg	0.60	0.71	0.66	0.61	0.72
Fe	2.14	1.98	1.97	1.90	1.99	Anorthite	0.17	0.16	0.20	0.17	0.17	Ca	0.39	0.42	0.42	0.39	0.38
Mn	0.01	0.00	0.01	0.00	0.00							Grossular	0.14	0.14	0.14	0.14	0.12
Mg	2.23	2.22	2.38	2.34	2.42							Pyrope	0.21	0.23	0.22	0.21	0.24
Ca	1.75	1.71	1.65	1.64	1.62							Almandine	0.62	0.61	0.61	0.64	0.62
Na	0.70	0.70	0.70	0.75	0.72							Spessartine	0.03	0.02	0.03	0.02	0.02
K	0.15	0.14	0.13	0.11	0.12												
Cl	0.26	0.26	0.23	0.19	0.20												

Table B.5 FIS09-2d Garnet Microprobe Data

Sample	FIS09-2d							
Mineral	Garnet							
Domain	1			2				
Points	80	81	82	91	92	93	94	95
SiO2	38.53	38.62	38.47	38.14	38.28	38.65	38.06	56.11
TiO2	0.04	0.02	0.01	0.02	0.07	0.03	0.10	0.03
Al2O3	21.31	21.37	21.43	21.06	21.19	20.82	21.08	14.40
FeO	29.43	29.20	28.37	29.16	28.92	28.73	29.11	21.14
MnO	0.91	0.95	0.79	0.90	0.80	0.78	1.00	0.63
MgO	6.67	6.70	6.63	6.39	6.77	6.46	6.29	4.20
CaO	3.68	3.71	3.49	4.17	4.02	4.05	4.36	2.93
Total	**100.57**	**100.58**	**99.19**	**99.83**	**100.06**	**99.52**	**99.99**	**99.44**
Si	3.00	3.00	3.02	3.00	2.99	3.04	2.99	4.07
Ti	0.00	0.00	0.00	0.00	0.00	0.00	0.01	0.00
Al	1.96	1.96	1.98	1.95	1.95	1.93	1.95	1.23
Fe	1.92	1.90	1.86	1.92	1.89	1.89	1.91	1.28
Mn	0.06	0.06	0.05	0.06	0.05	0.05	0.07	0.04
Mg	0.77	0.78	0.78	0.75	0.79	0.76	0.74	0.45
Ca	0.31	0.31	0.29	0.35	0.34	0.34	0.37	0.23
Grossular	0.10	0.10	0.10	0.11	0.11	0.11	0.12	0.11
Pyrope	0.25	0.25	0.26	0.24	0.26	0.25	0.24	0.23
Almandine	0.63	0.62	0.62	0.62	0.62	0.62	0.62	0.64
Spessartine	0.02	0.02	0.02	0.02	0.02	0.02	0.02	0.02
Mg#	0.29	0.29	0.29	0.28	0.29	0.29	0.28	0.26
Fe#	0.71	0.71	0.71	0.72	0.71	0.71	0.72	0.74

Sample	FIS09-2d							
Mineral	Garnet							
Domain	3		4			5		
Points	115	116	138	139	140	152	153	154
SiO2	38.37	38.04	38.49	38.16	38.41	38.54	38.69	38.16
TiO2	0.06	0.04	0.03	0.01	0.02	0.01	0.04	0.03
Al2O3	21.01	21.15	21.21	20.98	21.08	21.33	21.11	21.24
FeO	29.01	28.40	28.84	28.89	29.72	29.15	29.39	29.82
MnO	0.87	0.92	1.21	0.85	0.92	0.86	0.85	0.86
MgO	6.61	6.54	6.98	6.81	6.41	6.75	6.71	6.82
CaO	4.19	4.01	3.46	3.49	3.57	3.24	3.42	3.32
Total	**100.12**	**99.08**	**100.22**	**99.20**	**100.13**	**99.88**	**100.22**	**100.24**
Si	3.00	3.00	3.00	3.01	3.01	3.01	3.02	2.99
Ti	0.00	0.00	0.00	0.00	0.00	0.00	0.00	0.00
Al	1.94	1.97	1.95	1.95	1.95	1.97	1.94	1.96
Fe	1.90	1.87	1.88	1.91	1.95	1.91	1.92	1.95
Mn	0.06	0.06	0.08	0.06	0.06	0.06	0.06	0.06
Mg	0.77	0.77	0.81	0.80	0.75	0.79	0.78	0.80
Ca	0.35	0.34	0.29	0.30	0.30	0.27	0.29	0.28
Grossular	0.11	0.11	0.09	0.10	0.10	0.09	0.09	0.09
Pyrope	0.25	0.25	0.27	0.26	0.25	0.26	0.26	0.26
Almandine	0.62	0.62	0.61	0.62	0.64	0.63	0.63	0.63
Spessartine	0.02	0.02	0.03	0.02	0.02	0.02	0.02	0.02
Mg#	0.29	0.29	0.30	0.30	0.28	0.29	0.29	0.29
Fe#	0.71	0.71	0.70	0.70	0.72	0.71	0.71	0.71

Table B.6 FIS09-2d Hornblende Microprobe Data

Sample	FIS09-2d								
Mineral	Hornblende								
Domain	1		2				3	4	5
Point	248	250	252	254	255	256	257	263	267
SiO2	42.38	41.94	42.06	42.30	41.58	41.29	42.11	41.64	42.17
TiO2	0.64	0.74	0.38	0.35	0.41	0.60	0.51	0.52	0.52
Al2O3	15.60	15.91	15.93	16.40	16.11	16.14	15.82	15.94	15.62
FeO	14.92	15.40	15.60	14.82	15.13	15.54	14.91	14.55	14.99
MnO	0.00	0.11	0.00	0.12	0.05	0.00	0.11	0.03	0.03
MgO	11.44	11.09	11.09	10.99	10.92	10.59	11.47	11.49	11.27
CaO	10.61	10.66	10.63	10.64	10.89	11.00	10.89	10.48	10.90
Na2O	2.38	2.28	2.42	2.34	2.42	2.33	2.33	2.24	2.17
K2O	0.64	0.69	0.65	0.61	0.66	0.65	0.58	0.58	0.59
Cl	0.59	0.62	0.72	0.57	0.81	0.73	0.59	0.56	0.65
Total	**99.20**	**99.44**	**99.48**	**99.13**	**98.99**	**98.87**	**99.31**	**98.02**	**98.90**
Si	6.23	6.18	6.20	6.21	6.17	6.14	6.19	6.18	6.23
Ti	0.07	0.08	0.04	0.04	0.05	0.07	0.06	0.06	0.06
Al	2.70	2.76	2.77	2.84	2.82	2.83	2.74	2.79	2.72
Fe	1.83	1.90	1.92	1.82	1.88	1.93	1.83	1.81	1.85
Mn	0.00	0.01	0.00	0.01	0.01	0.00	0.01	0.00	0.00
Mg	2.51	2.43	2.44	2.41	2.42	2.35	2.51	2.54	2.48
Ca	1.67	1.68	1.68	1.68	1.73	1.75	1.72	1.67	1.72
Na	0.68	0.65	0.69	0.67	0.70	0.67	0.66	0.64	0.62
K	0.12	0.13	0.12	0.11	0.13	0.12	0.11	0.11	0.11
Cl	0.15	0.15	0.18	0.14	0.20	0.18	0.15	0.14	0.16
XMg	0.58	0.56	0.56	0.57	0.56	0.55	0.58	0.58	0.57
XFe	0.42	0.44	0.44	0.43	0.44	0.45	0.42	0.42	0.43

Table B.7 FIS09-2d Plagioclase Microprobe Data

Sample	FIS09-2d													
Mineral	Plagioclase													
Domain	1						2					3		
Point	220	221	222	223	224	225	226	227	228	230	231	204	205	206
SiO2	63.08	63.31	63.38	62.37	62.90	62.00	62.07	62.79	61.76	62.62	62.21	62.67	61.77	61.48
Al2O3	23.80	23.24	23.21	24.00	23.56	24.75	24.21	23.69	24.16	23.86	23.90	24.06	24.22	24.56
Fe2O3	0.08	0.07	0.00	0.14	0.04	0.13	0.12	0.16	0.16	0.16	0.00	0.09	0.03	0.07
CaO	4.38	4.20	3.96	4.72	4.66	4.96	4.55	4.02	4.48	4.46	5.11	4.54	5.04	5.07
Na2O	8.59	8.75	8.61	8.67	8.72	8.72	8.68	8.90	8.43	8.74	8.51	8.72	8.33	8.19
K2O	0.07	0.06	0.07	0.08	0.08	0.03	0.04	0.03	0.03	0.09	0.07	0.02	0.08	0.04
Total	**99.99**	**99.63**	**99.24**	**99.97**	**99.96**	**100.59**	**99.68**	**99.59**	**99.02**	**99.93**	**99.80**	**100.09**	**99.46**	**99.42**
Si	2.78	2.80	2.81	2.76	2.78	2.73	2.75	2.78	2.75	2.77	2.76	2.77	2.75	2.73
Al	1.24	1.21	1.21	1.25	1.23	1.28	1.27	1.24	1.27	1.24	1.25	1.25	1.27	1.29
Fe	0.00	0.00	0.00	0.00	0.00	0.00	0.00	0.01	0.01	0.01	0.00	0.00	0.00	0.00
Ca	0.21	0.20	0.19	0.22	0.22	0.23	0.22	0.19	0.21	0.21	0.24	0.21	0.24	0.24
Na	0.73	0.75	0.74	0.74	0.75	0.74	0.75	0.76	0.73	0.75	0.73	0.75	0.72	0.71
K	0.00	0.00	0.00	0.00	0.00	0.00	0.00	0.00	0.00	0.01	0.00	0.00	0.00	0.00
Albite	0.78	0.79	0.79	0.77	0.77	0.76	0.77	0.80	0.77	0.78	0.75	0.78	0.75	0.74
Anorthite	0.22	0.21	0.20	0.23	0.23	0.24	0.22	0.20	0.23	0.22	0.25	0.22	0.25	0.25

Sample	FIS09-2d												
Mineral	Plagioclase												
Domain	3		4						5				
Point	207	208	209	210	211	212	213	214	215	216	217	218	219
SiO2	62.86	62.24	63.28	62.46	62.07	61.83	62.67	61.86	62.15	62.24	62.20	62.33	62.40
Al2O3	24.18	24.05	23.36	24.02	23.95	23.99	23.88	24.17	23.75	23.82	23.64	23.92	23.59
Fe2O3	0.13	0.12	0.18	0.17	0.12	0.04	0.01	0.00	0.30	0.05	0.25	0.18	0.20
CaO	4.95	4.56	4.45	5.00	4.77	4.85	4.63	4.90	4.67	4.57	4.66	4.49	4.77
Na2O	8.42	8.70	8.79	8.68	8.74	8.44	8.57	8.76	8.61	8.50	8.49	8.58	8.60
K2O	0.06	0.06	0.06	0.09	0.06	0.03	0.08	0.05	0.06	0.05	0.03	0.05	0.03
Total	**100.61**	**99.72**	**100.12**	**100.41**	**99.72**	**99.18**	**99.83**	**99.75**	**99.53**	**99.22**	**99.28**	**99.55**	**99.60**
Si	2.76	2.76	2.79	2.75	2.75	2.76	2.77	2.75	2.76	2.77	2.77	2.77	2.77
Al	1.25	1.26	1.21	1.25	1.25	1.26	1.24	1.26	1.24	1.25	1.24	1.25	1.23
Fe	0.00	0.00	0.01	0.01	0.00	0.00	0.00	0.00	0.01	0.00	0.01	0.01	0.01
Ca	0.23	0.22	0.21	0.24	0.23	0.23	0.22	0.23	0.22	0.22	0.22	0.21	0.23
Na	0.72	0.75	0.75	0.74	0.75	0.73	0.73	0.75	0.74	0.73	0.73	0.74	0.74
K	0.00	0.00	0.00	0.00	0.00	0.00	0.00	0.00	0.00	0.00	0.00	0.00	0.00
Albite	0.75	0.77	0.78	0.75	0.77	0.76	0.77	0.76	0.77	0.77	0.77	0.77	0.76
Anorthite	0.24	0.22	0.22	0.24	0.23	0.24	0.23	0.24	0.23	0.23	0.23	0.22	0.23

Table B.8 FIS09-2d Representative Average Microprobe Data

Sample	FIS09-2d																
Mineral	Hornblende					Mineral	Plagioclase					Mineral	Garnet				
Domain	1	2	3	4	5	Domain	1	2	3	4	5	Domain	1	2	3	4	5
SiO2	42.16	41.81	42.11	41.64	42.17	SiO2	62.84	62.29	62.21	62.36	62.27	SiO2	38.54	38.28	38.21	38.35	38.47
TiO2	0.69	0.44	0.51	0.52	0.52	Al2O3	23.76	23.97	24.21	23.90	23.74	TiO2	0.02	0.05	0.05	0.02	0.02
Al2O3	15.76	16.14	15.82	15.94	15.62	Fe2O3	0.08	0.12	0.09	0.09	0.20	Al2O3	21.37	21.04	21.08	21.09	21.23
FeO	15.16	15.27	14.91	14.55	14.99	CaO	4.48	4.53	4.83	4.77	4.63	FeO	29.00	28.98	28.71	29.15	29.45
MnO	0.05	0.04	0.11	0.03	0.03	Na2O	8.68	8.65	8.47	8.66	8.56	MnO	0.88	0.87	0.89	0.99	0.85
MgO	11.26	10.90	11.47	11.49	11.27	K2O	0.06	0.05	0.05	0.06	0.04	MgO	6.67	6.48	6.57	6.73	6.76
CaO	10.63	10.79	10.89	10.48	10.90	***Total***	**99.90**	**99.60**	**99.86**	**99.83**	**99.44**	CaO	3.63	4.15	4.10	3.51	3.33
Na2O	2.33	2.38	2.33	2.24	2.17	Si	2.78	2.76	2.75	2.76	2.77	***Total***	**100.11**	**99.85**	**99.60**	**99.85**	**100.11**
K2O	0.66	0.64	0.58	0.58	0.59	Al	1.24	1.25	1.26	1.25	1.24	Si	3.01	3.00	3.00	3.01	3.01
Cl	0.60	0.71	0.59	0.56	0.65	Fe	0.00	0.00	0.00	0.00	0.01	Ti	0.00	0.00	0.00	0.00	0.00
Total	**99.32**	**99.12**	**99.31**	**98.02**	**98.90**	Ca	0.21	0.22	0.23	0.23	0.22	Al	1.97	1.95	1.95	1.95	1.96
Si	6.20	6.18	6.19	6.18	6.23	Na	0.74	0.74	0.73	0.74	0.74	Fe	1.89	1.90	1.89	1.91	1.93
Ti	0.08	0.05	0.06	0.06	0.06	K	0.00	0.00	0.00	0.00	0.00	Mn	0.06	0.06	0.06	0.07	0.06
Al	2.73	2.81	2.74	2.79	2.72	Albite	0.78	0.77	0.76	0.76	0.77	Mg	0.78	0.76	0.77	0.79	0.79
Fe	1.87	1.89	1.83	1.81	1.85	Anorthite	0.22	0.22	0.24	0.23	0.23	Ca	0.30	0.35	0.35	0.29	0.28
Mn	0.01	0.01	0.01	0.00	0.00							Grossular	0.10	0.11	0.11	0.10	0.09
Mg	2.47	2.40	2.51	2.54	2.48							Pyrope	0.26	0.25	0.25	0.26	0.26
Ca	1.68	1.71	1.72	1.67	1.72							Almandine	0.62	0.62	0.62	0.62	0.63
Na	0.67	0.68	0.66	0.64	0.62							Spessartine	0.02	0.02	0.02	0.02	0.02
K	0.12	0.12	0.11	0.11	0.11												
Cl	0.15	0.18	0.15	0.14	0.16												

Table B.9 FIS09-3a-1b Garnet Microprobe Data

Sample	FIS09-3a-1b										
Mineral	Garnet										
Domains	1			2		3			4		
Points	108	109	110	115	130	135	136	137	144	145	146
SiO2	37.04	36.93	37.13	36.92	36.95	36.75	36.53	36.62	36.52	36.40	36.44
TiO2	0.08	0.03	0.07	0.07	0.10	0.09	0.06	0.08	0.07	0.01	0.05
Al2O3	19.13	19.45	19.61	19.30	19.02	19.41	18.97	19.22	19.47	19.72	19.56
FeO	20.03	20.52	20.58	18.71	18.28	19.69	19.55	19.99	19.43	19.79	19.89
MnO	9.29	8.69	8.83	11.75	11.74	11.45	10.88	10.80	10.41	10.44	10.38
MgO	0.88	0.97	1.00	0.82	0.87	0.90	0.88	0.92	0.79	0.83	0.83
CaO	10.93	10.87	10.57	9.61	10.00	9.82	10.17	9.97	10.29	10.37	10.52
Total	**97.37**	**97.45**	**97.79**	**97.19**	**96.95**	**98.10**	**97.03**	**97.61**	**96.99**	**97.57**	**97.67**
Si	3.05	3.04	3.04	3.05	3.06	3.02	3.03	3.03	3.03	3.00	3.01
Ti	0.00	0.00	0.00	0.00	0.01	0.01	0.00	0.00	0.00	0.00	0.00
Al	1.86	1.89	1.89	1.88	1.86	1.88	1.86	1.87	1.90	1.92	1.90
Fe	1.38	1.41	1.41	1.29	1.27	1.35	1.36	1.38	1.35	1.37	1.37
Mn	0.65	0.61	0.61	0.82	0.82	0.80	0.77	0.76	0.73	0.73	0.73
Mg	0.11	0.12	0.12	0.10	0.11	0.11	0.11	0.11	0.10	0.10	0.10
Ca	0.96	0.96	0.93	0.85	0.89	0.87	0.90	0.88	0.91	0.92	0.93
Grossular	0.31	0.31	0.30	0.28	0.29	0.28	0.29	0.28	0.30	0.29	0.30
Pyrope	0.03	0.04	0.04	0.03	0.03	0.04	0.03	0.04	0.03	0.03	0.03
Almandine	0.44	0.46	0.46	0.42	0.41	0.43	0.43	0.44	0.44	0.44	0.44
Spessartine	0.21	0.20	0.20	0.27	0.27	0.26	0.24	0.24	0.24	0.23	0.23
Mg#	0.07	0.08	0.08	0.07	0.08	0.08	0.07	0.08	0.07	0.07	0.07
Fe#	0.93	0.92	0.92	0.93	0.92	0.92	0.93	0.92	0.93	0.93	0.93

Table B.10 FIS09-3a-1b Hornblende Microprobe Data

Sample	FIS09-3a-1b										
Mineral	Hornblende										
Domain	1			2					3		4
Points	268	269	270	272	273	274	275	276	277	278	282
SiO2	40.12	39.47	39.39	40.12	39.04	39.66	39.53	38.91	39.39	38.94	39.70
TiO2	1.09	1.00	0.97	0.94	1.05	1.03	1.02	1.18	1.05	1.05	0.83
Al2O3	12.87	13.01	12.30	12.16	12.76	12.89	13.01	13.21	12.68	12.42	13.01
FeO	23.72	23.73	23.56	22.84	24.23	23.33	23.61	23.55	24.55	24.70	23.99
MnO	0.63	0.78	0.62	0.76	0.60	0.53	0.56	0.71	0.58	0.73	0.83
MgO	6.28	6.21	6.23	7.22	6.27	6.30	6.63	6.23	6.21	6.36	6.54
CaO	10.36	10.65	10.54	10.84	10.34	10.56	10.41	10.59	10.54	10.44	10.51
Na2O	2.02	1.95	1.96	1.75	1.95	2.03	1.91	2.07	1.98	2.11	1.80
K2O	1.94	1.94	1.94	1.69	2.01	2.02	1.84	2.25	2.03	2.06	1.97
Cl	0.23	0.22	0.28	0.23	0.28	0.29	0.22	0.24	0.23	0.21	0.24
Total	**99.27**	**98.96**	**97.79**	**98.54**	**98.53**	**98.64**	**98.73**	**98.94**	**99.24**	**99.02**	**99.42**
Si	6.22	6.15	6.22	6.24	6.14	6.19	6.16	6.08	6.15	6.11	6.16
Ti	0.13	0.12	0.12	0.11	0.12	0.12	0.12	0.14	0.12	0.12	0.10
Al	2.35	2.39	2.29	2.23	2.36	2.37	2.39	2.43	2.33	2.30	2.38
Fe	3.07	3.09	3.11	2.97	3.18	3.05	3.08	3.08	3.20	3.24	3.11
Mn	0.08	0.10	0.08	0.10	0.08	0.07	0.07	0.09	0.08	0.10	0.11
Mg	1.45	1.44	1.47	1.67	1.47	1.47	1.54	1.45	1.44	1.49	1.51
Ca	1.72	1.78	1.78	1.81	1.74	1.77	1.74	1.77	1.76	1.76	1.75
Na	0.61	0.59	0.60	0.53	0.60	0.61	0.58	0.63	0.60	0.64	0.54
K	0.38	0.39	0.39	0.33	0.40	0.40	0.37	0.45	0.40	0.41	0.39
Cl	0.06	0.06	0.07	0.06	0.07	0.08	0.06	0.06	0.06	0.06	0.06
XMg	0.32	0.32	0.32	0.36	0.32	0.32	0.33	0.32	0.31	0.31	0.33
XFe	0.68	0.68	0.68	0.64	0.68	0.68	0.67	0.68	0.69	0.69	0.67

Table B.11 FIS09-3a-1b Plagioclase Microprobe Data

Sample	FIS09-3a-1b									
Mineral	Plagioclase									
Domain	1			2						3
Points	146	150	152	157	158	160	161	162	163	164
SiO2	62.40	63.28	62.97	62.61	62.49	61.88	63.19	61.81	60.87	64.54
Al2O3	21.93	21.57	21.33	21.78	22.29	23.14	22.06	22.61	23.03	21.55
Fe2O3	0.03	0.00	0.22	0.23	0.02	0.08	0.23	0.26	0.00	0.36
CaO	4.35	4.02	4.20	4.65	4.81	5.69	4.53	6.40	6.34	3.82
Na2O	9.92	9.64	9.48	9.80	9.67	9.25	9.22	8.86	8.87	10.20
K2O	0.13	0.13	0.14	0.11	0.16	0.17	0.20	0.09	0.18	0.12
Total	**98.77**	**98.64**	**98.33**	**99.18**	**99.44**	**100.21**	**99.42**	**100.03**	**99.28**	**100.59**
Si	2.81	2.84	2.84	2.81	2.79	2.75	2.82	2.76	2.74	2.84
Al	1.16	1.14	1.13	1.15	1.17	1.21	1.16	1.19	1.22	1.12
Fe	0.00	0.00	0.01	0.01	0.00	0.00	0.01	0.01	0.00	0.01
Ca	0.21	0.19	0.20	0.22	0.23	0.27	0.22	0.31	0.31	0.18
Na	0.01	0.01	0.01	0.01	0.01	0.01	0.01	0.01	0.01	0.01
K	0.86	0.84	0.83	0.85	0.84	0.80	0.80	0.77	0.77	0.87
Albite	0.80	0.81	0.80	0.79	0.78	0.74	0.78	0.71	0.71	0.82
Anorthite	0.19	0.19	0.20	0.21	0.21	0.25	0.21	0.28	0.28	0.17

Sample	FIS09-3a-1b									
Mineral	Plagioclase									
Domain	3				4					
Points	165	166	171	172	173	174	175	176	178	180
SiO2	63.78	64.23	63.53	63.57	62.06	62.57	62.02	61.99	62.26	64.51
Al2O3	21.57	21.36	21.75	21.74	22.52	22.16	22.26	22.55	22.32	21.14
Fe2O3	0.29	0.76	0.14	0.37	0.04	0.11	0.03	0.00	0.10	0.06
CaO	3.71	3.95	3.95	3.98	5.01	5.24	5.39	5.25	5.28	3.21
Na2O	9.59	10.00	10.07	9.56	9.50	9.64	9.30	9.12	9.47	10.12
K2O	0.10	0.07	0.28	0.13	0.20	0.16	0.24	0.21	0.18	0.17
Total	**99.05**	**100.38**	**99.73**	**99.35**	**99.34**	**99.88**	**99.25**	**99.13**	**99.60**	**99.21**
Si	2.84	2.84	2.83	2.83	2.78	2.79	2.78	2.78	2.78	2.87
Al	1.13	1.11	1.14	1.14	1.19	1.16	1.18	1.19	1.18	1.11
Fe	0.01	0.03	0.00	0.01	0.00	0.00	0.00	0.00	0.00	0.00
Ca	0.18	0.19	0.19	0.19	0.24	0.25	0.26	0.25	0.25	0.15
Na	0.01	0.00	0.02	0.01	0.01	0.01	0.01	0.01	0.01	0.01
K	0.83	0.86	0.87	0.83	0.83	0.83	0.81	0.79	0.82	0.87
Albite	0.82	0.82	0.81	0.81	0.77	0.76	0.75	0.75	0.76	0.84
Anorthite	0.18	0.18	0.18	0.19	0.22	0.23	0.24	0.24	0.23	0.15

Table B.12 FIS09-3a-1b Representative Average Microprobe Data

Sample	FIS09-3a-1b													
Mineral	Hornblende				Mineral	Plagioclase				Mineral	Garnet			
Domain	1	2	3	4	Domain	1	2	3	4	Domain	1	2	3	4
SiO2	39.66	39.45	39.17	39.70	SiO2	62.88	62.14	63.93	62.57	SiO2	37.03	36.93	36.63	36.45
TiO2	1.02	1.04	1.05	0.83	Al2O3	21.61	22.48	21.59	22.16	TiO2	0.06	0.05	0.07	0.04
Al2O3	12.73	12.80	12.55	13.01	Fe2O3	0.08	0.14	0.38	0.06	Al2O3	19.40	19.39	19.20	19.58
FeO	23.67	23.51	24.63	23.99	CaO	4.19	5.40	3.88	4.90	FeO	20.37	19.30	19.74	19.71
MnO	0.68	0.63	0.66	0.83	Na2O	9.68	9.28	9.89	9.53	MnO	8.94	11.00	11.05	10.41
MgO	6.24	6.53	6.28	6.54	K2O	0.13	0.15	0.14	0.19	MgO	0.95	1.14	0.90	0.82
CaO	10.52	10.55	10.49	10.51	***Total***	**98.58**	**99.59**	**99.82**	**99.40**	CaO	10.79	9.94	9.99	10.39
Na2O	1.98	1.94	2.05	1.80	Si	2.83	2.78	2.84	2.80	***Total***	**97.54**	**97.75**	**97.58**	**97.41**
K2O	1.94	1.96	2.04	1.97	Al	1.14	1.18	1.13	1.17	Si	3.04	3.03	3.03	3.01
Cl	0.24	0.25	0.22	0.24	Fe	0.00	0.00	0.01	0.00	Ti	0.00	0.00	0.00	0.00
Total	**98.67**	**98.67**	**99.13**	**99.42**	Ca	0.20	0.26	0.18	0.23	Al	1.88	1.88	1.87	1.91
Si	6.20	6.16	6.13	6.16	Na	0.84	0.80	0.85	0.83	Fe	1.40	1.33	1.36	1.36
Ti	0.12	0.12	0.12	0.10	K	0.01	0.01	0.01	0.01	Mn	0.62	0.77	0.77	0.73
Al	2.34	2.36	2.31	2.38	Albite	0.80	0.75	0.82	0.77	Mg	0.12	0.14	0.11	0.10
Fe	3.09	3.07	3.22	3.11	Anorthite	0.19	0.24	0.18	0.22	Ca	0.95	0.88	0.88	0.92
Mn	0.09	0.08	0.09	0.11						Grossular	0.31	0.28	0.28	0.30
Mg	1.45	1.52	1.47	1.51						Pyrope	0.04	0.04	0.04	0.03
Ca	1.76	1.77	1.76	1.75						Almandine	0.45	0.43	0.44	0.44
Na	0.60	0.59	0.62	0.54						Spessartine	0.20	0.25	0.25	0.23
K	0.39	0.39	0.41	0.39										
Cl	0.06	0.07	0.06	0.06										

Appendix C. Standard Microprobe Data

Table C.1 Gore Mountain Garnet National Museum Standard

STD 13	Gore Mt. Garnet #12442					MZbar=	11.592	Zbar=	13.520		
LMNT:	SiO_2	TiO_2	Al_2O_3	FeO	MnO	MgO	CaO	P_2O_5	H_2O	V_2O_3	Total
OWXT:	**39.060**	**0.060**	**22.01**	**22.360**	**0.490**	**11.530**	**4.200**	**0.040**	**0.140**	**0.010**	***99.900***
ELWT:	18.258	0.036	11.649	17.381	0.379	6.953	3.002	0.017	0.016	0.007	
K-FAC:	0.1415	0.0003	0.0850	0.1494	0.0032	0.0475	0.0283	0.0001	0.0000	0.0001	
MPCT:	41.835	0.048	13.892	20.028	0.445	18.410	4.820	0.018	0.500	0.004	
APCT:	13.945	0.016	5.557	10.014	0.222	9.205	2.410	0.005	0.333	0.002	
Fe_2O_3	0.75										
FeO	21.36										

Table C.2 Gore Mountain Garnet Analyzed Standard

Label	SiO_2	TiO_2	Al_2O_3	FeO	MnO	MgO	CaO	P_2O_5	H_2O	V_2O_3	Total
GorePts1	38.9726	0.0414	21.7167	22.8757	0.3443	11.8211	4.197	0	0	0	***99.9688***
GorePts2	39.4874	0.0558	22.3691	22.7402	0.4752	11.5498	4.1826	0	0	0	***100.8601***
GorePts3	38.6464	0.0358	21.7958	22.6664	0.5068	11.4822	4.1809	0	0	0	***99.3143***
GorePts4	39.3447	0.0319	22.0822	22.4996	0.4339	11.6792	4.1797	0	0	0	***100.2512***
GorePts5	38.8948	0.0199	21.9965	22.516	0.3636	11.6763	4.3047	0	0	0	***99.7718***
GorePts6	39.0863	0.0359	22.352	22.8838	0.4113	11.5106	4.2965	0	0	0	***100.5764***
GorePts7	38.8613	0.0853	22.1468	22.3935	0.3797	11.7183	4.2007	0	0	0	***99.7856***
GorePts8	38.3686	0.0677	22.1382	22.371	0.4273	11.4687	4.0064	0	0	0	***98.8479***
Average	**38.95776**	**0.046713**	**22.07466**	**22.61828**	**0.417763**	**11.61328**	**4.193563**	**0**	**0**	**0**	**99.92201**
Std. Dev.	0.359426	0.02143	0.234496	0.203598	0.05529	0.128282	0.091428	0	0	0	0.652795

Figure C.1 EID08-3a Garnet 1 Traverse

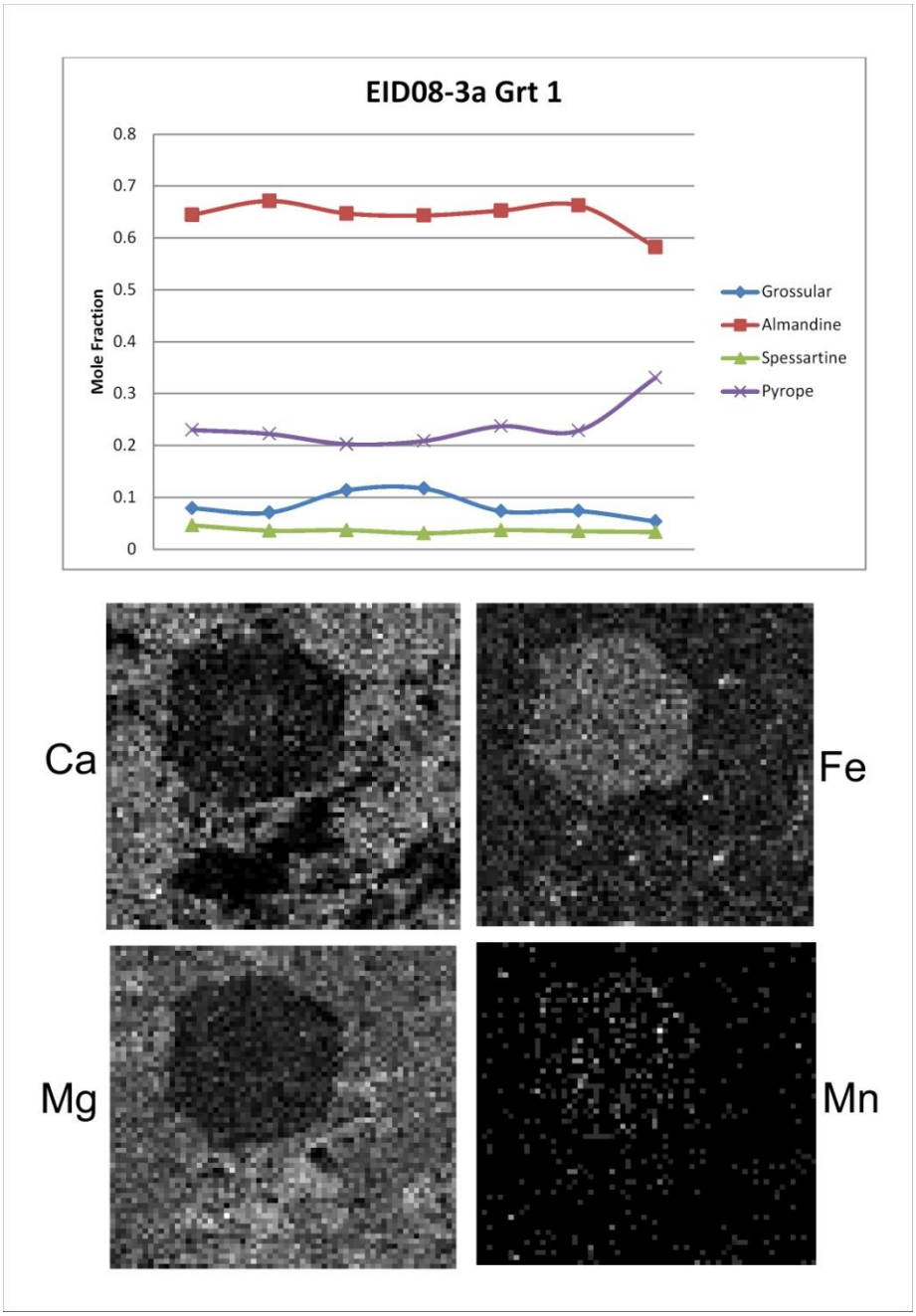

Figure C.2 EID08-3a Garnet 5 Traverse

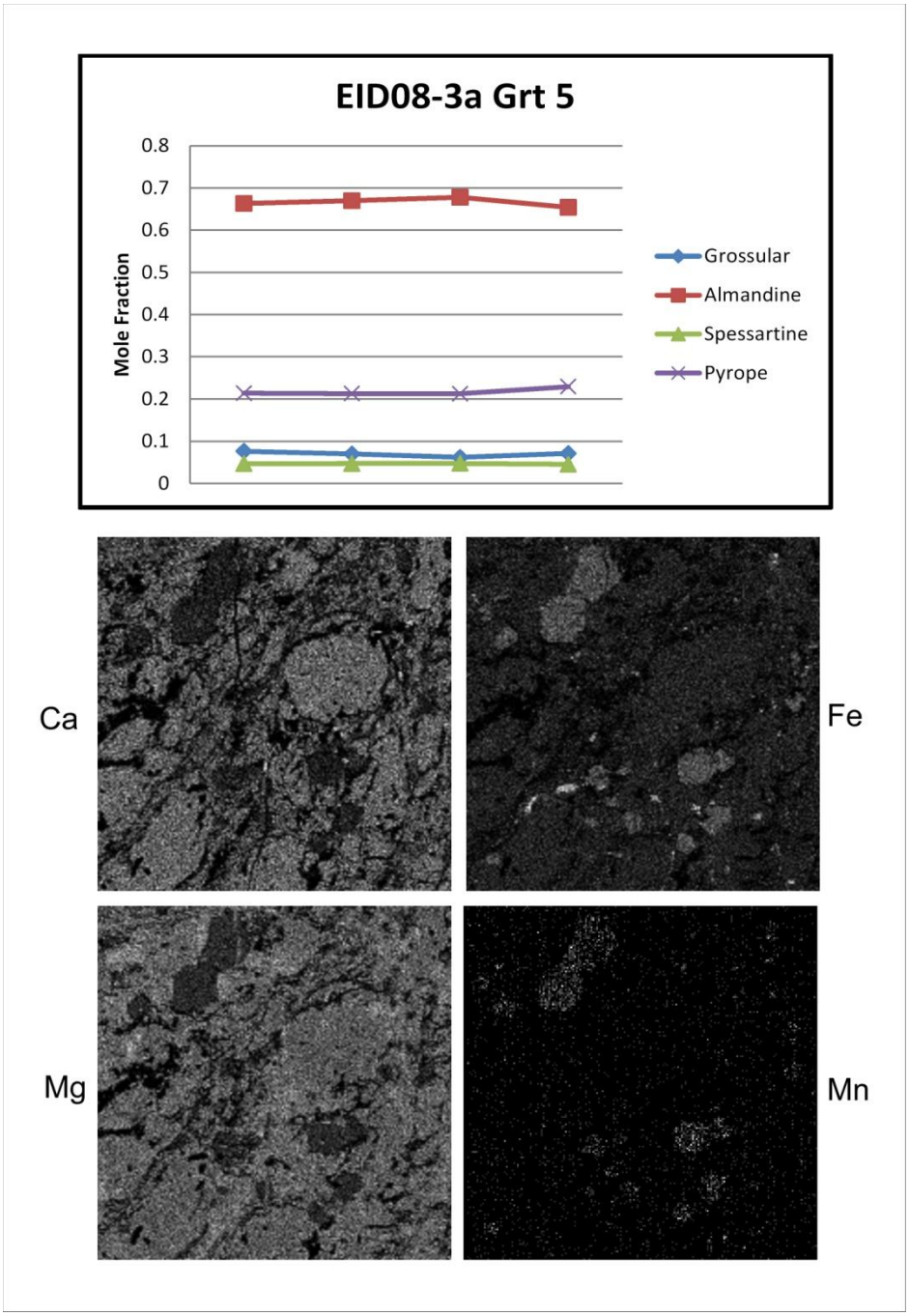

Figure C.3 EID08-3a Garnet 11 Traverse

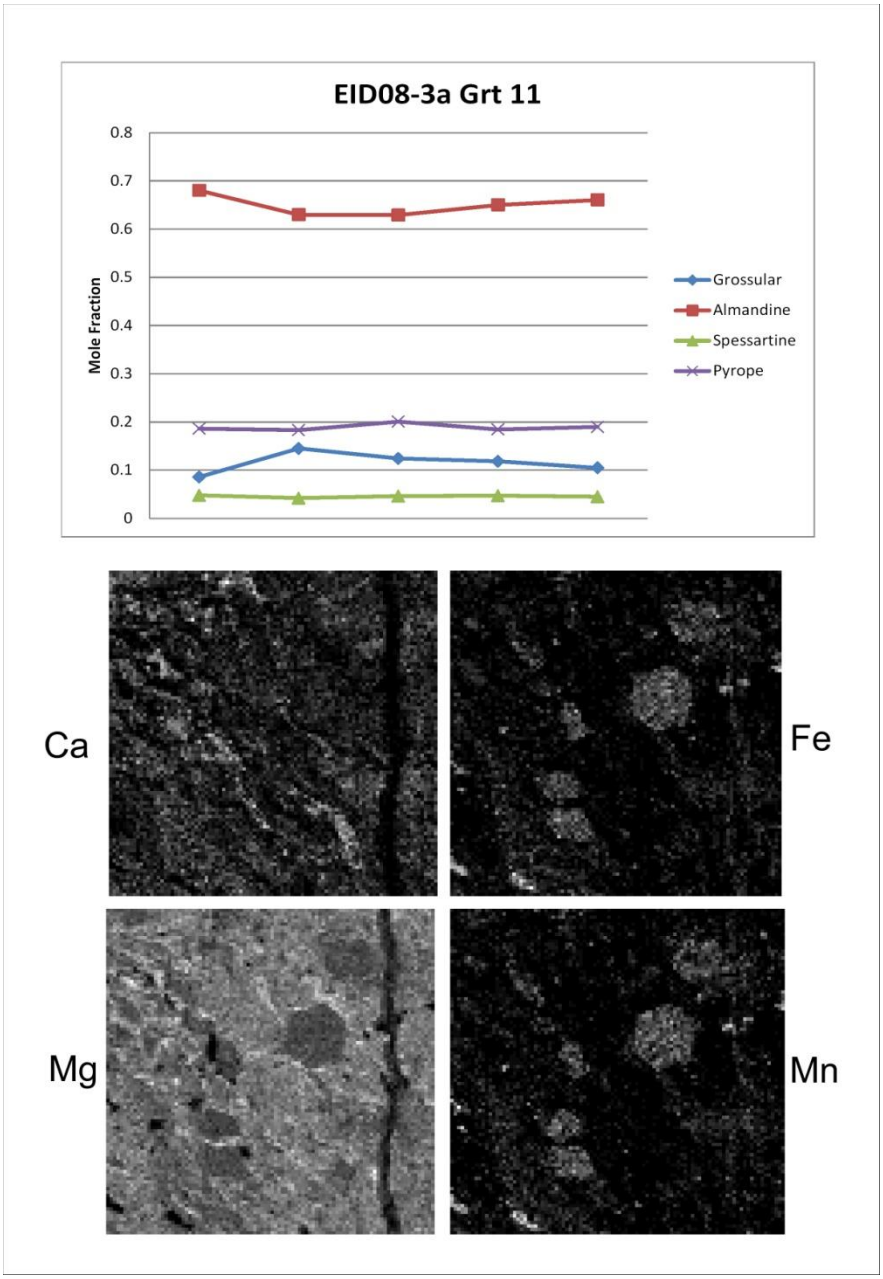

Figure C.5 EID08-4-6a-2 Garnet 1 Traverse

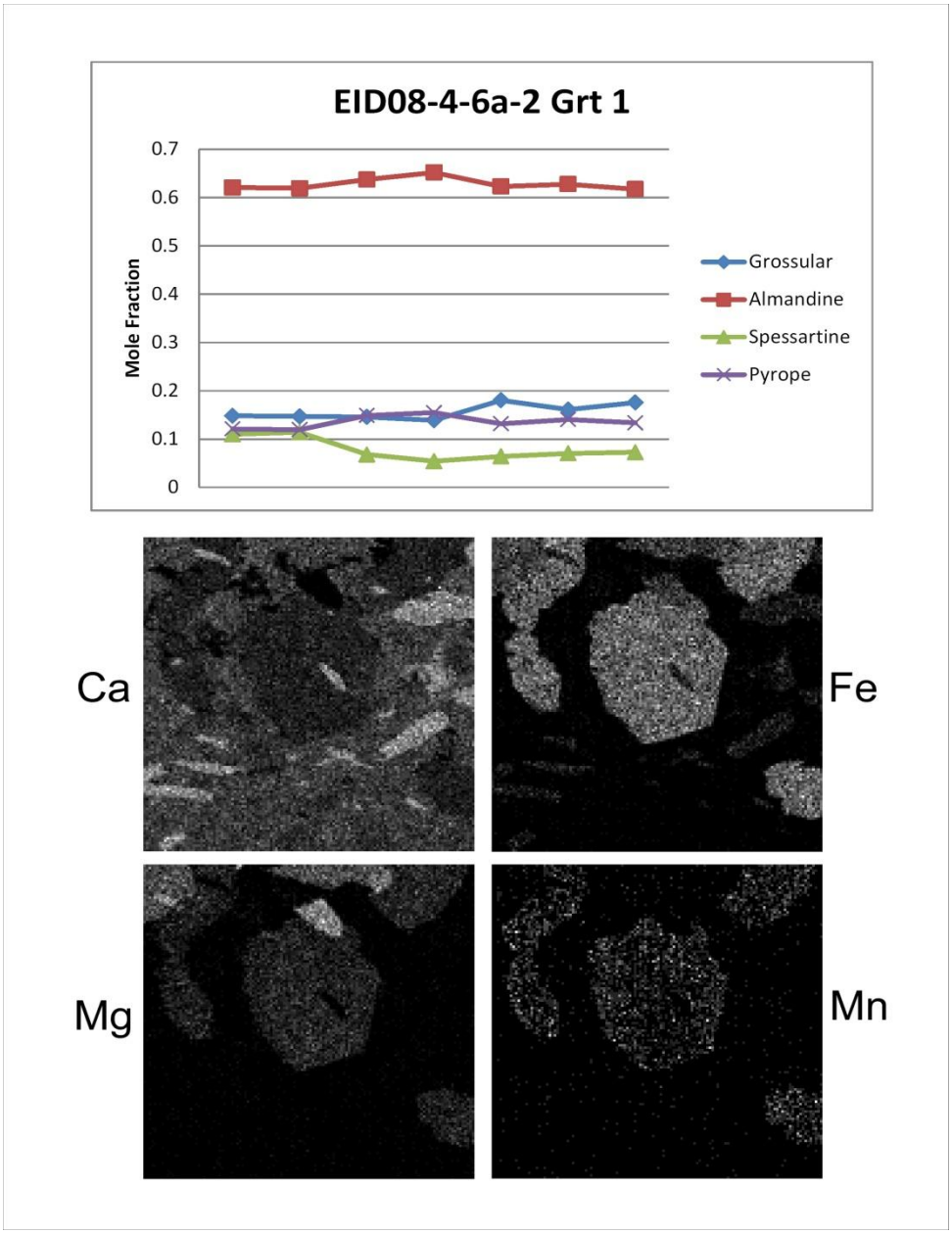

Figure C.7 EID08-4-6a-2 Garnet 4 Traverse

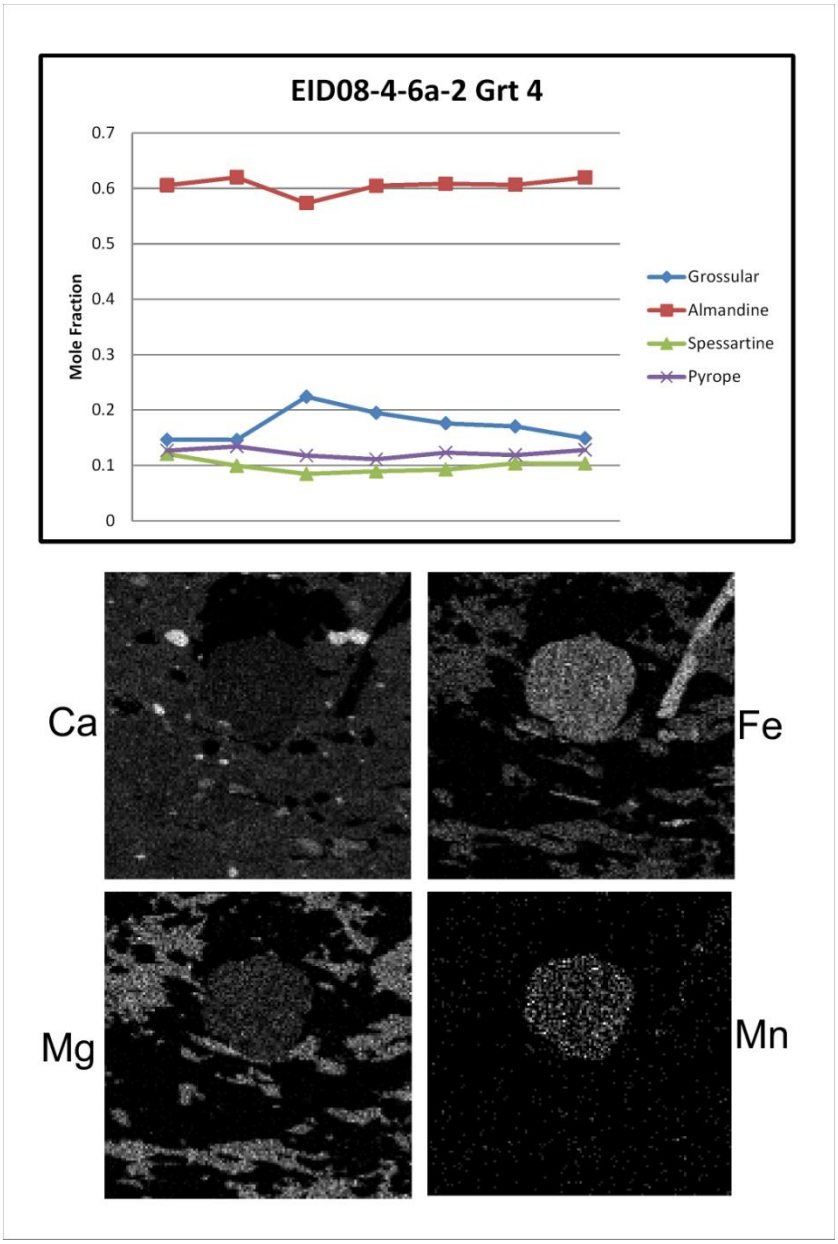

Figure C.8 EID08-7-2b Garnet 1 Traverse

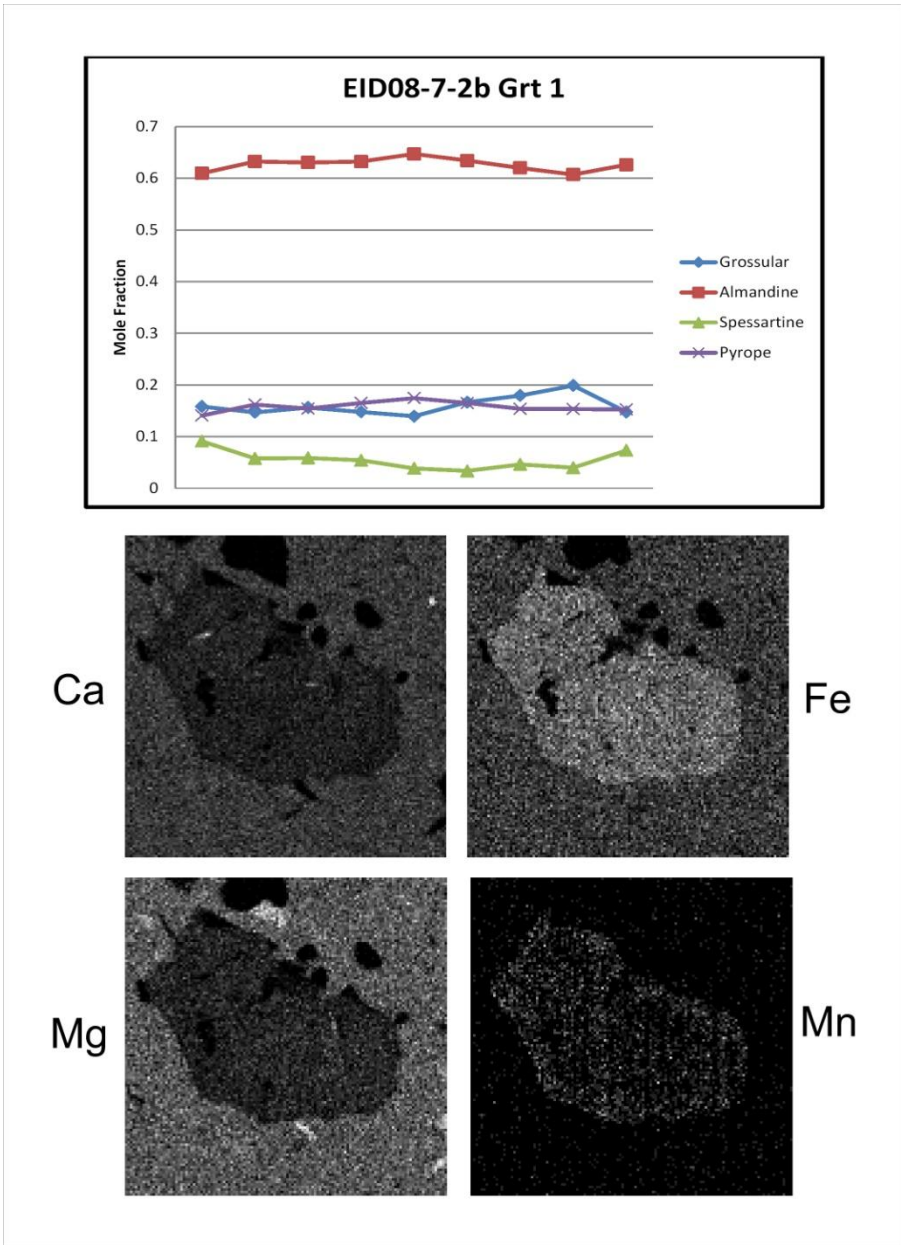

Figure C.9 EID08-7-2b Garnet 2 Traverse

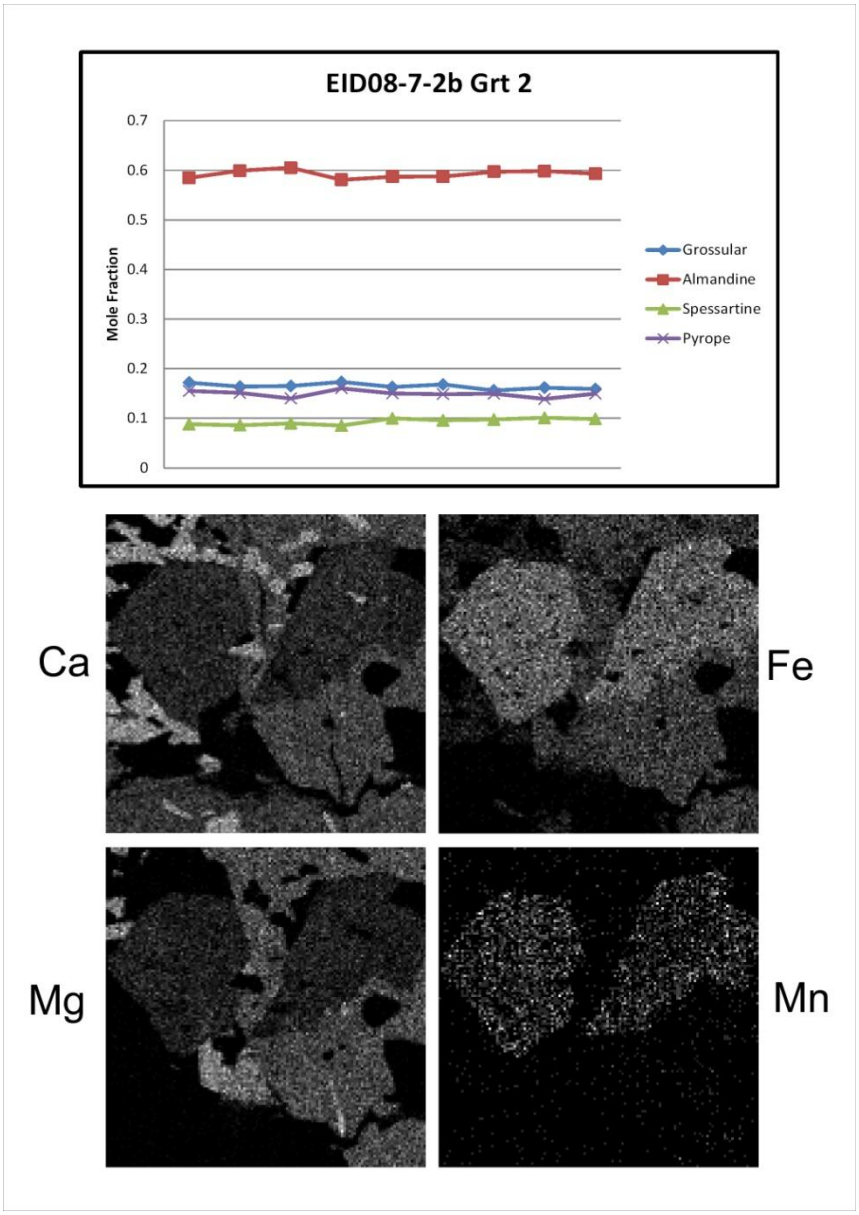

Figure C.10 EID08-7-2b Garnet 3 Traverse

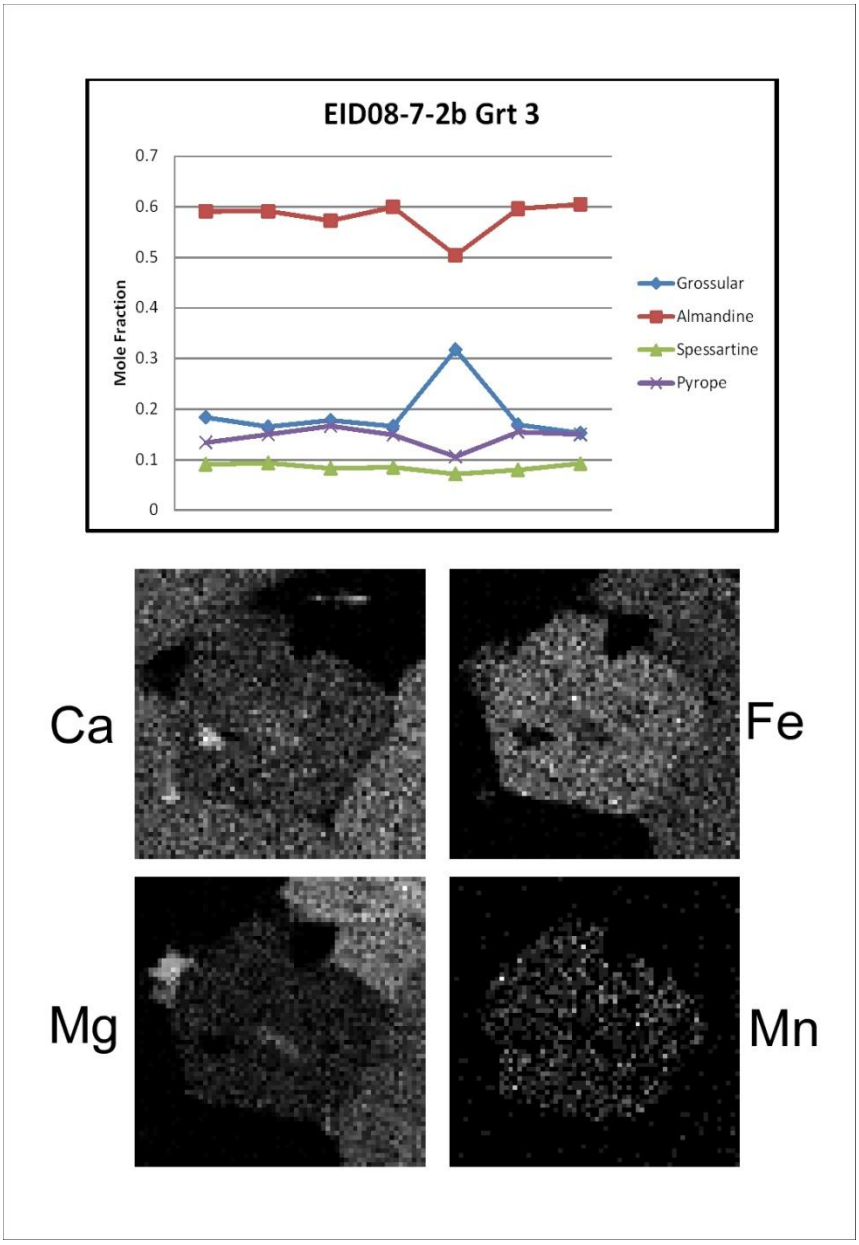

Figure C.12 EID08-7-2b Garnet 5 Traverse

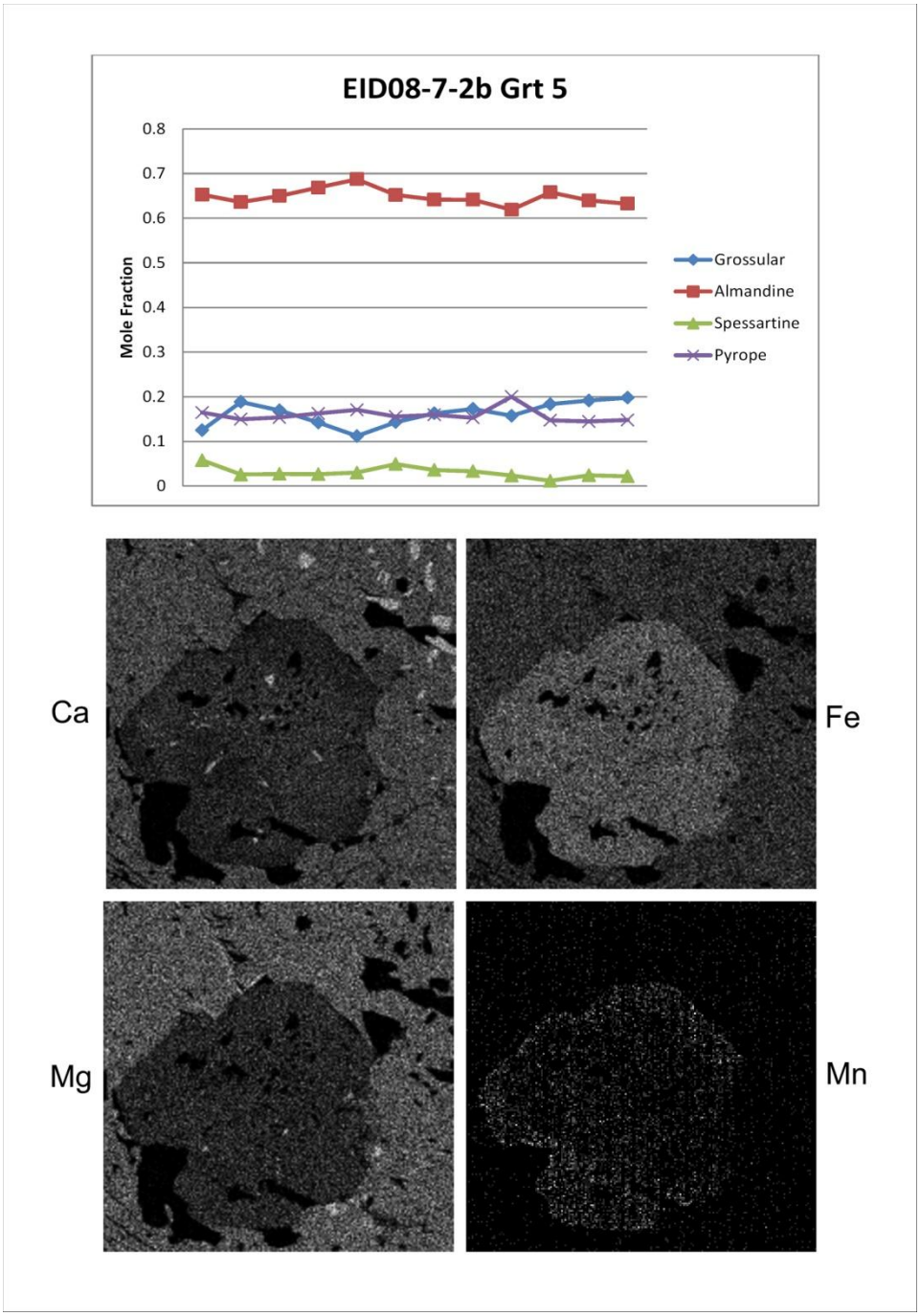

Figure C.13 EID08-7-2b Garnet 7 Traverse

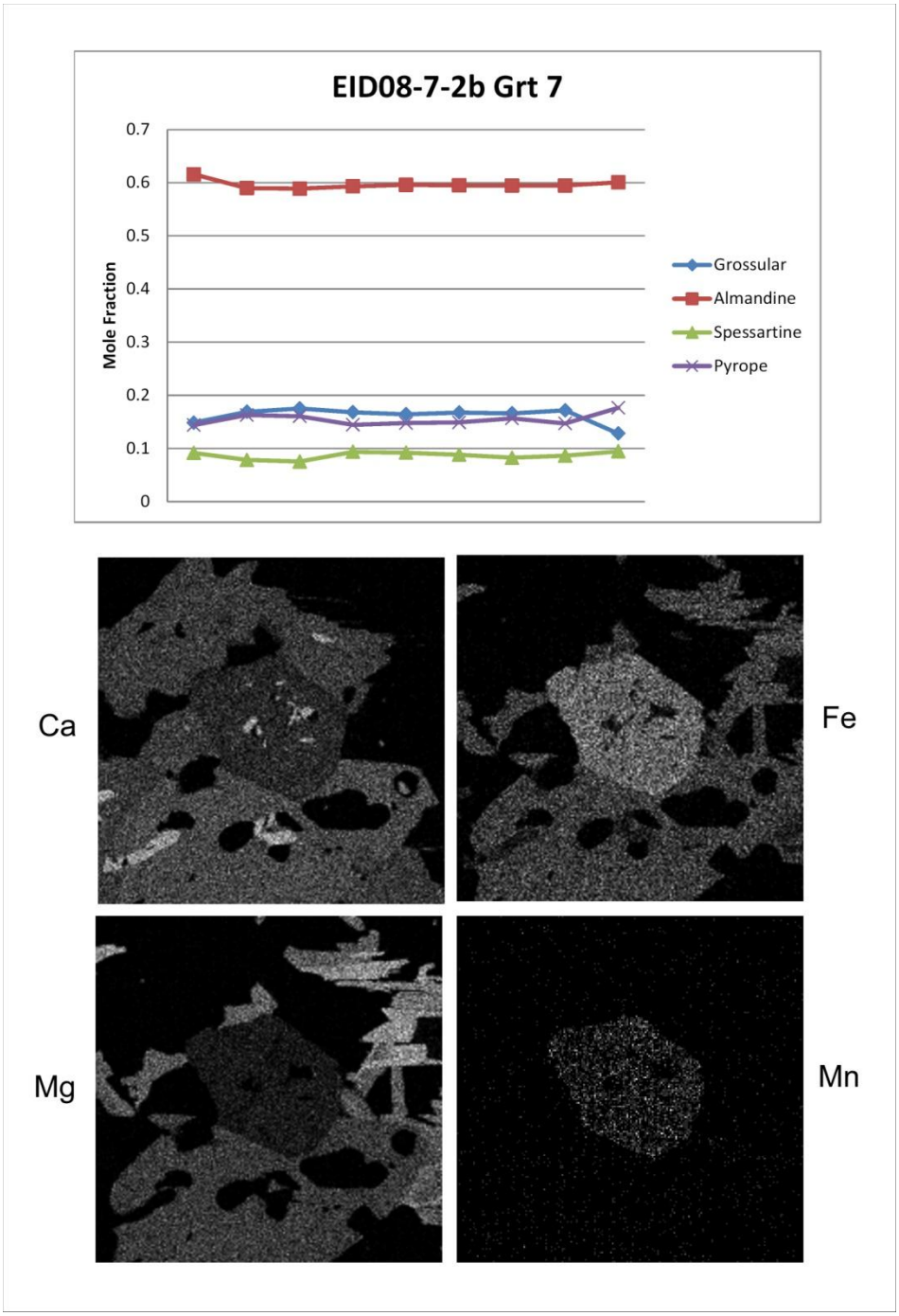

Figure C.14 FIS09-2b Garnet 2 Traverse

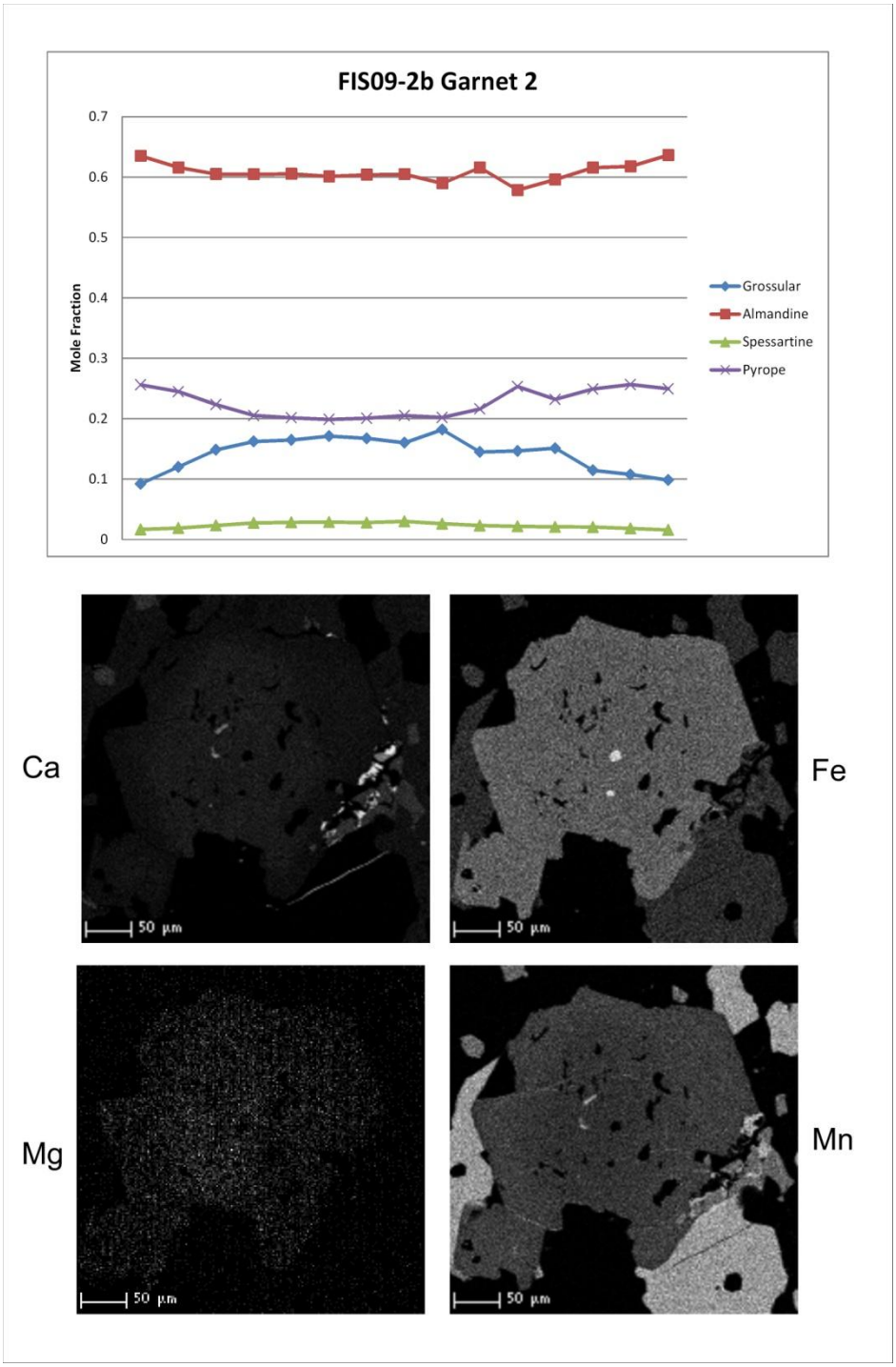

Figure C.15 FIS09-2b Garnet 3 Traverse

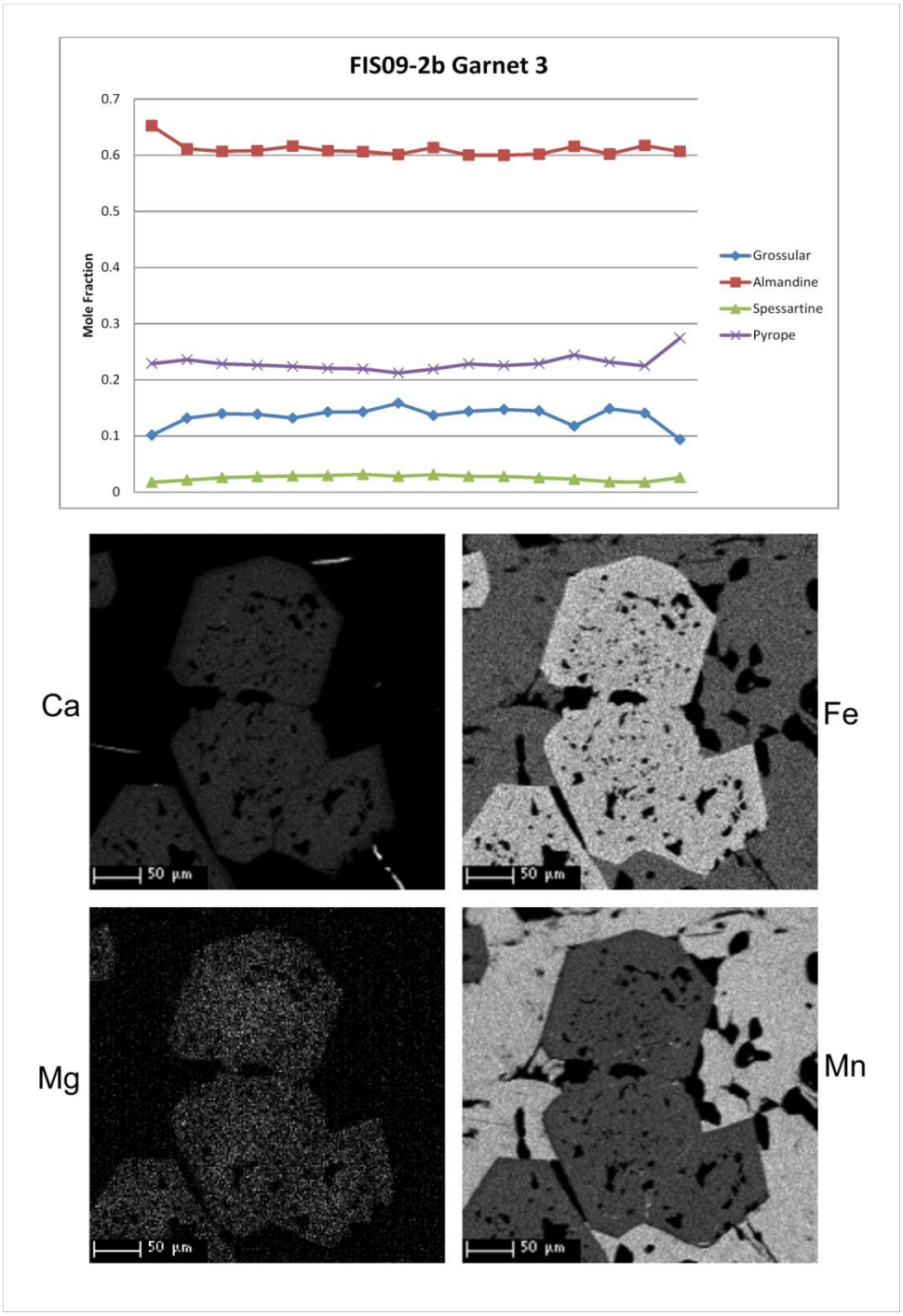

Figure C.16 FIS09-2b Garnet 4 Traverse

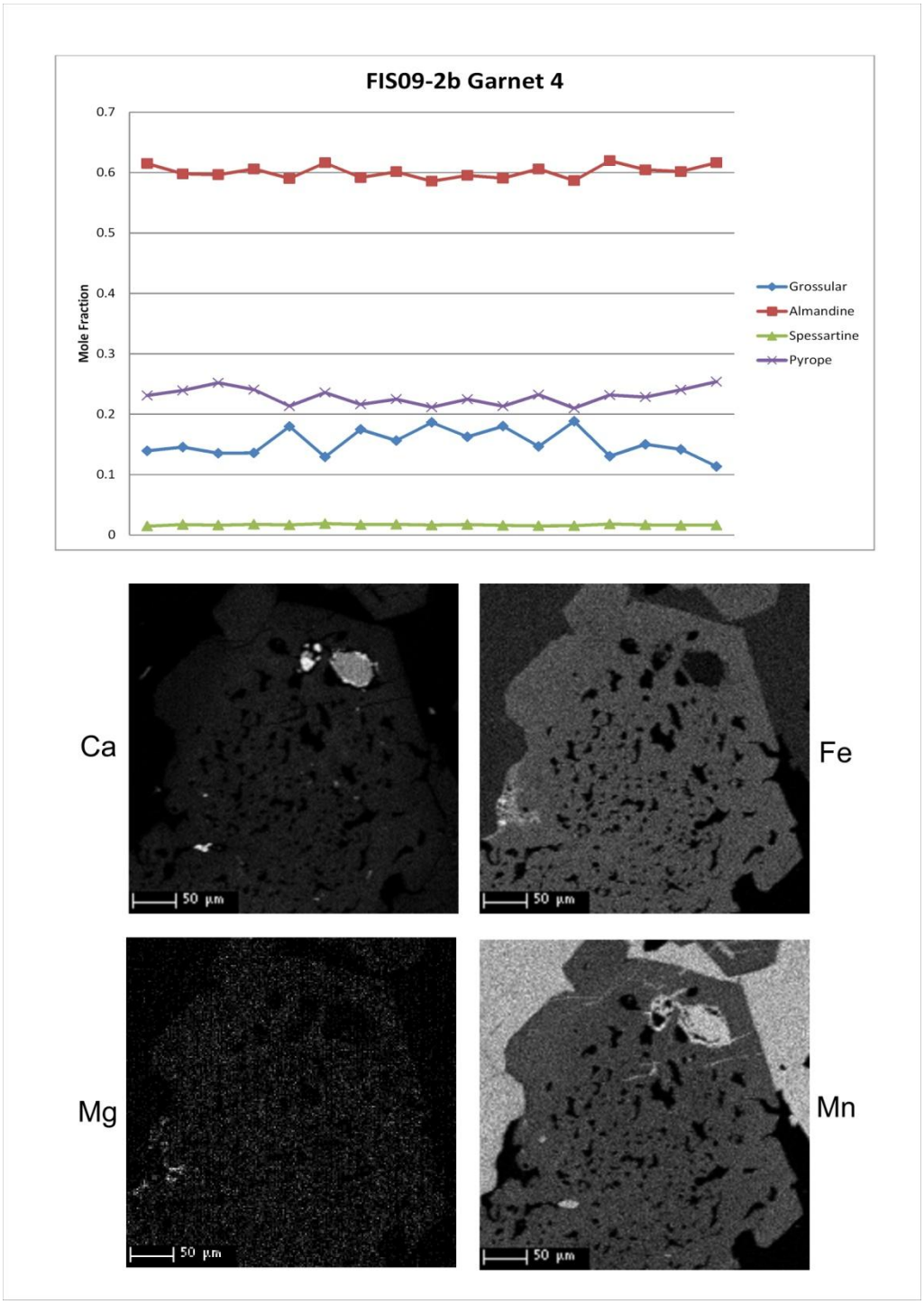

Figure C.17 FIS09-2b Garnet 5 Traverse

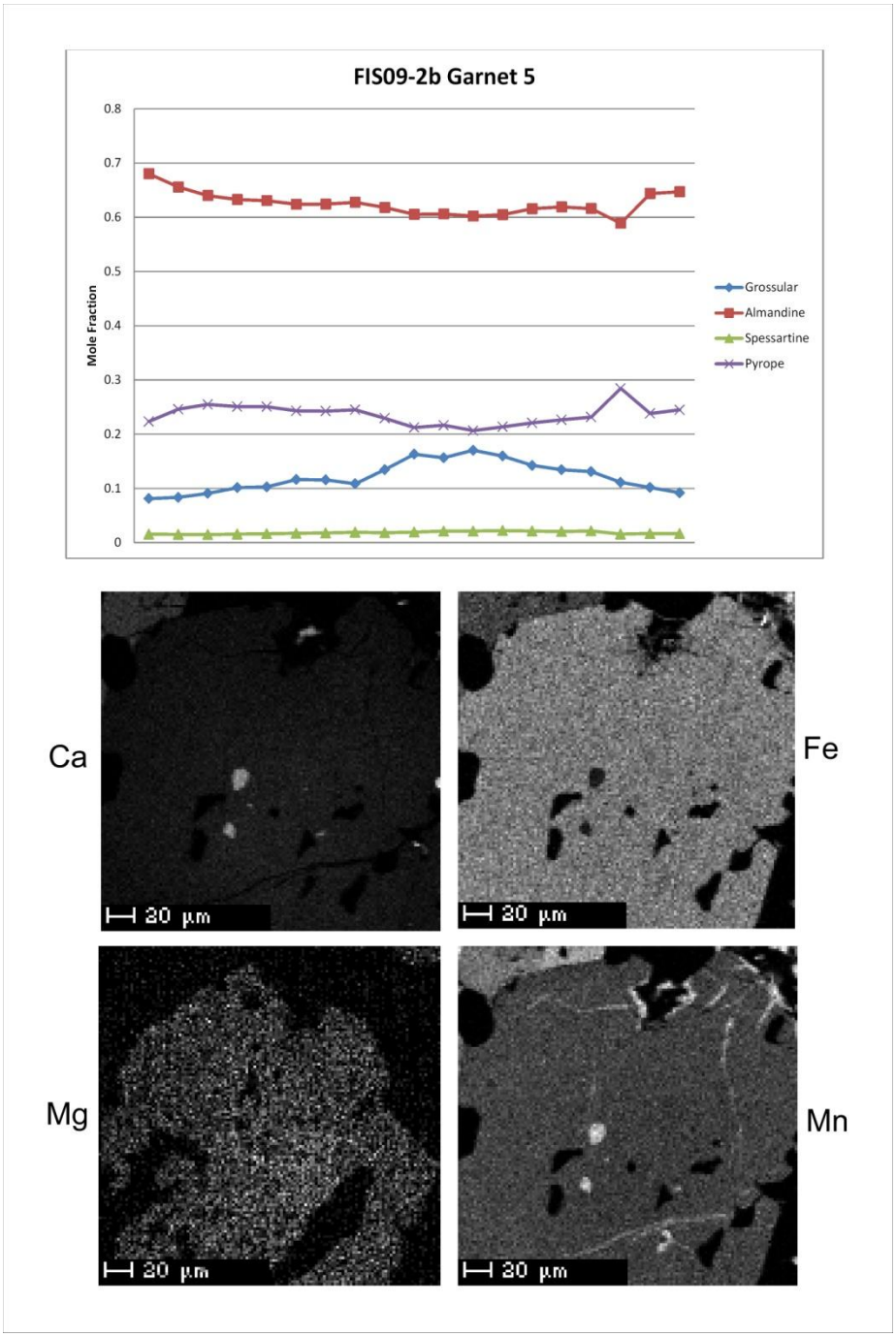

Figure C.18 FIS09-2d Garnet 1 Traverse

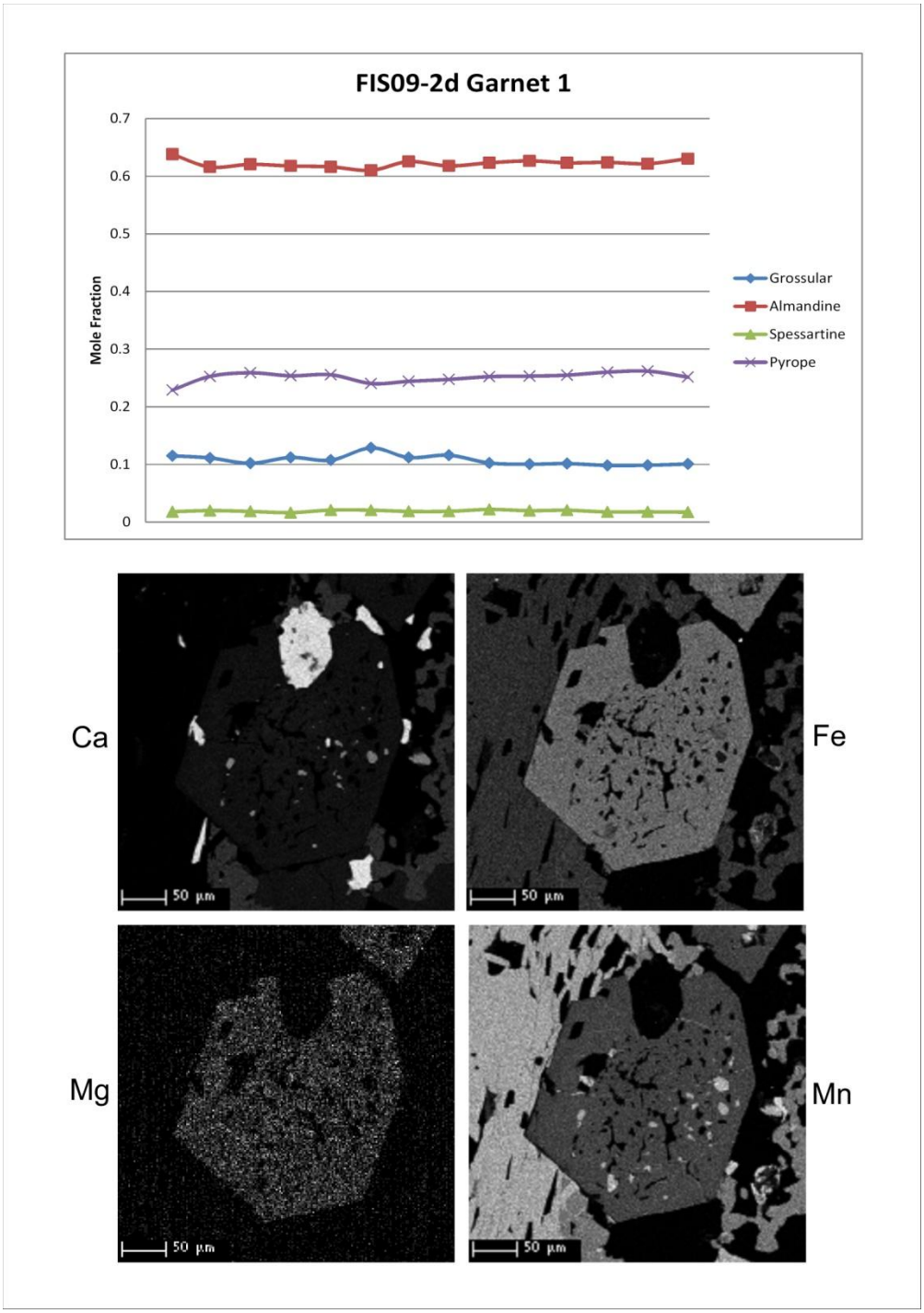

Figure C.19 FIS09-2d Garnet 2 Traverse

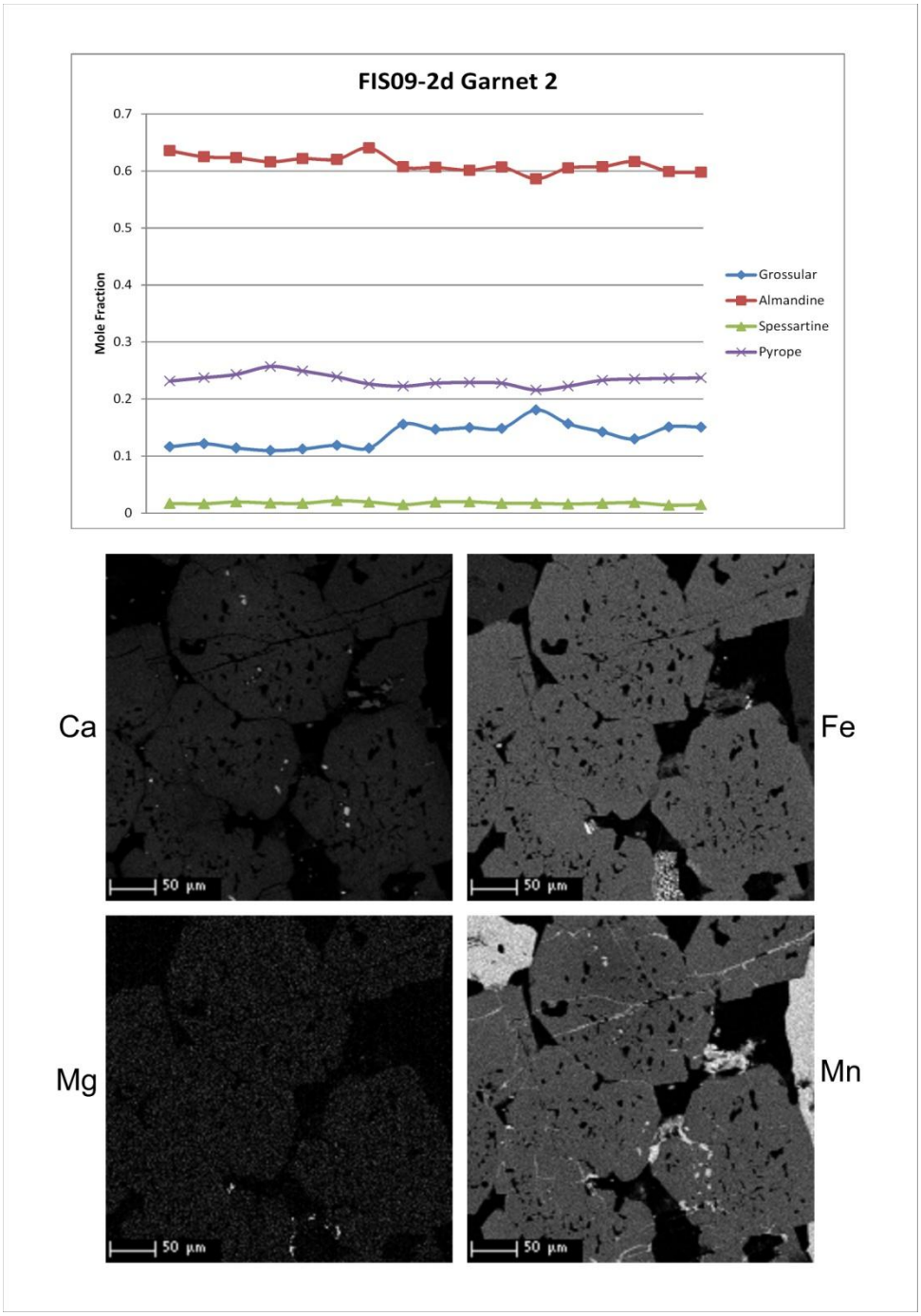

Figure C.20 FIS09-2d Garnet 3 Traverse

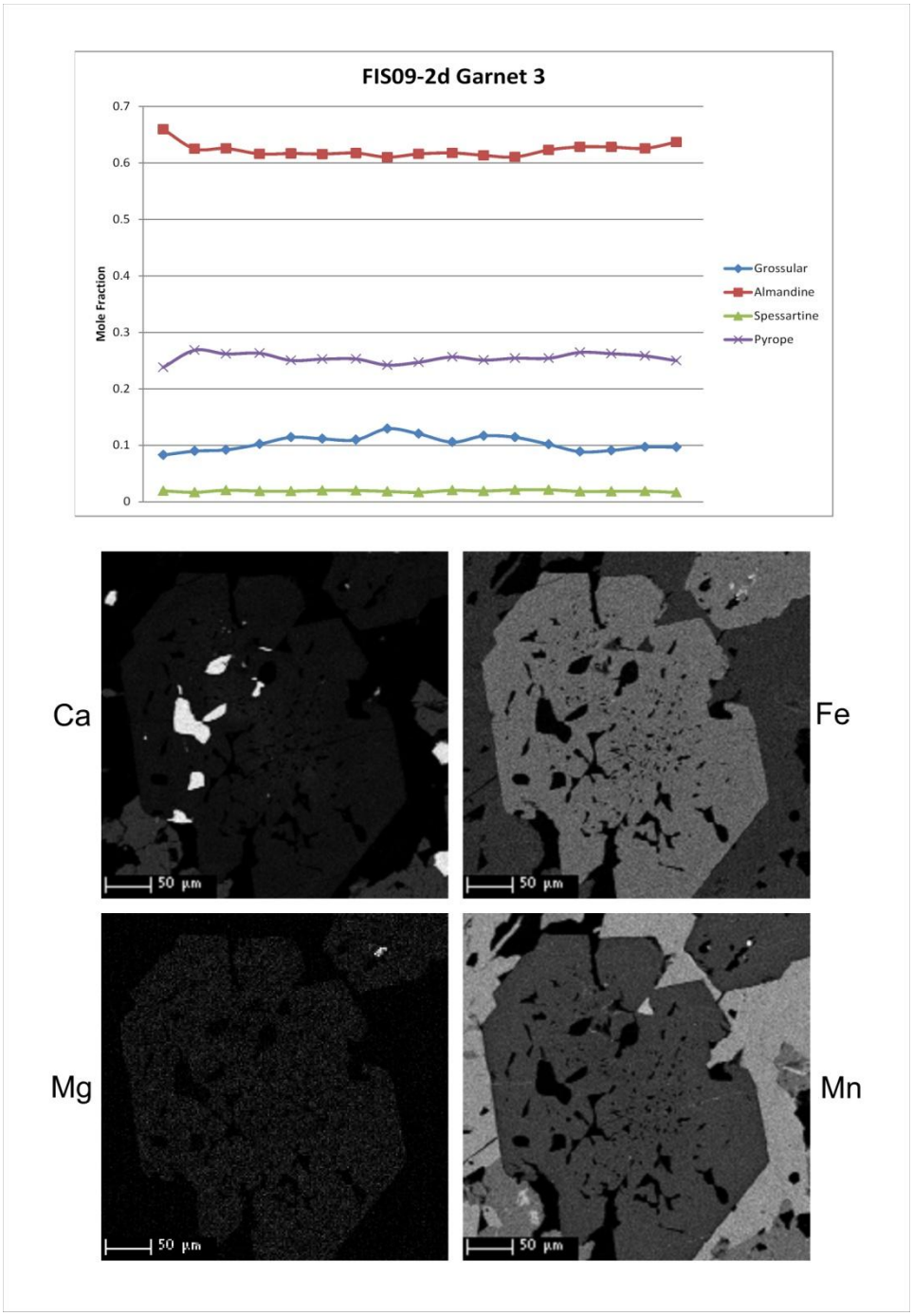

Figure C.21 FIS09-2d Garnet 5 Traverse

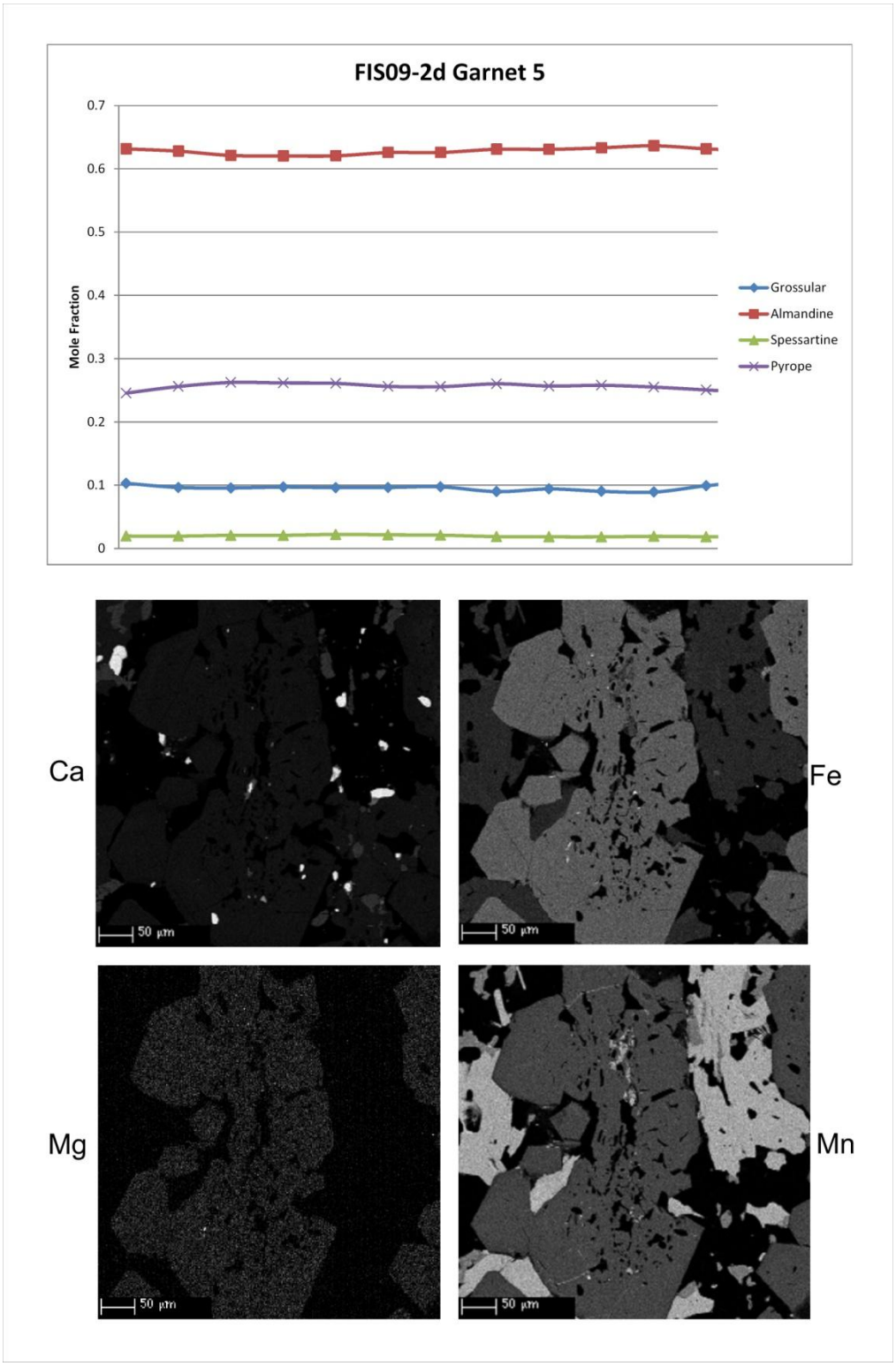

Figure C.22FIS09-3a-1b Garnet 1 Traverse

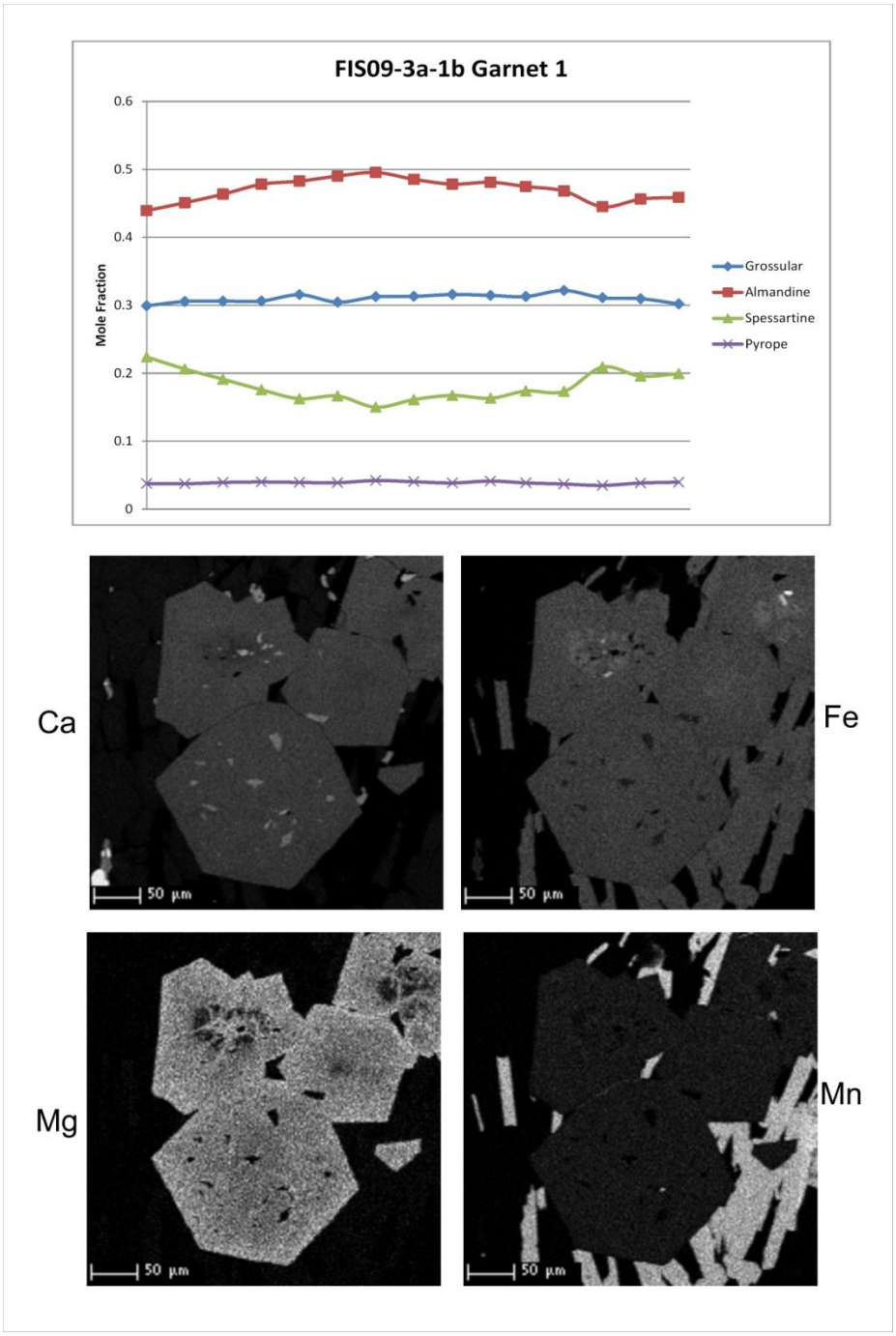

Figure C.23 FIS09-3a-1b Garnet 3 Traverse

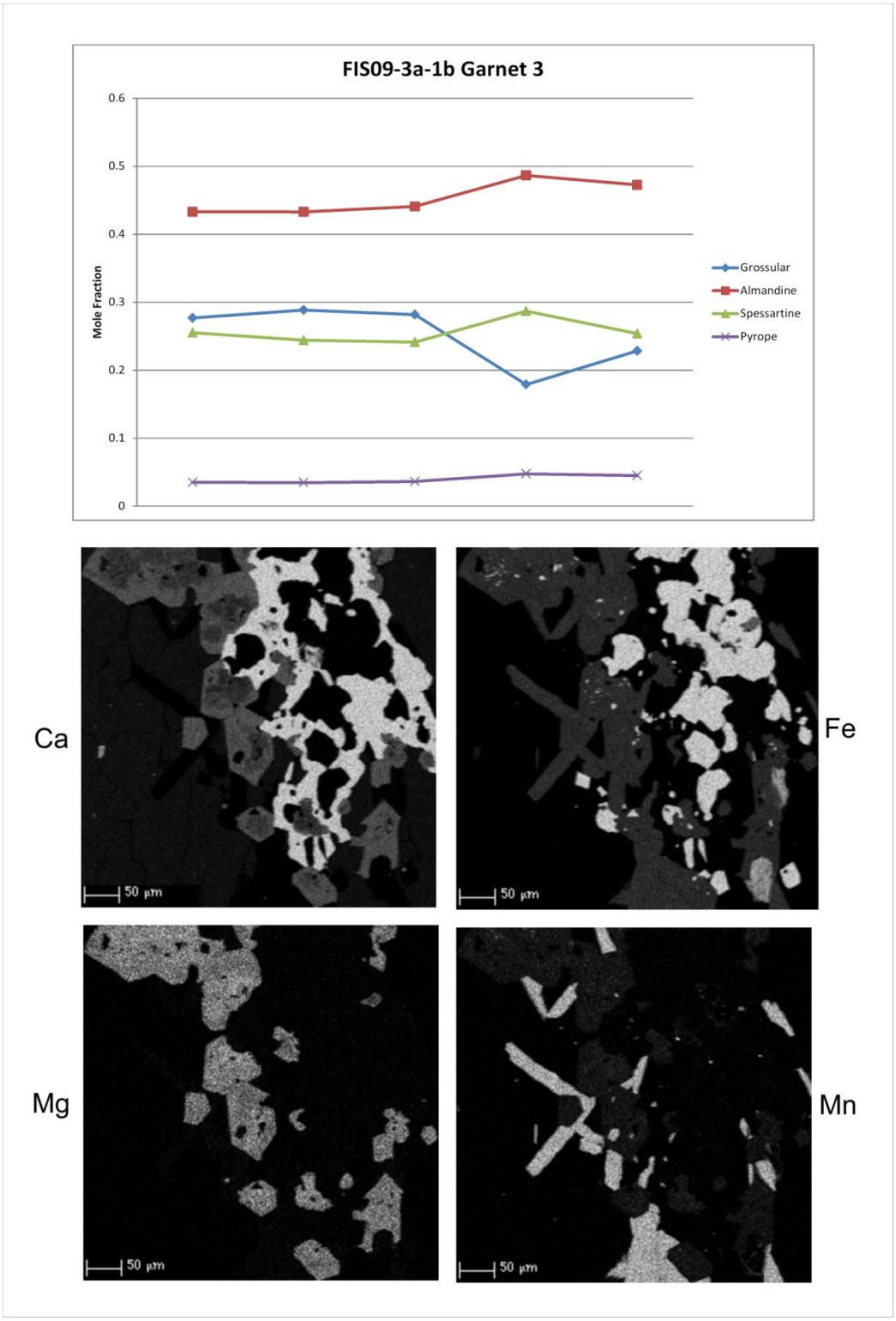

Figure C.24 FIS09-3a-1b Garnet 4 Traverse

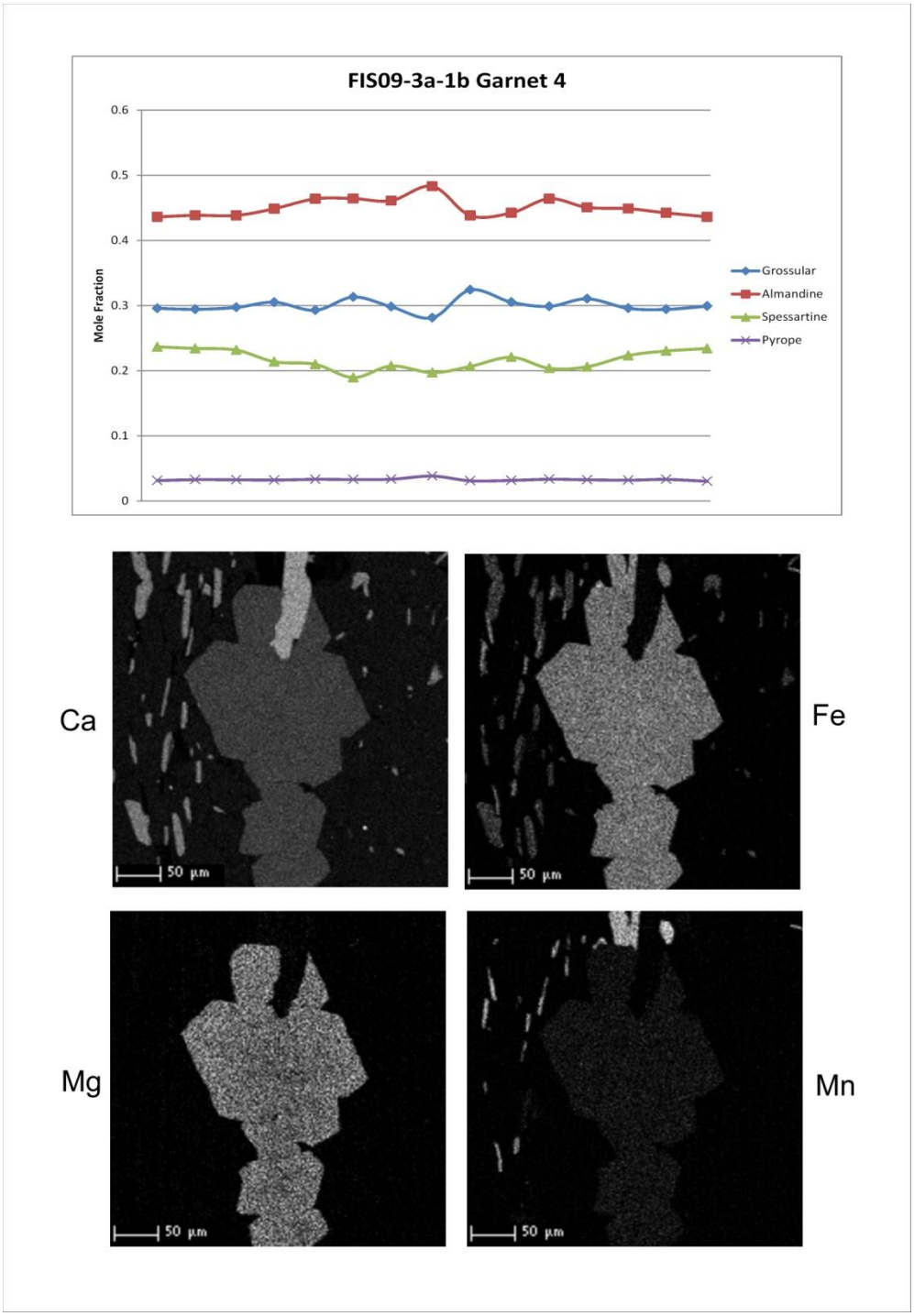

REFERENCES

Altenberger, U., Prosser, G., Ruggiero, M., and Günter, C. 2011. Microstructure and petrology of a Calabrian garnet-bearing pseudotachylyte—a link to lower-crustal seismicity. *In:* Fagereng, A., Toy, V.G., and Rowland, J.V. (eds). Geology of the Earthquake Source: A Volume in Honour of Rick Sibson. Geological Society of London, Special Publications, 359, p.153-168.

Austrheim, H., and Boundy, T.M. 1994. Pseudotachylyte generated during seismic faulting and eclogitization of the deep crust. Science, 265, p. 82-83.

Austrheim, H., Erambert, M., and Boundy, T.M. 1996. Garnets recording deep crustal earthquakes. Earth and Planetary Science Letters, 139, p. 223-238.

Bergh, S.G., Eig, K., Kløvjan, O.S., Henningsen, T., Olesen, O., and Hansen, J.A. 2007. The Lofoten-Vesterålen continental margin: a multiphase Mesozoic-Palaeogene rifted shelf as shown by offshore-onshore brittle fault-fracture analysis. Norwegian Journal of Geology, 87, p. 29-58. Trondheim, ISNN 029-196X.

Brueckner, H.K.. 1998. Sinking intrusion model for the emplacement of garnet-bearing peridotites into continent collision orogens. Geology, v. 26, n. 7, p. 631-634.

Brueckner, H.K., van Roermund, H.L.M. 2004. Dunk tectonics: A multiple subduction/education model for the evolution of the Scandinavian Caledonides. Tectonics, 23, TC2004, doi:10.1029/2003TC001502.

Devlin, S., Isacks, B.L, Pritchard, M.E., Barnhart, W.D., and Lohman, R.B. 2012. Depths and focal mechanisms of crustal earthquakes in the central Andes determined from teleseismic waveform analysis and InSAR. Tectonics, 31, TC2002, doi:10.1029/2011TC002914.

Di Toro, G., Hirose, T., Nielsen, S., and Shimamoto, T. 2006. Relating high-velocity rock-friction experiments to coseismic slip in the presence of melts. *In:* Abercrombie, R., McGarr, A., Di Toro, G., and Kanamori, H., (eds). Earthquakes: Radiated Energy and the Physics of Faulting. American Geophysical Union, Geophysical Monograph, 170, p. 121-134.

Fagereng, Å., and Toy, V.G. 2011. Geology of the earthquake source: an introduction. *In:* Fagereng, A., Toy, V.G., and Rowland, J.V. (eds). Geology of the Earthquake Source: A Volume in Honour of Rick Sibson. The Geological Society of London, Special Publications, 359, p. 1-16.

Fossen, Haakon. 1992. The role of extensional tectonics in the Caledonides of south Norway. Journal of Structural Geology, v. 14, no.8/9, p.1033-1046.

Gee, D.G. 1975. A Tectonic model for the central part of the Scandinavian Caledonides. American Journal of Science, 275-A, p. 468-515.

Gibbons, W., Doig, R., Gordon, T., Murphy, B., Reynolds, P., White, J.C. 1996. Mylonite to megabreccia: tracking fault events within a transcurrent terrane boundary in Nova Scotia, Canada. Geology, 24, p. 411-414.

Graham, C.M., Powell, R. 1984. A garnet—hornblende geothermometer: calibration, testing, and application to the Pelona Schist, Southern California. Journal of Metamorphic Geology, 3, p. 13-21.

Heier, K.S., and Thoresen, K. 1971. Geochemistry of high grade metamorphic rocks, Lofoten-Vesterålen, North Norway. Geochimica et Cosmochimica Acta, 35, p. 89-99.

Hendriks, B.W.H., Osmundsen, P.T., and Redfield, T.F. 2010. Normal faulting and block tilting in Lofoten and Vesterålen constrained by Apatite Fission Track data. Tectonophysics, 485, p. 154-163.

Hobbs, B.E., Ord, A., and Teyssier, C. 1986. Earthquakes in the Ductile Regime? Pure and Applied Geophysics, v. 124, 1-2, p. 309-336, DOI: 10.1007/BF00875730

Hobbs, B.E., Tanaka, H., and Iio, Y. 2002. Acceleration of slip motion in deep extensions of seismogenic faults in and below the seismogenic region. Earth Planets Space, 54, p. 1195-1205.

Iio, Y., and Kobayashi, Y. 2002. A physical understanding of large intraplate earthquakes. Earth Planets Space, 54, p. 1001-1004.

Kirkpatrick, J.D., Shipton, Z.K., and Persano, C. 2009. Pseudotachylytes: rarely generated, rarely preserved, or rarely reported? Bulletin of the Seismological Society of America, 99, n.1, p. 382-388.

Klein, A.C., Steltenpohl, M.G., Hames, W.E., and Andresen, A. 1999. Ductile and brittle extension in the southern Lofoten Archipelago, north Norway: Implications for differences in tectonic style along an ancient collisional margin. American Journal of Science, 299, p. 69-89.

Kohn, M.J., and Spear, F.S. 1989. Empirical calibration of geobarometers for the assemblage garnet+hornblende+plagioclase+quartz. American Mineralogist, 74, p. 77-84.

Kohn, M.J., and Spear, F.S. 1990. Two new geobarometers for garnet amphibolites, with applications to southeastern Vermont. American Mineralogist, 75, p. 89-96.

Krogh Ravna, E. 2000. The garnet—clinopyroxene Fe2+—Mg geothermometer: an updated calibration. Journal of Metamorphic Geology, v. 18, p. 211-219.

Lachenbruch, A.H., and Sass, J. 1980. Heat flow and energetic of the San Andreas fault zone. Journal of Geophysics Research, 85, p. 6185-6222.

Lin, A. 1999. Roundness of clasts in pseudotachylytes and cataclastic rocks as an indicator of frictional melting. Journal of Structural Geology, 21, p. 473-478.

Lin, A., Maruyama, T., Aaron, S., Michibayashi, K., Camacho, A., and Kano, K. 2005. Propagation of seismic slip from brittle to ductile crust: Evidence from pseudotachylyte of the Woodroffe thrust, central Australia. Tectonophysics, 402, p. 21-35.

Løseth, H. and Tveten, E. 1996. Post-Caledonian structural evolution of the Lofoten and Vesterålen offshore and onshore areas. Norsk Geologisk Tidsskrift, 76, p. 215-230.

Maddock, R.H. 1983. Melt origin of fault-generated pseudotachylytes demonstrated by textures. Geology, 11, p. 105-108.

Maddock, R.H., Grocott, J., and Van Nes, M. 1987. Vesicles, amygdales and similar structures in fault-generated pseudotachylytes. Lithosphere, 20, p. 419-423.

Magloughlin, J.F. 1992. Microstructural and chemical changes associated with cataclasis and frictional melting at shallow crustal levels: the cataclasite—pseudotachylyte connection. Tectonophysics, 204, p.243-260.

Magloughlin, J.F., and Spray, J.G. 1992. Frictional melting processes and products in geological materials—introduction and discussion. Tectonophysics, 204, p. 197-206.

McKerrow, W.S., Niocaill, C.M., & Dewey, J.F. 2000. The Caledonian Orogeny redefined. Journal of the Geological Society, London, 157, p. 1149-1154.

Moecher,D.P., and Brearley, A.J. 2004. Mineralogy and petrology of a mullite-bearing pseudotachylyte: Constraints on the temperature of a coseismic frictional fusion. American Mineralogist, 89, p. 1486-1495.

Moecher, D.P., and Steltenpohl, M.G. 2009. Direct calculation of rupture depth for an exhumed paleoseismogenic fault from mylonitic pseudotachylyte. Geology, v. 37, n. 11, p. 999-1002.

Moecher, D.P., and Steltenpohl, M.G. 2011. Petrologic evidence for co-seismic slip in extending middle to lower continental crust: Heier's Zone of Pseudotachylyte, North Norway. *In:* Fagereng, A., Toy, V.G., and Rowland, J.V. (eds). Geology of the Earthquake Source: A Volume in Honour of Rick Sibson. The Geological Society of London, Special Publications, 359, p. 169-186.

Osmundsen, P.T., Sommaruga, A., Skilbrei, J.R., and Olesen, O. 2002. Deep structure of the Mid Norway rifted margin. Norwegian Journal of Geology, 82, p. 205-224.

Osmundsen, P.T., and Ebbing, J. 2008. Styles of extension offshore mid-Norway and implications for mechanisms of crustal thinning at passive margins. Tectonics, v. 27, TC6016, doi:10.1029/2007TC002242.

Osmundsen, P.T., Redfield, T.F., Hendriks, B.H.W., Bergh, S., Hansen, J.A., Henderson, I.H.C., Dehls, J., Lauknes, T.R., Larsen, Y., Anda, E., and Davidsen, B. 2010. Fault-controlled alpine topography in Norway. Journal of the Geological Society in London, 167, p. 83-98.

Passchier, C.W. 1984. The generation of ductile and brittle shear bands in a low-angle mylonite zone. Journal of Structural Geology, v. 6, no.3, p. 273-281.

Pennacchioni, G., and Cesare, B. 1997. Ductile-brittle transition in pre-Alpine amphibolites facies mylonites during evolution from water-present to water-deficient conditions (Mont Mary nappe, Italian Western Alps). Journal of Metamorphic Geology, 15, p. 777-791.

Pickering, K.T., and Smith, A.G. 2004. The Caledonides—An essay., *in*, Earth Structure, 2nd Edition, p. 593-606. W. W. Norton and Co.

Plattner, U., Markl, G., and Sherlock, S. 2003. Chemical heterogeneities of Caledonian (?) pseudotachylites in the Eidsfjord Anorthosite, north Norway. Contributions to Mineralogy and Petrology, 145, p. 316-338.

Powell, R., and Holland, T.J.B. 2008. On thermobarometry. Journal of metamorphic Geology, 26, p. 155-179.

Price, N.A., Johnson, S.E., Gerbi, C.C., and West, D.P., Jr. 2012. Identifying deformed pseudotachylyte and its influence on the strength and evolution of a crustal shear zone at the base of the seismogenic zone. Tectonophysics, v. 518-521, p. 63-83.

Ravna, E.K. 2000. Distribution of Fe^{2+} and Mg between coexisting garnet and hornblende in synthetic and natural systems: an empirical calibration of the garnet—hornblende Fe—Mg geothermometer. Lithos, 53, p. 265-277.

Ray, S.K. 1999. Transformation of cataclastically deformed rocks to pseudotachylyte by pervasion of frictional melt: inferences from clast-size analysis. Tectonophysics, 301, p. 283-304.

Regenauer-Lieb, K., and Yuen, D.A. 2003. Modeling shear zones in geological and planetary sciences: solid- and fluid-thermal—mechanical approaches. Earth-Sciences Reviews, 63, p. 295-349.

Regenauer-Lieb, K., Rosenbaum, G., and Weinberg, R.F. 2008. Strain localization and weakening of the lithosphere during extension. Tectonophysics, 458, p. 96-104.

Rice, J.R., and Cocco, M. 2007. Seismic Fault Rheology and Earthquake Dynamics. *In:* Handy, M.R., Hirth, G., and Hovius, N. (eds). Tectonic Faults: Agents of Change on a Dynamic Earth. Dahlem Workshop on the Dynamics of Fault Zones. Cambridge, Mass: MIT Press, p. 99-137.

Ruff, L.J. 2004. Limits of the Seismogenic Zone. *In:* Karner, G.D., Taylor, B., Driscoll, N.W., and Kohlstedt, D.L. (eds). Rheology and Deformation of the Lithosphere at Continental Margins. New York: Columbia University Press, p. 138-165.

Scholz,C.H. 1988. The brittle-plastic transition and the depth of seismic faulting. Geologische Rundschau, 77, pg. 319-328.

Scholz, C.H. 2002. The Mechanics of Earthquakes and Faulting, 2nd Edition. Cambridge University Press.

Schuhmacher, R. 1991. Compositions and phase relations of calcic amphiboles in epidote- and clinopyroxene-bearing rocks of the amphibolites and lower granulite facies, central Massachusetts, USA. Contributions of Mineralogy and Petrology, 108, p. 196-211.

Sibson, R.H. 1975. Generation of pseudotachylyte by ancient seismic faulting. Geophysical Journal Royal Astronomical Society, 43, p. 775-794.

Sibson, R.H. 1977. Fault Rocks and fault mechanisms. Journal of the Geological Society of London, 133, p. 191-213.

Sibson, R.H. 1980. Transient discontinuities in ductile shear zones. Journal of Structural Geology, vol. 2, no. ½, p. 165-171.

Sibson, R.H. 1982. Fault zone models, heat flow, and the depth distribution of earthquakes in the continental crust of the United States. Bulletin of the Seismological Society of America, 72, 151-163.

Sibson, R.H. 1983. Continental fault structure and the shallow earthquake source. Journal of the geological Society of London, 140, p. 741-767.

Sibson, R.H. 2003. Thickness of the seismic slip zone. Bulletin of the Seismological Society of America, v. 93, no. 3, p. 1169-1178.

Sibson, R.H., and Toy, V.G. 2006. The habitat of fault-generated pseudotachylyte: Presence vs. Absence of Friction-Melt., *In:* Abercrombie, R., McGarr, A., Di Toro, G., and Kanamori, H., (eds). Earthquakes: Radiated Energy and the Physics of Faulting. American Geophysical Union, Geophysical Monograph, 170, p. 153-166.

Sloan, R.A., Jackson, J.A., McKenzie, D., and Priestley, K. 2011. Earthquake depth distributions in central Asia, and their relations with lithosphere thickness, shortening and extension. Geophysical Journal International, 185, p.1-29.

Spray, J.G. 1987. Artificial generation of pseudotachylyte using friction welding apparatus: simulation of melting on a fault plane. Journal of Structural Geology, vol. 9, no. 1, p. 49-60.

Spray, J.G. 1992. A physical basis for the frictional melting of some rock-forming minerals. Tectonophysics, 204, p. 205-221.

Spray, J.G. 1995. Pseudotachylyte controversy: Fact or friction? Geology, v. 23, no. 12, p.1119-1122.

Steltenpohl, M.G., Hames, W.E., and Andresen, A. 2004. The Silurian to Permian history of a metamorphic core complex in Lofoten, northern Scandinavian Caledonides. Tectonics, 23, TC1002, doi:10.1029/2003TC001522

Steltenpohl, M.G., Kassos, G., and Andresen, A. 2006. Retrograded eclogite-facies pseudotachylytes as deep-crustal paleoseismic faults within continental basement of Lofoten, north Norway. Geosphere, v. 2, no.1, p. 61-72.

Steltenpohl, M.G., Moecher, D.P., Andresen, A., Ball, J., Mager, S. 2011. The Eidsfjord shear zone: an Early Devonian, paleoseismogenic low-angle normal fault exposed in Lofoten-Vesterålen, north Norway. Journal of Structural Geology, 33, p. 1023-1043.

Swanson, M.T. 1992. Fault Structure, wear mechanisms and rupture processes in pseudotachylyte generation. Tectonophysics, 204, 223-242.

Tullis, J., and Yund, R.A. 1980. Hydrolytic weakening of experimentally deformed Westerly granite and Hale albite rock. Journal of Structural Geology, v. 2, n. 4, p. 439-451.

von Blanckenburg, F., and Davies, J.H. 1995. Slab breakoff: A model for syncollisional magmatism and tectonics in the Alps. Tectonics, 14, p. 120-131.

White, J.C. 2012. Paradoxical pseudotachylyte—Fault melt outside the seismogenic zone. Journal of Structural Geology, 38, p. 11-20.

Worley, B., and Powell, R. 2000. High-precision relative thermobarometry: theory and a worked example. Journal of Metamorphic Geology, v.18, p.91-101.

VITA

Full Name
Susan E. Leib

Birthdate
02-23-1987

Degrees Held
B.S. Geology (Olivet Nazarene University, 2009)
M.S. Geology (University of Kentucky, 2013)

Professional Positions Held
President; Olivet Geological Society (Olivet Nazarene University, 2006-2009)
Curator; Geology Department (Olivet Nazarene University, 2007-2009)
Teaching Assistant (Olivet Nazarene University, 2006-2009; University of Kentucky, 2010-2012)

Scholastic and Professional Honors
First Place, Graduate Research Competition (Kentucky Academy of Science, 98th Annual Meeting, October 2012)
Departmental Honors (Olivet Nazarene University, Dec. 2009)
Pence-Boyce Student Research Grant (Olivet Nazarene University, summer 2009)
Dean's List (Olivet Nazarene University, 2005-2008)

Professional Memberships
Geological Society of America (2008-present)
Mineralogical Society of America (2009-present)
American Association of Petroleum Geologists (2011-present)

Publications
Leib, S.E., Quinn, R.J., RiCharde, G.E., and Moecher, D.P., 2011. Geothermobarometry on mafic and pelitic gneisses from Winding Stair to Dellwood, NC: Filling the gap in Taconian P-T data in the central Blue Ridge. *Geological Society of America Abstracts with Programs*, 43, 2, 30.

Leib, S.E. and Brewer, K., 2010. Mapping the Bedrock Topography of Kankakee County, Illinois. *Geological Society of America Abstracts with Programs*, 42, 2, 64.